Design of High-Performance Antennas and Novel Electromagnetic Radiation Measurement Techniques for Biological Cells

by

Menglou Rao

A dissertation submitted in partial fulfillment
of the requirements for the degree of
Doctor of Philosophy
(Electrical and Computer Engineering)
in The University of Michigan
2022

Doctoral Committee:

Professor Kamal Sarabandi, Chair
Professor Ehsan Afshari
Associate Research Scientist Dr. Adib Nashashibi
Professor Fawwaz T. Ulaby
Assistant Professor J. Scott VanEpps

Menglou Rao

menglrao@umich.edu

ORCID iD: 0000-0002-2983-9753

This dissertation is dedicated to my mother Min Lou and my father Yanquan Rao.

ACKNOWLEDGMENTS

First and foremost, I would like to thank my parents, Yanquan Rao and Min Lou, for their unconditional love and support. They encouraged me to pursue my dreams and have been my rock during difficult times. I could not have come this far without them.

I am extremely grateful to my advisor, Professor Kamal Sarabandi, for giving me the opportunity to work with him and guiding me throughout this journey. He is a brilliant scientist, my role model and life-long inspiration. I have learned so much from him, both professionally and personally.

Special thanks go to Professor Fawwaz T. Ulaby, who is not only a great mentor, but also family to me. He is loving, caring and always very supportive of me. He made me believe in myself. I will forever treasure the perspective and insights he has shared with me and the skills he has taught me.

I would also like to take this opportunity to thank Professor Ehsan Afshari, Professor J. Scott VanEpps and Dr. Adib Nashashibi for their support and advice while serving as my dissertation committee members, especially Dr. Adib Nashashibi, who has helped me tremendously with all my experiments.

Last but not least, I would like to extend my gratitude to the former and current members in the Radiation Laboratory for their friendship and valuable input to my research. I am very fortunate to meet these amazingly talented people and get the chance to learn from them. I also want to thank all my friends at Ann Arbor. They brought a lot of fun in my life and I appreciate every moment that we have spent together.

This is a very special journey that I will remember forever. I am certain that all the friendships will continue well beyond this chapter of my life.

Menglou
May 2022
Ann Arbor

TABLE OF CONTENTS

CHAPTER

LIST OF FIGURES

Figure

LIST OF TABLES

Table

LIST OF APPENDICES

Appendix

ABSTRACT

The pursuit of compact wireless communication systems has been a major force driving research efforts toward miniaturization. Antennas, as one of the key components, are of no exception. At low frequencies, the prohibitively large size of conventional antennas constitutes a major hurdle in the realization of compact systems. In the first part of this dissertation, an extremely low-profile frequency-tunable composite antenna with enhanced gain and operational bandwidth is designed for wireless mobile systems in the very high frequency (VHF) band. The antenna is based on a recently developed miniaturized two-legged monopole antenna. By introducing 8 parasitic elements and utilizing the mutual couplings between them, we are able to enhance the antenna gain by about 10 dB. The design is further modified for frequency tunability. It achieves an operational bandwidth of 3.32%, which is about 20 times greater than the bandwidth of the original monopole. The total dimensions of the composite antenna are 470 mm × 470 mm × 50 mm ($\lambda_0/16 \times \lambda_0/16 \times \lambda_0/150$, where λ_0 is the free-space wavelength at 40 MHz). In addition, a new method for measuring the performance of a monopole antenna with an electrically small ground plane using cascaded transformers is developed and presented.

The second part of the dissertation is focused on high-performance miniaturized millimeter-wave (mmWave) antennas for 5G smartphones. To address various system requirements, three antenna arrays are proposed for mmWave 5G smartphones. The first design is a 28 GHz differential dual-polarized antenna array. The array element is composed of two discrete sub-elements, a folded dipole and a substrate integrated waveguide cavity-backed slot antenna, to provide two orthogonal linear polarizations. The array can cover the entire 28 GHz band allocated for 5G applications. The second design is a low-profile dual-band dual-polarized phased array that can simultaneously cover 26–30 GHz and 38–40 GHz. A prototype of a 1×4 phased array is designed, fabricated and tested. Good agreement against full-wave simulation is achieved. In the last design, a very compact dual-polarized array topology consisting of four sub-arrays is presented. The array can support multiple 5G bands, including the 26 GHz, 28 GHz, 37 GHz and 39 GHz bands. The overall dimensions of the array are 25 mm × 6 mm × 0.97 mm. This dissertation addresses many design challenges associated with implementing low-cost mmWave antennas in smartphones, and provides practical solutions to mmWave 5G mobile devices.

In the last part of this dissertation, novel measurement techniques are developed to explore the existence of electromagnetic (EM) radiation from bacterial biofilms. Several special measurement systems capable of measuring extremely weak signals are designed and implemented, including a wideband near-zone radiative system, a spiral antenna system and a regenerative RF sensing system. We successfully identified EM radiation from *Staphylococcus aureus* biofilms in the 3–4 GHz frequency range. Furthermore, long-term and short-term cycles of the total radiation intensity are observed over the course of a 70-day experiment. This is the first time that EM radiation from bacterial biofilms has been detected in the gigahertz frequency range. This work confirms the existence of EM radiation within bacterial communities, which is a key requirement to demonstrate EM signaling among bacterial cells.

CHAPTER I

Introduction

1.1 Motivation

With the unprecedented growth of wireless technologies, the demand for compact wireless communication systems is higher than ever. Miniaturization has made a significant impact on military, industrial, and commercial areas, and has opened up numerous avenues of new applications. The world has witnessed the development of integrated circuits which has brought about the evolution of electronic devices. It is hard to believe that computers nowadays are so compact that they can be held in the palm of a hand. Figure 1.1 illustrates the size reduction of Intel's transistors over the past 15 years. The area scaling has been improved at the rate of about 0.5 times every two years. On the other hand, regardless of significant efforts that have been devoted to antenna miniaturization, integrated antennas are still bulky and typically occupy most of the area in an RF module.

The transition from the current 4G mobile network to 5G has been driving large-scale research and development efforts to millimeter-wave (mmWave) technologies. Considering the importance of cellular devices in the mobile network industry, mmWave antennas for 5G smartphones can be considered as one of the key parts in the realization of mmWave-based mobile networks. However, implementing mmWave antennas within smartphones faces some unprecedented challenges. It is well un-

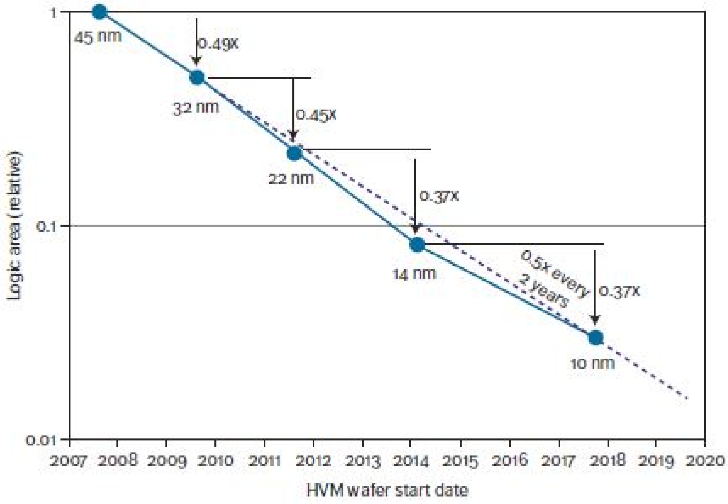

Figure 1.1: Intel's trend for scaling logic circuit area over the past five generations [1].

derstood that free-space path loss and signal attenuation, due to conductive and dielectric dissipation, are more sever at mmWave frequencies compared with the sub-6 GHz region [7]. To compensate for the excessive loss and ensure the reliability of communication links, mmWave antennas must feature high antenna gain. Meanwhile, the mobility nature of smartphones requires coverage in all directions. The inherent dilemma of antenna gain and coverage has driven the antenna community to come up with alternative solutions, such as beam-selection antenna arrays and phased-array antennas for mmWave 5G mobile antenna scenarios. Figure 1.2 illustrates a possible array configuration for 5G cellular mobile terminals. Two arrays with fan-shaped radiation patterns are located on the upper and lower edges of the smartphone to realize isotropic spherical coverage.

Nevertheless, the design of mmWave antenna arrays for 5G smartphones is a complicated task. In addition to certain general requirements for array elements, such as large bandwidth, low mutual coupling and broad beam, polarization flexibility is another important consideration for mmWave 5G mobile antennas because the polarization loss factor heavily affects the overall quality of the wireless link at mmWave frequencies [8]. Furthermore, 5G antennas need to adapt to the evolution

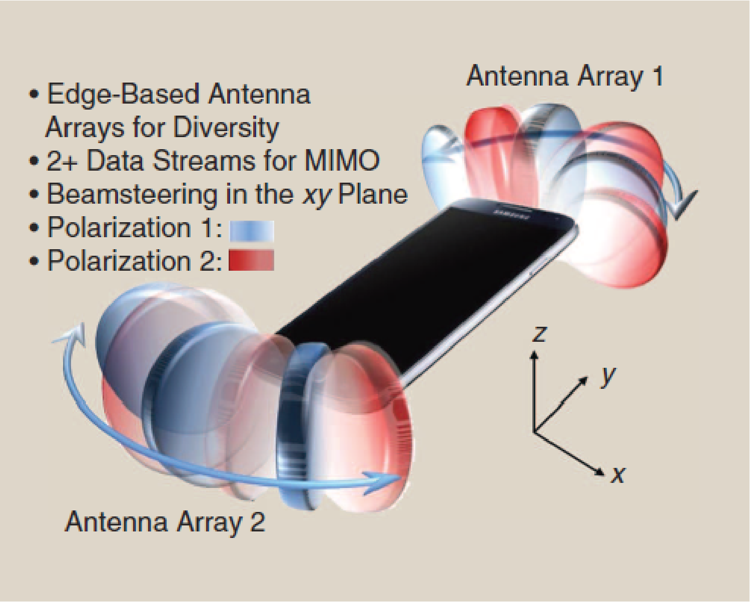

Figure 1.2: A conceptual illustration of mmWave 5G mobile antennas for smartphones [2].

of the phones. As the demand for new features emerges, the number of antennas as well as other integrated modules has been growing drastically. Stringent design constrains such as ultra-thin printed circuit boards (PCBs), limited real estate and power capacity require minimizing antenna size, which is usually in conflict with antenna bandwidth and radiation efficiency. Moreover, aesthetic trends for larger metallic displays and thinner phone chassis further restrict the maximum coverage a mobile phone can achieve. Therefore, it is imperative to design compact antennas with good radiation performance.

In addition to antenna design, characterization of antenna performance is also challenging at mmWave frequencies. Conventionally, antennas are connected to test equipment using standard coaxial cables or waveguides. However, introducing such transitions imposes sever limitations on antenna measurements in the millimeter-wave frequency region because their sizes are comparable with or even larger than the antenna under test (AUT). The uncertainty introduced by the interaction between the transition fixtures and the antenna itself is difficult to predict. It has been experimentally demonstrated that connectors can strongly disturb the antenna radiation pattern and cause serious measurement errors [9]. Additionally, unlike sub-6 GHz antennas which are treated as independent design blocks, mmWave antennas are frequently integrated with RF circuits on semiconductor chips. Measurements using transition fixtures do not fully present the true antenna performance. For these reasons, it is preferred to feed the AUT with a RF probe during measurements so that the AUT can be characterized at the point where the RF component is connected in the final application. Probe-based mmWave antenna measurements have been developed for more than two decades. Although measurement capabilities have greatly advanced, many difficulties still remain, such as pattern distortion caused by the surrounding environment, radiation from the probe body, and so on. New techniques that can further improve measurement performance are much needed.

Compared with mmWave systems, antenna miniaturization is even more demanding for low-frequency wireless communications. Studies have shown that signal reflection, scattering, and diffraction in the High Frequency (HF) and Very High Frequency (VHF) bands are much less severe than those in higher frequency bands [10] [11]. Therefore, low-frequency mobile systems can provide more reliable communication links, especially in highly clustered environments. For near-ground applications such as land mobile systems used in vehicles or unattended ground sensors, it has been shown that the propagation path-loss for vertical polarization is far less than that for horizontal polarization [12]. Monopoles are commonly preferred in such applications, primarily because of their simple structures and capability to provide an omnidirectional vertically polarized radiation pattern. However, typical quater-wavelength monopoles are too large to be implemented on mobile platforms at low frequencies. For this reason, advanced miniaturization techniques that serve to balance antenna size against performance are much needed for monopole antennas.

Another aspect of this dissertation is focused on the detection of electromagnetic radiation from bacterial cells in biofilms. Biofilms are one of the most ubiquitous forms of biological systems on earth, and are commonly associated with infections in plants and animals, including humans [13]. Moreover, they are responsible for the contamination of medical devices and implants [14], deterioration of water quality [15], and microbial corrosion [16]. Bacterial biofilms exhibit a set of emergent properties that are substantially different from free-living bacterial cells [17], including social cooperation, resource capture, and enhanced resistance to antibiotics, disinfectants and removal by host defenses. Understanding the communication mechanisms within the biofilm communities is of critical importance to effective biofilm control and management.

The most widely accepted theory for cell communication is based on chemical signaling. In recent years, a growing body of research has suggested that EM waves play a role in cell communication. In certain types of biofilms (e.g., *S. aureus*, and *Bacillus subtilis*), there are biological elements called amyloid fibrils which are basically characterized as elastic helical fibers with permanent dipole charges at their ends [18] [19] [20]. A recent study [21] indicates that these charged amyloid fibrils can act as mechanical antennas and may play a role in intra- and inter-cell communications in biofilms. However, no experimental evidence has been found to support such hypothesis. In order to explore the existence of such signals, extremely sensitive measurement systems and advanced measurement techniques are needed. If we are able to validate EM biosignaling claims, or even understand the functionality of such signal, we may be able to fight infectious diseases by EM signal jamming, or inhibit the growth of certain cells to fight cancer.

1.2 Literature Review

1.2.1 Advanced Antenna Miniaturization Techniques

The need for compact communication systems has led to continuous exploration and development of miniaturized low-profile monopole antennas. Top-loading techniques are commonly used to reduce antenna height. This type of antenna has the potential to provide wideband impedance matching. In [22], a dielectric-loaded monopole antenna is proposed. To achieve broadband impedance matching, a distributed capacitive sleeve is employed at the feed to cancel the inductive reactance of the antenna. The antenna is $0.16\lambda_0$ in both height and diameter at the center frequency of 2121 MHz. In [23], a capacitive circular disk with shorting pins is attached to the top of a monopole. This structure is able to achieve a height of $0.1\lambda_0$, but at the expense of having relatively large lateral dimensions. In [24], an inductively coupled, capacitively loaded monopole antenna is presented. The overall size of the monopole is $\lambda_0/40 \times \lambda_0/16 \times \lambda_0/8$. Another effective way of shrinking the vertical size of a monopole is to use a folded structure. Inverted L and inverted F antennas are two simplest forms of this type of miniaturized antenna. This technique is usually combined with more complicated structures (e.g., adding parasitic elements) to enhance antenna performance. In [25], a short monopole based on a quarter-wave microstrip resonator is reported. The lateral dimension of the antenna is miniaturized by meandering the microstrip line into a spiral shape. An identical element is superimposed in parallel to the driven element to improve the polarization purity. The antenna measures less than $\lambda_0/40$ in height and $\lambda_0/10$ in both lateral dimensions.

In [3], an extremely small two-legged monopole for HF band applications is presented. The antenna achieves dimensions of $\lambda_0/87 \times \lambda_0/87 \times \lambda_0/263$ at 23 MHz. The topology of the antenna is shown in Figure 1.3. The two vertical pins (i.e., the feeding pin and the shorting pin) are the radiating elements for the vertically polarized electric field. In order to create in-phase currents on the two pins, a T-type 180° phase shifter is introduced. The circuit model shown in Figure 1.4 (a) demonstrates the operating concept of the phase shifter. In practice, the grounded capacitor is realized by a parallel plate capacitor to avoid the undesired currents I_4 as shown in Figure 1.4 (b). Like many other electrically small antennas, this antenna suffers from narrow fractional bandwidth and low efficiency due to its exceedingly small radiation resistance. Although the air-core inductors used in the phase shifter have relatively high quality factor (Q), the AC resistance of the inductors still dominates over the radiation resistance. As a results, most of the power is consumed by the inductors rather than being radiated. In addition, in order to match the small input impedance of the antenna to 50 Ω, an extra shorting pin and a chip inductor are required as a matching network, which further reduces the antenna efficiency. In [26], a folded dipole version is introduced. The modified antenna features a fully balanced structure and achieves higher bandwidth and radiation efficiency. The overall dimensions of the antenna are $0.013\lambda_0 \times 0.013\lambda_0 \times 0.02\lambda_0$ at 40 MHz.

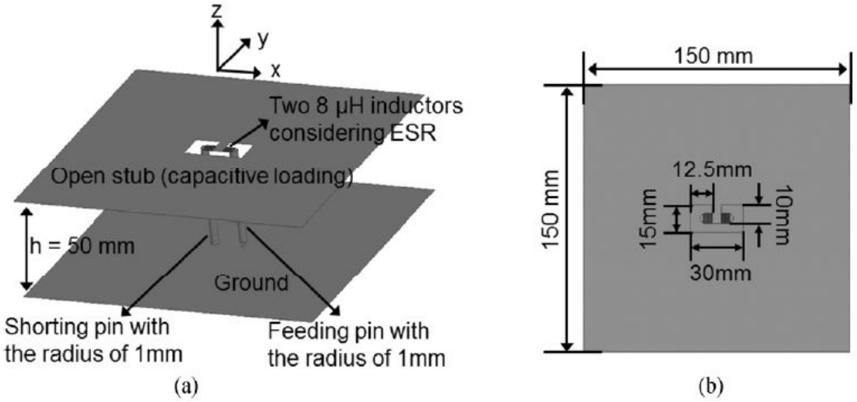

Figure 1.3: The topology of the extremely small two-legged monopole. (a) Side view and (b) top view [3].

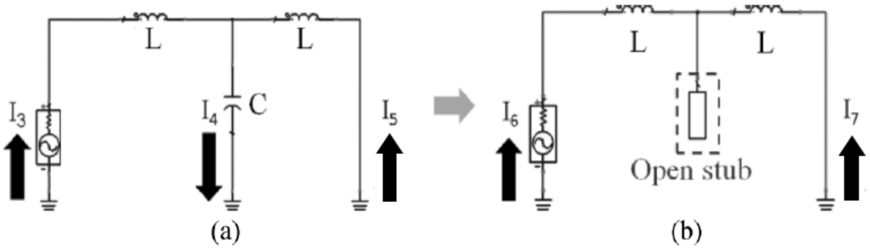

Figure 1.4: (a) Circuit model of the T-type 180° phase shifter and (b) actual implementation of the grounded capacitor using an open stub [3].

1.2.2 mmWave Antenna Design for 5G Smartphones

Exploration of the mmWave spectrum dates back to the earliest stage of electromagnetic theory. However, it was not until recent advancements in semiconductors and increasing demand for higher date rate, that mmWave technologies for cellular usage attracted worldwide research attention. The potential large bandwidth and capacity of mmWave bands have energized the need for advanced mmWave antennas. Beamforming is considered an effective approach to mitigate the lossy nature of mmWave communications. In one of the very first publications on this subject [27], a 28 GHz array is used to continuously sweep the atmosphere to identify the strongest connection. The theoretical analysis and experimental results of the prototype demonstrate the feasibility of mmWave systems as cellular access links. Subsequently, various antenna designs were proposed for mmWave smartphones. In [4], a mesh grid patch antenna operating at 28 GHz is proposed. This topology takes advantage of the thickness of the PCB to form a patch-like mesh grid in the vertical plane. The entire radiating body of the antenna is made of closely spaced vias as shown in Figure 1.5 (a). Unlike commonly used planar dipole antennas which are typically placed on the PCB and require removal of the metallic patterns underneath the structure to maintain the fan beam, this newly devised structure is completely devoid of the impact of the metal traces on the PCB. Moreover, it has the flexibility to provide different polarizations. The antenna is expanded into two sets of 1×16 phased arrays integrated along the edges of a Samsung cellular phone prototype as shown in Figure 1.5 (b).

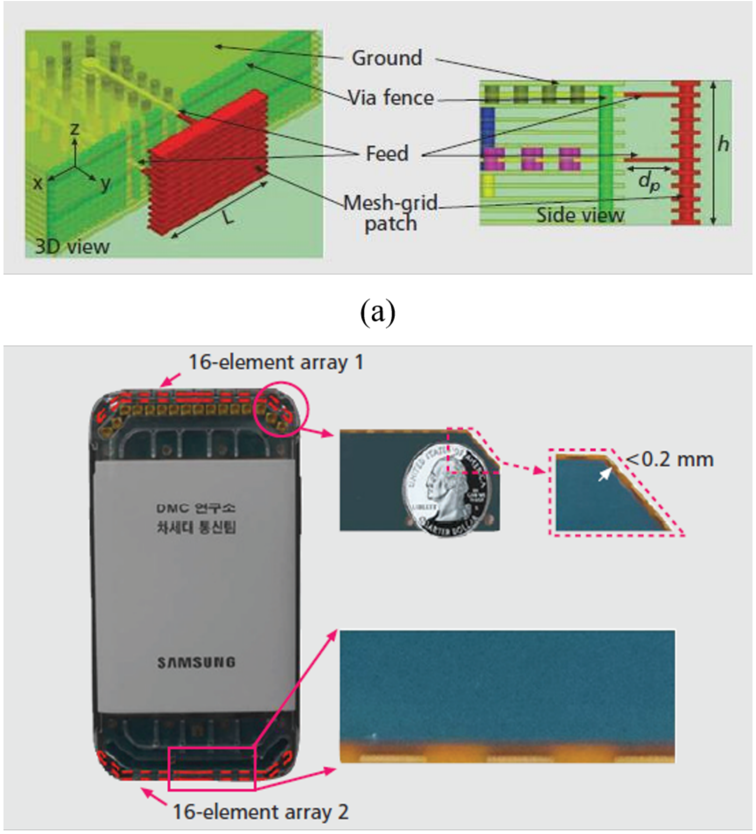

(a)

(b)

Figure 1.5: (a) The mesh grid antenna. (b) The phased-array in the Samsung cellular phone prototype [4].

This antenna is later scaled into a 60 GHz horizontally polarized version [5]. To produce the vertical polarization, a folded structure that generates electric fields emulating a vertical monopole is proposed. The topology of the antenna is shown in Figure 1.6. The short vertical pin in the front is the driven radiator directly fed by the feed line. Two parallel plates are attached to the ends for antenna miniaturization. The via-fence behind the driven element acts as a reflector. Two ground pads connected to the via fence are added above and below the driven element, respectively. The capacitive coupling between the folded reflector (the via fence and the ground pads) and the driven element creates a second resonance which enhances the bandwidth of the antenna.

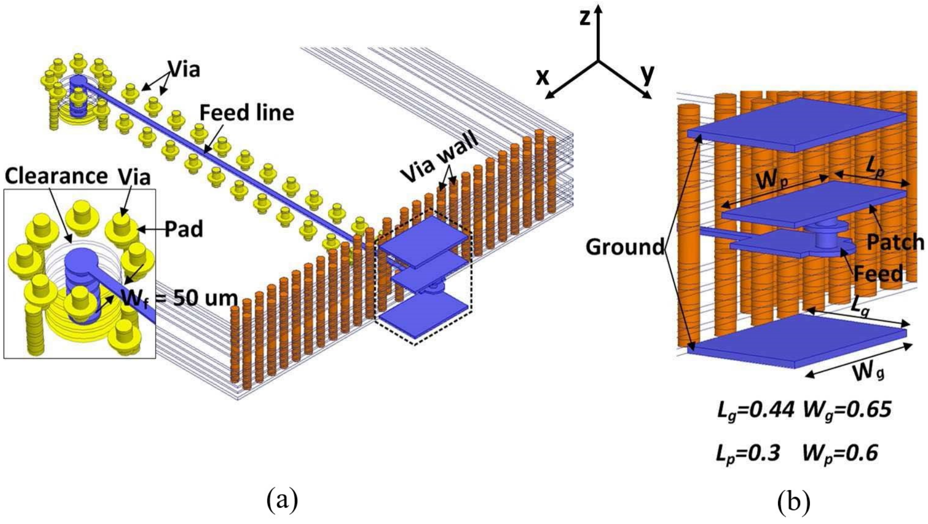

Figure 1.6: Vertically polarized folded monopole antenna.(a)3-D view.(b) Zoomed-in view of the radiator [5].

In [28], two types of Yagi-Uda antennas are employed to provide two orthogonal polarizations. For the horizontal polarization, a conventional planar Yagi-Uda antenna is utilized. The vertically polarized Yagi-Uda is constructed by a collection of vertical vias loaded with metallic blocks. Substrate-integrated dipole antennas that can be incorporated along smartphone edges are investigated in [29]. The dipoles are implemented by vias using a standard PCB process to fit at the edges of a phone or a tablet. The vias surrounding the dipole structure function as a fence to suppress back radiation. Parasitic elements are also added in front of the driven element as directors to enhance the gain. This structure features wideband operation with broad half-power beamwidth in the elevation plane. However, the near half-wavelength profile makes it impractical for smartphones that are only a few millimeters thick. A very low-profile substrate-integrated vertically polarized cavity-backed slot antenna is presented in [30]. This antenna features a height of less than $0.1\lambda_0$ at 39 GHz. However, the antenna suffers from having a very narrow bandwidth, which is common in cavity-type structures. Designing electrically small, highly-efficient wideband antennas for smartphones continues to remain a difficult challenge in the realization of 5G mobile networks.

1.2.3 Probe-Fed mmWave Antenna Measurement

In addition to antenna design, accurate characterization of antennas is also of great importance. The matching performance of an antenna can be directly evaluated from the reflection coefficient measurement using a network analyzer, whereas the gain and radiation pattern measurements are more complicated. The first gain measurement of an on-wafer antenna was reported in [31], where a pair of identical antennas were place at a distance R, and the gain was extracted from the S_{21} measurement. Since the positions of the antennas were fixed, only the gain in the maximum radiation direction was measured. An improved setup that allows for antenna radiation pattern measurements was presented in [32]. An open-ended waveguide was attached to a customized Plexiglas fixture, and was used as a sampling antenna. The fixture arm was rotated by a stepper motor along a virtual arc extending from $-90°$ to $90°$, thus the pattern in the upper half plane can be measured. Similar far-field pattern measurements of on-chip antennas were reported in [33, 34]. The first 3D radiation pattern measurement setup was proposed in [9]. With two rotating arms, the sampling antenna can move on the surface of a sphere around the AUT except the region blocked by the probe positioner. All the aforementioned gain and radiation pattern measurements are conducted in the far-field region of both the test and sampling antennas. They involve expensive customized probe station design and complex mechanical structures. Moreover, at mmWave frequencies, reflections and scattering from the measurement setup, the twist of cables and the misalignment of the sampling antenna can cause significant errors. As a consequence, inconsistent gain, distorted radiation patterns and intense ripples are always reported.

Near-field to far-field (NF to FF) methods can alleviate these issues and can be implemented in a much more compact range. However, performing such techniques on probe-fed mmWave antennas is extremely challenging. Conventional near-field measurement systems use small metallic antennas such as a short dipole [35] or an open-ended waveguide [36] as the near-field sampling probe. The AUT needs to be placed in the far-field region of the probe so that the probe does not perturb the measured near-field. For a short dipole, the far-field criterion can be obtained by requiring the radiating component to be much larger than the Bio-Savart's component, i.e.,

$$\frac{1}{kR} << 1 \tag{1.1}$$

where R is the distance between the source and the observation point, and k is the wavenumber in free space. If we set a factor of 10 for the ratio of the radiating component to the nonradiating component, the far-field distance is

$$R = \frac{10}{k} = 1.6\lambda \tag{1.2}$$

With this constraint, it is very difficult to accurately measure the near-field of a mmWave antenna on a probe station because the magnitude of the multiple scattering from the probe station and from the probe itself is comparable to the direct signal from the AUT. In addition, based on the sampling distance, a certain scan area is required to ensure the accuracy of the far-field pattern over a specified angular range. Nevertheless, the scan range on a probe station is very limited. As a result, the far-field pattern is only valid over a very small angular range or may be even completely wrong [35].

To circumvent the issues with conventional metallic probes, electro-optic (EO) probes have been exploited as an alternative solution. Successful implementation of EO systems to characterize antennas and arrays has been reported in the past [37–41].

In [37], EO crystals are used to measure the near-field patterns of a 4 GHz patch antenna. The amplitude and phase maps of three orthogonal electric-field components are presented. A continuous-wave-electro-optic near-field mapping system is developed to characterize a dual-band (2.1 GHz and 4.8 GHz) circularly-polarized phased array [38] and an X-band active electronically-scanned array [39]. In [40], a commercial EO near-field scan system is employed to obtain the far-field radiation pattern of a miniaturized VHF antenna. In [41], an EO sensor is utilized to map the near-field of a 20 GHz pyramidal horn antenna. The far-field radiation pattern is then computed using the near-field to far-field transformation. However, none of the aforementioned measurements are performed in the mmWave frequency region (most of them are performed at frequencies below 10 GHz), and the antennas are tested in cluster-free environments. It is not clear if the EO near-field measurement is effective at mmWave frequencies, especially on a probe station where the reflection and scattering from the probe station and surrounding environment can be very strong. Furthermore, [37–39, 41] only provide the radiation patterns of the AUTs. In [40], a standard transverse electromagnetic (TEM) cell is used to calibrate the EO probe so that the absolute gain of the AUT can be determined based on the near-field data. Unfortunately, TEM cells are not available at mmWave frequencies. Another way to obtain the gain of the AUT based on a near-field setup is to use the near-field gain comparison technique [42]. In this approach, the gain of the AUT is determined by establishing a comparison between the measured near-field of the AUT and that of a standard antenna with a known gain. In [36], a pyramidal horn antenna is used as the reference. However, since the horn antenna has a different feeding structure, it is not feasible to replace the AUT with the horn antenna while maintaining all measurement parameters unchanged. A more practical and accurate way is to have a probe-fed standard gain antenna. Unfortunately, such an antenna does not currently exist.

1.2.4 Existing Theories and Measurements of Electromagnetic Signals in Biological Systems

All biological organisms are complex systems consisting of a large number of interacting elements. They are constantly exchanging information with each other and with their external environment in order to adapt to various conditions. Chemical signaling is considered the dominant communication mechanism in biological organization and activities, where messages are carried by ligands and are usually transmitted through diffusion [43]. However, this type of signaling typically supports communication in the range of nanometers, whereas biological systems interact and manifest a certain degree of order even on a macroscopic scale [44]. Since many proteins and their derivatives are electrically-polarized, any oscillations of these structures can generate electromagnetic fields. The strong electrical polarity of biological objects suggests electromagnetic waves may play a role in intra- and inter-cell signaling. There have been extensive postulations of the existence, nature, and function of electromagnetic fields in biological systems. H. Frohlich first proposed the idea that metabolic activities in biological systems may excite coherent electric vibrations, which enable long-range interactions and energy transfer within the system [45–47]. This theory builds the foundation for future studies on electromagnetic activities in biological cells. The structure that generates the EM waves in biological cells has not been identified yet, however, recent research has pointed to microtubules as one of the possibilities [48–50]. It has been proven that microtubules are lattices of oriented dipoles [48]. [49] analyzed the vibrations of microtubules and actin filaments and showed that such vibrations can generate electromagnetic fields, which mediate the energy exchange with surrounding environment. The vibration frequencies are in the MHz range. [50] calculated the electric field generated by axial logitudinal vibration modes of microtubules for random and coherent excitations. These hypotheses are supported by a number of experiments [51–55]. Changes of electric field in the frequency range 8–9 MHz were detected in the vicinity of the plasma membrane of yeast mitotic cells in the M phase of the cell cycle, which coincided with the period when the kinetochore microtubules in the mitotic spindle bind chromatids [51]. Microtubule electromagnetic activities were also suggested to occur when a low-intensity electric field at 100-300 kHz was applied to mitosis cells [52]. The most profound evidence may be the discovery of the resonant frequencies of a single microtubule reported in [53]. Through several elaborated experiments, the authors identified the resonance peaks of a single microtubule in the frequency range of 10-30 MHz and 100-200 MHz. They also demonstrated that the resonant frequencies did not depend on the length of the microtubules, and the water channel inside the structure was essential for the resonances to take place. Other studies have shown that some bacterial DNA sequences induce electromagnetic waves in the kHz range in high aqueous dilutions [54]. Delocalized modes in proteins are also identified in the terahertz frequency domain [55]. A recent study indicates that bacterial cells in biofilms may use EM signals to communicate [21]. A model based on an electromagnetically coupled system of mechanical oscillators is developed to evaluate the characteristics of the EM signals. The model predicts that possible EM radiation could happen within the kHz–GHz frequency range, depending on the mechanical properties of the cells and the amyloid fibrils. In [56], EM signaling is compared with quorum sensing. It is demonstrated that EM signaling could provide a higher data rate over a longer distance while requiring far less energy than quorum sensing. Therefore, EM signaling may be the preferred method of communication used by cells in biofilms. However, there is no experimental evidence to prove the existence of EM communications within biofilms so far.

1.3 Dissertation Overview

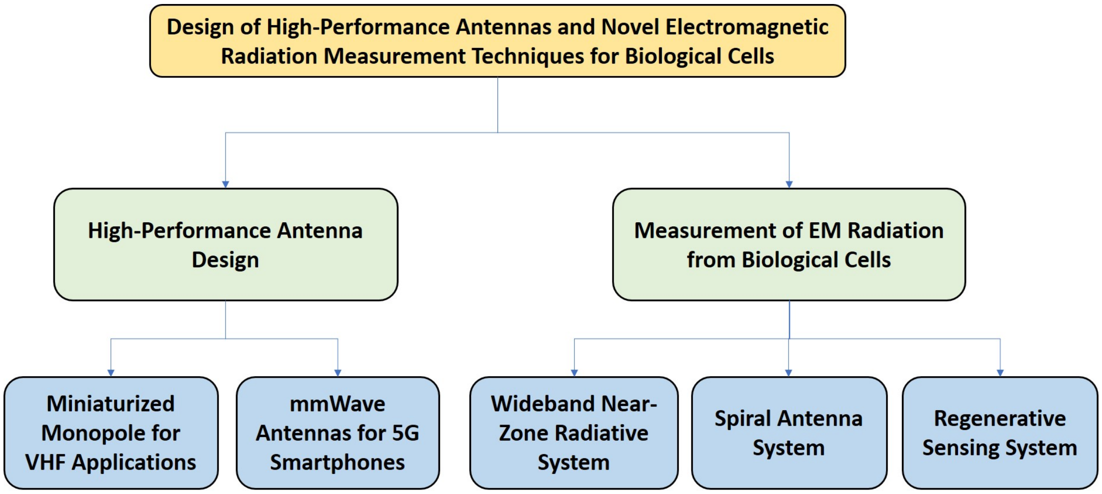

Figure 1.7: Dissertation Overview

Chapter II: A Tunable, High Gain, Very Low-Profile Composite Monopole Antenna for Low-Frequency Applications

In this chapter, an extremely low-profile tunable composite antenna with enhanced gain and an omnidirectional vertically polarized radiation pattern is presented. The antenna is based on a recently developed very short two-legged monopole antenna [3]. It consists of one driven element and eight identical parasitic coupled elements. By utilizing the mutual coupling between elements, the radiation resistance of the antenna is increased significantly, leading to considerable gain enhancement and better matching performance. The composite antenna has the same height as the single monopole ($\lambda_0/150$) but larger lateral dimensions ($\lambda_0/16 \times \lambda_0/16$). The performance of the proposed antenna is compared with that of a single monopole antenna. It is shown that the peak gain of the composite antenna is about 10 dB higher than that of the monopole antenna. The design is then modified for frequency tunability to achieve frequency agility and higher bandwidth for certain modulations like frequency hopping spread spectrum. The tuning bandwidth (FBW) of the tunable antenna is

3.32%, and the gain is further improved at higher frequencies. A new method of effectively measuring a monopole antenna with an electrically small ground plane using cascaded transformers is also presented and discussed.

Chapter III: mmWave Antennas for 5G Smartphones

In this chapter, novel antenna design techniques are devised to realize compact high-performance mmWave antennas for 5G cellular devices. Three antenna arrays based on different specifications are presented.

The first design is a 1 × 4 differential dual-polarized phased array operating at 28 GHz. The array element consists of two discrete antennas, i.e., a folded dipole and a substrate integrated waveguide (SIW) cavity-backed slot antenna, which are responsible for the horizontal and vertical polarizations, respectively. Advanced bandwidth enhancement techniques are introduced to increase the bandwidth of the SIW cavity-backed slot antenna. A coplanar-stripline-to-coplanar-waveguide balun is implemented in the slot antenna to realize the single-ended to differential feed transition. The array can cover the entire 28 GHz band allocated for 5G applications with peak gains larger than 7 dBi for both polarizations. The total dimensions of the array are 7.5 mm × 20 mm × 0.89 mm.

In the second design, a very low-profile dual-band dual-polarized phased array is proposed. The array element is based on two distinct dual-band antennas to realize two orthogonal linear polarizations. A planar folded dipole with a parasitic strip is used to produce horizontally polarized radiation, and a novel hexagonal bridge antenna is devised to generate vertically polarized radiation while maintaining a very low profile. A prototype of a 1 × 4 phased array is designed and implemented on a multilayer laminate using a standard printed-circuit-board process. The real estate of the array is kept within 6.5 mm × 23 mm × 1.12 mm. Advanced measurement techniques are used to characterize the performance of the individual array element and the whole array. For both polarizations, the -10 dB bandwidth covers 25.4–30.84 GHz and 38–40 GHz with peak gains of 11.31 and 11.93 dBi at the two center frequencies, respectively. The overlapped scan range between both polarizations is ±45° at 28 GHz and ±39° at 39 GHz.

The last design is a very compact dual-polarized antenna array that allows for operation in the 26 GHz, 28 GHz, 37 GHz and 39 GHz bands designated for 5G uses. Four 1×4 sub-arrays, namely low-band horizontally polarized (LB H-pol) array, high-band horizontally polarized (HB H-pol) array, low-band vertically polarized (LB V-pol) array and high-band vertically polarized (HB V-pol) array, are designed on a 12-layer laminate with total dimensions of 25 mm × 6 mm × 0.97 mm. The LB arrays achieve reflection coefficients of less than -10 dB from 24–30 GHz, and the HB arrays can operate from 37–43 GHz. Special techniques are used to reduce the mutual coupling between elements and enhance the array gain. Each sub-array features a peak gain of more than 9.7 dBi at its center frequency. The 3-dB beam scanning ranges for the H-pol and V-pol arrays are ±45° and ±56° at 27 GHz, and ±42° and ±28° at 40 GHz, respectively.

Chapter IV: Measurement of Electromagnetic Signaling in Biofilms

This chapter reports the work on detecting EM radiation from bacterial cells in biofilms. First, a wideband near-zone radiative system operating from 1 to 50 GHz is designed to examine the possibility of EM emission from bacterial biofilms. The system can detect the change in background emission with a signal level as low as -191 dBm/Hz. Using this system, we successfully detected radiation from *Staphylococcus aureus* biofilms in the 3–4 GHz frequency range. Zinc oxide nanopyramids (ZnO-NPY) exposure experiments are conducted to verify that the signals are produced by living cells rather than material thermal emission.

Afterwards, a spiral antenna system is exploited to further examine the band of interest in the near-field region. Radiation from 3 identical biofilm samples is monitored and recorded over 70 days. Two distinct frequency bands, namely the 3.18 GHz and the 3.45 GHz bands, are identified as potential "communication bands". Furthermore, long-term and short-term cycles of the total radiation intensity within the band are observed over the course of the experiment.

The maximum signal measured using the wideband near-zone radiative system and the spiral antenna systems is around 0.3 dB above the background noise. To improve the signal to noise ratio, a narrow-band regenerative sensing system is developed. The system uses the concept of regeneration (also known as positive feedback) for the amplification of the signal. Significant difference was observed between the PNG medium measurement (baseline) and the biofilm sample measurement, which validates the existence of electromagnetic radiation from *S. aureus* biofilms. Furthermore, an external signal at 3.18 GHz is used to illuminate the biofilms through the system. The radiation from the illuminated biofilms is stronger than that from regular biofilms. This work confirms EM radiation from bacterial biofilms, which is a key requirement to demonstrate EM signaling among bacterial cells.

CHAPTER II

A Tunable, High Gain, Very Low-Profile Composite Monopole Antenna for Low-Frequency Applications

2.1 Introduction

The difficulties with ad hoc communication in a highly cluttered environment has re-stimulated research attention on HF and VHF band applications. It is well understood that signal reflection, scattering, and diffraction in the HF and VHF bands are much less severe than those in higher frequency bands [10, 11]. For near-ground applications such as land mobile systems used in vehicles or unattended ground sensors, it has been established that the propagation path-loss of vertical polarization is far less than that of horizontal polarization [12]. Monopoles are commonly preferred in such applications for both their simple structures and their capability to provide an omnidirectional vertically polarized radiation pattern. However, the height of a conventional $\lambda_0/4$ monopole is prohibitively large at these frequencies. The need for compact communication systems has led to continuous exploration in miniaturized low-profile monopole antennas [3, 22–25]. In [22] and [23], a capacitive loading technique is used to effectively reduce the height of monopoles. This type of antenna typically has a height of around $\lambda_0/10$ and a relatively large lateral dimension, but can provide high gain and bandwidth. In [25], a short monopole based on a quarter-wave microstrip resonator is reported. The antenna measures less than $\lambda_0/40$ in height and $\lambda_0/10$ in lateral dimensions. In [24], an inductively-coupled, capacitively-loaded monopole antenna is presented. The size of the monopole is further reduced to $\lambda_0/40 \times \lambda_0/16 \times \lambda_0/8$.

Recently, an extremely small two-legged monopole consisting of two vertical pins and a modified T-type 180° phase shifter was proposed [3]. This antenna achieves dimensions of $\lambda_0/87 \times \lambda_0/87 \times \lambda_0/263$ at 23 MHz. However, this design suffers from high ohmic loss and narrow fractional bandwidth due to the exceedingly small radiation resistance of the antenna. Although the inductors used in the phase shifter have a relatively high quality factor (Q), the AC resistance of the inductors is still dominant over the radiation resistance. Therefore, most of the power is consumed by the inductors, resulting in low antenna gain. In addition, in order to match the small input impedance of the antenna to a 50 Ω feed, an extra shorting pin and a chip inductor are required as a matching network, which further reduces the antenna efficiency.

Besides the aforementioned difficulties in designing extremely short antennas, measuring the performance of a monopole antenna with an electrically small ground plane is also a challenging task due to the cable effects on the antenna performance [57]. The strong near-field coupling between the coaxial-feeding cable and the antenna causes erroneous measurement results. Ferrite chokes or baluns are used to suppress cable currents and reduce the measurement errors [26, 58]. However, the effectiveness of this method is quite limited. In [24], a balanced version of the proposed monopole is fabricated to indirectly examine the antenna performance. In [3], a small source module is employed to avoid using a long coaxial cable, but the reflection coefficients of the antenna can only be evaluated by observing the variation of received power versus frequency.

In this chapter, a low-profile tunable composite antenna with enhanced gain and an omnidirectional vertically polarized radiation pattern is presented. The design is based on the extremely small two-legged monopole antenna proposed in [3]. Parasitic coupled elements with identical structures are placed around the driven element to increase the radiation resistance of the antenna through the mutual magnetic coupling among the elements. Methods of using parasitic elements to achieve better performance of electrically large antennas have been reported in the past [59–62]. However, for extremely small antennas that are in very close proximity of each other, it is not clear whether the entire antenna would act as a single resonant radiator or not because the coupling among elements are very strong. For such structures, the coupling mechanisms, the level of coupling, the arrangement of elements, and the orientations of the inductors as well as the radiating pins are all important design considerations in order to achieve high gain performance. It is shown that the radiation resistance is improved by a factor of 45 when eight parasitic elements are added. In this way, enhanced gain and better matching performance are achieved without increasing the height of the antenna.

The rest of the chapter is organized as follows: Section 2.2 presents the design concept and two different antenna configurations. The feasibility of both configurations is evaluated, and the parallel parasitic configuration is chosen for further design. A detailed design procedure of the parasitic coupled composite antenna is given in Section 2.3. In Section 2.4, a new method for measuring electrically small antennas with small ground planes using transformers is described, and the measurement results of the composite antenna are presented. In Section 2.5, the proposed design is further modified into a tunable antenna to achieve higher bandwidth, and its performance is examined and discussed.

2.2 Multi-Element Composite Antenna

2.2.1 Design Concept

As mentioned before, the two-legged monopole antenna design reported in [3] suffers from low gain due to the exceedingly small radiation resistance (0.23 Ω when simulated at 40 MHz). The equivalent series resistance of the inductors utilized in the phase shifter is prohibitively large (about 17 times) compared with the radiation resistance of two vertical pins in spite of the relatively high Q of the inductors. As a consequence, most of the power is consumed as ohmic loss rather than radiated out of the antenna. Also, the effectiveness of matching is severely limited due to the high Q impedance of the electrically small antenna, resulting in a narrow bandwidth and poor gain [62]. The external matching network also inevitably introduces extra loss, which further reduces the antenna efficiency. In order to resolve the aforementioned problems, the radiation resistance of the antenna needs to be increased significantly. This can be accomplished by either increasing the actual height of the antenna or increasing the number of radiating pins with in-phase currents flowing over them while maintaining the physical height of the antenna unchanged. The latter can be pursued following two possible antenna configurations, specifically a series configuration and a parallel parasitic configuration that are explained in what follows.

2.2.2 Series Configuration

The series configuration continues the design approach proposed in [3]. By producing in-phase currents on more vertical pins using 180° phase shifters, the effective height of the monopole can be further increased, resulting in larger radiation resistance. The topology of this design is shown in Figure 2.1 (a). The antenna is excited at one end of the first pin, and the phase shifters are utilized both above and below the ground plane to connect two adjacent vertical pins.

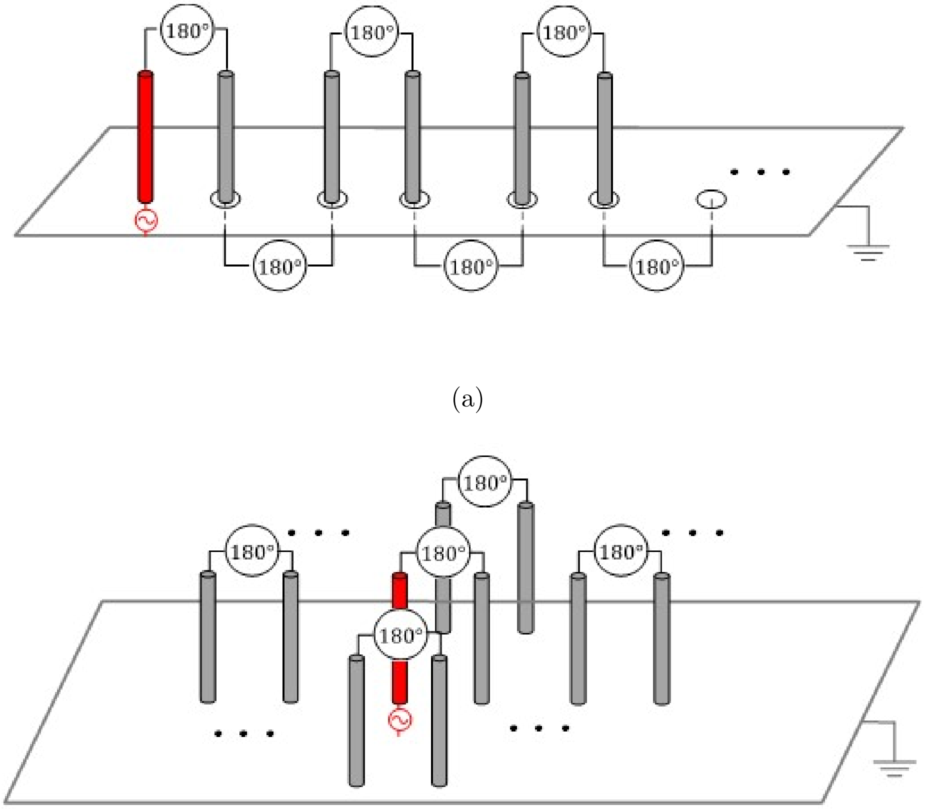

(a)

(b)

Figure 2.1: (a) Series configuration and (b) parallel parasitic configuration of the composite antenna (the T-type phase shifters are denoted by the circles marked with 180°)

The values of inductors and capacitors used in the T-type phase shifters are first calculated based on the circuit model [63], and the entire antenna structure is simulated using a full-wave solver. Nonetheless, a deformed pattern is observed as more pins are added to the design. This is because the resonant frequency varies with the number of pins added, creating a nonuniform current on the pins which changes the radiation pattern of the antenna. To achieve an omnidirectional pattern, the inductance of each inductor should be carefully tuned. Moreover, there are some other practical issues associated with realizing this configuration. The modified T-type phase shifter cannot be used to connect two pins below the ground plane due to its large size and lumped inductors are too lossy. Basically the loss due to cascaded phase shifters is more than any gain that can be achieved by the series pins. The limited accuracy of the phase shifters also causes difficulty in producing in-phase currents on the pins.

2.2.3 Parallel Parasitic Configuration

The input impedance of a single antenna can be altered considerably in the presence of other identical antennas due to the mutual coupling among them [64]. Inspired by the possibility that the input impedance of an electrically small antenna can be improved through the mutual coupling effects on the antenna, a parallel parasitic configuration is proposed (Figure 2.1). In this configuration, the antenna is fed from one of the vertical pins of the driven element (the other pin is shorted to the ground plane), and identical parasitic elements with both pins shorted to the ground plane are added around the driven element.

This configuration has several advantages compared with the series configuration. First of all, it reduces the number of phase shifters needed in the antenna to achieve the same radiation resistance, which simplifies the antenna structure and reduces design uncertainty. The overall ohmic loss of the phase shifters is also reduced. Furthermore, an omnidirectional radiation pattern can be easily achieved by properly adjusting the positions of parasitic elements without the need to change the inductance of each inductor.

2.3 Composite Antenna with Parasitic Coupled Elements

2.3.1 Coupling Effects on Antenna Performance

By virtue of its simple geometry and reliability, the parallel parasitic configuration was chosen for further antenna design. The simulation model of the single antenna

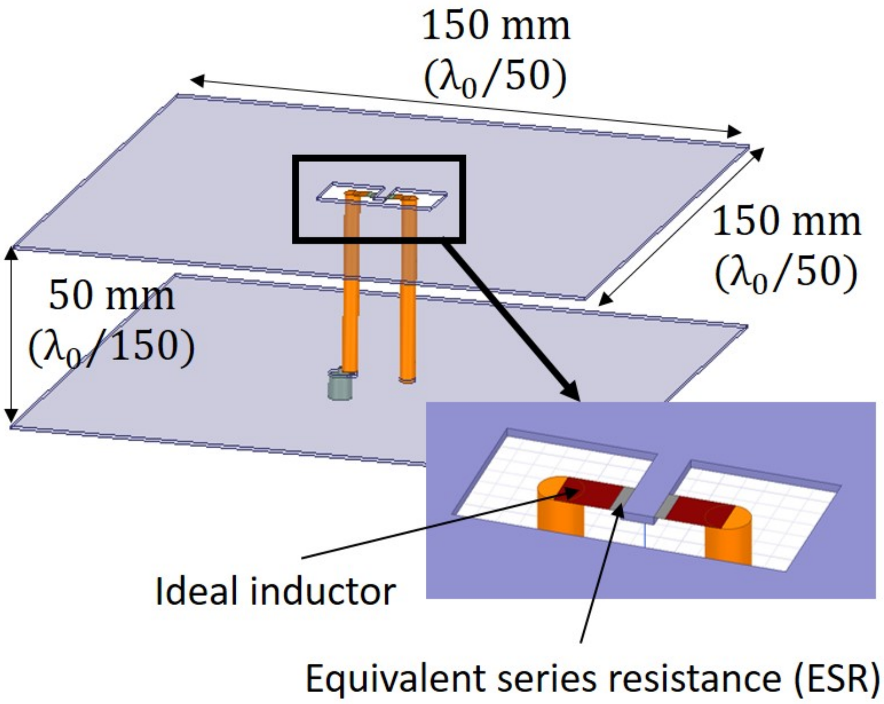

Figure 2.2: The simulation model of the single antenna element (driven element).

element (driven element) is shown in Figure 2.2. The inductors are modeled as ideal inductors connected via series with resistors. To investigate the effects of coupling on the radiation resistance, bandwidth, and gain of the antenna, we gradually increased the number of parasitic elements around the driven element. Figures 2.3 (a)–(d) illustrates the configuration of the antenna with 1, 3, 5 and 8 parasitic elements. First, we consider the idealized lossless version in our simulations, i.e., all the metallic traces are treated as perfect electric conductors (PEC) and the equivalent series resistance (ESR) of the inductors is set to 0 Ω. Since there are no losses in the materials used in the antenna simulation, the radiation resistance is simply the real part of the input impedance. Figure 2.4 shows the radiation resistance at resonance and the 10-dB return loss bandwidth of the antenna as a function of the number of parasitic elements. The radiation resistance improves significantly from 0.23 Ω with no parasitic elements to 10.25 Ω with eight parasitic elements, and the 10-dB return loss bandwidth increases from 2.9 kHz to 19.1 kHz. It should be noted that an excellent dipole radiation pattern is maintained for all parallel parasitic configurations.

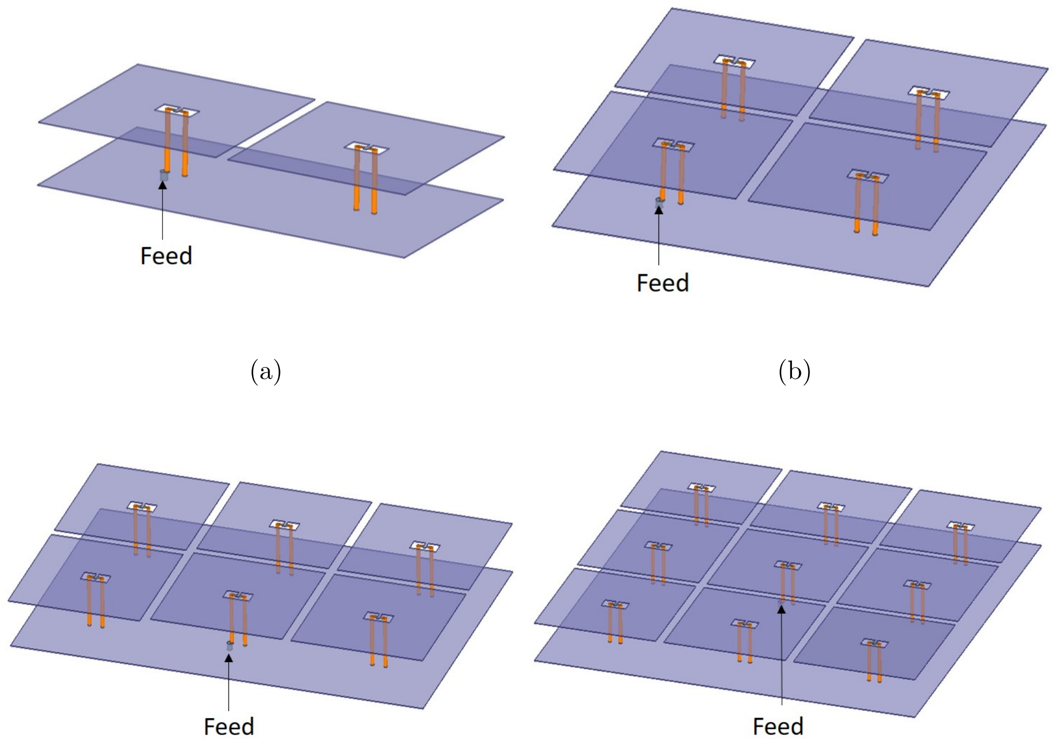

(a) (b)

(c) (d)

Figure 2.3: Configurations of the antenna with (a) 1, (b) 3, (c) 5 and (d) 8 parasitic elements

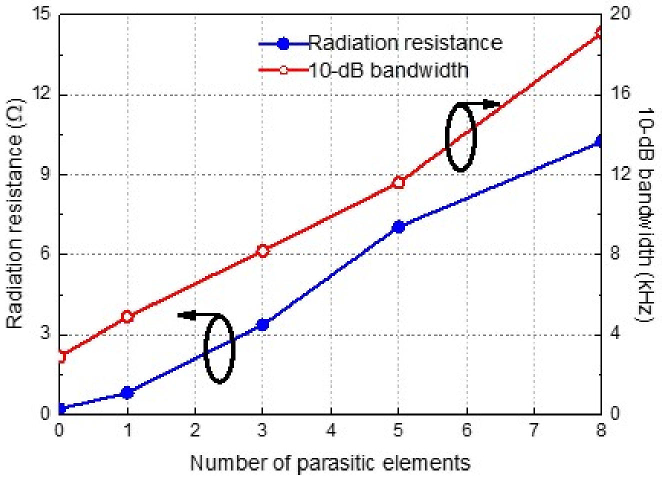

Figure 2.4: Simulation results for the radiation resistance and 10-dB bandwidth of the antenna (lossless) as a function of the number of parasitic elements.

In order to examine the actual input impedance and gain of the antenna, conductive loss is then included in the simulation by assigning the finite conductivity of copper to all metallic traces and vertical pins. Finally, the influence of the ESR of the inductors used in the phase shifters is analyzed. The simulation results are tabulated in Table 2.1. For a fixed ESR of 2 Ω, both the input impedance and realized gain increase with the number of parasitic elements. The input impedance keeps increasing whereas the gain decreases with higher ESR for the same number of parasitic elements. Therefore, high Q inductors are required for antenna gain enhancement. However, different from the lossless case where the 10-dB bandwidth of the antenna increases significantly with the number of parasitic elements, there is no substantial improvement in the bandwidth when losses are included in the simulation. This is because the bandwidth of the single element is dominated by its ohmic resistance as opposed to by the radiation resistance. An interesting case occurs when eight parasitic elements are added and all inductors have 2 Ω ESR (corresponding to the maximum achievable Q at 40 MHz). The input impedance of the antenna at resonance becomes 54.25 Ω, indicating that the antenna can be matched to a 50 Ω feed without the need for external matching. In this case, the gain is enhanced by 10.65 dB compared with a single element.

Number of Parasitic Elements	ESR of Inductors (Ω)	Resonant Frequency (MHz)	Input Impedance (Ω)	10-dB Bandwidth (kHz)	Gain (dBi)
0	2	40.0	5.95	60.1	-17.1
1	2	41.4	12.66	62.5	-10.18
3	2	43.4	27.91	64.7	-7.35
8	2	44.7	54.25	68.2	-6.05
8	3	44.7	77.92	93.7	-7.88
8	4	44.7	94.91	129.6	-8.95

Table 2.1: Simulation results for the resonant frequency, input impedance and gain of the antenna with different number of parasitic elements and ESR of the inductors.

2.3.2 Air-Core Inductor Design and Measurement

Based on the previous analysis, a composite antenna with one driven element and eight parasitic coupled elements was designed and fabricated. The inductance of the inductor is first calculated based on the circuit model provided in [63]. This inductance is used as an initial value in the full-wave simulation. Further tuning of the inductance is required to achieve the resonance at 40 MHz. The inductance for a single element resonating at 40 MHz is 3.6 μH. However, once the parasitic elements are added, the resonant frequency shifts to 44.7 MHz due to the coupling effects, thus the inductance is tuned to 4.5 μH in order to make the antenna resonate at 40 MHz. In order to improve the antenna gain to the greatest extent, air-core inductors are chosen to be used in the phase shifters for their relatively high Q [65–69].

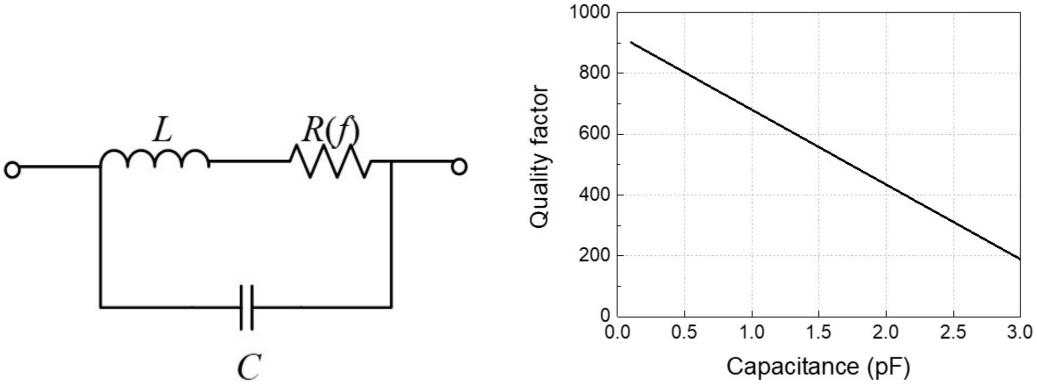

(a) (b)

Figure 2.5: (a) Equivalent circuit of the air-core inductor and (b) Q of the inductor as a function of C with $L = 4.2$ μH and $R = 1.14$ Ω at 40 MHz.

The behavior of an air-core inductor at high frequencies is very different from that at low frequencies. Existing models used to predict the inductance and Q of coils mainly address the aspects related to the AC resistance without considering parasitic capacitances, which leads to unrealistic predictions of the inductor Q [3]. The behavior of an air-core inductor can be explained using the equivalent circuit shown in Figure 2.5 (a). The model consists of an ideal inductor L and a series resistance R shunted by a capacitor C. L is the self-inductance of an n-turn coil; R is the overall RF resistance; and C is the stray capacitance of the inductor. The actual inductance L_c and resistance R_c of the coil seen by the antenna are expressed as

$$R_c = \frac{R}{(1-\omega^2 LC)^2 + (\omega CR)^2} \tag{2.1}$$

$$L_c = \frac{L(1-\omega^2 LC) - R^2 C}{(1-\omega^2 LC)^2 + (\omega CR)^2} \tag{2.2}$$

from which the Q of the inductor is calculated using

$$Q = \frac{\omega L_c}{R_c} \tag{2.3}$$

Figure 2.5 (b) shows the Q as a function of C with $L = 4.2$ μH and $R = 1.14$ Ω at

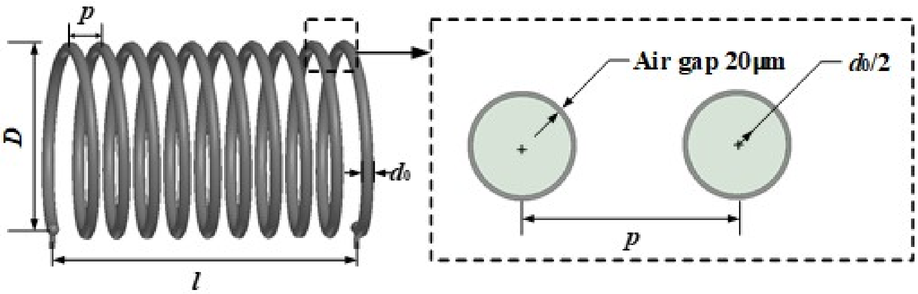

Figure 2.6: The air-core inductor model and design parameters.

40 MHz. The Q degrades from 900 to 185 as C increases only from 0.1 pF to 3 pF. For a more accurate coil design, a nylon-coated copper coil model was developed in the full-wave simulation. This model considers both turn-to-turn and turn-to-shield parasitic capacitances. The side view and the cross-sectional view of the coil, along with the design parameters are shown in Figure 2.6. The 20μm air gap distance between the conductor and the shield is extracted from the datasheet provided by the manufacturer [70]. Based on the model, parametric analysis and optimization are conducted. The design procedure is summarized as follows:

1. The maximum allowable winding diameter D and length l of the coil are defined. For our design, the size of the coil is confined by the dimensions of the single element, i.e.,$0 < D \leq 50$ mm and $0 < l < 90$ mm must be satisfied. Three different winding diameters, 30 mm, 45 mm, and 50 mm are chosen for further exploration of the design.

2. For each specified value of D, the effects of d_0 and p on Q are investigated iteratively to determine the maximum Q. Note that once the values of d_0 and p are fixed, the number of turns N is determined automatically so as to achieve the desired inductance.

3. The Q of the three inductors are compared and the optimal coil is chosen.

The optimized values of $D, d_0, p,$ and N are 45 mm, 2 mm, 4.5 mm, and 10, respectively. It is interesting to note that the optimal coil in terms of quality factor is a coil with $D/l \approx 1$. This is understandable because with such a geometry, the coil achieves a maximum inductance at a minimum wire length [71]. The simulated inductance and resistance are shown in Figure 2.7, compared with the simulated results obtained from the bare copper model. It can be seen that both the inductance and the resistance increase when insulating coating is considered.

As discussed in Section 2.3.1, the Q of the inductors significantly affects antenna performance. Therefore, it is important to validate the coil design before implementing it in the antenna. The air core inductors are fabricated using 12 AWG nylon-coated copper wire. It should be pointed out that measuring a high Q inductor with a vector network analyzer (VNA) can produce incorrect results due to the accuracy limitations of the VNA in the reflection coefficient measurement. Such limitations can result in significant errors in the measured value of Q when the impedance is near the outer boundary of the Smith Chart. According to [72], a magnitude uncertainty of 1% in the reflection coefficient measurement can easily be translated into a variance of more than 200% in the measured Q. In addition, calibration with only open, short and load (OSL) standards cannot effectively remove the error factors from the instrument when performing high Q measurements. To precisely characterize the inductor, a one-port measurement is conducted using an impedance analyzer (IA). Low-loss capacitor calibration is executed after completing the OSL calibration to ensure higher measurement accuracy. The L and R of the inductor measured from 35 to 45 MHz by (a) a network analyzer (Agilent 8753D) and (b) an impedance analyzer (Agilent E4991A) are shown in Figure 2.7, compared with the simulation results. Corresponding values at 40 MHz are tabulated in Table 2.2. As expected, the measured resistance of a high Q inductor fluctuates across the frequency range due to measurement noise. Significant discrepancies are observed between the simulated and the VNA-measured results. The VNA-measured resistance is about 7.4 times that computed in the simulation at 40 MHz, whereas the inductance is 1.6 times, which renders an unreasonably poor Q. In contrast, The measured results obtained from the impedance analyzer are consistent with the simulation results. The higher resistance can be attributed to fabrication and measurement errors.

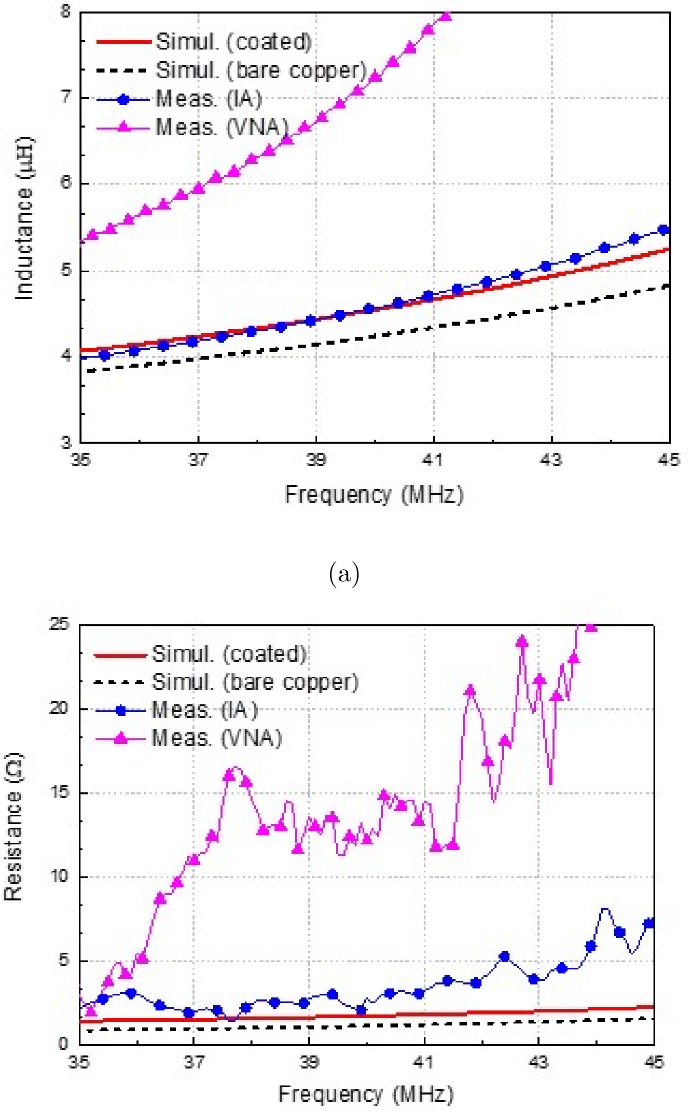

(a)

(b)

Figure 2.7: Measured and simulated (a) inductance L and (b) resistance R of the air core inductor. The impedance analyzer (IA) measurements are considered more reliable than those using the vector network analyzer.

	$R(\Omega)$	$L(\mu\text{H})$	Q
Simulated (coated)	1.73	4.55	661
Simulated (bare wire)	1.14	4.20	935
Measured (IA)	2.81	4.58	410
Measured (VNA)	12.84	7.17	140

Table 2.2: Simulated and measured air-core inductor

2.3.2.1 Antenna Design and Fabrication

The optimized inductors are used in the T-type phase shifters of the proposed antenna. Figure 2.8 illustrates the side and top views of the antenna along with the dimensions of its parts. The geometry of a single two-legged monopole is also shown in Figure 2.8. The composite antenna has a 3×3 array of identical elements with the driven element fed by a coaxial feed at the center to realize a symmetrical structure and maximize the overall coupling effect. The top metallic plates and the ground plane are fabricated with Rogers RO4003C with a thickness of 0.813 mm, dielectric constant of $\epsilon_r = 3.55$ and loss tangent of $\tan\delta = 0.0021$. To reduce the overall weight, hollow copper tubing with a diameter of 4 mm is used for the radiation pins. Each pair of pins is first soldered to the ends of the coils in the phase shifter, then all monopole elements are soldered onto a common ground. The center-to-center distance between adjacent elements is 160 mm. The lateral dimension and height of the composite antenna are 470 mm ($\lambda_0/16$) and 50 mm ($\lambda_0/150$), respectively (λ_0 is the wavelength at the center frequency).

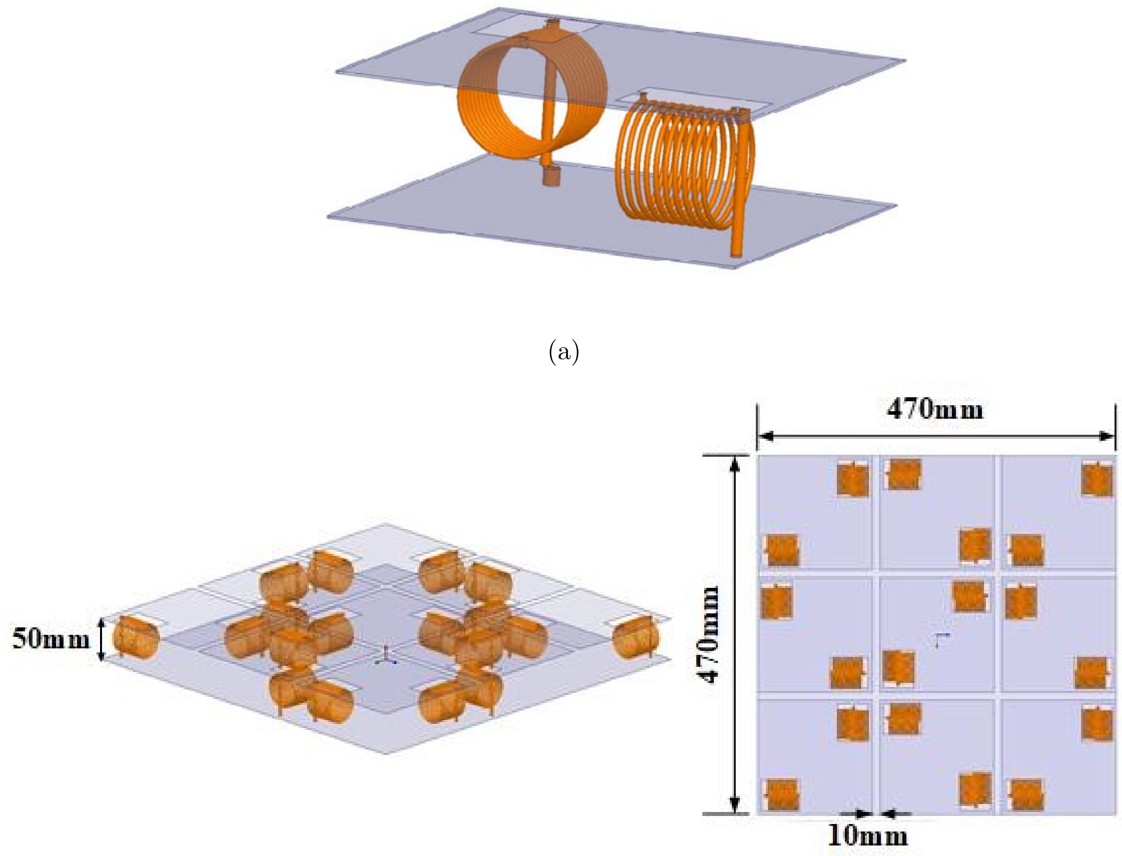

(a)

(b) (c)

Figure 2.8: (a) Geometry of the single element. (b) Side view and (c) top view of the composite antenna.

2.4 Antenna Measurement

2.4.1 Cable Effects on Antenna Measurement

Measuring a monopole antenna with an electrically small ground plane using a long coaxial feeding cable leads to incorrect results [25]. This is because the currents on the ground plane flow over the edge of the ground plane and run on the backside toward the coaxial cable. The currents then flow back to the outer surface of the feeding cable, resulting in secondary radiation. The strong near-field coupling between the coaxial cable and the antenna changes the resonant frequency, input impedance, and radiation pattern of the antenna. Figure 2.9 (a) illustrates the cable effects on the antenna measurements. The measured input impedance of the proposed antenna at resonance varied between 113.1 Ω and 265.8 Ω when we touched different parts of the feeding cable, indicating the strong coupling between the cable and the proposed antenna.

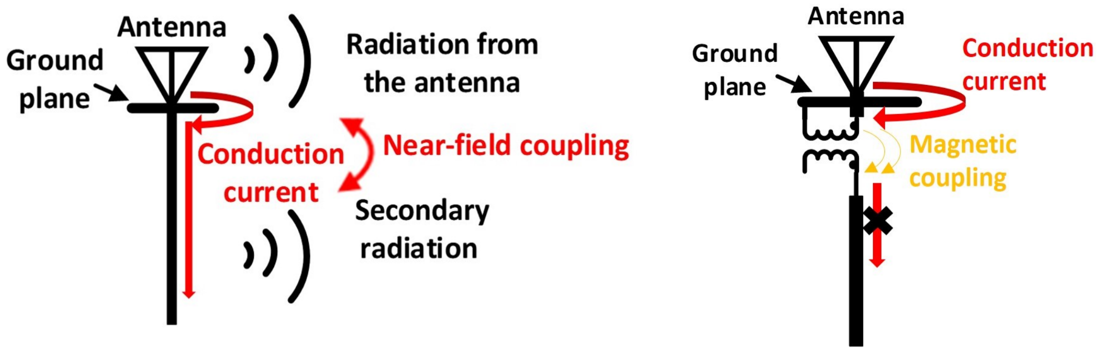

(a) (b)

Figure 2.9: Cable effects on antenna measurement and (b) basic configuration of the transformer.

2.4.2 Antenna Measurement Using Transformers

In order to prevent currents flowing back to the feeding cable, one can use transformers to magnetically couple the signal from the feeding cable to the antenna feed without allowing the flow of electric currents that can run on the outer surface of the feeding cable. In this way, the ground plane and the outer surface of the cable are physically isolated. The basic mechanism is illustrated in Figure 2.9 (b). 1:1 impedance transformers are utilized in our design. Figure 2.10 shows the system setup for measuring S_{11} of the proposed antenna. The isolation effectiveness can be evaluated by observing the variation of the measured input impedance. Table 2.3 lists the measured resonant frequencies and input impedances when 0, 1, 2, and 4 transformers are used. The input impedance still varies drastically when only one transformer is utilized, but the uncertainty is reduced to about 3 Ω with four cascaded transformers. Figure 2.11 shows the measured S_{11} of the antenna with four transformers. The resonant frequency of the antenna is 39.58 MHz, which is in good agreement with the simulation. It should be noted that when the transformers are considered as part of the antenna, the measured reflection coefficient changes due to the parasitic inductance and high insertion loss (3.05 dB) of the four transformers. The simulated and measured S_{11} of the antenna with transformers is also shown in Figure 2.11. The measured resonant frequency of the antenna with transformers shifts to 39.55 MHz. Better matching and lower insertion loss of the antenna can be achieved by using only one impedance transformer (1:1.7) in practical applications where a long coaxial cable is no longer needed.

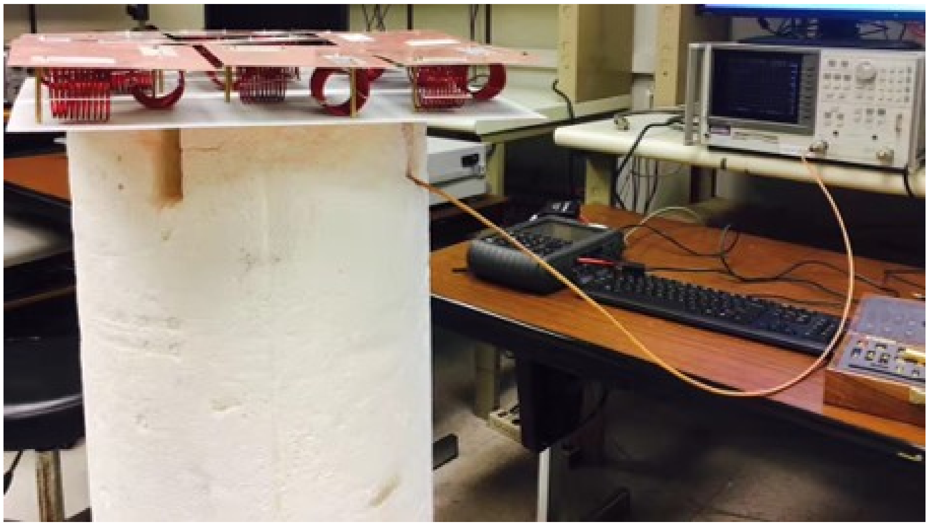

Figure 2.10: System setup for S_{11} measurement.

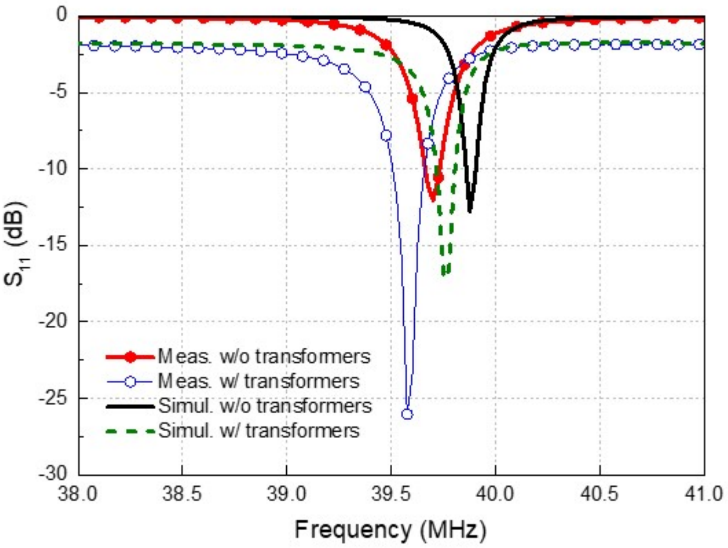

Figure 2.11: Simulated and measured S_{11} of the composite antenna with and without transformers.

Number of Transformers	Resonant Frequency min/max (MHz)	Input Impedance min/max (Ω)
0	40.1/40.15	113.1/265.8
1	39.52/39.55	166.5/263.1
2	39.55/39.57	90.146/102.829
4	39.58	831/86.5

Table 2.3: Measured resonant frequency and input impedance of the composite antenna with different numbers of transformers.

The absolute gain measurement of the proposed antenna is performed by applying the three-antenna method. Two folded dipole antennas and the proposed antenna are permuted as the transmitter and receiver pairs and the received power for each configuration is recorded. Both transmit and receive antennas are positioned on the top of two high platforms with a height of 3 m. Figure 2.12 shows the system setup when the proposed antenna is used as the transmit antenna and the folded dipole is used as the receive antenna. A portable network analyzer is used to feed the proposed antenna through a short cable to further reduce the cable effects. A spectrum analyzer is connected to the receive antenna to record the received power. For the purpose of comparison, a single element operating at 40 MHz is also fabricated and measured in the same way. The realized gain of the composite antenna and the single element is calculated from the measured data. Figure 2.13 shows the measured and simulated gain of the composite antenna. The measured peak gain of the composite antenna is -10.81 dBi, which is 9.24 dB higher than that of the single element. It should be noted that the measured gain is the overall realized gain of the antenna with transformers, which is slightly different from the actual realized gain of the antenna itself due to the extra loss and parasitic inductance introduced by the four transformers. In practice, higher gain can be realized by using a 1:1.7 impedance transformer with low insertion loss (0.5 dB) when the antenna is fed without a coaxial cable.

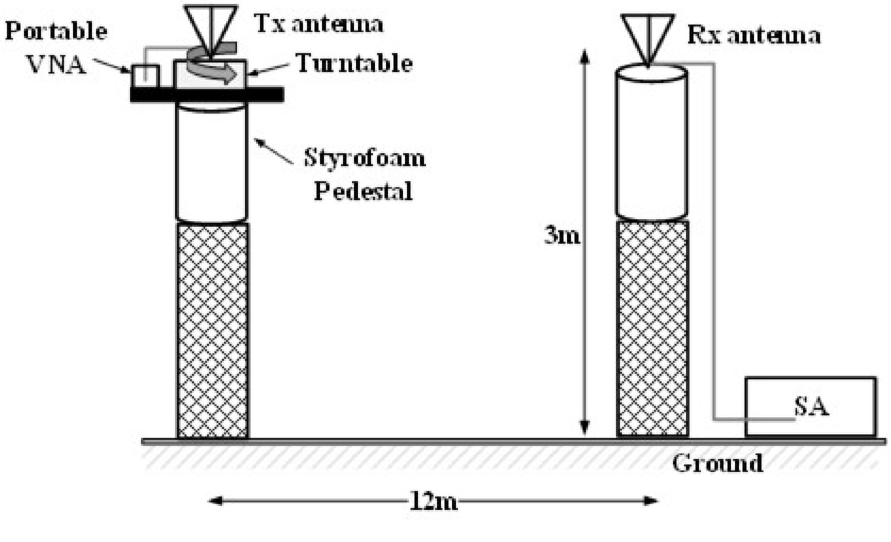

Figure 2.12: System setup for antenna gain and pattern measurement.

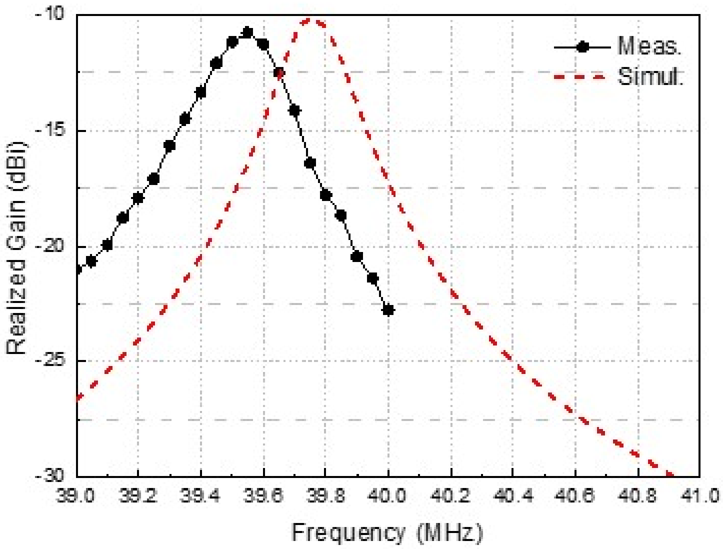

Figure 2.13: Measured and simulated gain of composite antenna.

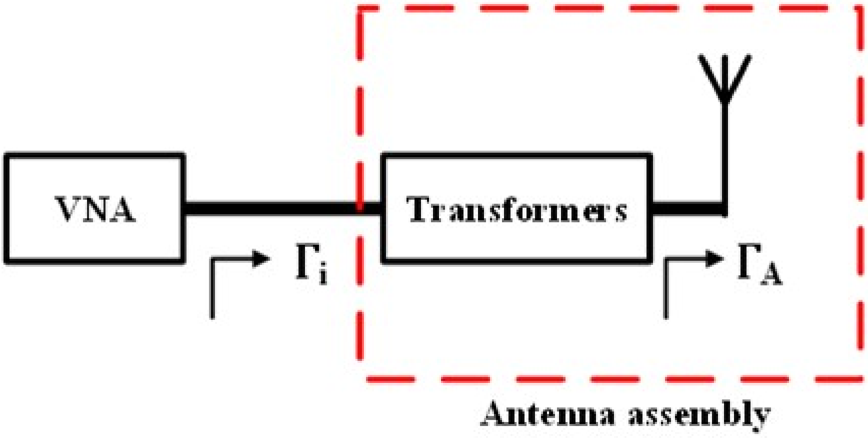

Figure 2.14: Measured and simulated gain of composite antenna.

Although the realized gain of the antenna cannot be measured directly, S_{11} correction can be applied in post-processing to calculate the actual gain of the antenna. We consider the case where the proposed antenna acts as a transmit antenna. A simplified block diagram of the transmit system is shown in Figure 2.14. According to Friis transmission formula, the actual received power P_r is expressed as

$$P_r = \alpha(1 - |\Gamma_i|^2)(1 - |\Gamma_r|^2)\frac{\lambda_0^2 G_t G_r}{(4\pi r)^2}P_i \tag{2.4}$$

and the expected received power without transformers P_r'

$$P_r' = \alpha(1 - |\Gamma_A|^2)(1 - |\Gamma_r|^2)\frac{\lambda_0^2 G_t G_r}{(4\pi r)^2}P_i \tag{2.5}$$

where P_i is the input power, α is the attenuation coefficient of the transformers, and Γ_i and Γ_A are measured reflection coefficients of the antenna assembly (i.e., the antenna with transformers) and antenna itself, respectively. Comparing (2.4) and (2.5), the realized gain of the proposed antenna can be obtained from

$$G_{rg} = \frac{G_m}{\alpha(1 - |\Gamma_i|^2)}(1 - |\Gamma_A|^2) \tag{2.6}$$

where G_{rg} is the realized gain of the antenna itself, and G_m is the measured realized gain of the antenna assembly (including the transformers). The gain of both composite antenna and single element are measured and corrected using 2.6. A comparison of antenna performance is summarized in Table 2.4. The measured results are in good agreement with the simulated results. The gain of the composite antenna is 9.84 dB higher than that of the single element whereas the fractional bandwidth is almost the same. The radiation patterns of the proposed antenna are measured using the same setup, where the single element acts as the receive antenna. Figure 2.15 shows the normalized radiation patterns in the E-plane and H-plane with 2° resolution. The measured patterns are in good agreement with the simulated results. The antenna features an omnidirectional radiation pattern in the H-plane.

	Single Element		Composite Antenna	
	Simulated	Measured	Simulated	Measured
Center Frequency (MHz)	40	39.73	39.88	39.58
Fractional Bandwidth	0.15%	0.16%	0.16%	0.18%
Peak Gain (dBi)	-15.85	-16.65	-6.03	-6.81
3-dB Gain Bandwidth (MHz)	0.2	0.17	0.23	0.26

Table 2.4: Comparison of simulated and measured antenna performance at 40 MHz.

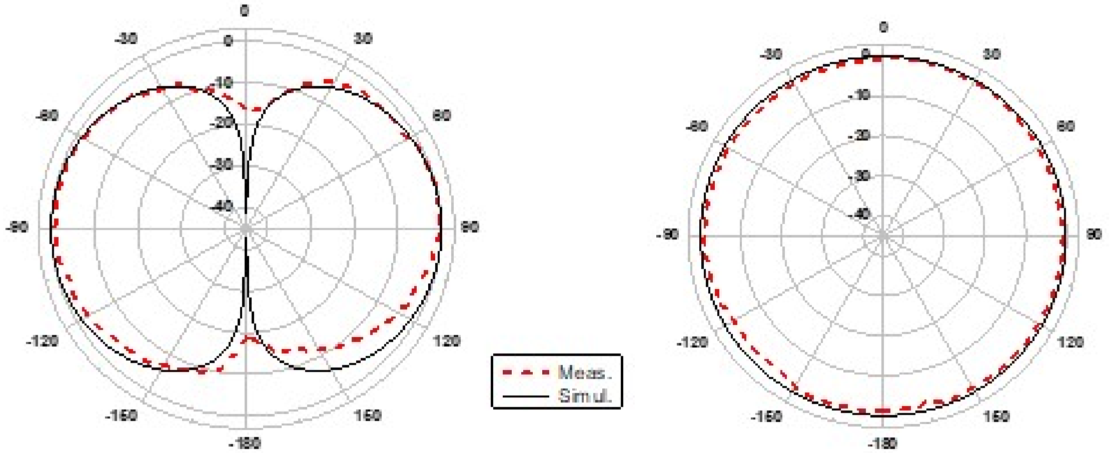

(a)

(b)

Figure 2.15: Simulated and measured antenna radiation patterns in the (a) E- plane and (b) H-plane.

2.5 Tunable Composite Antenna

As demonstrated in the previous section, the proposed composite antenna achieves a substantial gain enhancement but still suffers from the narrow fractional bandwidth, which may limit the utility of the antenna. To remedy this shortcoming, a tunable capacitor is applied to the transformer impedance matching circuit to adjust the center frequency of the antenna. The design schematic is illustrated in Figure 2.16 (a). The capacitor is inserted between the transformers and the feed of the antenna. The S-parameters of the four transformers and the antenna are extracted from the measurements so as to analyze their characteristic behavior. The fabricated tunable matching circuit is presented in Figure 2.16 (b), where a trimmer capacitor (part number: TZB4R500 by murata) is selected for its wide tunable range. The capacitance of the trimmer can be tuned by rotating the reel on the top. The capacitance as a function of the rotation angle of the reel is measured and shown in Figure 2.17. The maximum capacitance is about 81 pF at 0° and the minimum is 11 pF at 180°, corresponding respectively to the lowest center frequency of 39.48 MHz and highest center frequency of 40.67 MHz. It should be pointed out that the center frequency can be further extended if a capacitor with a wider tuning range is used. The maximum achievable center frequency is 41.52 MHz with a capacitance of 2 pF. The antenna cannot be matched with capacitances smaller than 2 pF. The minimum center frequency is about 39.12 MHz with capacitance of 200 pF. Further increasing the capacitance only slightly changes the center frequency. Figure 2.18 shows the simulated and measured S_{11} of the tunable antenna with the minimum and maximum capacitances. The measured center frequency and gain are shown in Figure 2.19 as a function of the capacitance of the trimmer capacitor. The maximum and minimum gains are -8.89 dBi and -10.59 dBi when the trimmer capacitor is set to 11 pF and 81 pF, respectively. The fractional bandwidth of the tunable antenna is 3.32%. For applications such as frequency hopping spread spectrum modulation, the mechanical trimmer can be replaced with a varactor so that the operating frequency can be tuned very quickly.

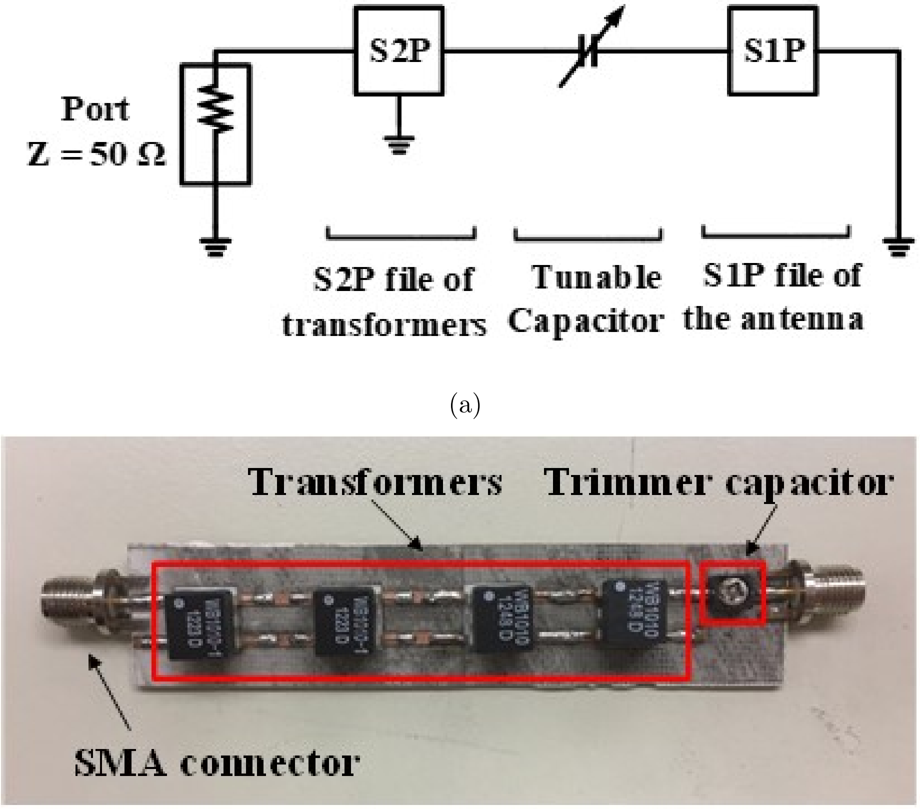

(a)

(b)

Figure 2.16: Schematic of tunable antenna and (b) fabricated tunable matching circuit.

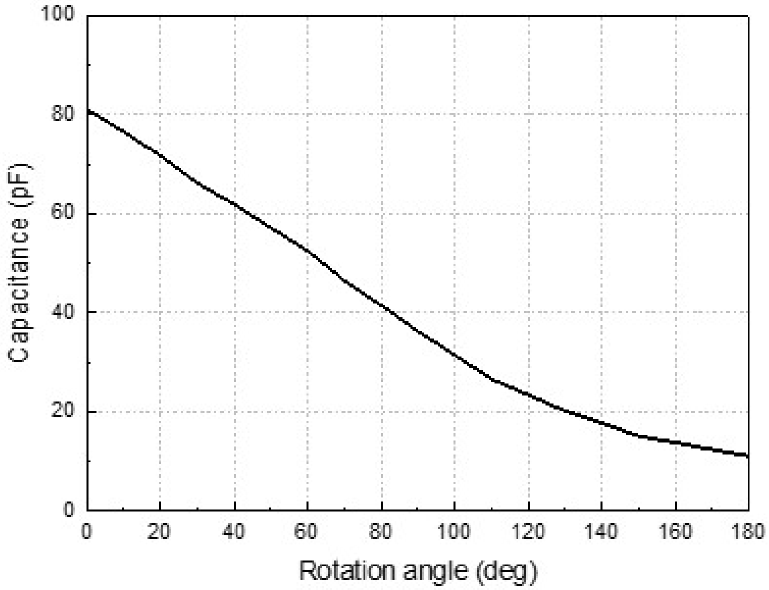

Figure 2.17: Trimmer capacitor capacitance as a function of the rotation angle.

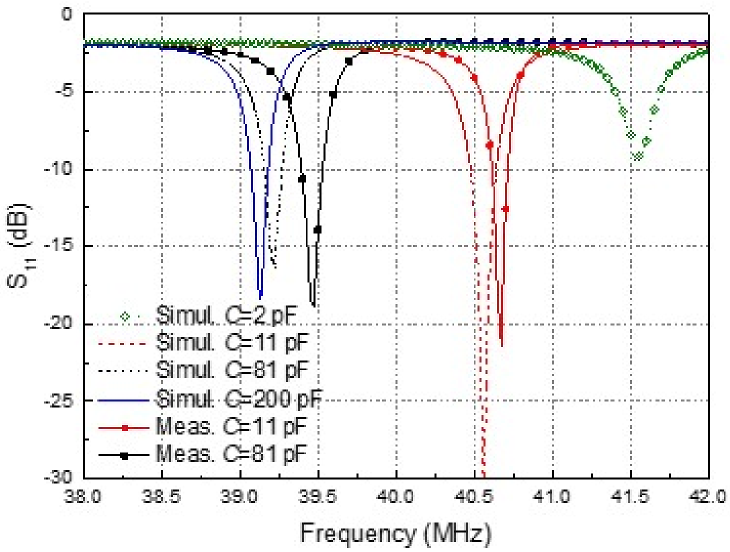

Figure 2.18: Simulated and measured S_{11} of the tunable antenna with various capacitances.

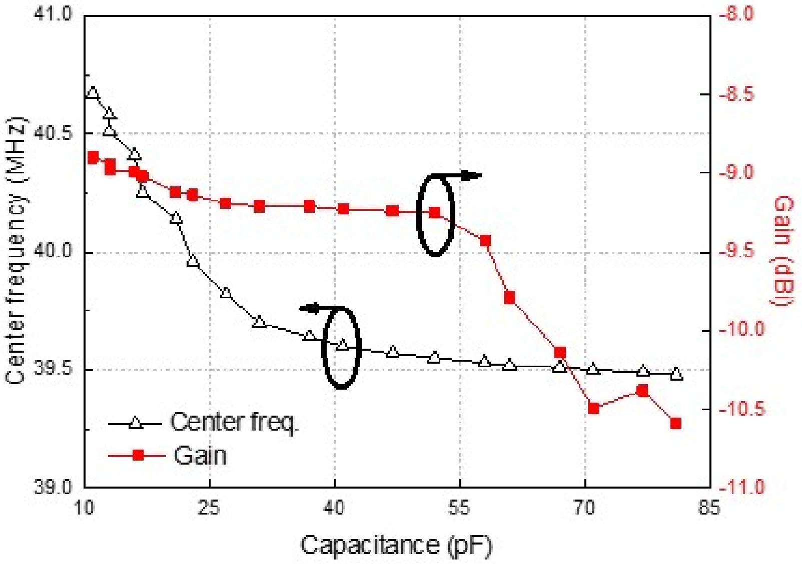

Figure 2.19: Center frequency and gain of the tunable antenna as functions of the capacitance of the trimmer capacitor.

Table 2.5 compares the performance of this work with that of some recently reported electrically small antennas. The proposed antenna achieves substantial gain and bandwidth improvement compared with [3] and [26] while maintaining a relatively small size.

Design	Dimension $h \times w \times l$	Realized Gain (dBi)	Bandwidth (%)
[25]	$\lambda_0/32 \times \lambda_0/9 \times \lambda_0/9$	-3.3	3.5
[24]	$\lambda_0/40 \times \lambda_0/16 \times \lambda_0/8$	-1.9	0.36
[3]	$\lambda_0/263 \times \lambda_0/87 \times \lambda_0/87$	-17.9	< 0.15
[26]	$\lambda_0/50 \times \lambda_0/78 \times \lambda_0/78$	-13.3	0.28
this work	$\lambda_0/150 \times \lambda_0/16 \times \lambda_0/16$	-6.81	3.32

Table 2.5: Performance comparison of latest electrically small antennas.

2.6 Conclusion

A composite antenna based on an extremely small two-legged monopole with enhanced gain and fractional bandwidth for low-VHF bands is proposed, fabricated, and tested. The antenna consists of one driven element and eight identical parasitic coupled elements, having a height of $0.0067\lambda_0$ and lateral dimensions of $0.0627\lambda_0$. By utilizing the mutual coupling between elements, it is shown that the antenna radiation resistance is improved significantly, leading to higher radiation efficiency. The peak gain of the composite antenna is shown to be about 10 dB higher than that of a single monopole. The composite antenna is further modified into a frequency-tunable antenna by adding a trimmer capacitor to its feed. The fractional bandwidth of the tunable antenna is 3.32%. A method for measuring monopole antennas with an electrically small ground plane using transformers is presented and discussed. It is shown that using cascaded transformers at the antenna feed can effectively suppress exterior currents on the feeding cable and thus significantly reduce undesirable cable effects on antenna performance.

CHAPTER III

mmWave Antenna Design for 5G Smartphones

3.1 Introduction

The world has witnessed the fast rollout of the fifth-generation wireless networks, denoted as 5G, for the past several years. This new wireless network promises to deliver ultra-high data rate, superior reliability and negligible latency. Among numerous enabling technologies for 5G, the deployment of the millimeter-wave (mmWave) spectrum is believed to be the key to making the ultimate performance a reality [73, 74]. By March 2020, the Federal Communications Commission (FCC) has completed auctions of multiple bands above 24 GHz for 5G uses, including the 24 GHz, the 28 GHz, and the upper 37 GHz, 39 GHz and 47 GHz bands, with a future plan to free up additional spectra in the 26 GHz and 42 bands, and to make more efficient use of the 70/80/90 GHz bands [75].

Despite substantial research and development efforts invested in mmWave 5G technology, the realization of standalone 5G is still a few years away. Full commercialization of 5G networks requires extensive implementation of 5G infrastructure. In view of the importance of handheld devices in daily life, mmWave antennas for 5G smartphones are considered a pivotal component in the realization of mmWave-based mobile networks. However, incorporating mmWave antennas into smartphones faces unprecedented challenges. In comparison to the sub-6-GHz frequency range, signal attenuation as well as conductive and dielectric dissipation becomes more sever at millimeter wave frequencies [74, 76, 77]. To compensate for the excessive loss and ensure the reliability of communication links, mmWave 5G antennas must feature high gain. Meanwhile, the mobility nature of smartphones requires coverage in all directions. The inherent dilemma of antenna gain and coverage has driven the antenna community to come up with alternative solutions, such as switched-beam arrays [78–80] and phased arrays [27,81–83], for mmWave 5G mobile applications. The very first conceptual design of a phased array antenna for 5G cellular devices is presented in [81]. Two sets of mesh grid patch antenna arrays are incorporated along the top and bottom edges of a cellular handset with each covering half of the sphere. Extensive measurements are conducted to demonstrate the feasibility of the antenna solution for 5G smartphones. Afterwards, various antenna designs are proposed for mmWave mobile devices [5, 29, 30, 84–87].

In addition to satisfying a number of design criteria shared with sub-6-GHz antennas [88], mmWave 5G mobile antennas have to meet several distinct requirements. First of all, they must feature polarization diversity in order to cope with unpredictable mobile channel environments. It has been demonstrated experimentally that the polarization mismatch becomes a substantial loss factor that heavily affects the overall quality of the wireless link at mmWave frequencies. Phased arrays with dual-polarized beam switching configurations provide more reliable Quality of Service (QoS) for mmWave 5G mobile phones than their single-polarized counterparts [5, 84]. Second, since spectrum harmonization across regions is limited, it is favorable to have antennas that feature wideband performance and/or can simultaneously cover multiple 5G frequency bands to meet different standards around the world. Last but not least, 5G antennas need to adapt to the evolution of the phones. As the demand for new features emerges, the number of antennas as well as other integrated modules has been increasing drastically. Stringent design constrains such as ultra-thin printed circuit boards (PCBs), limited real-estate and power capacity require minimizing antenna sizes, which is usually in conflict with antenna bandwidth and radiation efficiency. Moreover, aesthetic trends for larger metallic displays and thinner phone chassis further impair the overall performance of antennas.

There are mainly two types of antenna configurations widely adopted for beam steering in 5G smartphones, namely broadside antennas (antennas that radiate in the direction normal to the phone plane) and endfire antennas (antennas that radiate in the diretion parallel to the phone plane). Figure 3.1 illustrates the beam coverage of various antenna configurations. Broadside radiation is usually realized by planar phased array topologies such as patches or planar dipoles [89–95]. However, they inherently exhibit sub-hemispherical coverage, which may cause communication blind spots. Consider the use case scenario depicted in Figure 3.1 where the user is holding the cell phone with the antenna plane facing downwards. In this case, a broadside array alone cannot establish a reliable communication link with the Next Generation Node B (gNB) base station. Endfire antennas can effectively complement broadside arrays and have been investigated extensively in the past few years [5,29,30,85,96–98]. While horizontally polarized radiation in the endfire direction can be realized with relative ease using a planar dipole structure, exciting a vertically polarized electric field within a very thin substrate is extremely challenging. So far, only a few low-profile dual-polarized endfire antennas suitable for smartphones have been reported [5,85]. In [5], a dual-polarized endfire array with a total height of 0.52 mm is designed for 60 GHz applications. In [85], two types of Yagi-Uda antennas are designed on a 10-layer FR-4 laminate with a total height of 0.8 mm. However, the antennas can only cover a small portion of the 28 GHz band. Sometimes, stringent design constrains, such as the presence of a large metallic display closely below the antennas, make it almost impossible to create perfect endfire radiation. In such a case, antenna arrays with quasi-endfire radiation [99] can be considered possible alternatives as they are still able to establish a connection with the base station as demonstrated in Figure 3.1. So far, very few dual-band dual-polarized endfire or qusi-endfire [99] mmWave 5G antenna designs for smartphones have been reported in the literature. In [99], the gain of the vertically polarized antenna in the endfire direction is highly dependent on the substrate thickness; hence it cannot provide satisfying performance for thin smartphones.

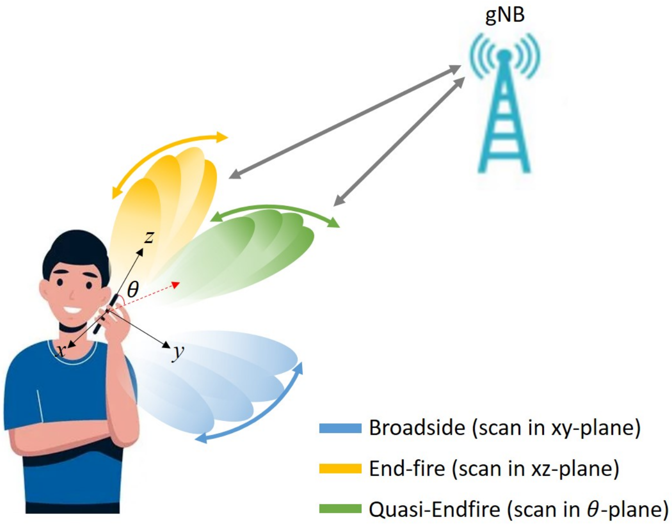

Figure 3.1: Beam coverage of different antenna configuration.

In this chapter, to address different system requirements, three antenna arrays are proposed for mmWave 5G smartphones: (1) a 28 GHz differential dual-polarized array, (2) a low profile 28/39 GHz dual-band dual-polarized array, and (3) a very compact dual-polarized array supporting multiple 5G bands. Figure 3.2 illustrates the conceptual architecture of the arrays and their potential locations in a smartphone. The design details for the three designs are presented in Section 3.2, 3.3 and 3.4, respectively. In addition, a near-field-based gain and pattern measurement technique is also developed to characterize the performance of probe-fed mmWave antennas.

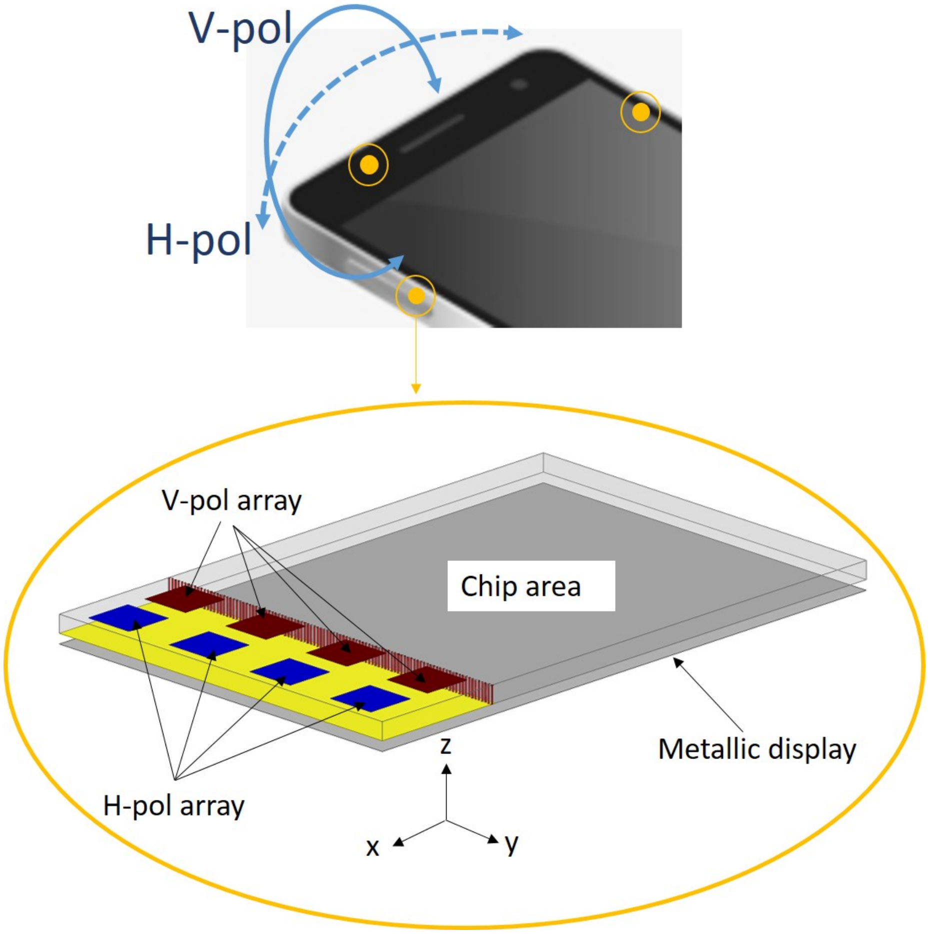

Figure 3.2: Conceptual illustration of the dual-polarized array.

3.2 A 28 GHz Differential Dual-Polarized mmWave Antenna Array for 5G Smartphones

This section presents a compact 28 GHz dual-polarized antenna array for 5G smartphones. The array element consists of two discrete antennas, a folded dipole and a substrate integrated waveguide cavity-backed slot antenna (SIW-CBSA), to provide two orthogonal linear polarizations. A coplanar waveguide (CPW)-to-coplanar stripline (CPS) balun is devised to realize the differential feed for the slot antenna. The bandwidth of the folded dipole is more than 6 GHz while that of the SIW-CBSA is 3 GHz. Both elements cover the 28 GHz band allocated for 5G communication.

The simulated peak gains of the horizontally and vertically polarized antennas are 3 and 4 dBi, respectively. The antenna is then expanded into a 1×4 phased array. The horizontally polarized array provides end-fire radiation and can steer the beam from -90° to 90° in the azimuth plane. The vertically polarized array features broadside radiation and can steer the beam from -50° to 50° in the elevation plane. The overall size of the array is 7.5 mm × 20 mm × 0.89 mm.

3.2.1 Antenna Element Design

3.2.1.1 Horizontally Polarized Folded Dipole

The planar half-wavelength dipole is by far the most popular choice for the realization of horizontally polarized fan-beam radiation in the endfire direction. In this design, we adopted the idea of the planar dipole but used a folded configuration to enhance the bandwidth. Furthermore, a ground plane is added to the back of the antenna to enhance the front-back ratio. Figure 3.3 (a) and (b) illustrate the 3D radiation patterns of the antenna with and without the ground plane. Clearly, the ground plane acts as a reflector, directing radiation toward the endfire direction, thereby creating an excellent fan-shaped pattern. The folded antenna inherently has a balanced feed, therefore it can be directly connected to the output of a differential circuit. Figure 3.3 (c) shows the reflection coefficients of the folded dipole with and without the ground plane. The port impedance is set to 100 Ω so as to be compatible with most commercial differential circuits. The antenna has a very wide bandwidth of more than 7 GHz, and the ground plane has little impact on antenna matching.

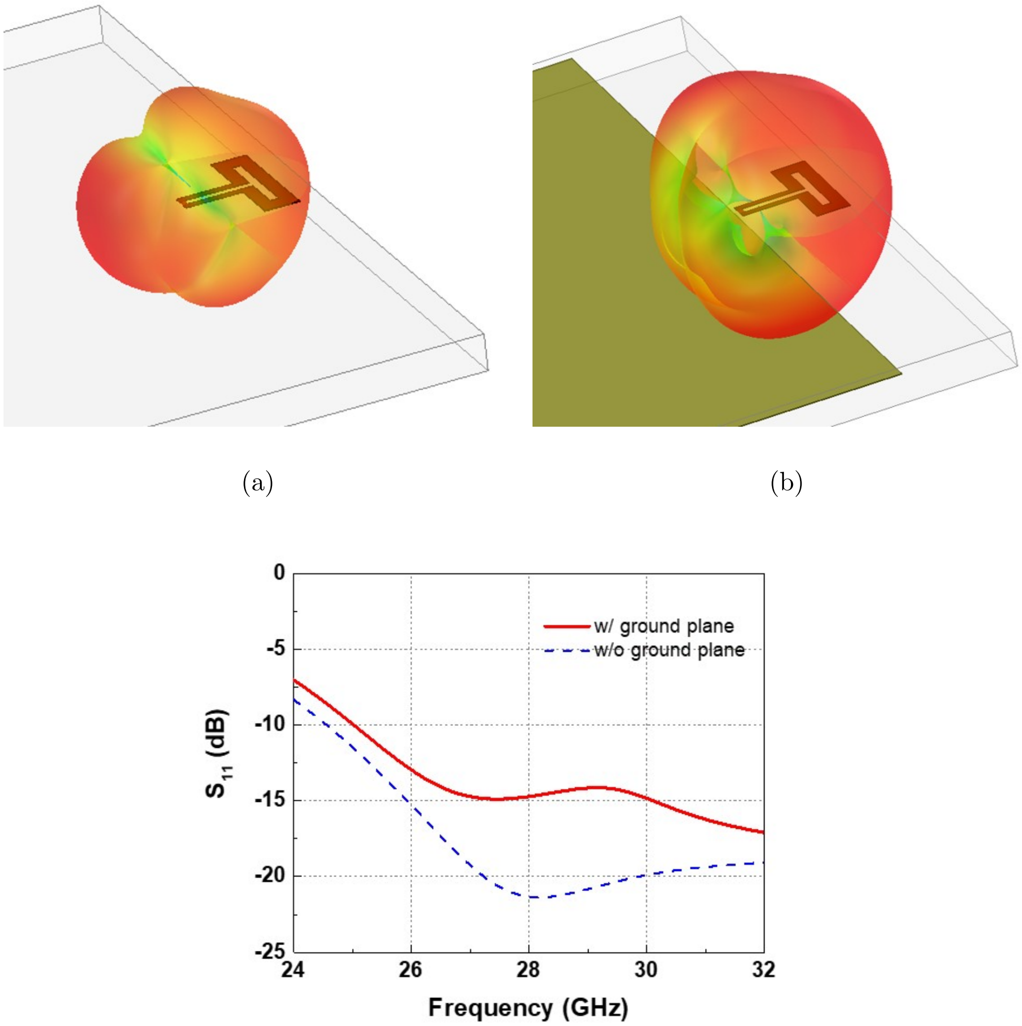

(a) (b)

(c)

Figure 3.3: The horizontally polarized folded dipole and simulated 3D radiation patterns (a) without and (b) with the ground plane. (c) The simulated reflection coefficients of the horizontally polarized folded dipole.

3.2.1.2 Vertically polarized differential SIW Cavity-Backed Slot Antenna

According to Babinet's Principle, a slot antennas, as the complementary structure of a dipole antenna, can provide vertically polarized radiation if placed horizontally on an infinite ground plane as illustrated in Figure 3.4. However, the realization of an omnidirectional slot antenna requires an infinite ground plane, which is practically unrealizable. As a consequence, conventional slot antennas always have radiation nulls along the ground plane. This can be explained by noting that the equivalent magnetic currents on the two sides of the ground plane are in the opposite directions [6]. The radiated electric fields cancel each other along the x-direction as shown in Figure 3.5.

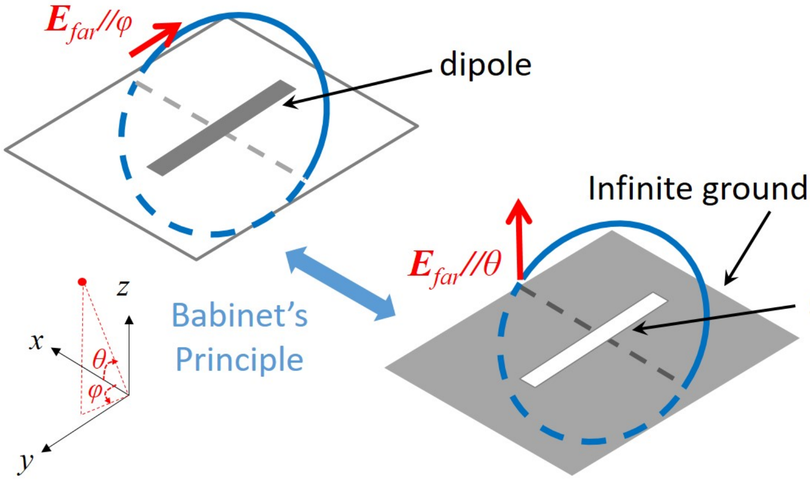

Figure 3.4: Babinet's Principle

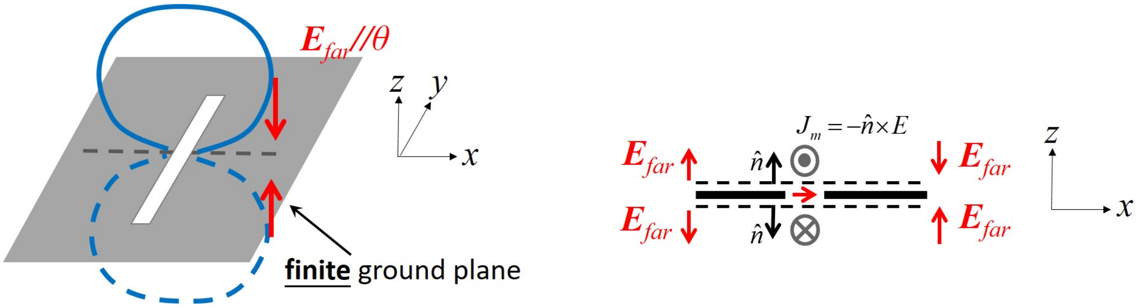

Figure 3.5: Radiation nulls of a slot antenna on a finite ground plane [6].

In order to remedy this issue, a substrate integrated waveguide cavity-backed slot antenna (SIW-CBSA) is devised as shown in Figure 3.6 (a). The cavity is realized by utilizing arrays of metallized through vias. The diameter and spacing of the vias are 0.2 mm and 0.4 mm, respectively, which are considered sufficient to ensure the performance of the SIW cavity [100]. The slot is fed by a coplanar waveguide (CPW). As shown in Figure 3.6 (a), the antenna features broadside radiation but also provides moderate radiation in the endfire direction, which is superior to conventional patch and slot antennas. The frequency response of the reflection coefficient of the antenna is plotted in Figure 3.6 (b). Similar to many other shallow cavity-backed slot antennas, this structure suffers from narrow bandwidth (27.8–28.9 GHz) due to the ultra-thin substrate (0.89 mm).

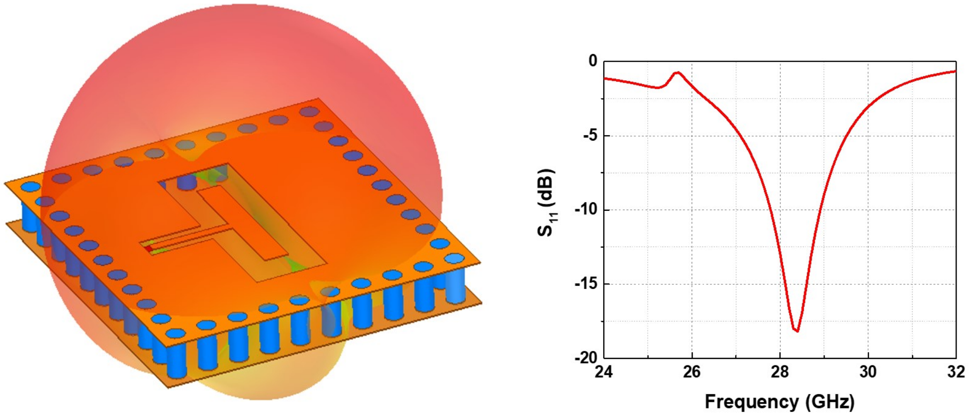

(a)

(b)

Figure 3.6: Single-sided SIW cavity-backed slot antenna. (a) Antenna configuration and simulated radiation pattern. (b) Simulated reflection coefficients.

A common way to enhance the bandwidth of an antenna is to combine multiple resonances. To create additional resonances, a second slot is introduced on the other side of the cavity, and a square metallic plate is then inserted into the cavity, parallel to the two slots. Figure 3.7 (a)–(c) shows the top, front and exploded views of the antenna. The metallic plate together with the CPW feed forms a parallel *LC* resonant circuit. The resonant frequency can be adjusted by tuning the size of the plate. Furthermore, the introduction of the second slot and the metallic plate changes the electric field distribution inside the cavity, moving the resonant frequency of the cavity into the band of interest. Figure 3.7 (d) shows the simulated input impedance of the double-sided SIW-CBSA. The first resonance is due to the cavity, the second resonance is created by the *LC* circuit at the feed, and the last resonance comes from the radiating slot on the top.

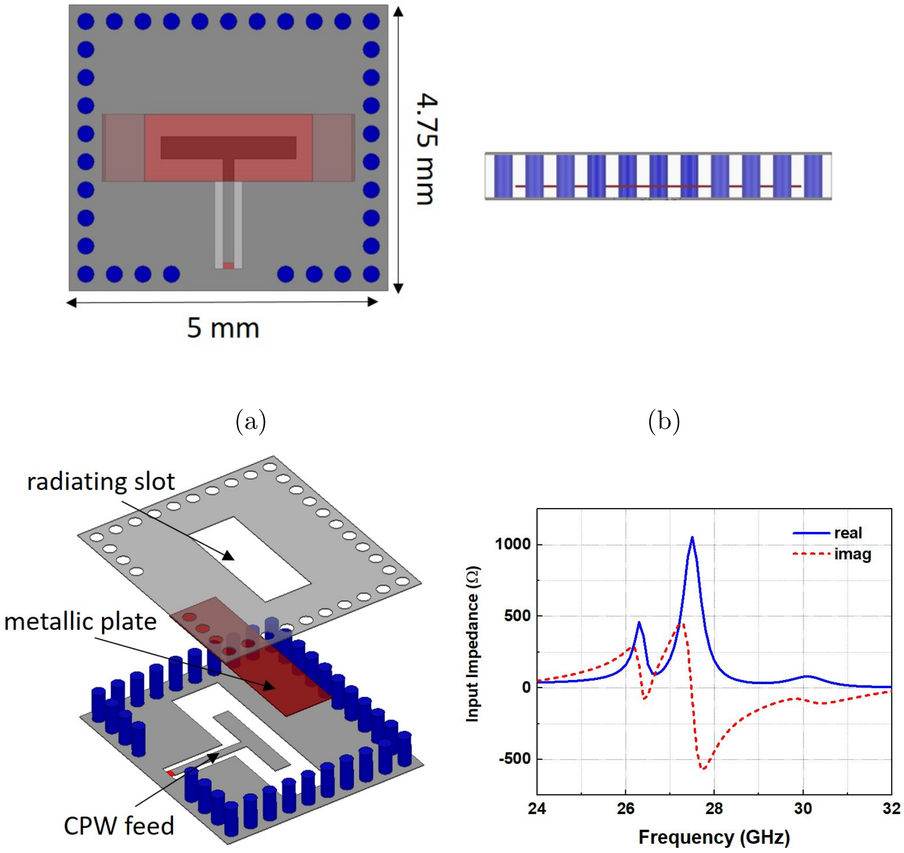

(a) (b)

(c) (d)

Figure 3.7: Double-sided SIW cavity-backed slot antenna with a metallic plate. (a) Top view. (b) Front view. (c) Exploded view. (d) Simulated input impedance of the double-sided SIW-CBSA.

Although there are three resonances in the band of interest, the first and second resonances are very difficult to match due to their large and rapid changes in the magnitude of the input impedance as a function of frequency. In order to make these resonances more matchable and to transform the unbalanced CPW feed to a balanced feed, a wideband CPW-to-CPS balun is designed. The geometry of the balun is shown in Figure 3.8. The balun is a modified version of the design in [101]. In addition to the unbalaced-to-balanced transition, it also provides a 100 Ω to 100 Ω impedance matching. The radial slot functions as a very wideband open circuit, forcing the electric field to propagate between the two conductors of the CPS. The two bond wires near the discontinuity ensure that the potential on the two ground planes stays the same and prevent unwanted modes. The performance of the balun is evaluated by connecting two identical baluns back-to-back as shown in Figure 3.9 (a). The CPW ports are internally connected together while the CPS ports are defined as the external ports. The simulated reflection coefficients (S_{11}) and transmission coefficients (S_{21}) are plotted in Figure 3.9 (b) and (c), respectively. The reflection coefficients are below -18 dB and the transmission coefficients are better than -2 dB across the frequency range from 24 to 32 GHz.

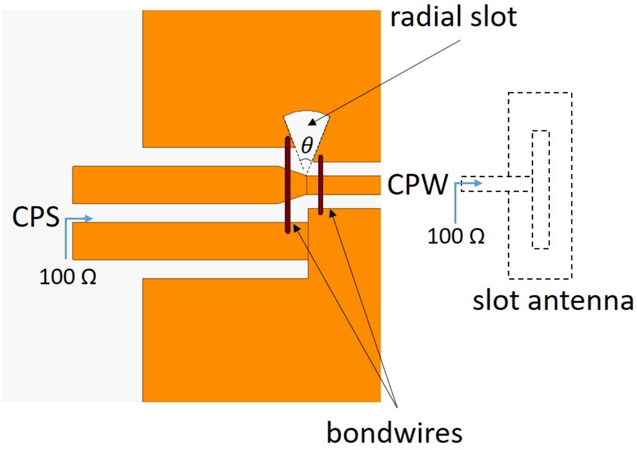

Figure 3.8: Geometry of the CPS-to-CPW balun.

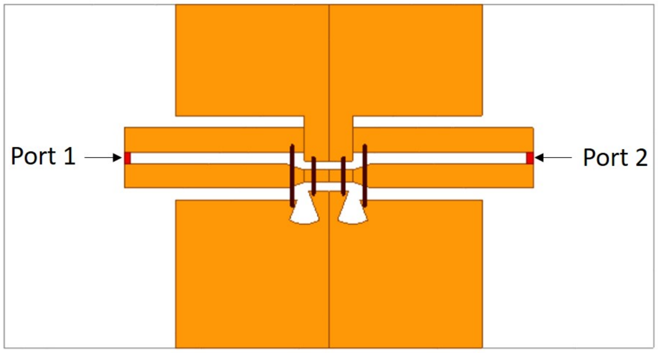

(a)

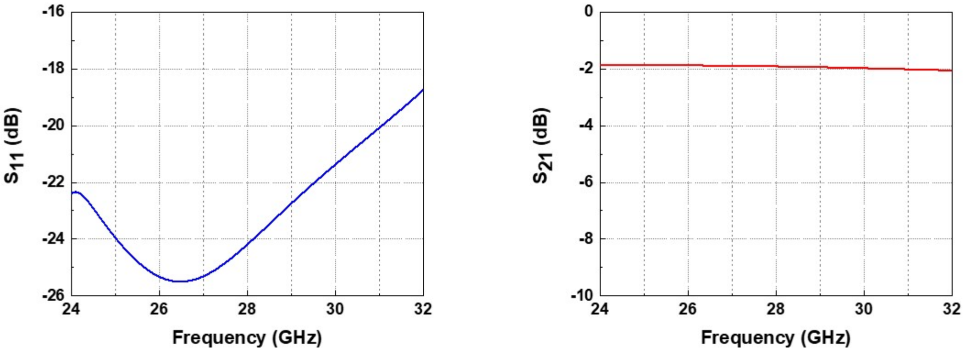

(b) (c)

Figure 3.9: (a) Back-to-back configuration of two identical baluns. The simulated (b) reflection coefficients (S_{11}) and (c) transmission coefficients (S_{21}) of the back-to-back configuration.

The differential-fed double-sided SIW cavity-backed slot antenna (DFDS-SIW-CBSA) with the balun is shown in Figure 3.10 (a). The top and bottom of the cavity are situated on the 2^{nd} and 4^{th} metal layers (M2 and M4), respectively, and the metal plate is placed on M3. Figure 3.10 (b) shows the input impedance of the antenna with the balun. The input impedance becomes much smoother after adding the balun, and the values at all three resonances can be easily matched to 100 Ω. The simulated reflection coefficients from 24–32 GHz are plotted in Figure 3.10 (c). The antenna can operate from 26.7–29.7 GHz, covering the entire 28 GHz band designated for 5G.

Figure 3.11 (a), (b) and (c) show the simulated radiation patterns of the antenna at 26.7 GHz, 28 GHz and 29.7 GHz, respectively. The pattern remains stable across the entire frequency band.

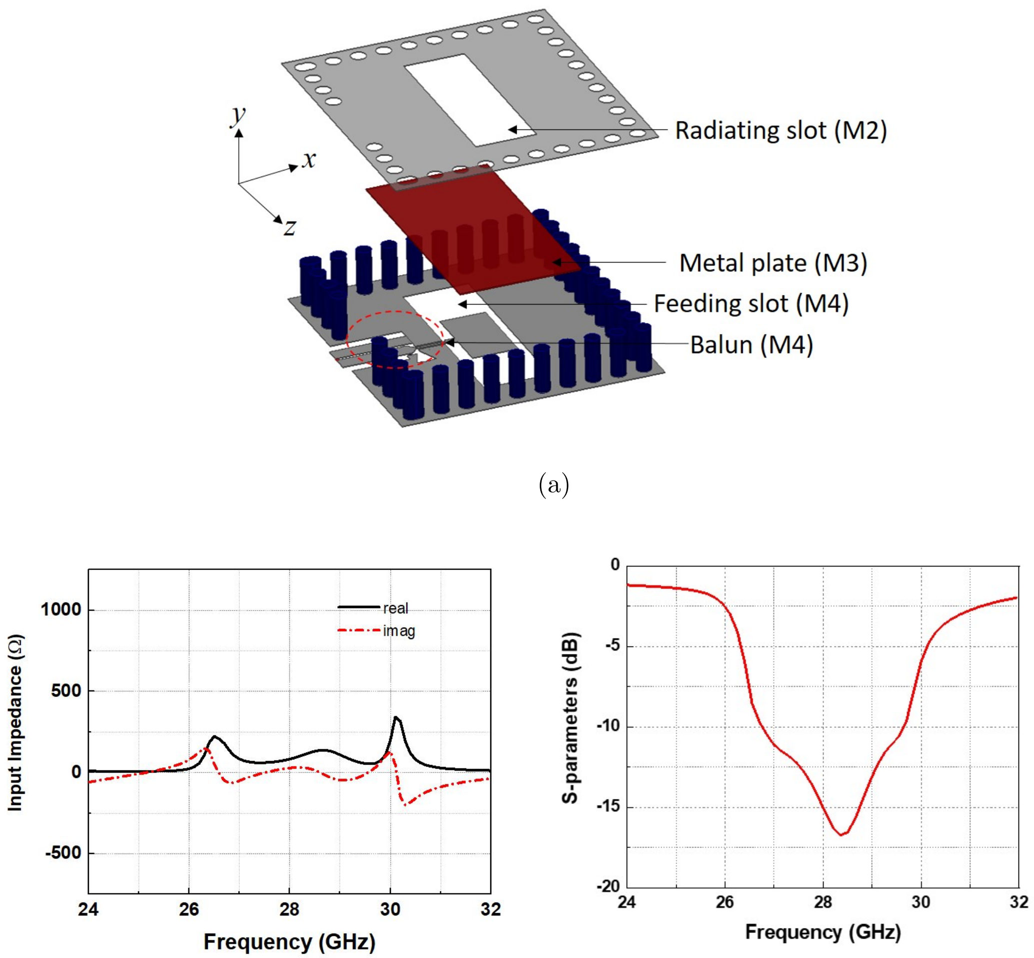

(a)

(b) (c)

Figure 3.10: (a) Geometry of the DFDS-SIW-CBSA. (b) Simulated input impedance and (c) reflection coefficients.

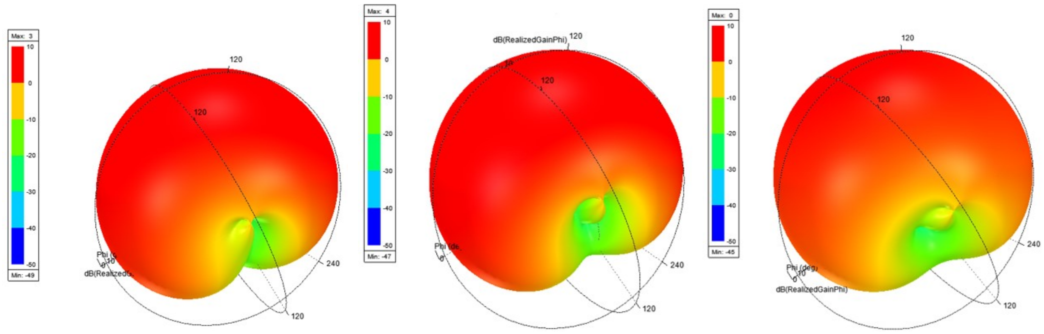

(a) (b) (c)

Figure 3.11: Simulated radiation patterns of the DFDS-SIW-CBSA at (a) 26.7 GHz, (b) 28 GHz and (c) 29.7 GHz.

3.2.1.3 Dual-Polarized Antenna

The final configuration of the dual-polarized antenna combining the horizontally polarized dipole and the vertically polarized DFDS-SIW-CBSA is shown in Figure 3.12. The folded dipole antenna is placed on the top metal layer (M1) along the edge of the PCB. The DFDS-SIW-CBSA is placed behind the folded dipole. The simulated S-parameters of the dual-polarized antenna are shown in Figure 3.13. The folded dipole has a bandwidth of more than 6 GHz and the DFDS-SIW-CBSA has 3 GHz bandwidth. Both elements can cover the entire 28 GHz band with stable patterns. The port-to-port isolation between the antenna elements is more than 20 dB within the band. The simulated 3D radiation patterns of the two antennas are shown in Figure 3.14 (a) and (b), respectively. The dipole creates a perfect fan-beam radiation pattern in the endfire direction and has a peak gain of 3 dBi. The DFDS-SIW-CBSA provides broadside radiation with a peak gain of 4 dBi, and a moderate gain of -0.47 dBi in the endfire direction.

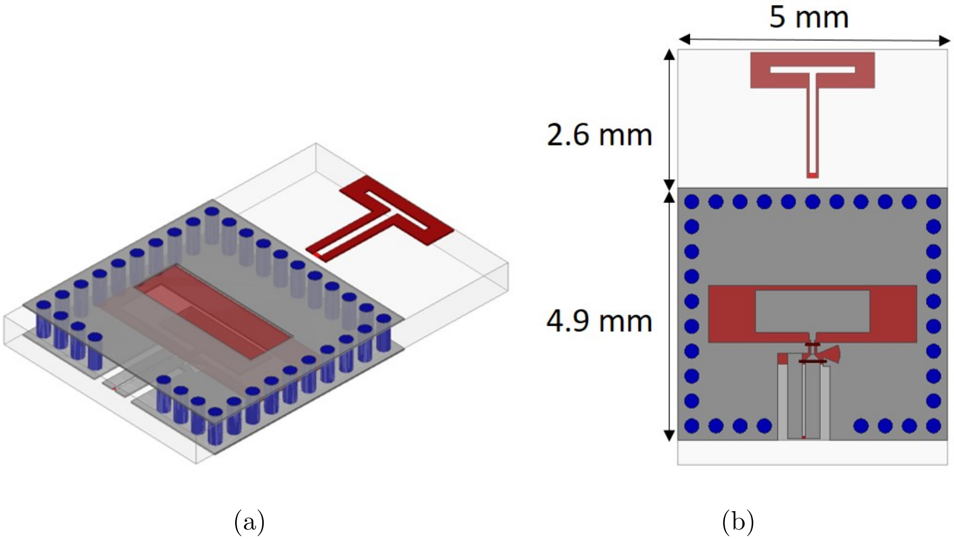

Figure 3.12: Topology of the dual-polarized antenna. (a) 3D view and (b) bottom view.

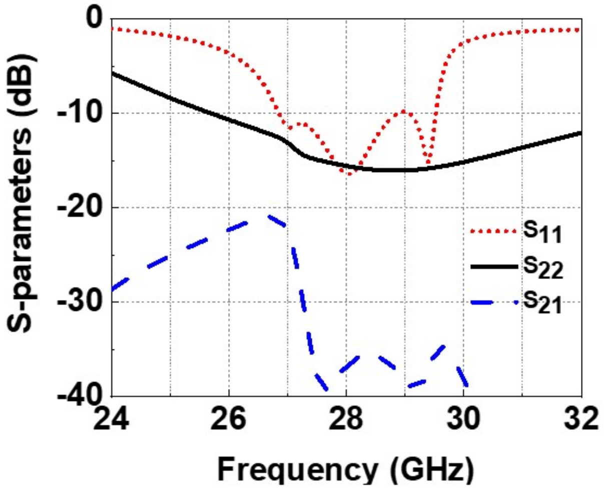

Figure 3.13: Simulated S-parameters of the combined V-pol (port 1) and H-pol (port 2) antennas.

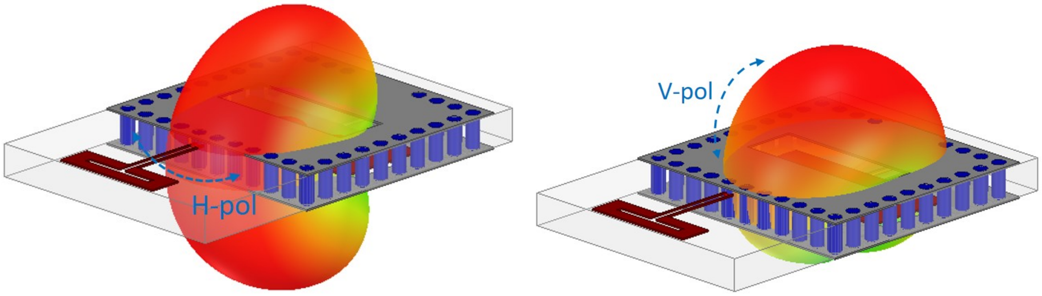

(a) (b)

Figure 3.14: Simulated 3D radiation patterns of (a) the folded dipole and (b) the DFDS-SIW-CBSA.

3.2.1.4 1 × 4 Dual-Polarized Phased Array

The dual-polarized antenna is expanded into a 1 × 4 phased array as shown in Figure 3.15. The total dimensions of the array are 7.5 mm × 20 mm × 0.89 mm. The simulated reflection coefficients of the H-pol and V-pol arrays are plotted in Figure 3.16 (a) and (b), respectively. The V-pol antennas have slightly degraded matching performance when formed into an array.

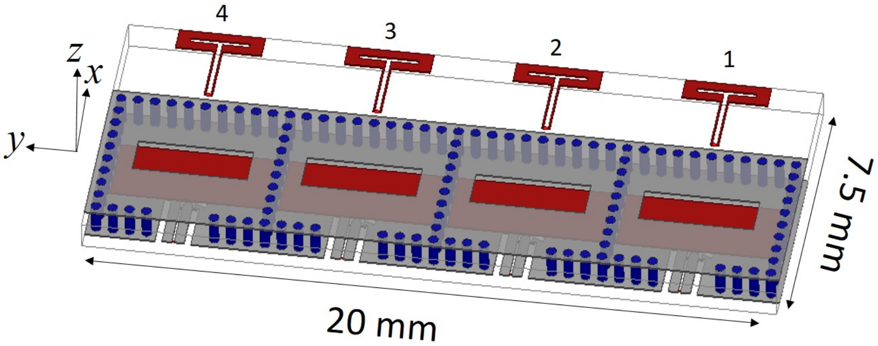

Figure 3.15: 1 × 4 phased array.

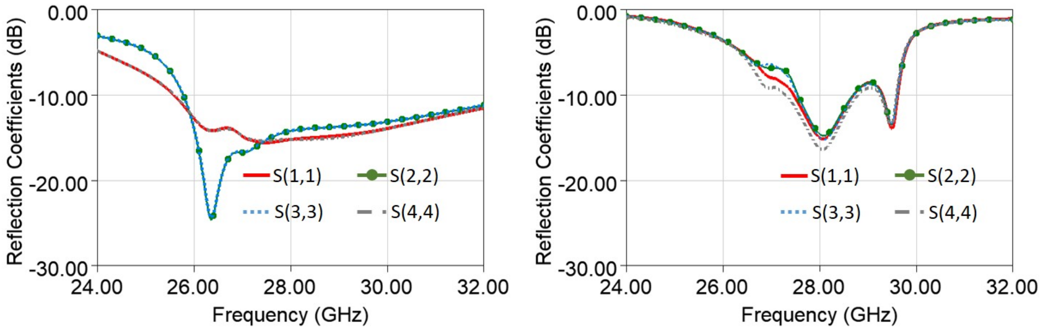

(a) (b)

Figure 3.16: Simulated reflection coefficients of the (a) H-pol array and (b) V-pol array. Port numbering from right to left: 1-4.

Figures 3.17 (a) and (b) show the simulated scan performance of the H-pol and V-pol arrays, respectively. The H-pol array can steer the beam from −90° to 90° in the *xy*-plane while maintaining a gain variation of less than 0.2 dB. The V-pol array has a scan range of −50° to 50° in the *yz*-plane

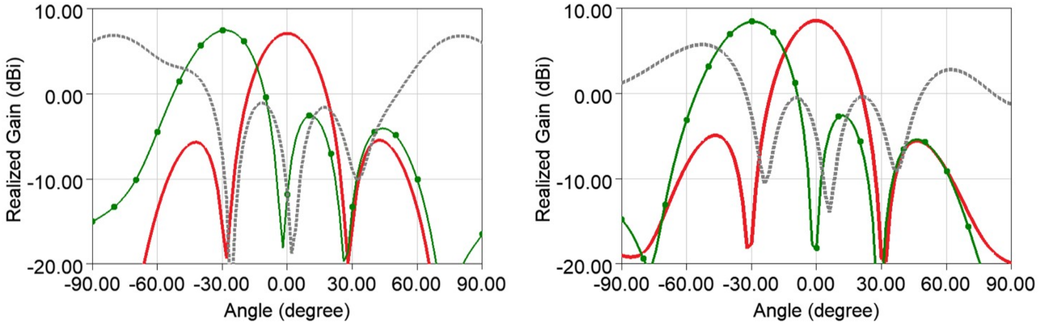

(a) (b)

Figure 3.17: Simulated scan performance of the (a) H-pol array in the *xy*-plane and (b) V-pol array in the *yz*-plane.

3.3 A Low-Profile Dual-Band Dual-Polarized Quasi-Endfire Phased Array for mmWave 5G Smartphones

This section presents a very compact dual-band dual-polarized array that can simultaneously cover the 28 GHz and the 39 GHz bands for mmWave 5G smartphones. The array element is based on two individual antennas, a planar folded dipole and a novel *hexagonal bridge antenna*, which respectively provide endfire horizontally polarized radiation and quasi-endfire vertically polarized radiation. The array element features lateral dimensions of 6.5 mm × 5 mm and a height profile of only 1.12 mm. A prototype of a 1 × 4 phased array is designed, fabricated and tested. The size of the array is 6.5 mm × 23 mm × 1.12 mm ($0.607\lambda_0 \times 2.147\lambda_0 \times 0.105\lambda_0$, where λ_0 is the free-space wavelength at 28 GHz), which is suitable for cellular applications. The array is intended to be incorporated along the edges of a mobile phone for beam steering.

3.3.1 Array Element Design

The design is realized on a multilayer RO 4003C ($\epsilon_r = 3.55, \tan\delta = 0.0027$) laminate. Figure 3.18 shows the PCB stack-up. The thickness of the three dielectric layers from the top to bottom are 0.203 mm, 0.508 mm and 0.203 mm, respectively. RO 4450F prepreg ($\epsilon_r = 3.52, \tan\delta = 0.004$) of thickness 0.102 mm is used for bonding. The total height of the laminate is 1.12 mm. The 3$^{\text{rd}}$ metal layer (M3) is fully metalized and is used as the RF ground. The potential impact of a large metallic display placed closely below the antennas is incorporated into the design process, which is a unique feature that previously reported studies have ignored.

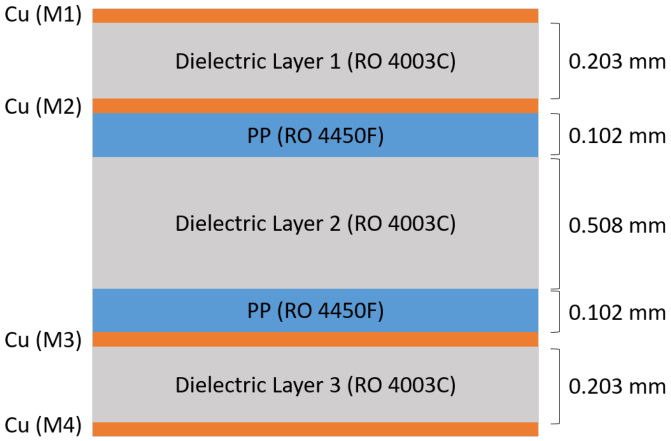

Figure 3.18: PCB stack-up

3.3.1.1 Dual-Band Horizontally Polarized Folded Dipole

We adopted the planar dipole described earlier in Section 3.2 as the radiating element in the 28 GHz band. To realize the operation in the 39 GHz band, a parasitic strip is added in front of the driven element. The capacitive coupling between the folded dipole and the strip creates a resonance at around 39 GHz. Because the addition of the parasitic strip changes the response in the lower band, iterative parametric tuning procedure is used to simultaneously match the antenna in both bands. The geometry of the antenna along with its design parameters is shown in Figure 3.19. The antenna is configured on M4, and the reference ground is located on M3. The portion of the ground plane (i.e., M3) right above the antenna is removed so that the antenna can achieve the desired matching performance. As the diffraction from the ground edge affects the radiation pattern of the antenna, the distance between the antenna and the edge of the ground plane d_1 is optimized for the maximum realized gain in the endfire direction.

Since the antenna will be connected to the output of a single-ended radio frequency integrated circuit (RFIC), a wideband balun is implemented to provide the transition from the balanced coplanar stripline to the unbalanced microstrip line as well as

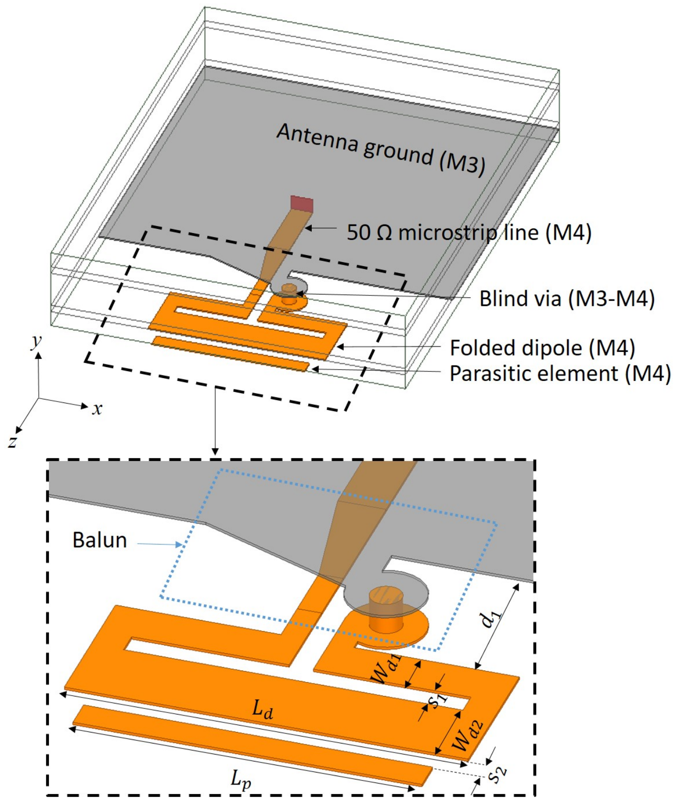

Figure 3.19: Dual-band folded dipole with the balun. $L_d = 2.5$ mm, $L_p = 2.16$ mm, $W_{d1} = 0.3$ mm, $W_{d2} = 0.5$ mm, $s_1 = 0.15$ mm, $s_2 = 0.15$ mm, $d_1 = 0.7$ mm.

100 Ω-to-50 Ω impedance matching. The close-up view in Figure 3.19 shows the coplanar-stripline-to-microstrip-line balun connected to the folded dipole. The ground is gradually tapered towards one leg of the coplanar stripline and then connected to it through a blind via. The other leg of the coplanar stripline is progressively widened while extending towards the ground plane, and eventually transforms into a 50 Ω mictrostrip line. Figure 3.20 (a) shows the 2-port configuration of the balun and its design parameters. The port impedance of Port 2 is set to 100 Ω, which is compatible with the folded dipole and most commercial differential circuits. Figure 3.20 (b) shows the S-parameters of the balun. The balun features a very wide bandwidth with maximum insertion loss of 0.74 dB in the lower band (26–30 GHz) and 0.89 dB in the higher band (38–40 GHz).

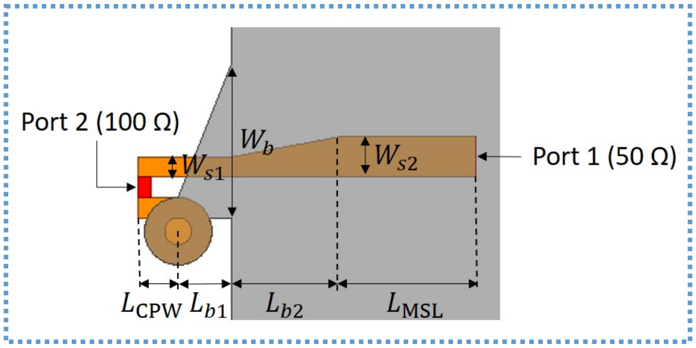

(a)

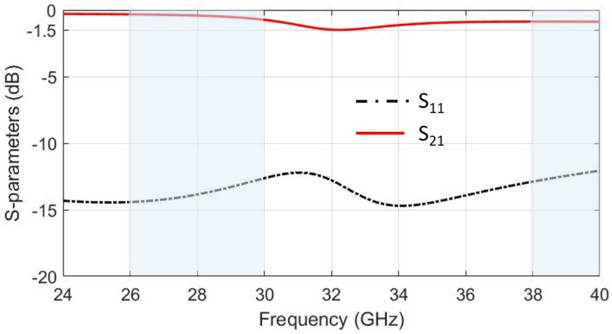

(b)

Figure 3.20: (a) The coplanar-stripline-to-microstrip-line balun. $W_{s1} = 0.15$ mm, $W_{s2} = 0.3$ mm, $W_b = 1.15$ mm, $L_{b1} = 0.4$ mm, $L_{b2} = 0.8$ mm, $L_{\text{CPW}} = 0.3$ mm, $L_{\text{MSL}} = 1$ mm. (b) Simuated S-parameters of the balun.

3.3.1.2 Dual-Band Vertically Polarized Hexagonal Bridge Antenna

Vertically polarized endfire radiation is usually realized by utilizing a vertical dipole or a monopole to support currents in the vertical direction. The ultra-thin substrates used in smartphones pose a tremendous challenge in supporting such structures. Conventional antenna miniaturization is usually achieved at the expense of bandwidth and efficiency [102–105]. In this section, a hexagonal bridge antenna is proposed for vertically polarized radiation. This novel antenna topology features a very low profile of 0.92 mm ($0.08\lambda_0$ at 28 GHz) and maintains less than -10 dB reflection coefficients from 26.63 GHz to above 32 GHz in the lower band and from 37.9 GHz to above 40 GHz in the higher band. It should be noted that we deliberately choose a structure that requires a large ground plane as the ground plane can isolate the antenna from the metallic display, leading to more robust performance.

The design procedure consists of a number of intermediate steps as illustrated in Figure 3.21. First, a wide nearly half-wavelength microstrip line is used as the basis of the design. The portion exceeding the height profile h is folded into a strip parallel to the ground with the end shorted to the ground. This structure constitutes a short-circuited half-wavelength microstrip line resonator. The 180° phase shift introduced by the half-wavelength transmission line results in the currents on the two vertical ends flowing in the same direction. These currents generate in-phase vertically polarized electric fields. Meanwhile, the horizontal current is canceled by its image on the ground plane. In addition, the horizontal current on the right side of the top plate is in the opposite direction of that on the left side; hence unwanted horizontal radiation from these currents cancel each other in the far field as well, producing good polarization purity. A metal plate is added behind the antenna as a reflector to suppress the back radiation and isolate the antenna module from the RFICs.

Next, instead of placing the vertical plates on the left and right sides of the top plate, we place them diagonally along the front and back edges of the top plate as shown in Figure 3.21 (b). This special arrangement allows the current to take different paths on the top plate, which leads to an additional resonance in the 28 GHz band. Figure 3.22 (a)–(d) illustrate the current distribution and 3D radiation patterns of Ant.1 at 28 GHz, Ant.1-1 at 26 GHz, 28 GHz and 30 GHz, respectively. At 26 GHz, the current path length is around half the wavelength, and at 30 GHz, the current path length is slightly less than three quarters of the wavelength. Figure 3.23 (a) compares the reflection coefficients of Ant.1 and Ant.1-1 from 24 GHz to 32 GHz. It is clear that Ant.1 has only one resonance with a very narrow bandwidth in the reported frequency range whereas Ant.1-1 has two wideband resonances. The influences of the width (W_t) and length (L_t) of the top plate on the reflection coefficients are investigated by

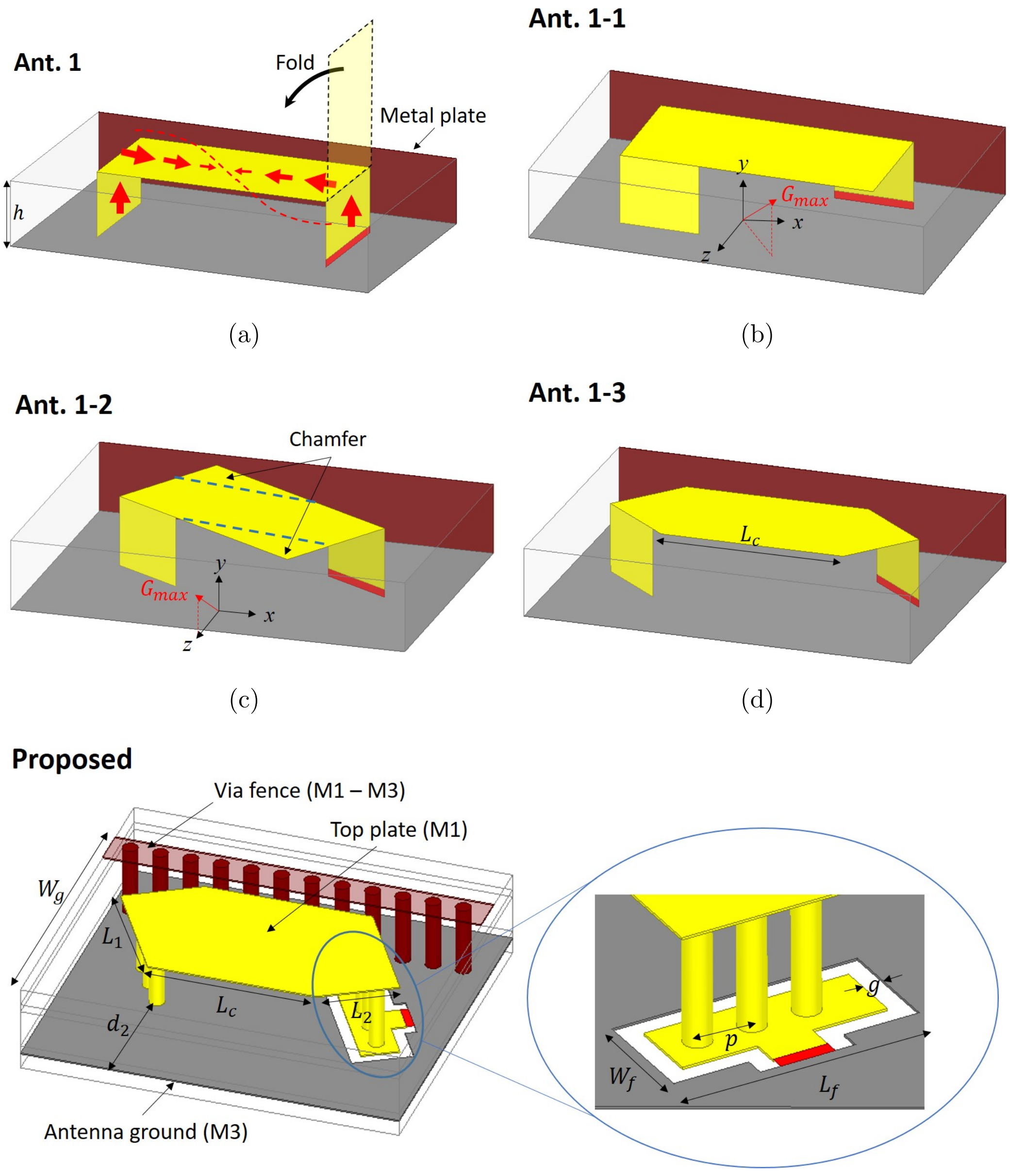

(a) (b)

(c) (d)

(e)

Figure 3.21: Design procedure of the dual-band vertically polarized hexagonal bridge antenna. (a) Fold a half-wavelength microstrip line. (b) Diagonally arrange the vertical plates. (c) Rotate the antenna. (d) Chamfer the corner. (e) The proposed antenna. $L_1 = 1.69$ mm, $L_c = 2.22$ mm, $L_2 = 1.07$ mm, $L_f = 1.8$ mm, $W_f = 0.8$ mm, $g = 0.15$ mm, $d = 0.4$ mm.

varying one parameter with the other fixed. The results are shown in Figure 3.23 (a) and (b), respectively. The width W_t has a much more significant impact on the higher resonance while the length L_t mainly controls the lower resonance, which indicates

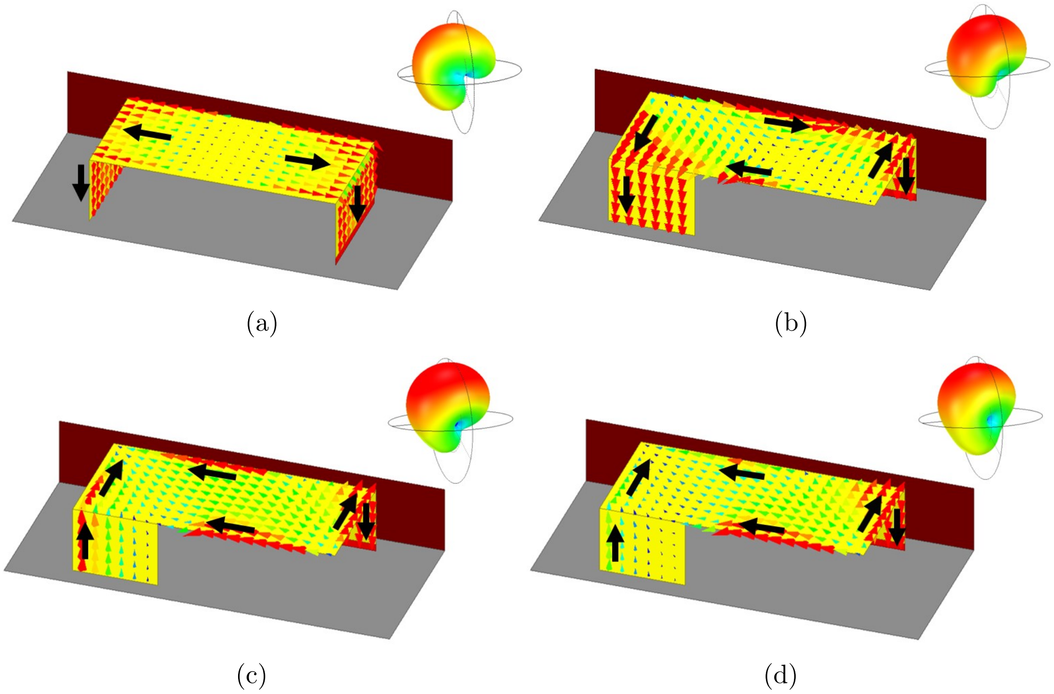
(a) (b)

(c) (d)

Figure 3.22: Current distribution and radiation patterns of (a) Ant.1 at 28 GHz, Ant.1-1 at (b) 26 GHz, (c) 28 GHz and (d) 30 GHz.

that bandwidth enhancement can be easily achieved by tuning the size of the top plate to merge the two resonances together. Furthermore, the radiation pattern of Ant.1-1 remains stable over the entire 28 GHz band.

However, the offset of the vertical plates in the z-direction causes the radiation pattern to rotate counterclockwise by 35° about the y-axis. To compensate for this offset, the entire element is rotated 35° clockwise. Figure 3.24 (a) shows the normalized radiation patterns in the xz-plane at 28 GHz before and after the rotation (Ant.1-1 and 1-2). The 3D radiation pattern of Ant.1-2 at 28 GHz is shown in Figure 3.24 (b). The antenna features a quasi-endfire radiation pattern due to the finite ground plane. It provides maximum radiation at $\theta = 43°$ in the yz-plane and moderate radiation in the endfire direction.

For the high-band operation, the top plate is formed into a hexagon (Ant.1-3). The two open corners without the vertical plates are chamfered (trimed edges) to create a full-wavelength current path at 39 GHz. Figure 3.25 (a) illustrates the current

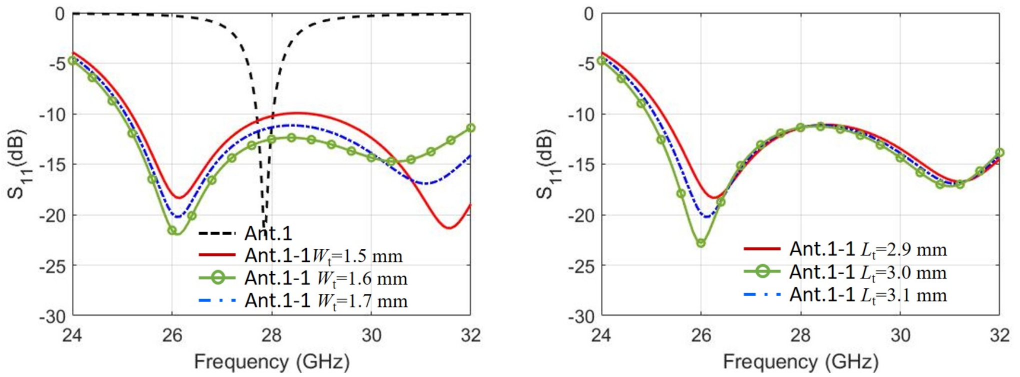

(a) (b)

Figure 3.23: (a) Simulated reflection coefficients of Ant.1 and Ant.1-1 with different W_t and fixed $L_t = 3$ mm. (b) Simulated reflection coefficients of Ant.1-1 with different L_t and fixed $W_t = 1.6$ mm.

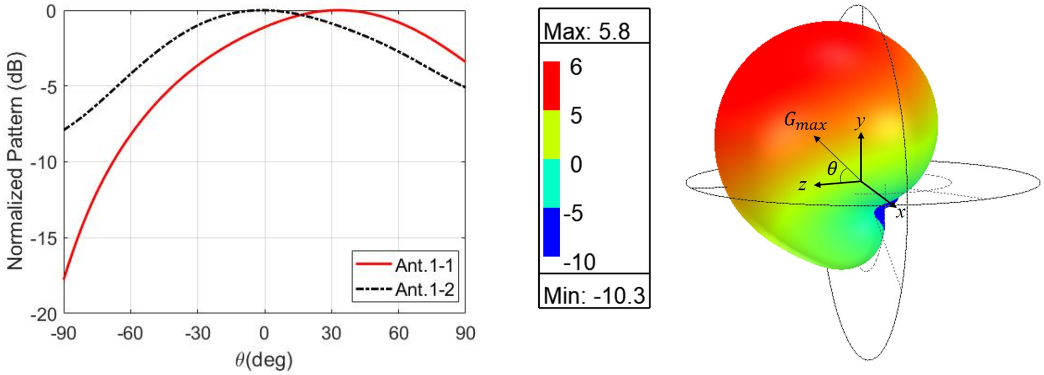

(a) (b)

Figure 3.24: (a) Normalized radiation patterns of Ant.1-1 and Ant.1-2 in the xz-plane at 28 GHz. (b) Simulated 3D radiation pattern of Ant.1-2 at 28 GHz.

distribution on the antenna at 39 GHz. The resonant frequency can be adjusted by changing the size of the chamfer L_c. Figure 3.25 (b) shows the reflection coefficients of the antenna in the 39 GHz band for different chamfer sizes. For comparison, the reflection coefficients of the antenna without the chamfer (Ant.1-2) is also plotted in the figure. The resonance moves to lower frequencies as L_c increases. The final version of the vertically polarized hexagonal bridge antenna and its design parameters are presented in Figure 3.21 (e). The structure is implemented between M1 and M3. The vertical plates and the reflector are realized by closely spaced blind vias with a

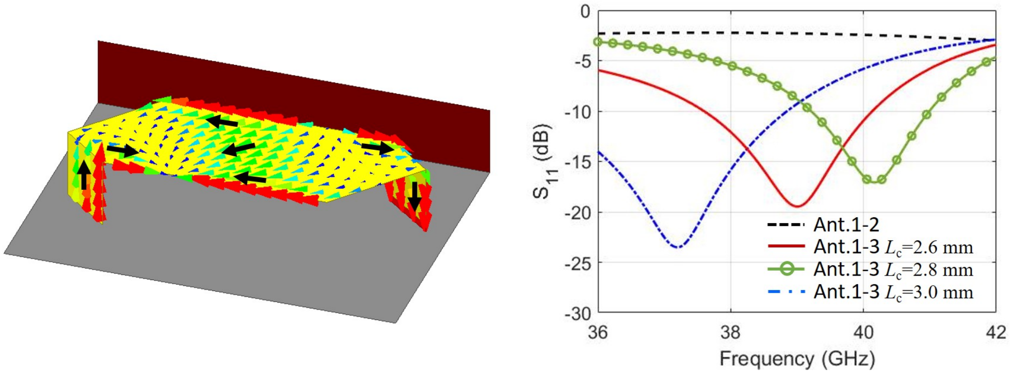

(a) (b)

Figure 3.25: (a) Current distribution of Ant.1-3 at 39 GHz. (b) Reflection coefficients of Ant.1-3 for different chamfer sizes.

diameter of 0.2 mm. Spacing of 0.4 mm between adjacent vias is found sufficient. The feed vias are connected together using a rectangular pad on M3 and are fed using a coplanar waveguide. The distance from the antenna to the edge of the ground plane d_2 is adjusted for the best radiation performance while minimizing the width of the ground plane W_g.

3.3.1.3 Dual-Band Dual-Polarized Array Element

The two antennas are combined into a dual-band dual-polarized array element as shown in Figure 3.26. The folded dipole is placed at the edge of the PCB with the hexagonal bridge antenna located behind it. Even though this configuration has a slightly larger dimension along the z-axis compared with the side-by-side configuration, it significantly reduces the footprint along the x-axis, and has a better scanning capability when forming an array. The total size of the array element is 6.5 mm × 5 mm × 1.12 mm.

The impact of a metallic display on antenna input impedance is also investigated. The reflection coefficients of the horizontally polarized (H-pol) and vertically polarized (V-pol) antennas for different display distance d are plotted in Figure 3.27 (a) and (b), respectively. Thanks to the ground plane, the V-pol antenna is only slightly affected

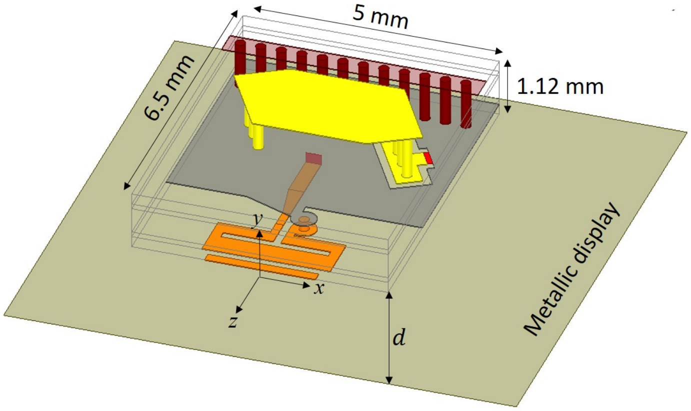

Figure 3.26: The proposed dual-band dual-polarized array element.

by the display and has a good matching performance even when the display is placed as close as 1 mm. The H-pol antenna is more vulnerable to the position of the display since there is no ground plane to shield the antenna. Nevertheless, it is well matched when the display is placed more than 3 mm away from the bottom of the substrate. Considering that the typical thickness of smartphones is about 7.5 mm − 10 mm [106], a distance of 3 − 5 mm is adequate for most smartphone manufacturers. If a smaller distance is desired, the H-pol antenna can be optimized for that specific distance.

3.3.2 Antenna Measurements

Since the signal lines of the H-pol antenna and the V-pol antenna are located on M4 and M3, respectively, it is impractical to directly characterize the antennas using an RF probe-based setup. In order to excite the H-pol antenna with an RF probe from M1, the microstrip line on M4 is elongated to the back of the via-fence and then connected to M1 through a vertical through via. A small circular incision is made into the ground plane for the signal via to pass through. A grounded coplanar waveguide (GCPW) to microstrip line transition is implemented on M1 to route the signal from the ground-signal-ground (GSG) probe to the via interconnect. The reference ground of the microstrip line (which is also the bottom ground of the GCPW) is configured on M2. The final configuration of the antenna with the GSG probe feeding network

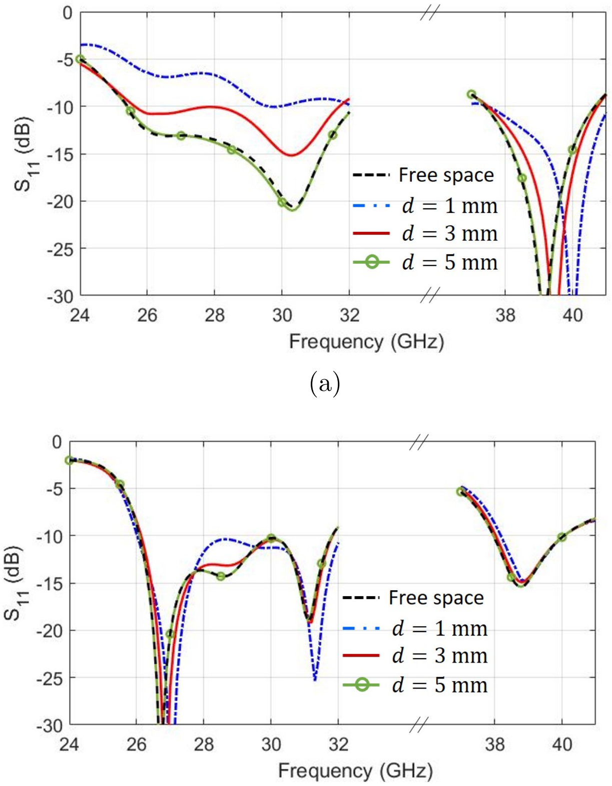

(a)

(b)

Figure 3.27: Simulated reflection coefficients of the (a) H-pol and (b) V-pol antennas for different display distances.

is shown in Figure 3.28. It should be noted that the feeding network is only for testing purposes and is not considered part of the antenna. The close-up view shows the details of the transition from the original ports to the GSG ports. The width of the center signal line W_{CPW} and the gap between the signal line and the ground g_{CPW} at the probe end is predetermined by the tip size and pitch of the GSG RF probe. The gap is gradually widened to ensure a smooth transition of the electric field from the GCPW to the microstrip line. The tapered microstrip line is matched to 50 Ω. The three ground planes (i.e., the CPW ground on M1, the micrstrip line ground on M2, and the antenna ground on M3) are electrically connected by a series of through vias surrounding the transmission line and the via at the interconnect. The diameters of the vias and via pads are configured to be 0.2 mm and 0.5 mm,

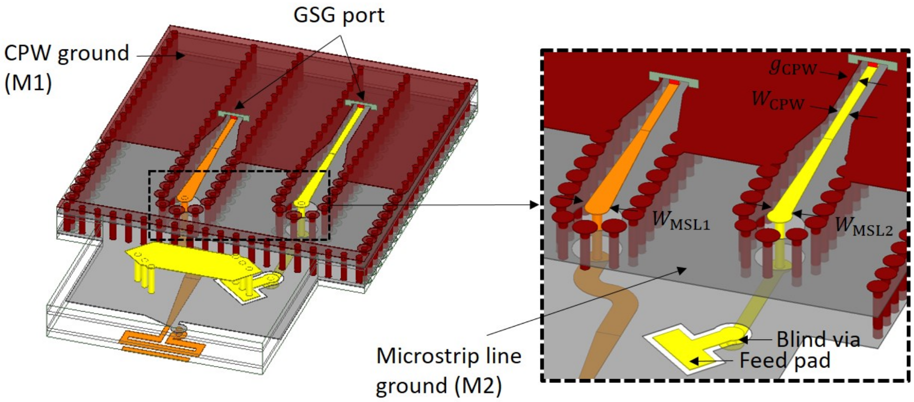

Figure 3.28: The proposed array element with the feeding network for testing. $W_{\mathrm{CPW}} = 0.2$ mm, $g_{\mathrm{CPW}} = 0.18$ mm, $W_{\mathrm{MSL1}} = 0.5$ mm, $W_{\mathrm{MSL2}} = 0.4$ mm.

respectively. The vias not only serve the purpose of electrical connection, but also suppress unwanted parallel plate waveguide modes and surface waves. For the V-pol antenna, a similar GCPW to microstrip line transition using a combination of strip lines and through vias is implemented. The signal is first routed from the GSG probe to the microstrip line on M1, then passed onto the micrstrip line on M4 through the interconnect via, and eventually fed into the antenna by a blind via that connects the end of the micrstrip line (M4) to the center signal line of the CPW on M3. The fabricated array element is shown in Figure 3.35.

A GSG RF probe from GGB Industries (Picoprobe 50A-GSG-350-DP) and a network analyzer (Agilent 8722ES) are used to extract the reflection coefficients of the antennas. The system is calibrated to the probe tips using a standard calibration substrate (GGB Industries Inc. Model CS-9). The array element is suspended on a 5 mm thick Styrofoam layer. To include the impact of a metallic display in antenna characterization, a metal plate is added at the bottom of the supporting Styrofoam to mimic the display. During the measurement process, only one port is excited at a time, with the other port terminated with a high-frequency 50 Ω resistor. The measured reflection coefficients of the H-pol and V-pol antennas are plotted in Figure 3.29 (a) and (b), respectively, and are compared with the simulated results. Overall,

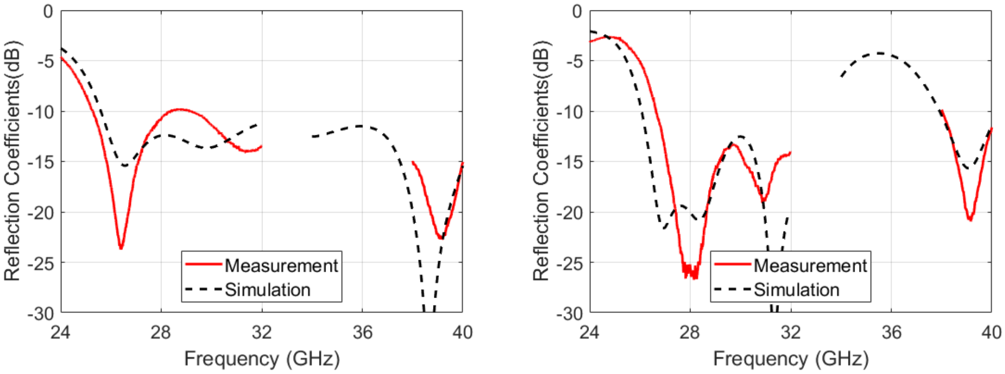

(a) (b)

Figure 3.29: Measured and simulated reflection coefficients of the (a) H-pol and (b) V-pol antennas.

the measurements are in good agreement with the simulation results. Both antennas achieve the desired bandwidth. The discrepancies are attributed to fabrication errors; in particular, the thickness of the prepreg bonding layer, the diameter of the via holes and the spacing between adjacent vias. It should be noted that the simulated reflection coefficients in Figure 3.29 are slightly different from those in Figure 3.27. This is because the measured and simulated reflection coefficients in Figure 3.29 include the GSG probe feeding network whereas the results in Figure 3.27 are obtained without the feeding network.

The radiation patterns of the antennas are characterized using the near-field to far-field (NF/FF) method. An electro-optic (EO) near-field scan system, NeoScan [107], is used to map the near-fields of the antennas. The scan configuration is illustrated in Figure 3.30. The scan plane is 1 mm away from the edge of the antenna. The scan area is set to 46 mm × 20 mm and the sampling resolution is 0.5 mm.

The measured near-field electric field distribution of the H-pol and V-pol antennas at 28 GHz and 39 GHz are presented in Figure 3.31 (a)–(d), respectively. The corresponding normalized far-field radiation patterns in the xz- and yz-planes are plotted in Figure 3.32, along with the simulated patterns. Since the cross-polarized signal level is below the sensitivity of the near-field scan system, we are unable to

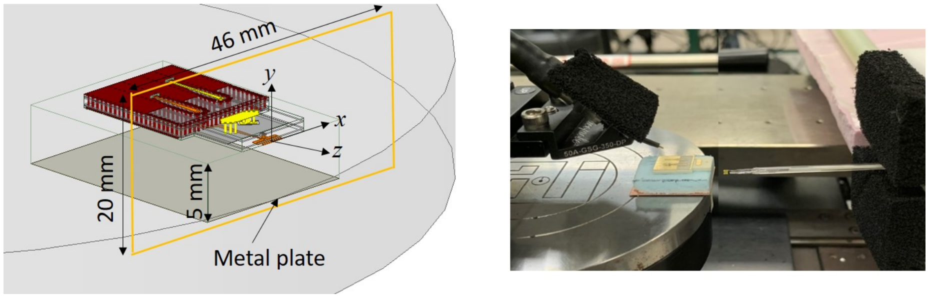

Figure 3.30: Near-field scan configuration.

accurately measure the cross-polarized radiation. However, this also proves that the antennas have good polarization purity.

In general, the measured co-polarized patterns are in good agreement with the simulated ones. The discrepancies mainly stem from the finite size of the scan area. As expected, the measured patterns diverge from the simulated results at large angles. This issue is more severe in the yz-plane than that in the xz-plane, especially for the V-pol antenna because of the limited measurable range in the y-direction (maximum 20 mm). The ripples in the measured patterns are due to the abrupt truncation of the scan plane. The H-pol antenna provides excellent endfire radiation at both 28 GHz and 39 GHz. The V-pol antenna produces a quasi-endfire radiation pattern at 28 GHz. At 39 GHz, the maximum V-pol radiation slightly shifts toward the $-x$ direction. This is due to the phase differences of the currents on the vertical vias at 39 GHz. Another point worth noting is that the simulated 39 GHz patterns have some ripples in the yz-plane for $\theta > 60°$. After careful investigation, it is determined that the ripples are caused by edge diffraction from the metallic display underneath the antenna. This phenomenon is not captured by the measurement due to the limited scanning capability.

The absolute gains of the antennas in the endfire direction (along $+z$) are obtained using the image method described in Section 3.5.1 and are plotted in Figure 3.33 (a)–(d), respectively. The gains are relatively flat across the two operating bands, indicating consistent radiation performance over the entire bands. The gains at 28

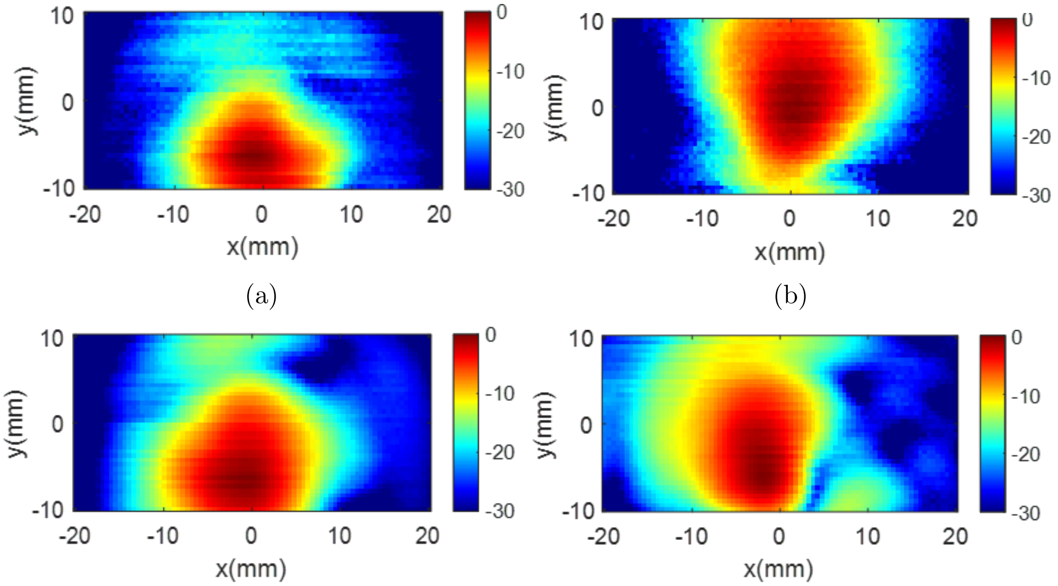

(a) (b) (c) (d)

Figure 3.31: Measured near-field distribution of (a) H-pol and (b) V-pol antennas at 28 GHz; (c) H-pol and (d) V-pol antennas at 39 GHz.

and 39 GHz are summarized in Table 3.1. The measured results agree well with the simulated ones. The peak gains are then determined based on the radiation patterns in the *yz*-plane. Due to limited measurement capability, we are not able to obtain the maximum radiation of the V-pol antenna in the *yz*-plane; therefore, only simulated peak gains of the V-pol antenna are reported. Considering the good agreement in all other measurements, we believe that the simulated results are accurate.

Table 3.1: Absolute gain of the array element (Unit: dBi)

	28 GHz		39 GHz	
	H-pol	V-pol	H-pol	V-pol
Endfire Meas.	5.59	1.16	6.33	1.11
Endfire Simu.	5.88	1.15	6.53	1.42
Peak Meas.	5.59	-	6.51	-
Peak Simu.	6.15	5.95	7.02	6.91

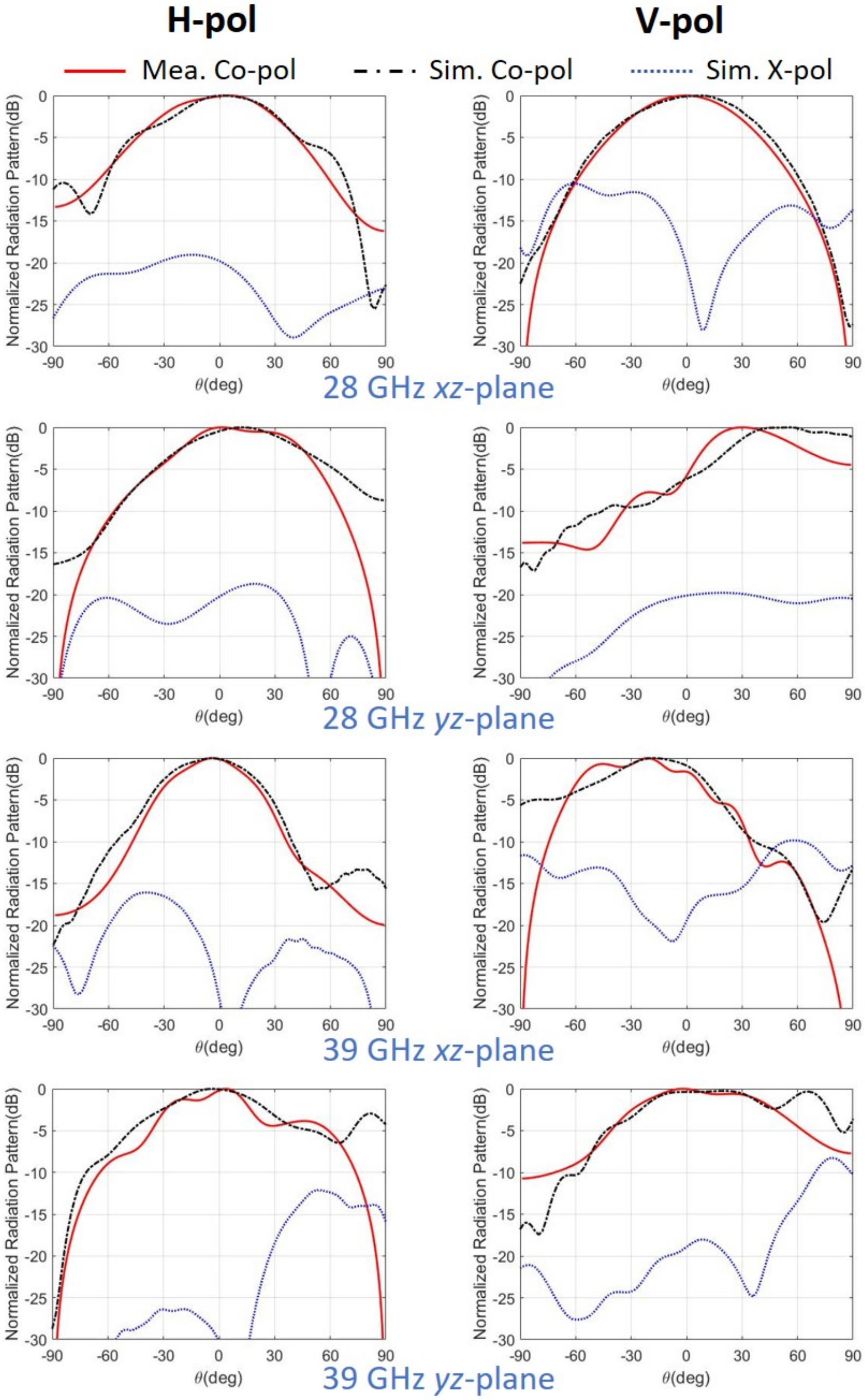

Figure 3.32: Measured and simulated far-field radiation patterns of H-pol and V-pol antennas in xz- and yz-planes at 28 GHz and 39 GHz.

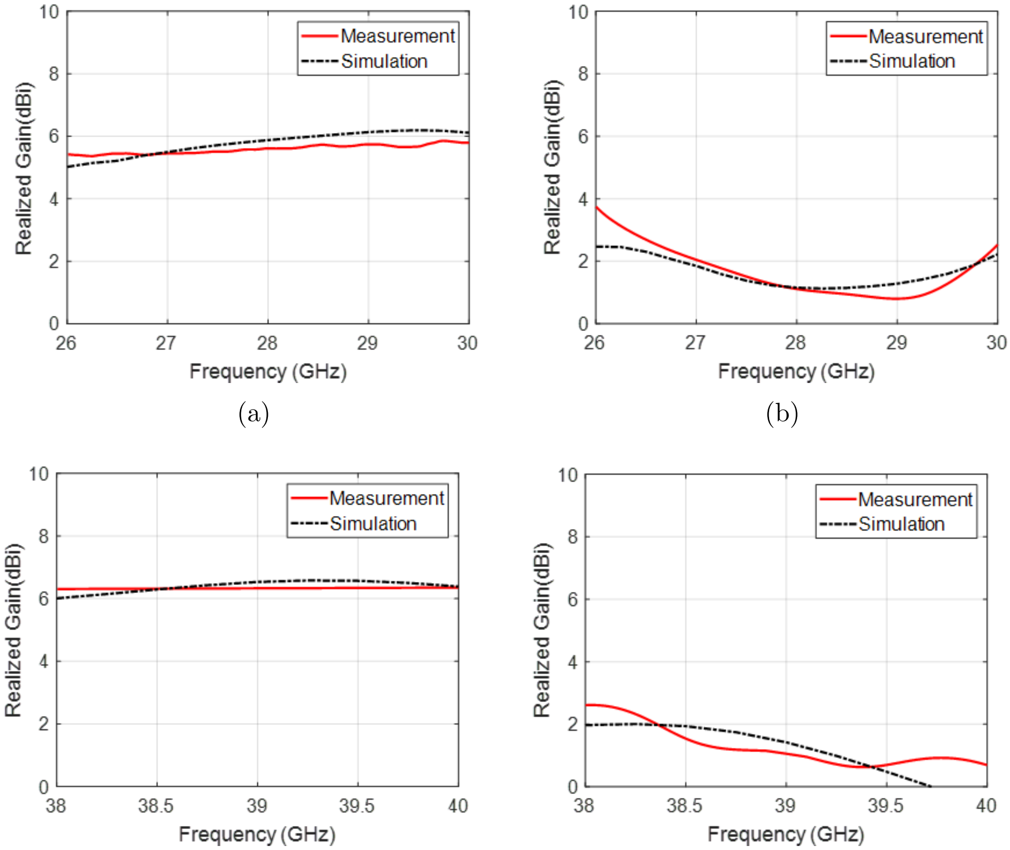

(a)

(b)

(c)

(d)

Figure 3.33: Measured absolute gains of the antennas in the endfire direction. (a) H-pol and (b) V-pol antennas in the 28 GHz band; (c) H-pol and (d) V-pol antennas in the 39 GHz band.

3.3.3 Phased Array Design

The array element is expanded into a 1×4 phased array as shown in Figure 3.34. The array is symmetric about the center line (dotted orange line). The inter-element spacing is set to 6 mm ($0.56\lambda_0$ at 28 GHz, $0.78\lambda_0$ at 39 GHz) to achieve a minimum of 10 dB port-to-port isolation in the 28 GHz band. The overall real estate of the array is 6.5 mm $\times$ 23 mm $\times$ 1.12 mm, excluding the feeding network behind the via fence. Figure 3.35 shows the fabricated array.

The reflection coefficients of each element are measured using the GSG RF probe with the other 7 ports terminated with 50 Ω resistors. Only 4 ports (H-pol port 1 and

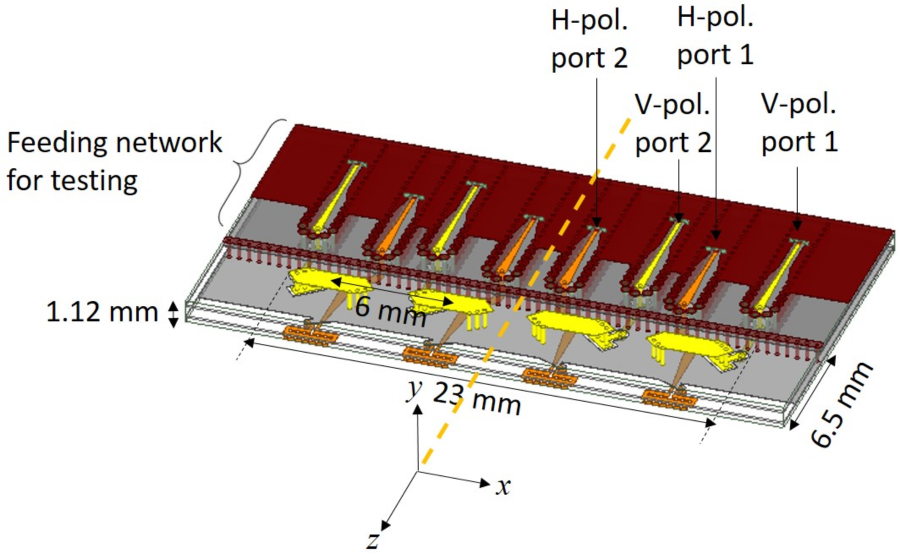

Figure 3.34: The proposed 1 × 4 phased array with the feeding network used for testing. Array port numbering from the right to the left: port 1-4.

2, V-pol port 1 and 2) need to be measured due to the symmetry of the array. The measured reflection coefficients are plotted in Figure 3.36, along with the simulated results. Better than -10 dB reflection is achieved in the desired 26–30 GHz and 38–40 GHz bands. The center frequencies of V-pol port 1 and 4 shifted down slightly in the high band. The V-pol antennas are found to be more susceptible to fabrication errors than the H-pol antennas because of the extensive use of blind vias in the structure. The port-to-port couplings between elements are plotted in Figure 3.37. Due to the close spacing between the ports, we are unable to place two RF probes simultaneously to measure the coupling; therefore, only simulated results are reported. For the sake of clarity in the figure, only four pairs of ports with the highest couplings are presented in each band. The couplings are below -13.89 dB in the lower band and below -20.65 in the higher band.

The radiation patterns of the array are also obtained using the NF/FF method. A metal plate is again placed 5 mm below the array to emulate a metallic display. We measure the near-field of each element (with the other elements terminated with

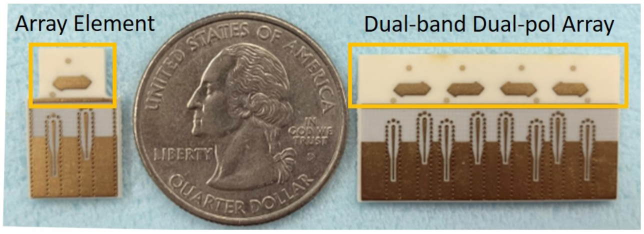

Figure 3.35: The fabricated dual-band dual-polarized array element and the full array.

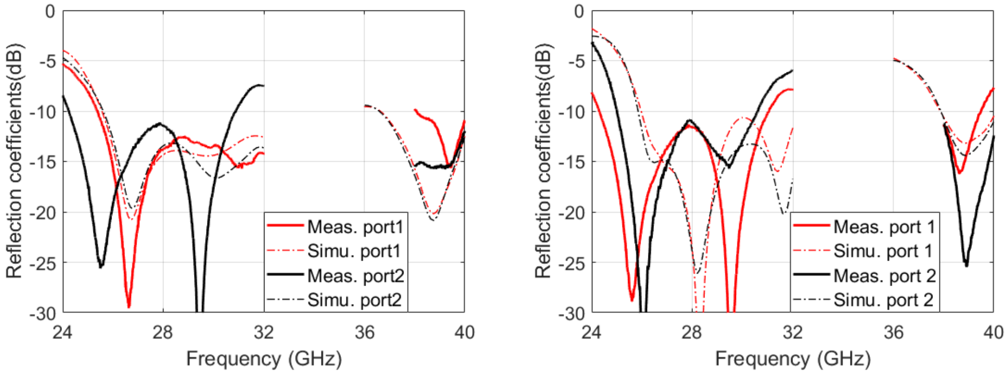

(a) (b)

Figure 3.36: Measured and simulated reflection coefficients of the phased arrays. (a) H-pol port 1 and 2. (b) V-pol port 1 and 2.

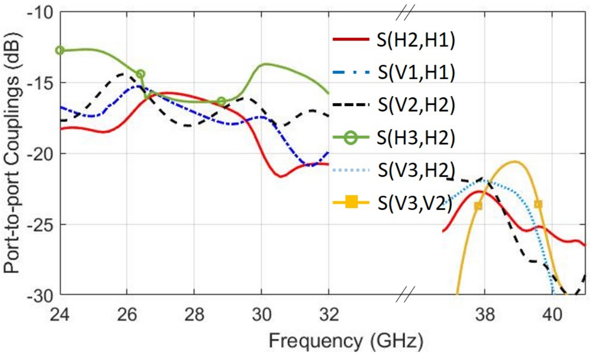

Figure 3.37: Simulated port-to-port coupling between elements.

50 Ω resistors), and the total near-field of the H-pol (V-pol) array is formed from the superposition of the measured near-fields of the H-pol (V-pol) elements. The total near-fields of the H-pol and the V-pol arrays with uniform excitation at 28 GHz and 39 GHz are shown in Figure 3.38 (a)–(d), and the normalized far-field patterns in the

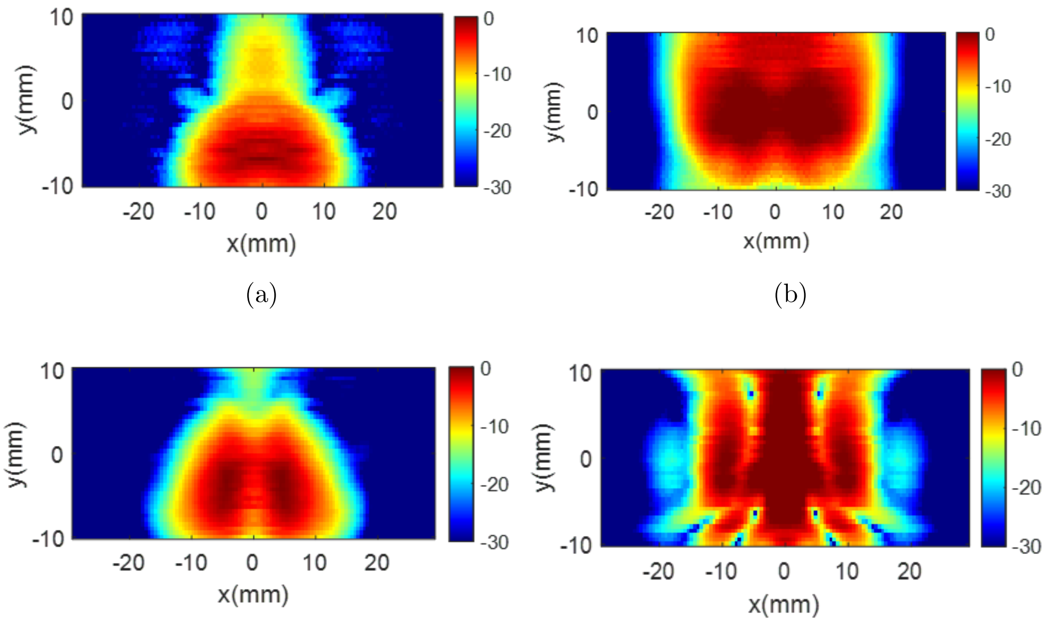

(a) (b) (c) (d)

Figure 3.38: Measured near-field distribution of (a) H-pol array in the xz-plane at 28 GHz; (b) V-pol array at 28 GHz; (c) H-pol array at 39 GHz; (d) V-pol array at 39 GHz.

xz- and yz-planes are plotted in Figure 3.39, along with the simulated results. As desired, the H-pol array provides an endfire radiation pattern while the V-pol array provides a quasi-endfire radiation pattern. The main beams of the array in the xz-plane are in excellent agreement with the simulated results, and the deviations of the first sidelobe level are within 2.5 dB. Similar to the single element measurement, the patterns diverge from the simulation for large angles due to the finite scan area, and the issue is more severe in the yz-plane for the V-pol array. Unlike the single element patterns, all array patterns are completely symmetrical in the xz-plane owing to the symmetric arrangement of the elements. It should be noted that the cross-polarized radiation level in the yz-plane is more than 50 dB below the co-polarized radiation level; therefore, it is not shown in the figures.

The gains of the arrays are characterized using the NF/FF gain comparison method described in Section 3.5.2. We chose the array element as the standard

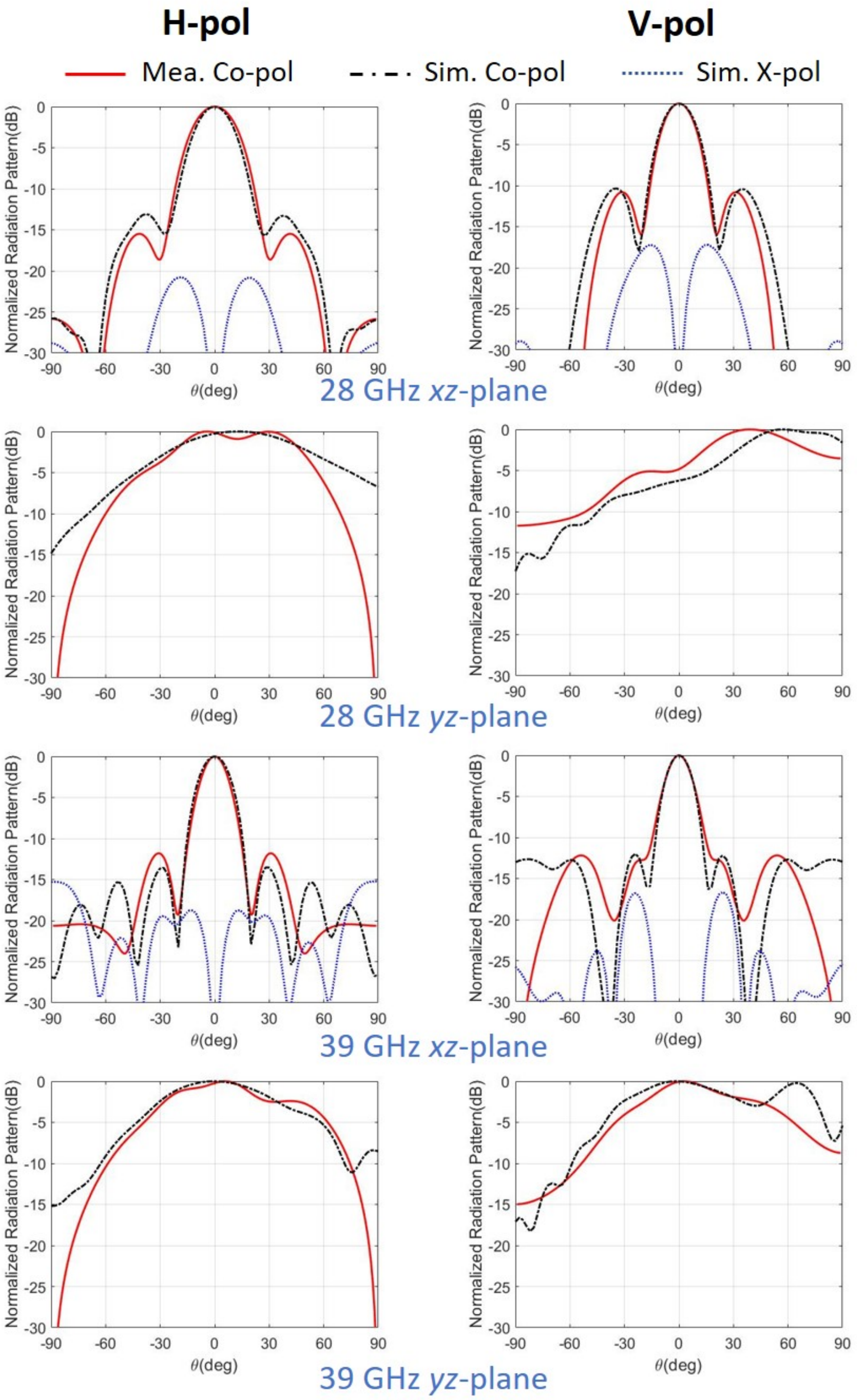

Figure 3.39: Measured and simulated far-field radiation patterns of the H-pol and V-pol arrays in the xz- and yz-planes at 28 GHz and 39 GHz.

Table 3.2: Measured absolute gains of the array with uniform excitation (Unit: dbi)

	28 GHz		39 GHz	
	H-pol	V-pol	H-pol	V-pol
Endfire Meas.	11.05	5.55	11.7	6.65
Endfire Simu.	10.15	5.47	10.93	6.96
Peak Meas.	11.31	-	11.93	-
Peak Simu.	10.41	11.71	11.29	12.42

gain antenna, and used the measured gains listed in Table 3.1 in the calculations. The complete array gains for both polarizations at 28 GHz and 39 GHz are tabulated in Table 3.2, along with the simulated gains. The measured gains agree well with the simulation. Similar to the single array element, we are not able to accurately obtain the peak gains of the V-pol array, therefore, only simulated peak gains are presented.

The scan performance of the array is demonstrated in Figure 3.40. The overlapped 3 dB scan ranges for the two polarizations are ±45° at 28 GHz and ±39° at 39 GHz. The smaller scan range at 39 GHz can be explained by noting that the maximum scan angle θ_m without grating lobes is related to the inter-element spacing d_e by [108]

$$d_e < \frac{\lambda_0}{1 + |\cos\theta_m|} \tag{3.1}$$

Since the inter-element spacing is larger in terms of wavelength at higher frequencies, grating lobes start to appear at smaller scan angles at 39 GHz. The different scan ranges of the H-pol and V-pol arrays at the same frequency are attributed to the difference in array element pattern. However, it should be noted that, for 5G communications, grating lobes are not critical as long as the gain and spatial coverage align with the specifications [99, 109]. This is different from radar applications where the presence of grating lobes or large sidelobes is problematic. In fact, for 5G applications, grating lobes may even help enlarge the spatial coverage [109]. The overall influence of grating lobes on mmWave communication still needs more investigation.

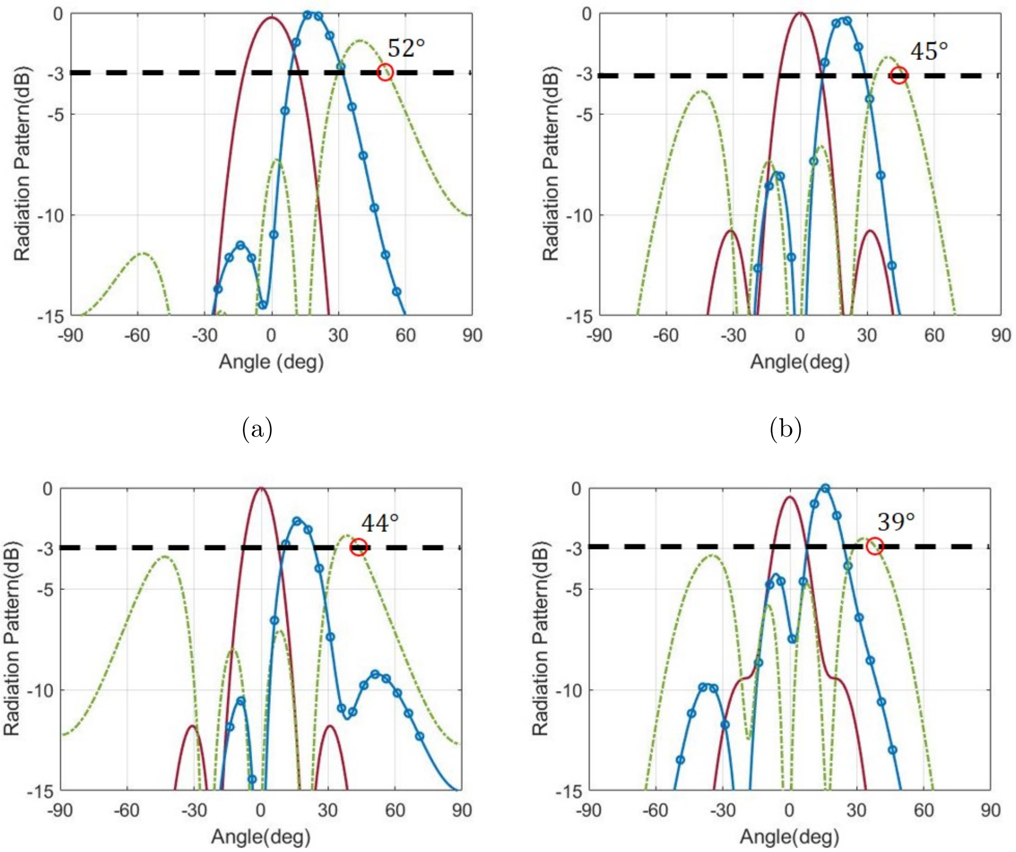

(a) (b)

(c) (d)

Figure 3.40: Measured scan performance of the array. (a) H-pol and (b) V-pol arrays at 28 GHz; (c) H-pol and (d) V-pol arrays at 39 GHz.

3.4 A Very Compact Dual-Polarized Antenna Array Topology Supporting Multiple 5G bands for Smartphones

This section presents a very compact dual-polarized antenna array topology that allows for operation in the 26 GHz, 28 GHz, 37 GHz and 39 GHz bands designated for 5G uses. Four 1×4 sub-arrays, namely low-band horizontally polarized (LB H-pol) array, high-band horizontally polarized (HB H-pol) array, low-band vertically polarized (LB V-pol) array and high-band vertically polarized (HB V-pol) array, are designed on a 12-layer laminate with total dimensions of 6 mm × 25 mm × 0.97 mm.

The LB arrays achieve reflection coefficients of less than -10 dB from 24—30 GHz, and the HB arrays can operate from 37—43 GHz. Each sub-array features a peak gain of more than 9.7 dBi at its center frequency. The 3-dB beam scanning ranges for the H-pol and V-pol arrays are ±45° and ±56° at 27 GHz, and ±42° and ±28° at 40 GHz, respectively.

3.4.1 Design Challenges

Before we move onto the design details, it is worth highlighting the major design challenges, as this design has more stringent specifications compared with the previous two antenna arrays. Major design challenges include:

1. **Larger bandwidth.** The required bandwidth is 24–30 GHz for the LB antennas and 37–43 for the HB antennas.
2. **Mutual couplings between elements.** Four 1 × 4 sub-arrays (total 16 antenna elements) need to be accommodated in a 6 mm × 25 mm × 0.97 mm multilayer substrate. A critical design factor of compact antennas is to reduce the strong mutual coupling between elements.
3. **Impact of a metallic display.** The potential impact of a metallic display placed closely below the antenna must be considered in the design process.

3.4.2 Horizontally Polarized Arrays

The antenna array is designed on a multilayer PCB with a total thickness of 0.97 mm as shown in Figure 3.41. The substrate consists of 12 metal layers and 11 dielectric layers. The 10th metal layer is used as the RF ground.

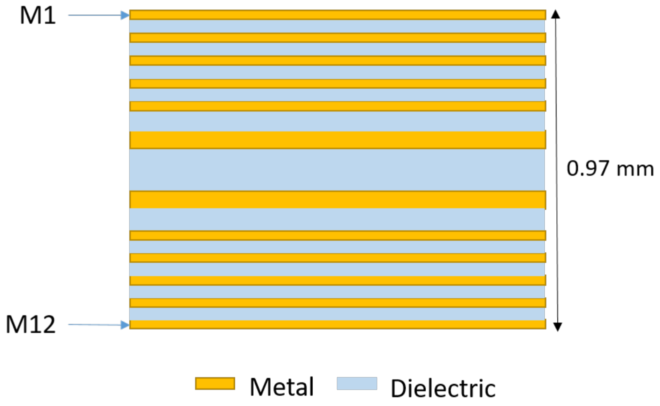

Figure 3.41: The stack-up of the 12-layer laminate. In the dielectric layer, $\epsilon_r = 3.59, \tan\delta = 0.0068$.

Two folded dipoles are used to produce horizontally polarized radiation in both the LB and the HB. The arrangement of the antennas is shown in Figure 3.42 (a). The LB and HB elements are placed on M1 and M2, respectively. The relative positions of the antennas D_x and D_y are chosen such that the port-to-port coupling between the two antennas is less than -10 dB in both the LB and HB. D_y is limited by the average available length for each element, which is determined by the total length of the array. We chose the maximum possible $D_y = 3$ mm and then increased D_x to meet the isolation requirement. Figure 3.42 (b) shows the port-to-port couplings between the two antennas for $D_x = 0$ mm and $D_x = 1.2$ mm for a fixed $D_y = 3$ mm. The port-to-port coupling is around -5 dB in the LB for $D_x = 0$, and decreases to less than -10 dB as D_x increases to 1.2 mm. It should be noted that the bandwidths of the antennas decrease drastically as they move closer to the ground layer, therefore, the H-pol antennas must be kept on the top two layers (M1 and M2).

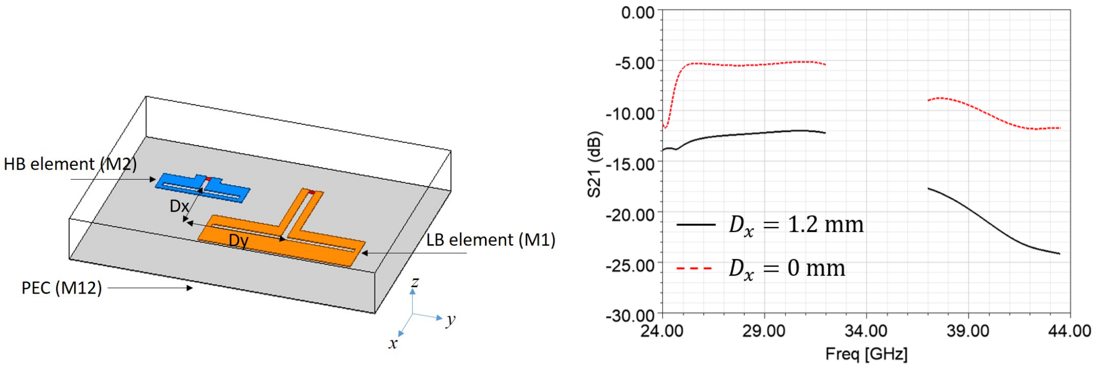

(a) (b)

Figure 3.42: (a) Arrangement of the LB and HB H-pol antennas. (b) Simulated port-to-port coupling.

The reflection coefficients of both antennas are shown in Figure 3.43. The reflection coefficients of the HB elements remain less than -10 dB from 37 GHz to 45 GHz. However, the matching performance of the LB element deteriorates significantly due to the metal ground. This can be intuitively explained using image theory. When the antenna is closely placed above a perfect electric conductor (PEC), the EM field associated with the antenna and that of its image overlap strongly, resulting in a significant increase of the stored electromagnetic energy, which in turn increases the quality factor of the antenna, or equivalently, decreases the bandwidth of the antenna.

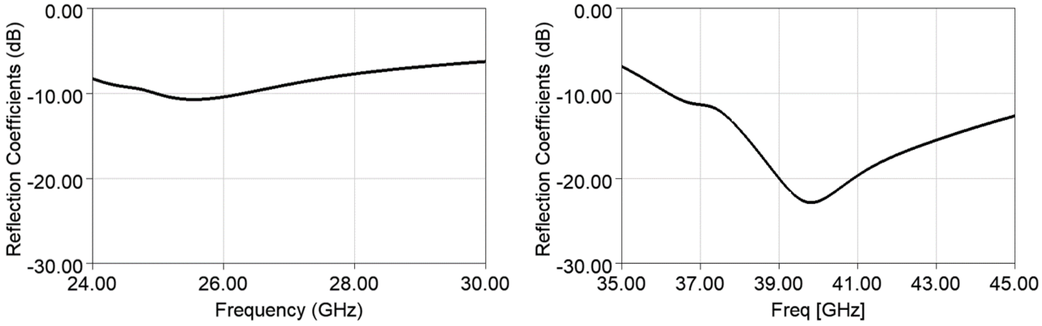

(a) (b)

Figure 3.43: Simulated reflection coefficients of (a) the LB H-pol antenna and (b) the HB H-pol antenna.

To enhance the bandwidth of the LB antenna, a reactive impedance surface (RIS) substrate [110] is utilized. An RIS substrate is a periodic structure exhibiting purely reactive impedance. Such a structure, when placed below a dipole antenna, can significantly reduce the mutual coupling between the antenna and its image, providing a wider bandwidth. In this design, a periodic array of square patches backed with a PEC is used to form the RIS structure.

The H-pol antennas with the RIS substrate are shown in Figure 3.44. The LB folded dipole antenna is replaced with a regular dipole. A 2×4 patch array is constructed below the dipole antenna on M6. The input impedance of the LB antenna can be manipulated by adjusting the size of the patches (W_p and L_p) and the gaps (g_1 and g_2) in between. The drawback of implementing the RIS substrate is that it leads to an increase in the mutual coupling between the HB and LB antennas. To solve this problem, we further increase D_x and shorten the two patches on the sides of the second row. The optimized values of the major design parameters are given in Figure 3.44. The reflection coefficients of the antennas with and without the RIS substrate are shown in Figure 3.45. With the RIS substrate, the LB dipole can operate from 24 to 30 GHz, while the HB dipole can operate from 35 GHz to 44 GHz. The port-to-port coupling in the LB and HB is shown in Figure 3.45 (c) and (d). The coupling level remains below -10 dB in both bands.

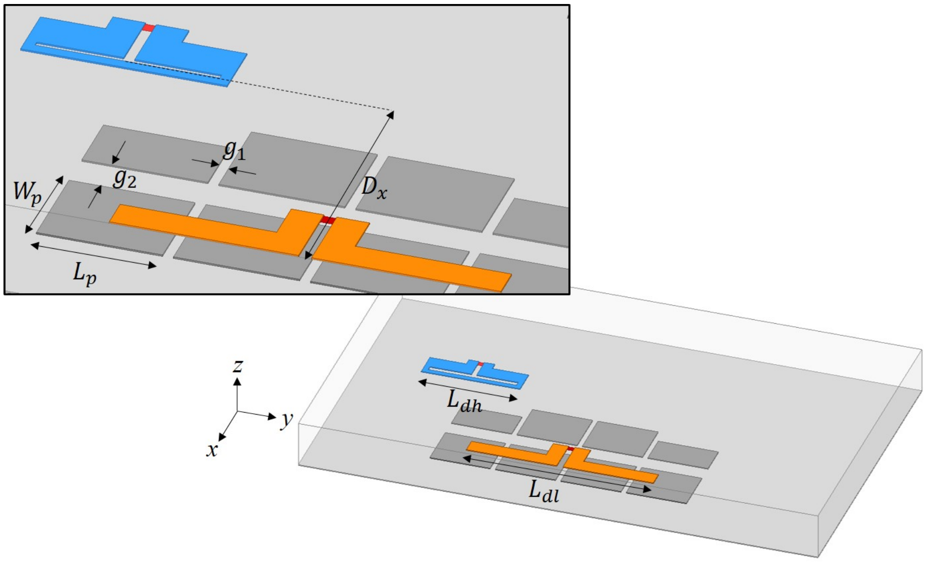

Figure 3.44: H-pol antennas with the RIS substrate. $L_{dl} = 3.6$ mm, $L_{dh} = 1.9$ mm, $D_x = 2.5$ mm, $W_p = 0.9$ mm, $L_p = 1.16$ mm, $g_1 = 0.1$ mm, $g_2 = 0.35$ mm.

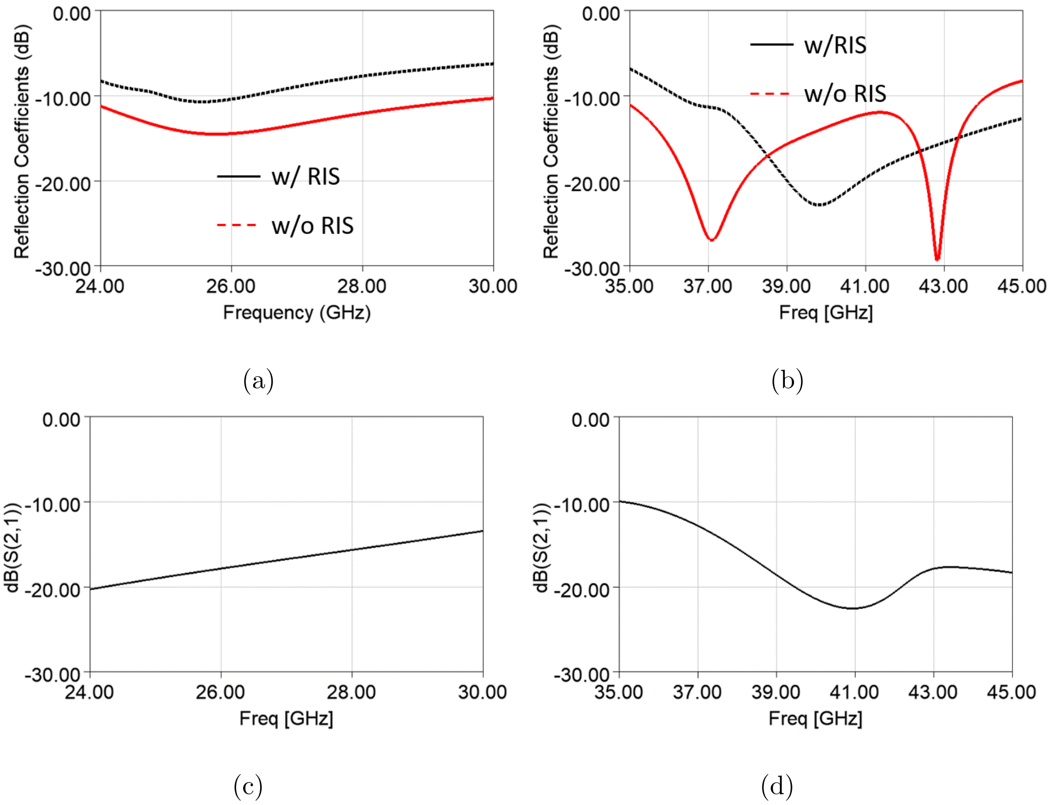

(a) (b)

(c) (d)

Figure 3.45: Simulated reflection coefficients of (a) LB and (b) HB antennas with and without the RIS substrates. Simulated port-to-port coupling in the (c) LB and (d) HB.

The antennas are expanded into a 1×4 phased array (H-pol Array 1) as shown in Figure 3.46. The inter-element spacing is set to 5 mm. The total length of the array is 21 mm. The issue with this arrangement is that the RIS structure acts as a reflector for the HB array, directing its maximum radiation towards the back (-$x-$direction). To remedy this issue, the HB array is moved in front of the LB array. Furthermore, the two ends of the LB dipoles are bent inwards 90° for miniaturization. The modified array configuration (H-pol Array 2) is shown in Figure 3.47. Figure 3.48 compares the radiation patterns of Array 1 and 2 in the xy-plane at 27 GHz and 40 GHz. At 27 GHz, the patterns are almost the same for the two configurations, whereas at 40 GHz, the realized gain in the endfire direction is improved drastically from -7.3 dBi to 5.9 dBi.

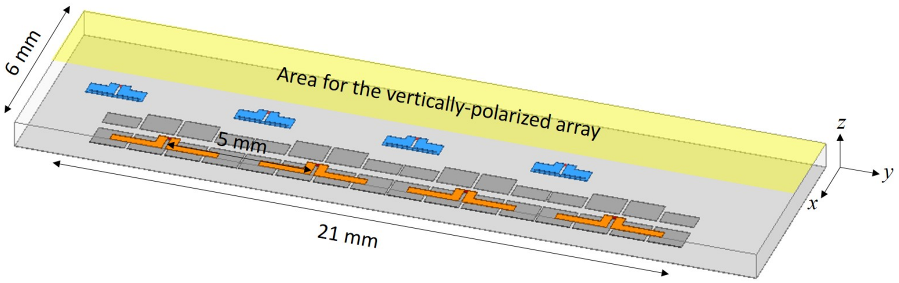

Figure 3.46: Configuration of H-pol Array 1.

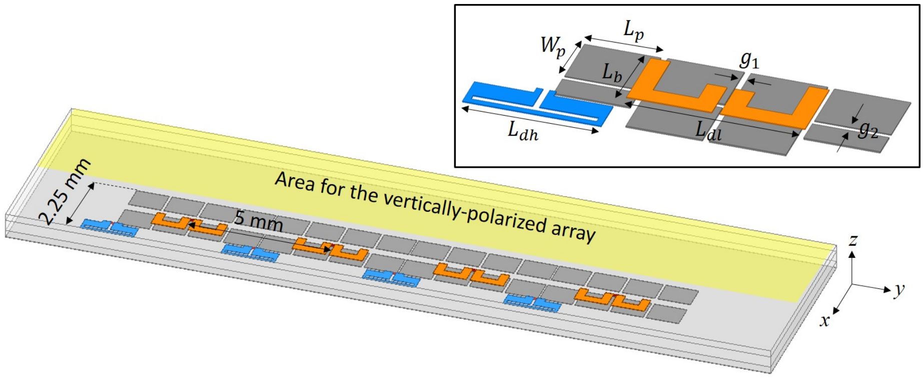

Figure 3.47: Configuration of H-pol Array 2 with $L_{dl} = 2.7$ mm, $L_b = 0.9$ mm, $L_{dh} = 2$ mm, $W_p = 0.9$ mm, $L_p = 1.16$ mm, $g_1 = 0.1$ mm, $g_2 = 0.1$ mm.

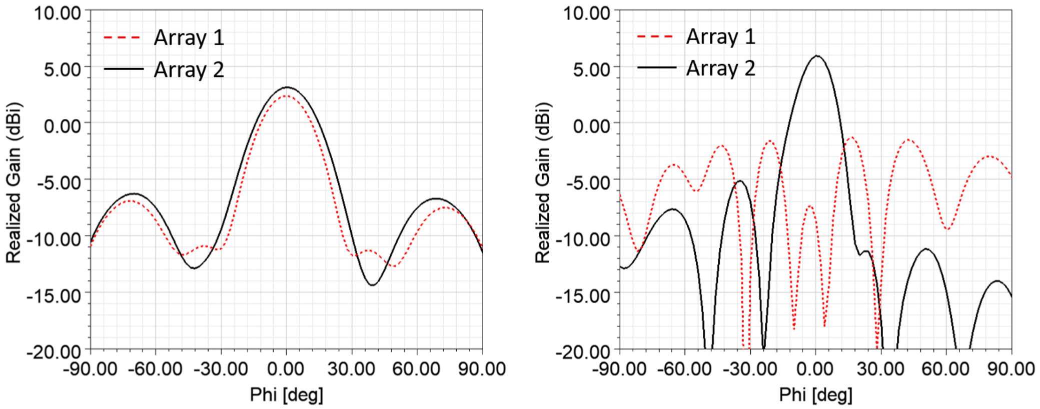

(a) (b)

Figure 3.48: Simulated radiation patterns of H-pol Array 1 and 2 in the xy-plane at (a) 27 GHz and (b) 40 GHz.

The reflection coefficients of each array are plotted in Figure 3.49. Port 1-4 and 5-8 are respectively LB and HB antennas from the right to the left. All elements achieve reflection coefficients of less than -10 dB in the desired frequency range. The port-to-port coupling between elements is shown in Figure 3.50. For the clarity of the figures, only four pairs of ports with the strongest couplings are presented. The couplings are less than -13.6 dB in the LB and less than -10 dB in the HB. Figure 3.51 summarizes the evolution of the H-pol arrays.

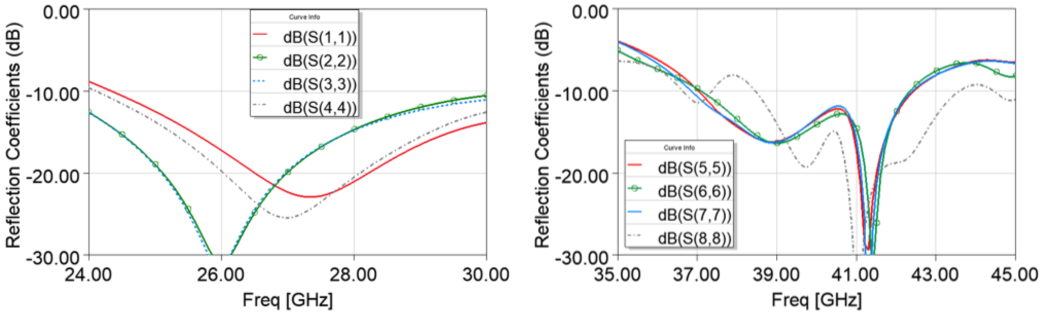

(a)

(b)

Figure 3.49: Simulated reflection coefficients of the H-pol Array 2 in the (a) LB and (b) HB.

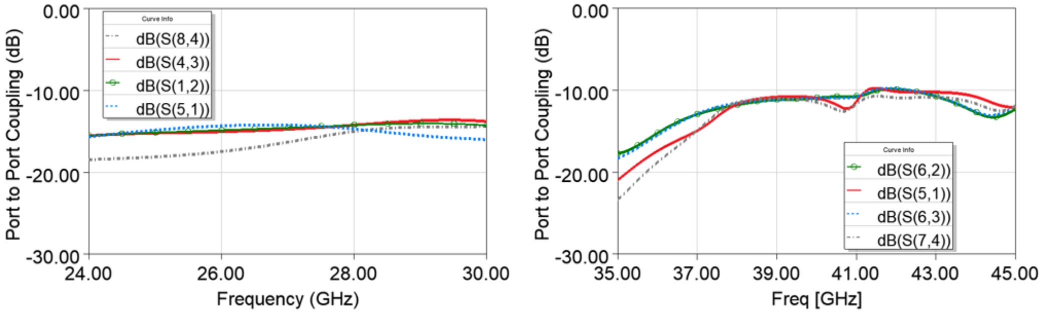

(a)

(b)

Figure 3.50: Simulated port-to-port coupling of adjacent elements of H-pol Array 2 in the (a) LB and (b) HB.

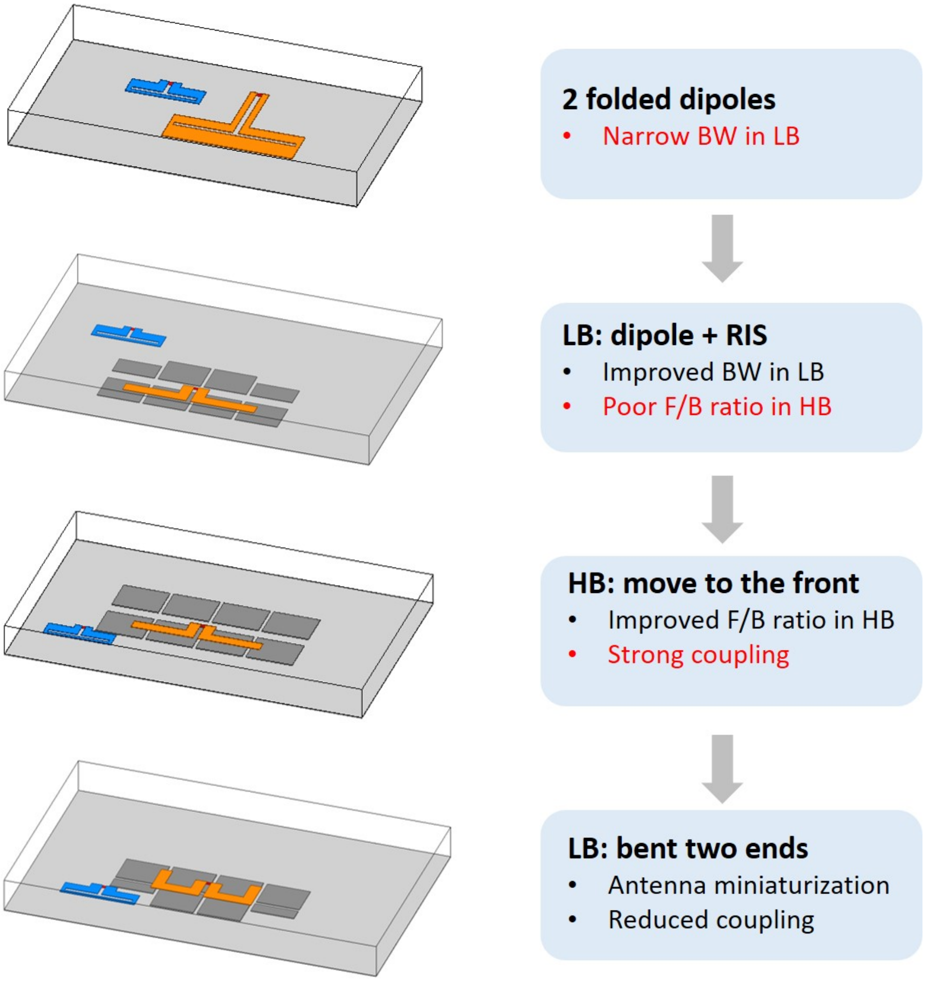

Figure 3.51: The evolution of the H-pol arrays.

3.4.3 Vertically Polarized Arrays

The configuration of the 1×4 V-pol antenna array is shown in Figure 3.52. The LB and HB elements are alternately placed along the y-axis. The inter-element spacing is chosen to be 6 mm for both the LB and HB arrays to meet the isolation requirement. The total length of the array is 23.73 mm.

The LB V-pol element (M1–M10) is a modified version of the dual-band folded monopole antenna presented in [111], where a parasitic element is placed near the feeding vias for the HB operation. In this design, the parasitic element is removed, and a standalone folded monopole (M6–M10) with a capacitively coupled parasitic element is utilized as the radiating element of the HB V-pol array. The close-up view of the V-pol antennas is shown in Figure 3.52. The HB driven element is similar to a short-ended half-wavelength transmission line that resonates around 40 GHz. The bow-tie geometry of the top plate functions as an impedance transformer to match the input impedance of the antenna to 50 Ω. The parasitic element is positioned very close to the middle of the driven element, where the electric field is the maximum. The strong capacitive coupling creates a second resonance in the HB. The resonant frequency can be controlled by changing the gap g_p and the size of the top plate (L_c and W_c). Bandwidth enhancement can be achieved by merging the two resonances together. In addition, a small director constructed from M7 to M10 is placed in front of each HB V-pol antenna to improve the front to back ratio.

The reflection coefficients of each V-pol element are plotted in Figure 3.53. The bandwidth of the LB sub-array is more than 24–30 GHz and that of the HB sub-array is 35.6–44 GHz. The four highest mutual couplings are reported in Figure 3.54. The couplings are below -10 dB in both bands.

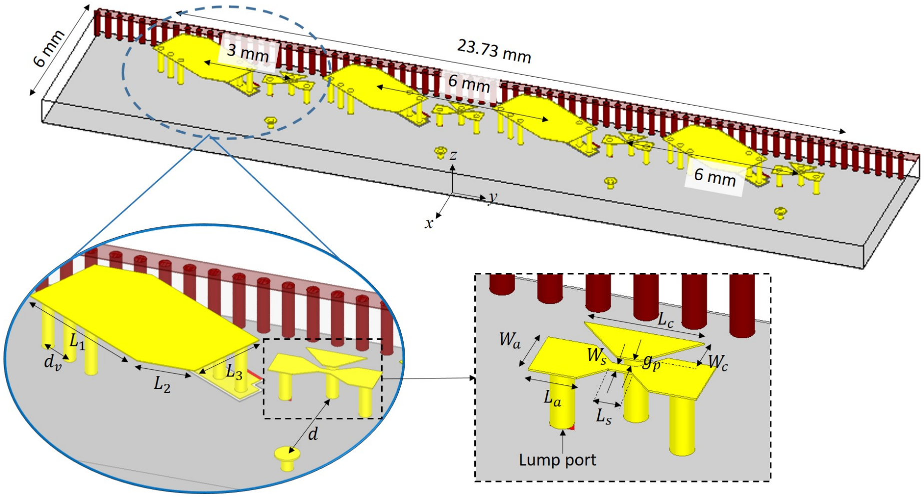

Figure 3.52: V-pol array configuration. $L_1 = 2.49$ mm, $L_2 = 0.93$ mm, $L_3 = 1.33$ mm, $d_v = 0.2$ mm, $d = 2.2$ mm, $W_a = 0.5$ mm, $W_s = 0.1$ mm, $W_c = 0.4$ mm, $L_a = 0.4$ mm, $L_s = 0.2$ mm, $L_c = 1$ mm, $g_p = 0.1$ mm

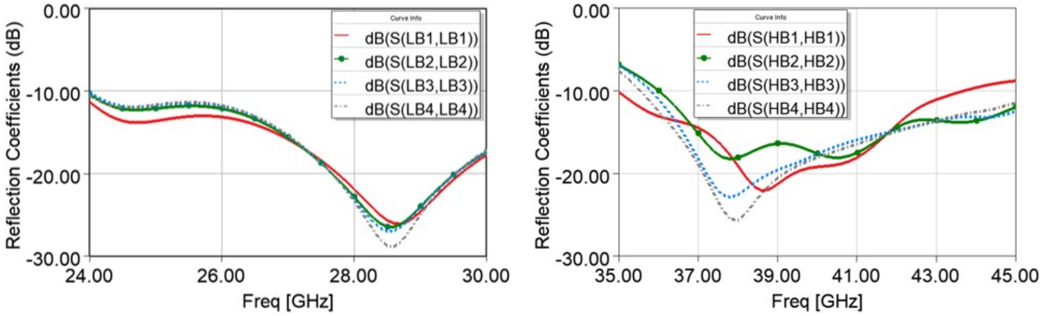

(a) (b)

Figure 3.53: Simulated reflection coefficients of the (a) LB and (b) HB V-pol array elements. Port numbering from right to left: 1-4.

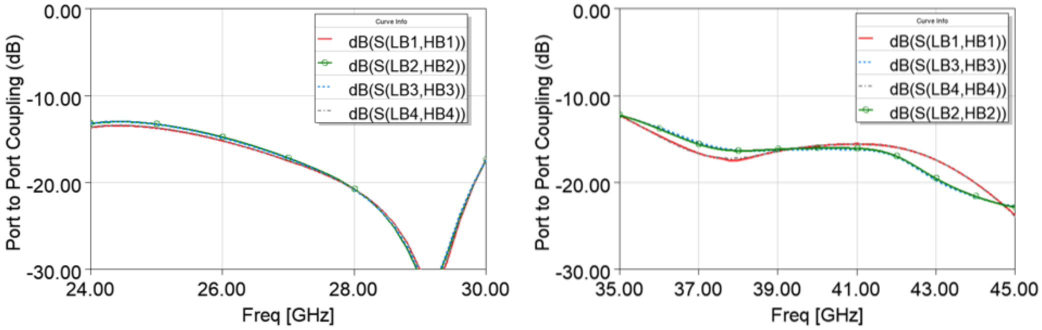

(a) (b)

Figure 3.54: Simulated port-to-port coupling between adjacent elements of the V-pol array in the (a) LB and (b) HB. Port numbering from right to left: 1-4.

3.4.4 Dual-Polarized Array Topology

The H-pol and V-pol arrays are combined into a dual-polarized array as shown in Figure 3.55. The total dimensions of the array are 6 mm × 23.73 mm × 0.97 mm.

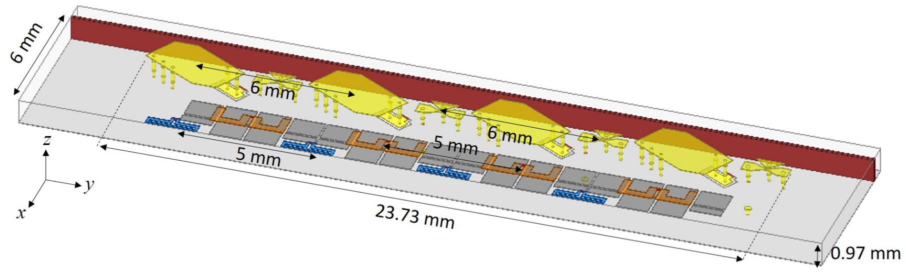

Figure 3.55: Dual-polarized array configuration.

The reflection coefficients for all array elements are plotted in Figure 3.56. As shown in the figure, both the H-pol and V-pol arrays maintain good matching performance after being placed close to each other. Figure 3.57 shows the radiation patterns of the H-pol and V-pol arrays in the *xy*- and *xz*-planes at 27 GHz and 40 GHz. It is clear that both V-pol arrays and the HB H-pol array can provide quasi-endfire radiation patterns with moderate gain in the endfire direction, while the LB H-pol array has a broadside radiation pattern due to the ground plane underneath the antenna.

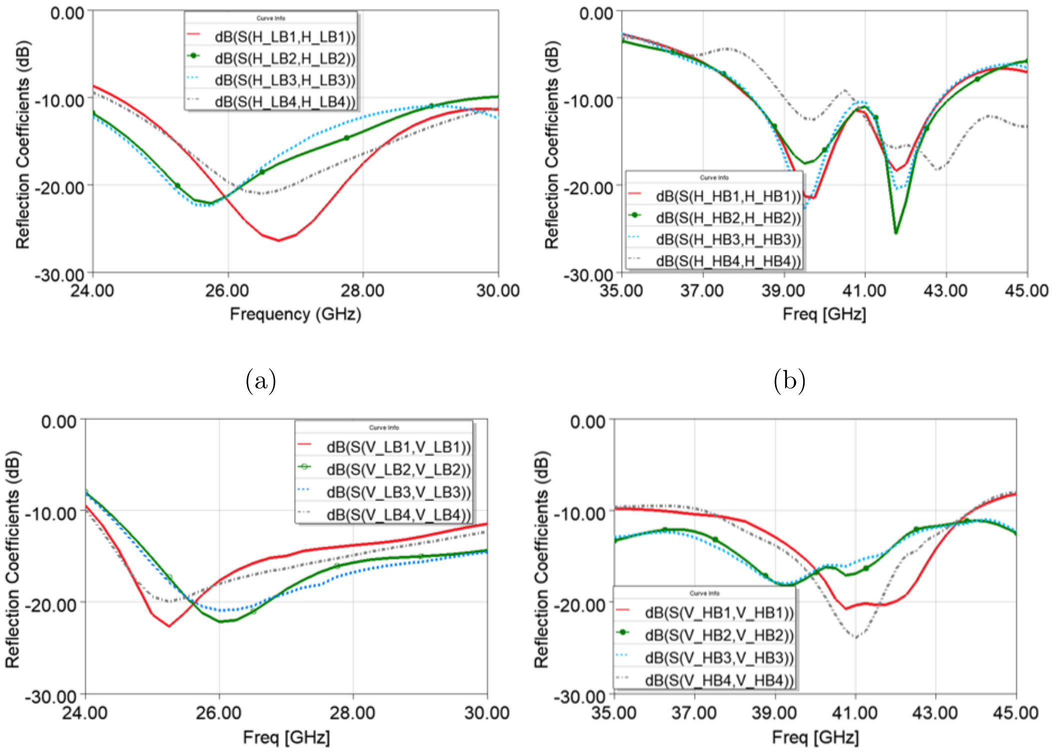

(a) (b)

(c) (d)

Figure 3.56: Simulated reflection coefficients of the (a) LB H-pol elements, (b) HB H-pol elements, (c) LB V-pol elements and (d) HB V-pol elements.

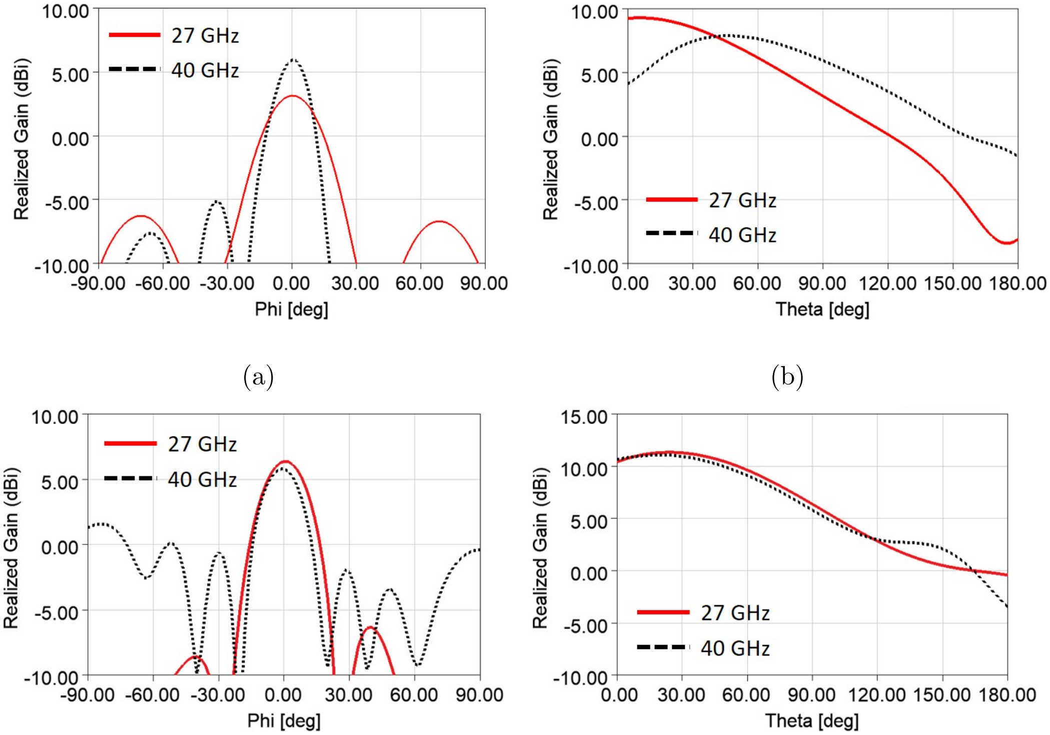

(a) (b)

(c) (d)

Figure 3.57: Simulated radiation patterns of H-pol arrays in (a) xy- and (b) xz-planes and patterns of V-pol arrays in (c) xy- and (d) xz-planes.

The scan performance of the H-pol and V-pol arrays is shown in Figure 3.58 and Figure 3.59, respectively. The scan ranges of the four sub-arrays are summarized in Table 3.3. The overlapped 3 dB scan ranges for both polarizations at 27 GHz and 40 GHz are $-67^\circ \sim 59^\circ$ and $-28^\circ \sim 19^\circ$, respectively. It is clear that the V-pol sub-arrays determine the overall scan performance of the array.

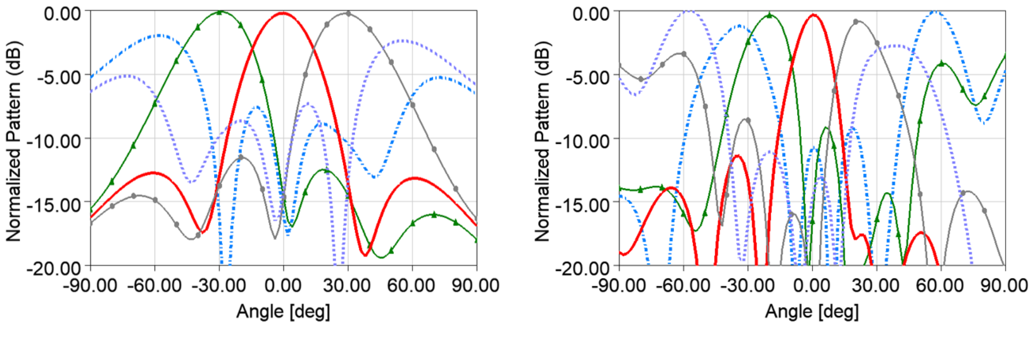

(a)

(b)

Figure 3.58: Simulated scan performance of the H-pol arrays. (a) The LB array at 27 GHz. (b) The HB array at 40 GHz.

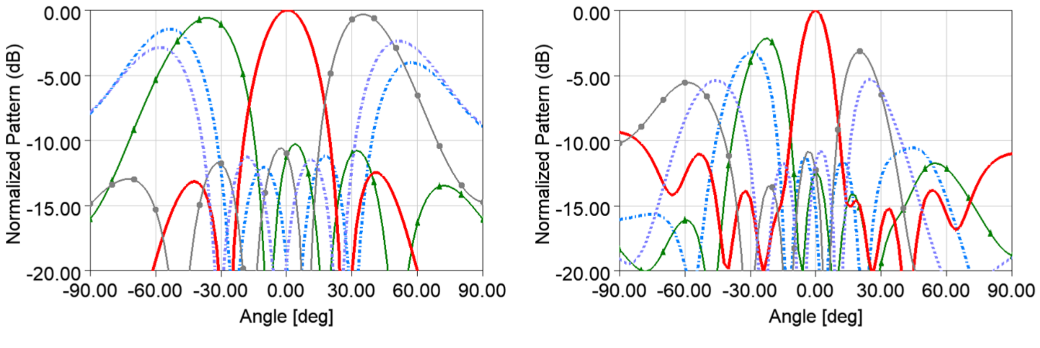

(a)

(b)

Figure 3.59: Simulated scan performance of the V-pol arrays. (a) The LB array at 27 GHz. (b) The HB array at 40 GHz.

27 GHz		40 GHz	
H-pol	V-pol	H-pol	V-pol
$-73° \sim 67°$	$-67° \sim 59°$	$-71° \sim 68°$	$-28° \sim 19°$

Table 3.3: Scan ranges of the four sub-arrays

3.4.5 Corrugated Ground Plane for LB H-pol Array Gain Enhancement

The PEC on M10 causes a broadside radiation pattern for the LB H-pol array, which is inevitable if a complete ground plane is required. However, if endfire or quasi-endfire radiation is desired, a trade-off between antenna pattern and sensitivity to the metallic display underneath the array needs to be considered. Here we present a solution to improving the LB H-pol array gain in the endfire direction by partially removing the ground plane underneath the LB H-pol elements. To save simulation costs, a smaller array with a fewer number of elements is first simulated to verify the design concept and to determine the optimum values of the design parameters, and then the complete 1×4 array is simulated in the final stage. The small array with corrugated ground (CG-S-array) is shown in Figure 3.60. Figure 3.61 shows the radiation pattern of the CG-S-array in the xy-plane at 27 GHz with $L_c = 3$ mm and $W_c = 2.25$ mm. The pattern of the dual-polarized array with full metal ground (FG-L-array) is (Figure 3.55) also plotted in the figure for comparison. The CG-S-array achieves a gain of 5 dBi in the endfire direction with only 2 LB elements whereas the FG-L-array provides only 3 dBi in gain in the endfire direction even with 4 LB elements. Another advantage of removing the metal underneath the LB dipole antennas is that the antennas can meet the bandwidth requirement without the RIS substrate, which significantly reduces the fabrication complexity and costs. However, as expected, the LB array is now more vulnerable to the placement of the metallic display. Figure 3.62 shows the simulated input impedance of the LB H-pol antenna and radiation patterns of the CG-S-array when the metallic display is placed 0.5 mm, 1.5 mm and 2 mm below the substrate. The array maintains good radiation performance for $d \geq 1.5$ mm.

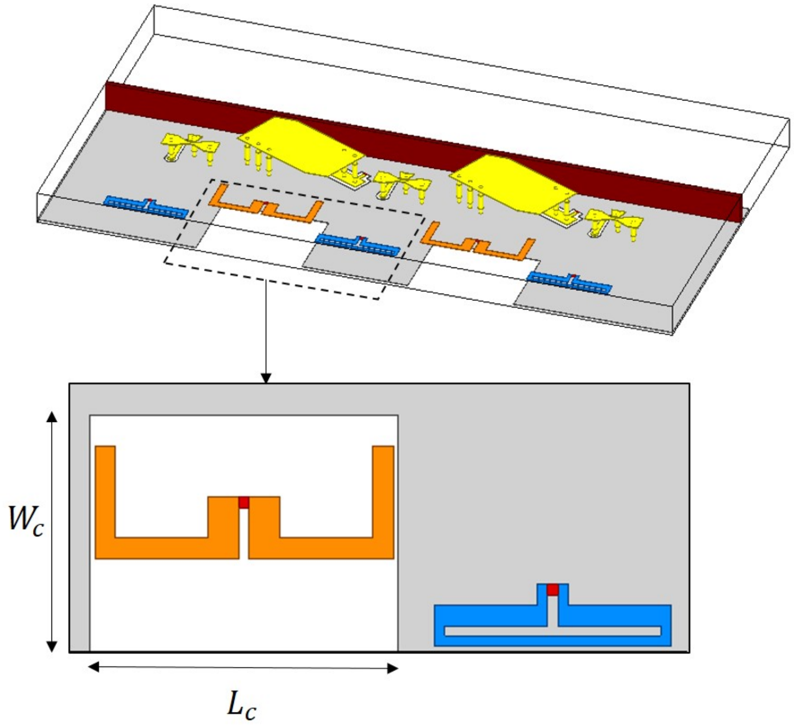

Figure 3.60: Small array with corrugated ground plane (CG-S-array). $L_c = 3$ mm, $W_c = 2.3$ mm.

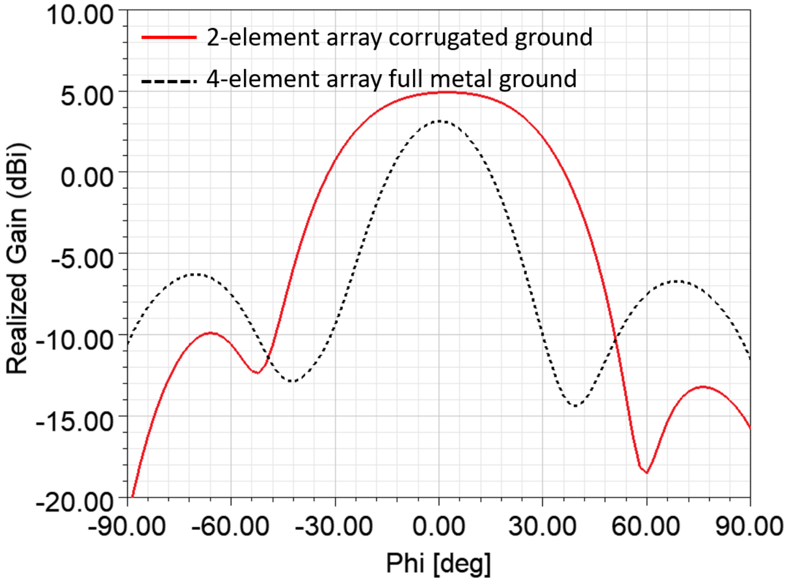

Figure 3.61: Simulated radiation patterns of the CG-S-array and FG-L-array at 27 GHz.

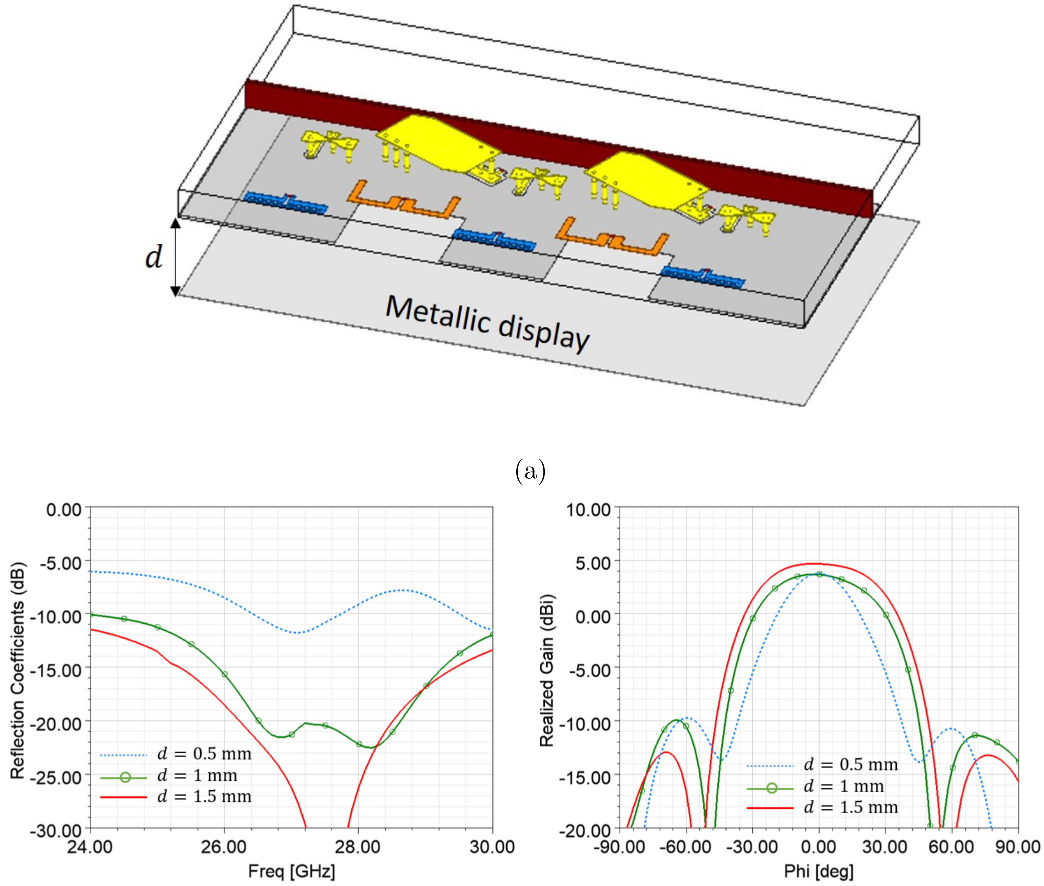

(a)

(b)

(c)

Figure 3.62: Simulated input impedances of the LB H-pol antenna and radiation patterns of the CG-S-array for different display distances d.

3.4.6 Coplanar Stripline-to-Microstrip line Balun

For applications where the H-pol arrays need to be fed by single-ended circuits, baluns are required for the unbalanced-to-balanced transition. In this section, two coplanar-stripline-to-microstrip-line (CPS-to-MSL) baluns are designed for the H-pol arrays. Figure 3.63 shows the CG-S-array with the baluns. Close-up views of the LB and HB baluns are shown in Figure 3.64 (a) and (b), respectively. The baluns are very similar to the one presented in Section 3.3.1.1. For the LB dipole, one strip of the CPS is connected to the ground plane on M10 with a through via while the other strip is connected to the microstrip line on M12 in the same manner. The two vias are placed side-by-side along the y-axis. For the HB folded dipole, similar through vias are used to connect the antennas to the ground and microstrip line. Small rectangular incisions are made on the ground plane to allow the vias to pass through. Unlike the LB baluns, the vias are aligned along the x-axis. This is because the long through vias in front of the HB V-pol antennas act as reflectors, significantly degrading the realized gain of the HB V-pol array in the endfire direction. Aligning vias along the x-direction reduces the effective area of the reflectors, thus minimizing the impact on the HB V-pol array. Due to this arrangement, the curved strip on the right is longer than the straight one on the left, which breaks the symmetry of the currents on the two radiating arms and results in low radiation efficiency. To compensate for the path length difference, the right arm of the folded dipole is shortened slightly. Consequently, the desired current distribution is restored.

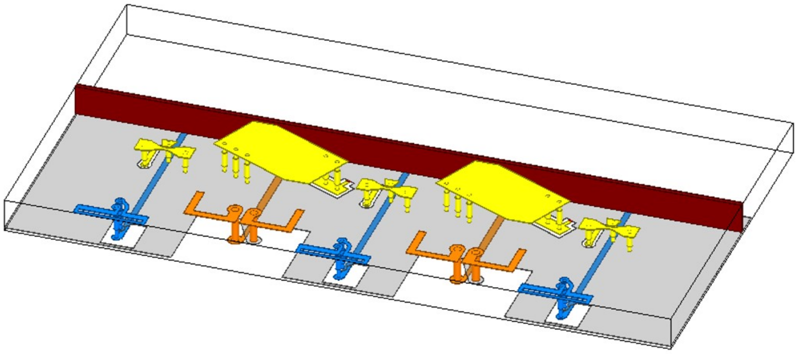

Figure 3.63: CG-S-array with the baluns.

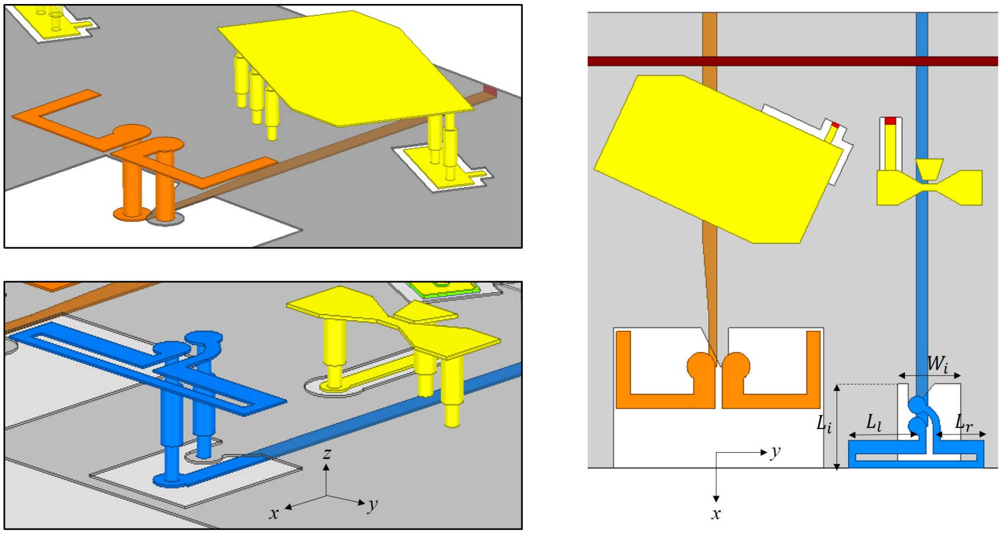

(a) (b)

Figure 3.64: (a) 3D view and (b) top view of the baluns. $L_l = 1$ mm, $L_r = 0.62$ mm, $L_i = 1.1$ mm, $W_i = 0.9$ mm.

3.4.7 Curved Reflector for HB V-pol Array Gain Enhancement

Aligning the vias in the HB baluns can mitigate their impact on the HB V-pol array, but only to a limited extent. To further enhance the gain of the HB V-pol array in the endfire direction, a curved metallic reflector is added behind each HB V-pol element as shown in Figure 3.65. The center of the curvature is the phase center of the antenna. The major design parameters are the distance between the antenna and the via d_1, the distance between the antenna and the reflector d_2, and the angle α. The optimum values are found by iteratively tuning d_1 and d_2 to maximize the endfire gain. Afterwards, the impact of the angle α is investigated independently. The optimized values of the parameters are indicated in Figure 3.65.

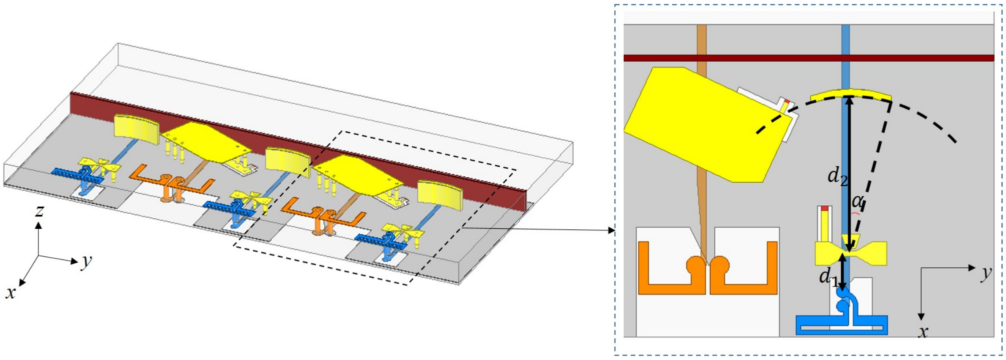

Figure 3.65: CG-S-array with curved reflectors. $d_1 = 3.35$ mm, $d_2 = 0.75$ mm, $\alpha = 41°$.

The final version of the small array is presented in Figure 3.66. The large metallic wall at the back (red) and curved reflectors for the HB V-pol sub-array are realized by stacked vias with spacing of 0.4 mm. The reflection coefficients and radiation patterns of the array are shown in Figure 3.67 and Figure 3.68, respectively, in conjunction with the results obtained from the simplified model (Figure 3.65). As clearly shown in the figures, excellent agreement is achieved.

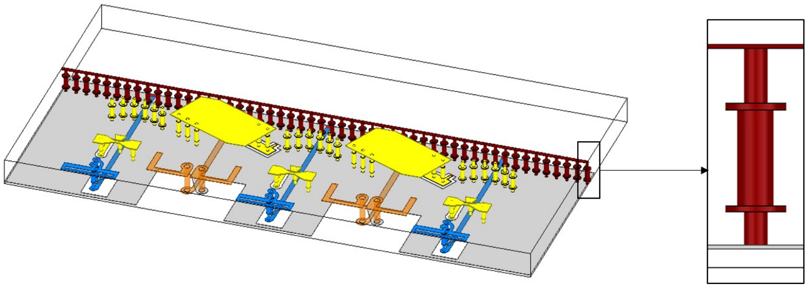

(a)

Figure 3.66: The final version of the small array.

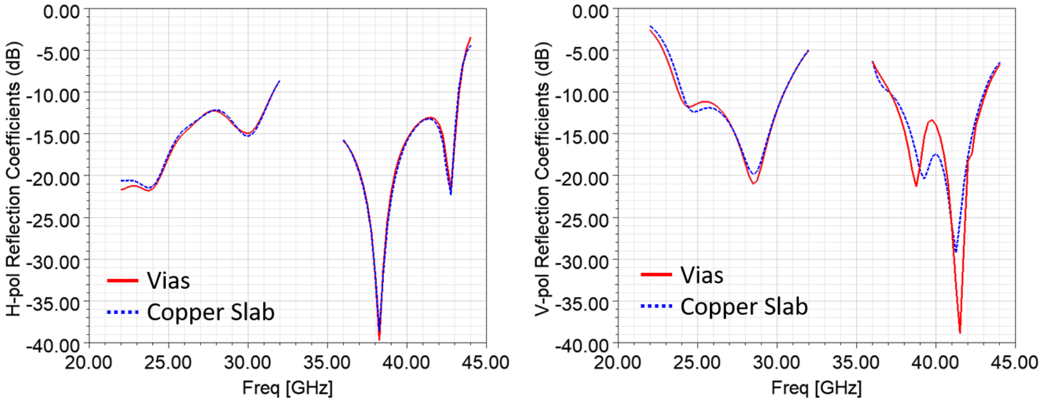

(a) (b)

Figure 3.67: Simulated reflection coefficients of the small array.

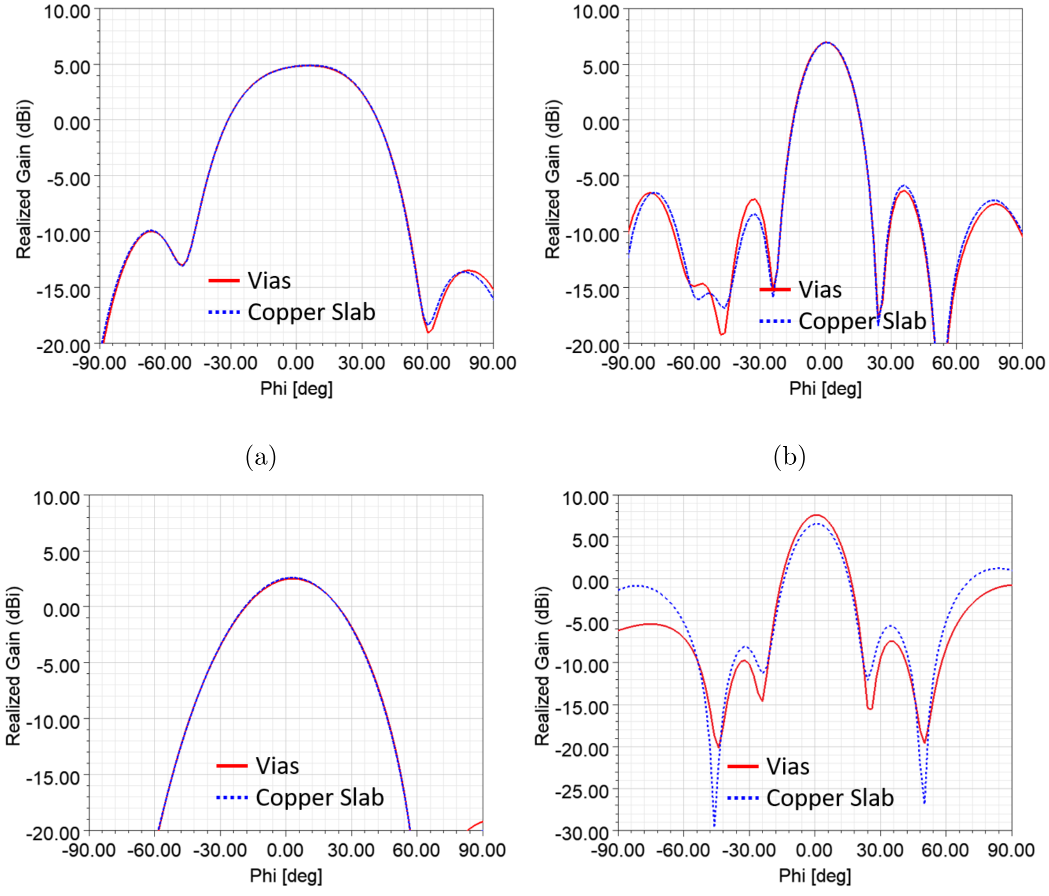

(a) (b)

(c) (d)

Figure 3.68: Simulated radiation patterns of the small array.

3.4.8 Modified Quasi-Endfire Dual-polarized Array

The configuration of the complete 1×4 array with enhanced quasi-endfire radiation is shown in Figure 3.69. The whole array is kept within 25 mm × 6 mm × 0.97 mm.

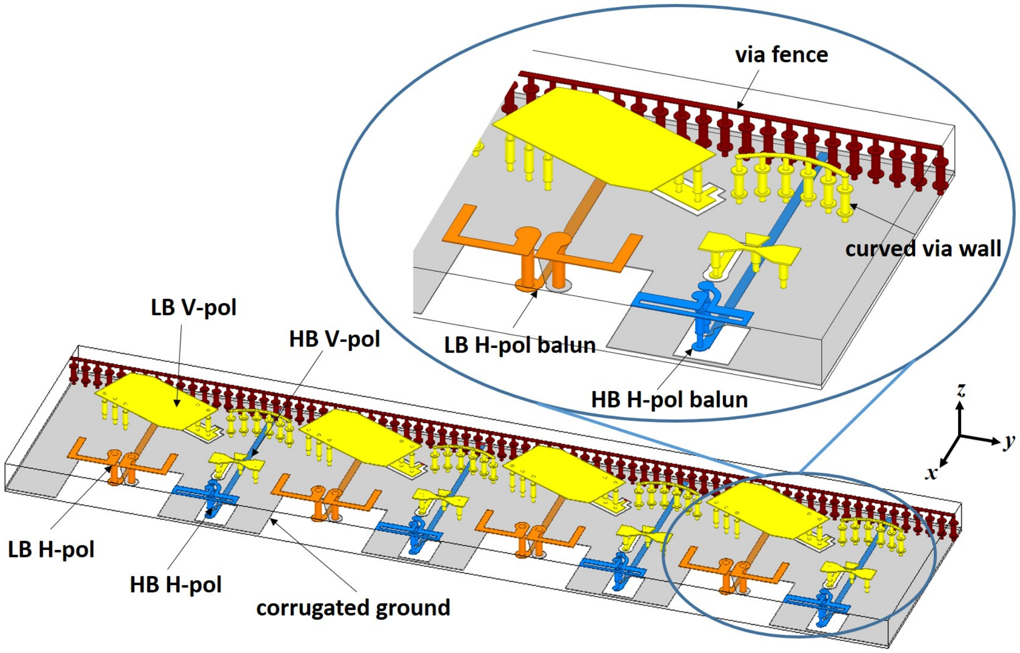

Figure 3.69: The complete 1 × 4 array with enhanced quasi-endfire radiation.

The simulated reflection coefficients of the array elements are plotted in Figure 3.70. The overlapped bandwidths (reflection coefficients less than -10 dB) of the LB and HB arrays are 22.2% (24–30 GHz) and 17.2% (36.2–43 GHz), respectively. Figure 3.71 shows the simulated port-to-port coupling between elements. For the clarity of the figure, only four pairs of elements with the strongest couplings are presented here. The mutual coupling is lower than -15.8 dB in the LB and lower than -14.7 dB in the HB. The radiation patterns of the array in the xy- and xz-planes are plotted in Figure 3.72. The peak gains and endfire gains of the array for different polarizations at the center frequencies of the two bands are listed in Table 3.4. For comparison, the endfire gains of the dual-polarized array with a full ground plane are also listed in the table. The modified array achieves peak gains of more than 9.7

dBi in different operating modes. More importantly, the modified configuration can provide much improved gains in the endfire direction.

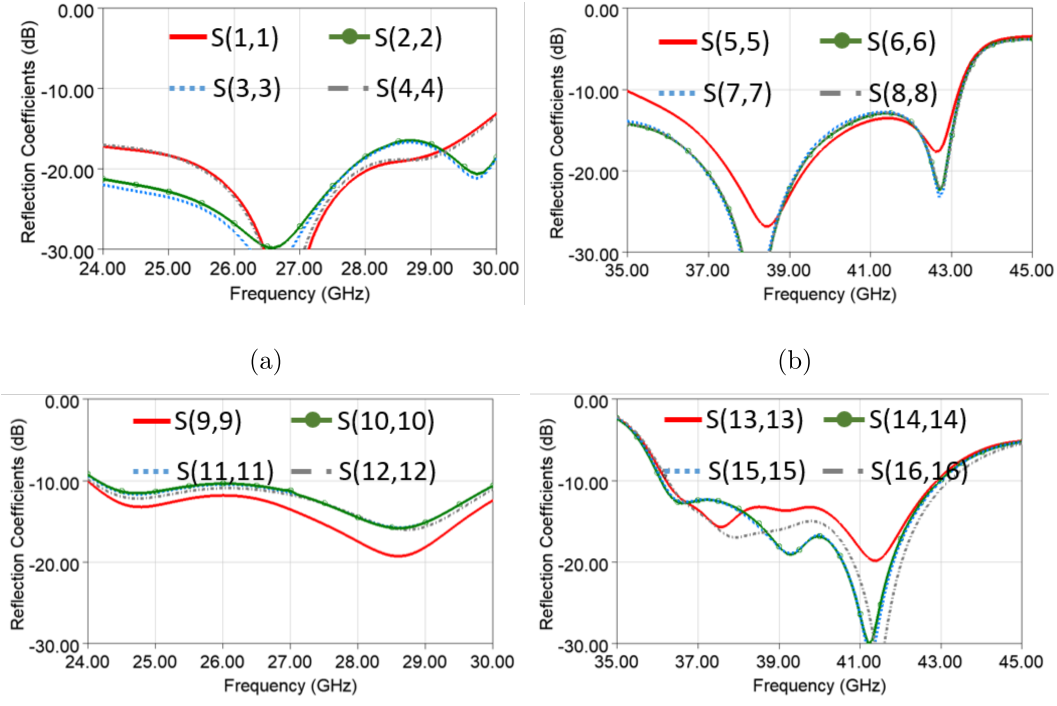

(a) (b)

(c) (d)

Figure 3.70: Simulated reflection coefficients of (a) LB H-pol, (b) HB H-pol, (c) LB V-pol and (d) HB V-pol arrays. (Port numbering from right to left: LB H-pol 1-4; HB H-pol 5-8; LB V-pol 9-12; HB V-pol 13-16.)

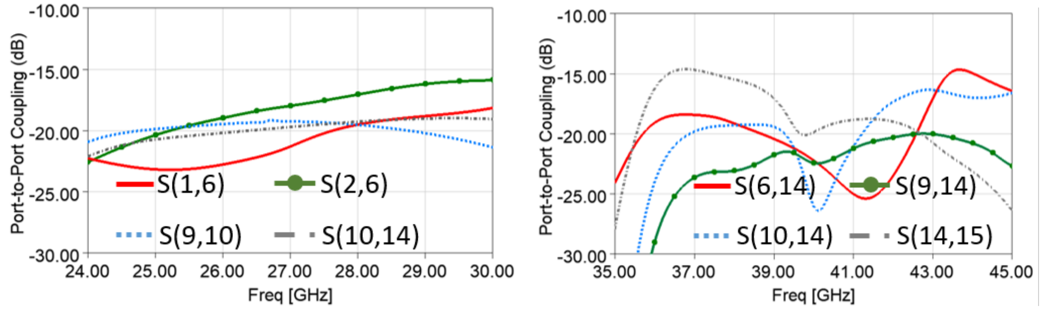

(a) (b)

Figure 3.71: Simulated port-to-port coupling between elements in the (a) LB and (b) HB. (Port numbering from right to left: LB H-pol 1-4; HB H-pol 5-8; LB V-pol 9-12; HB V-pol 13-16.)

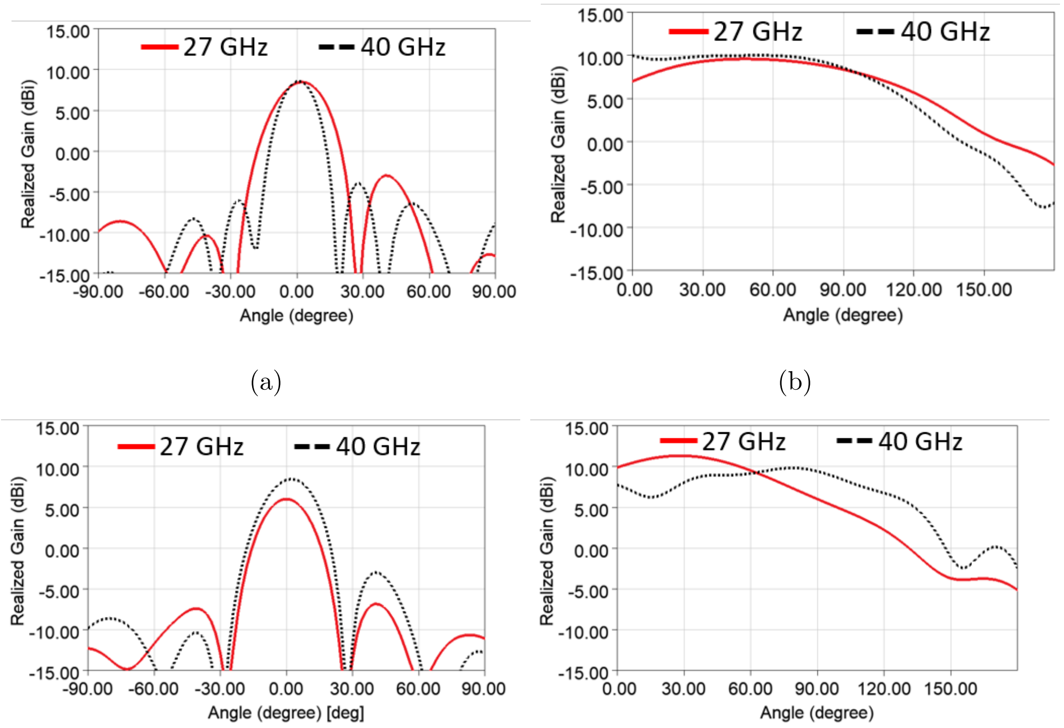

(a)

(b)

(c)

(d)

Figure 3.72: Simulated radiation patterns of the (a) H-pol arrays in the *xy*-plane and (b) *xz*-plane, and (c) V-pol arrays in the *xy*-plane and (d) *xz*-plane.

	H-pol @27 GHz	V-pol @27 GHz	H-pol @40 GHz	V-pol @40 GHz
Version 1* Endfire gain	3.1 dBi	6.3 dBi	5.9 dBi	5.8 dBi
Version 2** Endfire gain	8.4 dBi	8.5 dBi	6.0 dBi	8.4 dBi
Version 2** peak gain	9.7 dBi	11.3 dBi	11.2 dBi	9.8 dBi

*Version 1: Dual-polarized array with full ground

**Version 2: Modified quasi-endfire dual-polarized array

Table 3.4: Simulated gains of the modified quasi-endfire dual-polarized array based on the simulation model.

The simulated scan performance of the array at 27 and 40 GHz are demonstrated in Figure 3.73. The maximum 3-dB beam scanning angles for the H-pol and V-pol are ±45° and ±56°, respectively, at 27 GHz and are ±42° and ±28° at 40 GHz.

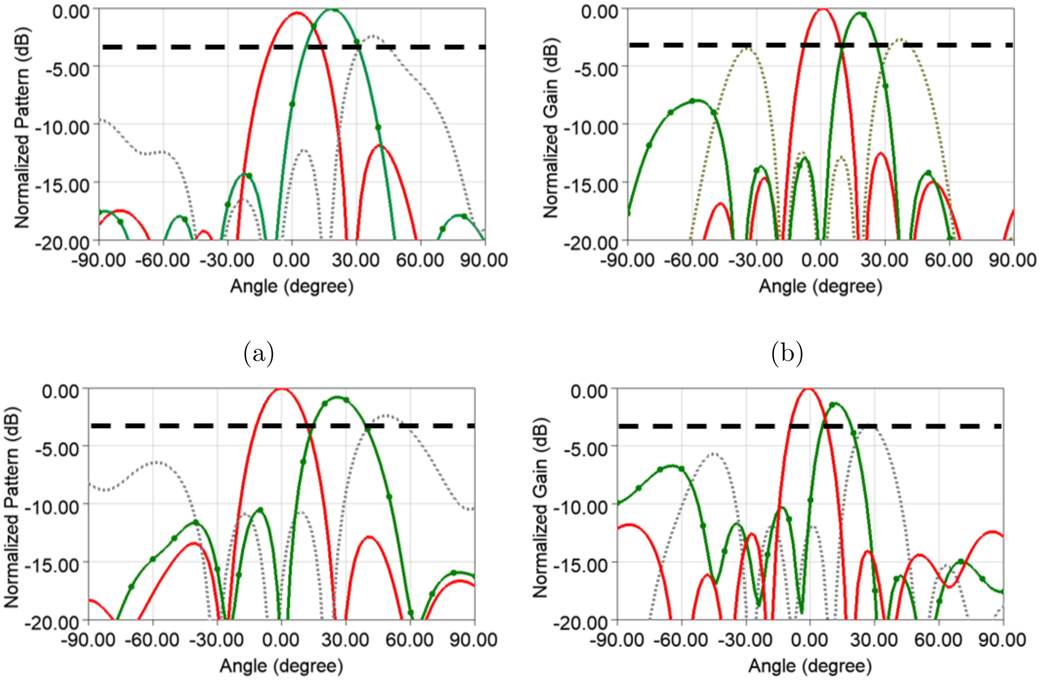

(a) (b)

(c) (d)

Figure 3.73: Simulated scan performance of the modified quasi-endfire dual-polarized array. (a) H-pol at 27 GHz, (b) H-pol at 40 GHz, (c) V-pol at 27 GHz and (d) V-pol at 40 GHz.

3.5 A Near-Field-Based Gain and Pattern Measurement Technique for Probe-Fed mmWave Antennas

This section addresses the measurement issues reported in the literature review in Section 1.2, and presents a simple and inexpensive near-field to far-field (NF to FF) technique that can simultaneously obtain the gain and radiation pattern of a probe-fed mmWave antenna. A commercial near-field scan system (NeoScan [107], developed by EMAG Technologies) is used to map the near-field of the antenna. The system utilizes an extremely small non-metallic electro-optic probe that has the capability to accurately sample electric fields in close proximity to the antenna surface (< 1 mm) with very high spatial resolution (minimum sampling interval $< 10\ \mu m$). Thanks to the small sampling distance, multi-path effects become negligible compared with the direct signal, and the required scan area is reduced substantially. To directly characterize the gain of the AUT on the same setup, we created a probe-fed ground-backed dipole antenna, implemented the image method to accurately characterize its gain, and then used it as the gain standard. With the standard gain antenna, the NF to FF method can provide both gain and radiation pattern of any type of probe-fed mmWave antennas. This measurement technique eliminates the need for numerous custom-built test fixtures and complicated measurement setups, and provides very accurate results.

3.5.1 Image Method for Gain Measurement

The image method proposed by Purcell [112] is an alternative approach to the standard two-antenna method, where two identical antennas are required to determine the antenna gain. In the method, instead of employing a twin antenna, a flat perfect conductor is used to generate an image of the AUT. The distance between the reflector and the AUT is $r/2$, and r must satisfy the far-field criterion

$$r > \frac{2D^2}{\lambda_0} \tag{3.2}$$

where D is the maximum dimension of the antenna, and λ_0 is the free space wavelength at the operating frequency. Based on the Friis transmission formula, the gain of the antenna along the boresight direction can be calculated from

$$G(\mathrm{dB}) = 10\log_{10}(\frac{4\pi r}{\lambda_0}) + 5\log_{10}(\frac{P_r}{P_t}) \tag{3.3}$$

where P_t is the transmitted power and P_r is the received power. The ratio $\frac{P_r}{P_t}$ is given by

$$\frac{P_r}{P_t} = |S'_{11} - S_{11}|^2 \tag{3.4}$$

where S'_{11} and S_{11} are the reflection coefficients of the AUT with and without the reflector, respectively. The feasibility of this method at mmWave frequencies has been demonstrated in [113–115]. In [115], the impact of the size and alignment of the reflecting plate has been thoroughly studied. As a rule of thumb, the size of the reflector needs to be much larger than the wavelength and also larger than the 3-dB footprint of the antenna on the reflector in order to produce accurate results. The image method is a very efficient way to measure the absolute gain of a linearly-polarized probe-fed antenna since it obviates the need for multiple antennas. This method is most suitable for antennas with a small electrical aperture and relatively short far-field distance. For antennas with a large electrical aperture and narrow beamwidth, the size of the reflector becomes impractically large, and even slight misalignment can cause significant errors. Furthermore, if the antenna radiates elliptically-polarized waves, (3.3) needs to be modified to account for the polarization mismatch between the reflected waves and the antenna [64]. This method fails for circularly-polarized antennas since the polarization of the reflected wave is perpendicular to that of the antenna. In the proposed technique, the image method is used as an auxiliary step to provide an accurate gain measurement of a probe-fed ground-backed dipole antenna, which is then used as the gain standard in the NF to FF method. A detailed design and measurement procedure will be presented in Section 3.5.3 and 3.5.2.

3.5.2 Near-Field to Far-Field Gain and Pattern Measurements

A more versatile way of measuring the gain of an antenna is the gain comparison method. Unlike the conventional gain comparison method which is usually performed in the far-field region, the NF gain comparison method is completely based on near-field measurements. Therefore, it can be implemented in a much more compact range, and can avoid issues commonly associated with far-field measurements. The technique requires a probe-fed standard gain antenna. Initially, near-field measurements are performed, and the far-field patterns are computed using the near-field to far-field transformation. Then the relative gains are compared with the known gain of the standard antenna to yield the absolute values. The method needs two sets of measurements. In one set, the near-field measurement is performed on the standard antenna, and the radiation pattern (uncalibrated) is evaluated based on the near field data. In the other set, the standard antenna is replaced by the AUT, and the same procedure is repeated to obtain the radiation pattern of the AUT. Based on the uncalibrated radiation patterns, the relative gain of the AUT to the standard antenna ΔG can be obtained. Knowing the actual gain of the standard antenna G_r^{std}, we can derive the absolute gain of the AUT from

$$G_{\mathrm{AUT}}\ (\mathrm{dB}) = G_{\mathrm{std}}\ (\mathrm{dB}) + \Delta G\ (\mathrm{dB}) \tag{3.5}$$

where ΔG is the difference between the values in the direction where the absolute gain of the standard antenna is evaluated. It should be noted that the system setup, geometrical arrangement, placement of the cables and the input power in both sets need to be maintained the same. This requirement is very difficult to satisfy if a standard pyramidal horn antenna is used as the reference since a horn antenna has a different feeding structure and it is hard to place it properly on a chuck. The use of the EO probe is the key to the success of the NF to FF method. Traditional NF measurements use either a short dipole or an open-ended waveguide as the sampling probe, which is typically placed far away from the AUT to avoid disturbing the fields. As a consequence, measurements usually suffer from multipath effects from the probe station and do not provide satisfactory results. In contrary, EO probes can sample the electric field in close proximity to the antenna surface with very high spatial resolution due to their non-invasive nature and small size, which substantially eliminates the multipath effects and reduces the scan area. In this study, we use a commercial EO near-field scan system called NeoScan. The EO field probe is all-dielectric and can be placed as close as 1 mm to the antenna surface, corresponding to 0.1 λ_0 at 28 GHz. The system setup is shown in Figure 3.74.

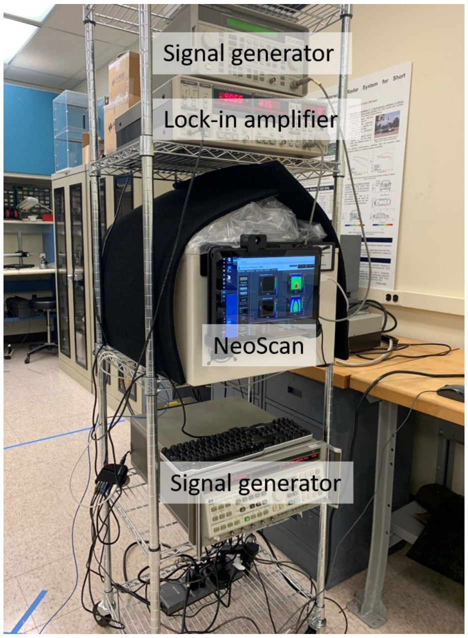

Figure 3.74: The NeoScan system.

The NF to FF method can be used to measure antennas with arbitrary patterns and polarizations. The limiting factor here is the probe station. A typical probe station has a metallic chuck and a built-in microscope, which can affect antenna performance. For this type of probe station, only antennas having boresight radiation patterns can be characterized accurately. To measure antennas that have upwards and/or downward radiation, necessary modifications to the measurement setup are needed, including replacing the metallic chuck with a wafer chuck, or using a dielectric foam holder, and replacing the fixed microscope with a moveable one [116]. The accuracy of the measurement is closely related to the precision of the phase center. For antennas without a well-defined phase center, this method may not predict accurate results.

3.5.3 Standard-Gain Ground-Backed Dipole Antenna

As mentioned in Section 3.5.2, the NF to FF method needs a standard gain antenna to obtain the gain of the AUT. Unfortunately, there are no probe-fed standard gain antennas currently available on the market. Half-wavelength dipoles are universally accepted as gain standards due to their high degree of polarization purity. Here, we design a 28 GHz ground-backed planar dipole antenna as the gain standard. The geometry of the antenna, along with its dimensions, is illustrated in Figure 3.75. The dipole is fabricated on a Rogers 4003C laminate ($\epsilon_r = 3.55, \tan\delta = 0.0027$) with a thickness of 0.801 mm, and is placed 5 mm above the ground plane. Styrofoam is used to support the antenna above the ground plane. The reason for adding a ground plane to the dipole is that the performance of the standard gain antenna needs to be stable to ensure the accuracy of the gain comparison method. Without the ground plane, the performance would be affected by the chuck, which would compromise the accuracy of the NF to FF gain measurement. A balun is implemented for the transition from the standard GSG probe terminal to the balanced coplanar stripline. It should be noted that the balun is considered an integral part of the antenna. Proper de-embedding techniques are needed if measuring the differential input impedance of the antenna is desired [35].

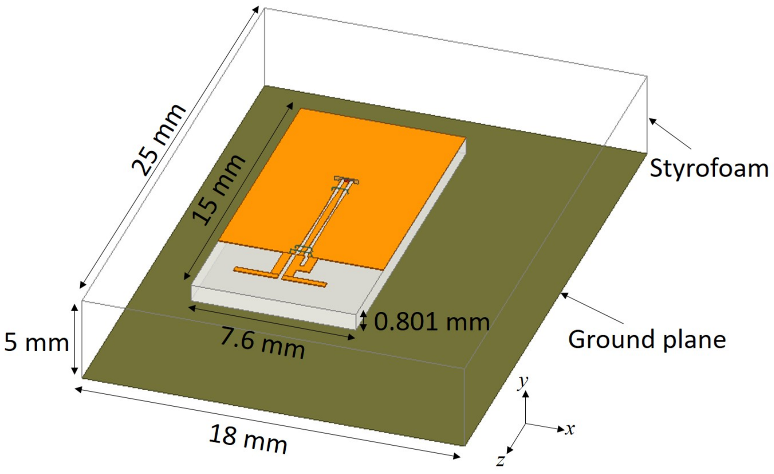

Figure 3.75: The ground-backed dipole antenna.

The image method is used to calibrate the gain of the ground-backed dipole antenna. Figure 3.76 shows the arrangement of the antenna on the probe station for the measurement. The antenna is placed at the edge of the chuck, and is fed by a GSG RF probe (Picoprobe 50A-GSG-350-DP). A network analyzer (Agilent 8722ES) is connected to the RF probe to measure the reflection coefficients of the antenna. The system is calibrated to the probe tips using a standard calibration substrate (GGB Industries Inc. Model CS-9). A large flat conductor is placed in front of the antenna. The dimensions of the reflector are 12 cm × 12 cm. The distance between the phase center of the antenna and the reflector is 52.7 mm. We first measure the reflection coefficients of the AUT with the reflector (S'_{11}), then we remove the reflector and take the measurement again (S_{11}). In order to reduce the effects of multiple reflection and edge diffraction, proper gating is applied to the time domain response [117]. The absolute gain in the $+z$-direction from 26-30 GHz is obtained using (3.3) and (3.4), and is plotted in Figure 3.77. The measurement is in excellent agreement with the simulation. The absolute gain of the ground-backed dipole antenna is 7.123 dBi at 28 GHz.

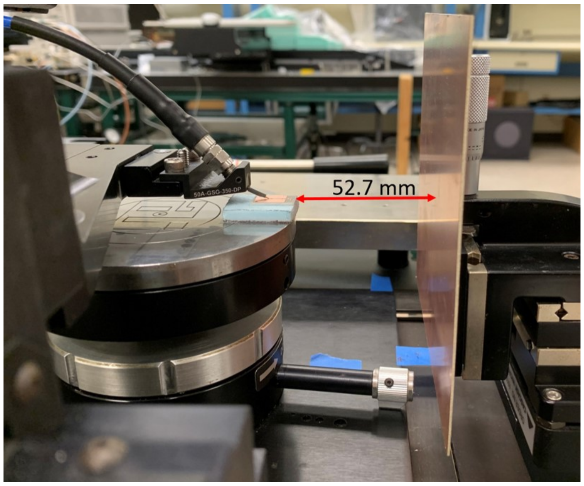

Figure 3.76: The setup for the absolute gain measurement using the image method.

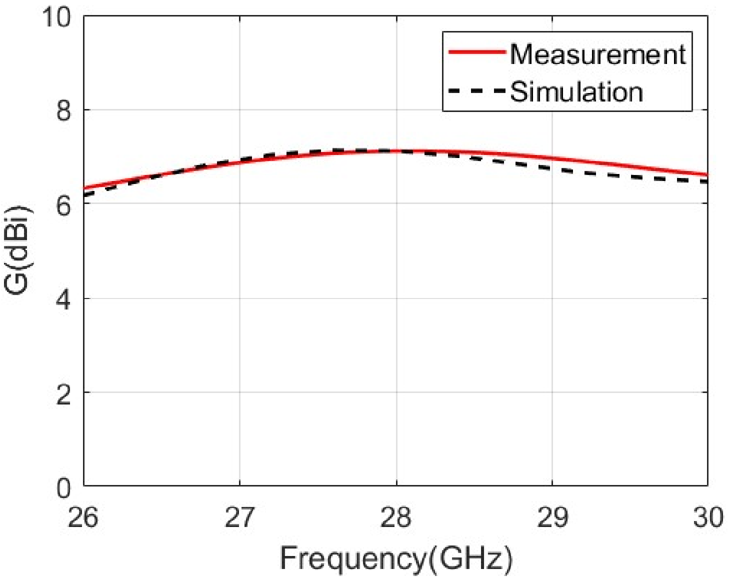

Figure 3.77: Measured and simulated absolute gain of the dipole antenna from 26-30 GHz.

3.5.4 Examples of Using the NF to FF Method

For demonstration purposes, two 28 GHz antennas are fabricated and then tested using the NF to FF method. The first antenna is a horizontally polarized tapered slot antenna [118], and the second one is a vertically polarized folded monopole antenna

[111, 119].

3.5.4.1 Horizontally Polarized Tapered Slot Antenna

The tapered slot antenna is fabricated on a Rogers 4003C substrate with a thickness of 0.801 mm. The geometry of the antenna together with the simulated and measured refection coefficients are shown in Figure 3.78. We first measure the near-field distribution of the standard gain dipole antenna and then compute its radiation pattern. For a planar scanning configuration illustrated in Figure 3.79, the probe moves on a rectangular grid at a fixed distance $z_0 = 1$ mm from the center of the antenna. The scan area is 46 mm × 20 mm, and the sampling resolution is set to 0.5 mm.

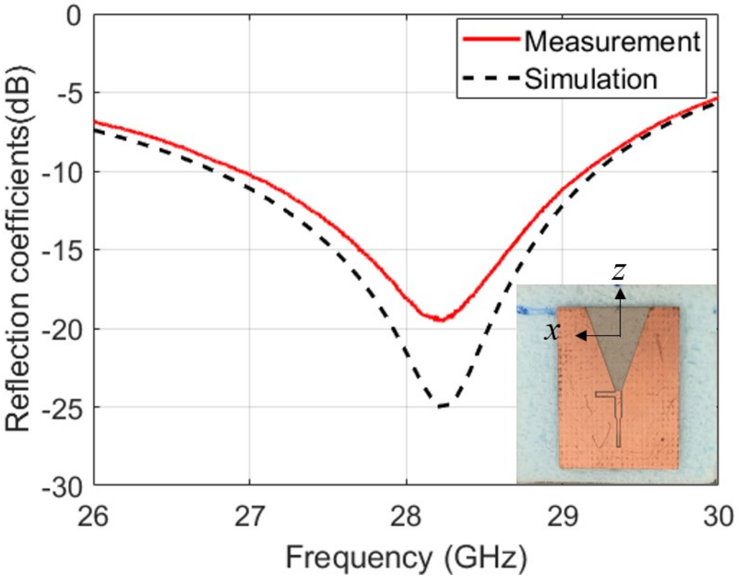

Figure 3.78: Geometry and reflection coefficients of the tapered slot antenna.

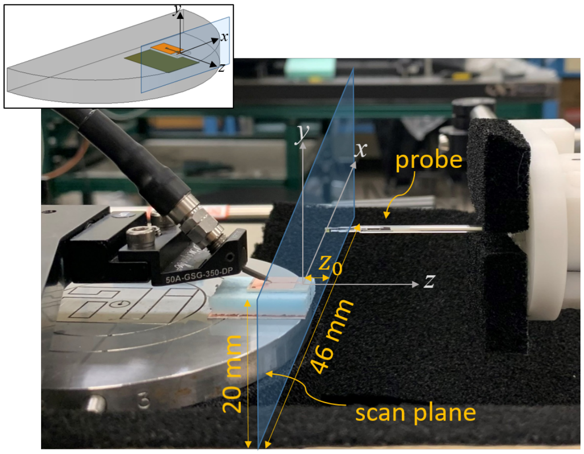

Figure 3.79: Near-field scanning configuration.

In the far-field region, the electric field can be expressed as [120]

$$\boldsymbol{E(r)} = jk_0 \frac{e^{-jk_0 r}}{2\pi r}[\hat{\boldsymbol{\theta}}(A_x \cos\phi + A_y \sin\phi) + \hat{\boldsymbol{\phi}} \cos\theta (A_y \cos\phi - A_x \sin\phi)] \tag{3.6}$$

where θ and ϕ denote the direction of observation. A_x and A_y are the tangential components of the vector amplitude $\boldsymbol{A_t}$ on the scanned plane, and are related to the measured electric field by

$$\boldsymbol{A_t}(k_x, k_y) = e^{jk_0 z_0} \iint\limits_{-\infty}^{\infty} \boldsymbol{E_t}(x, y, z_0) e^{jk_x x + jk_y y}\, dx\, dy \tag{3.7}$$

In the observation direction (θ, ϕ),

$$\begin{aligned} k_x &= k_0 \sin\theta \cos\phi \\ k_y &= k_0 \sin\theta \sin\phi \\ k_z &= \sqrt{k_0^2 - k_x^2 - k_y^2} \end{aligned} \tag{3.8}$$

The measured near-field distribution of the planar dipole is mapped in Figure 3.80. The asymmetry in the y-direction is due to the ground plane underneath the antenna.

The small asymmetry in the x-direction is due to the presence of the balun on one side of the antenna which perturbs the symmetry. The normalized radiation patterns in the xz- and yz-planes are plotted in Figure 3.81 (a) and (b), respectively. For comparison, the simulated far-field radiation patterns are also plotted in the figure. The measured patterns diverge from the simulation at large angles because of the finite size of the scan area. To better evaluate the measured results, we extract the near-field distribution from the simulation and use it to compute the far-field patterns. As shown in Figure 3.81, the measured radiation patterns agree well with the simulated NF to FF patterns. The drop in the gain value at around $\theta = -5^\circ$ in the yz-plane is due to the abrupt truncation of the scan plane. Then the near-field measurement is performed on the tapered slot antenna, and the radiation pattern in the xz-plane is computed and calibrated to obtain the absolute gain using (3.5). It should be pointed out that the entire process only requires lifting/landing the RF probe and replacing the standard dipole antenna with the tapered slot antenna (the AUT); all other measurement parameters for the two sets of measurements are maintained exactly the same. Figure 3.82 shows the near-field distribution of the tapered slot antenna. The asymmetry in the x-direction is due to the open-stub, while the asymmetry in the y-direction is because of the metallic chuck under the antenna. Figure 3.83 (a) and (b) show the normalized radiation patterns of the tapered slot antenna in the xz- and yz-planes, respectively. Due to the metallic chuck, the maximum radiation shifts upwards by about 10° in the yz-plane. If we include the chuck in the simulation, the measured radiation pattern agrees well with the simulation. The uncalibrated radiation pattern of the tapered slot antenna in the xz-plane is then compared with that of the standard antenna as shown in Figure 3.84. The value at $\theta = 0^\circ$ for the tapered slot antenna is 1.377 dB higher than that for the standard gain antenna. Since the absolute gain of the standard gain antenna is 7.123 dBi, the absolute gain of the tapered slot antenna in the $+z$ direction is 8.5 dBi.

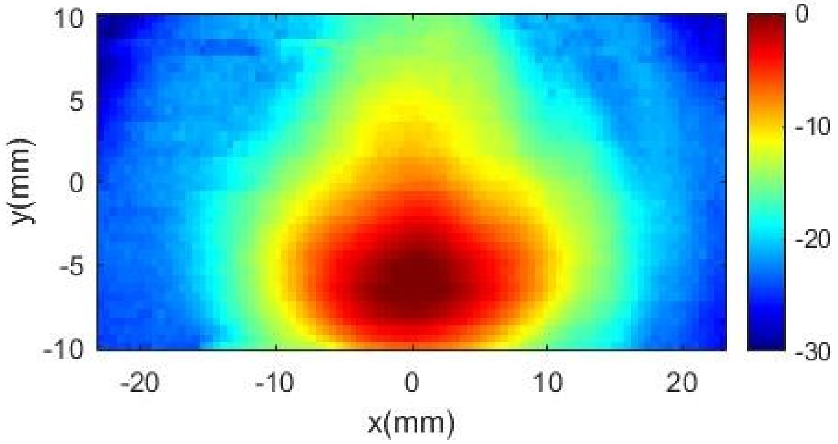

Figure 3.80: Measured near-field distribution of the planar dipole antenna. (Unit: dB).

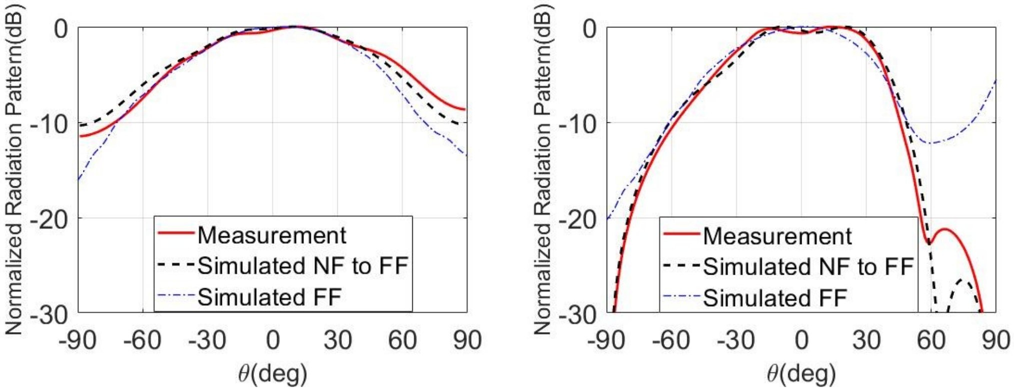

(a)

(b)

Figure 3.81: Normalized radiation patterns of the planar dipole in the (a) xz-plane and (b) yz-plane.

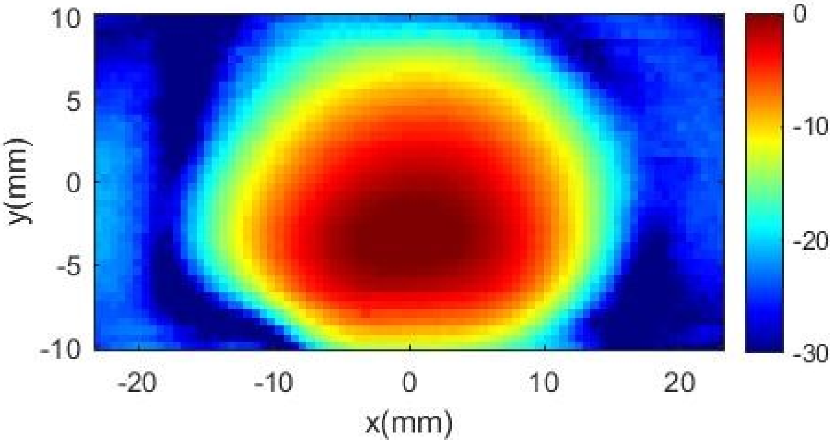

Figure 3.82: Measured near-field distribution of the tapered slot antenna. (Unit: dB)

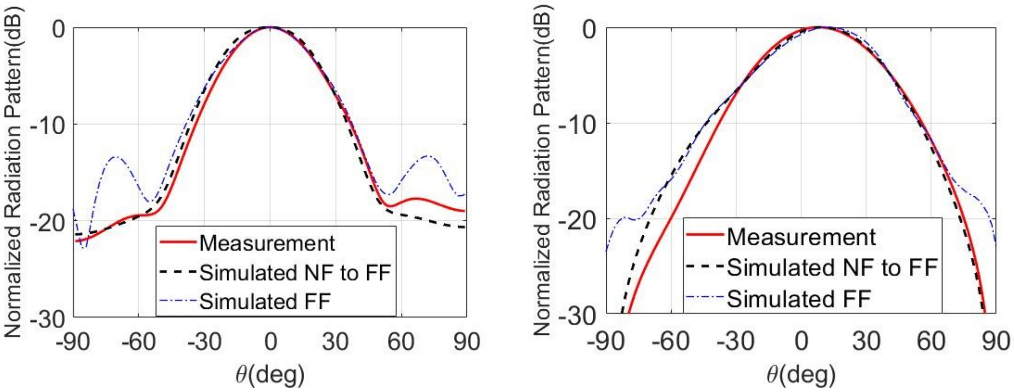

(a)

(b)

Figure 3.83: Normalized radiation patterns of the tapered slot antenna in the (a) xz-plane and (b) yz-plane.

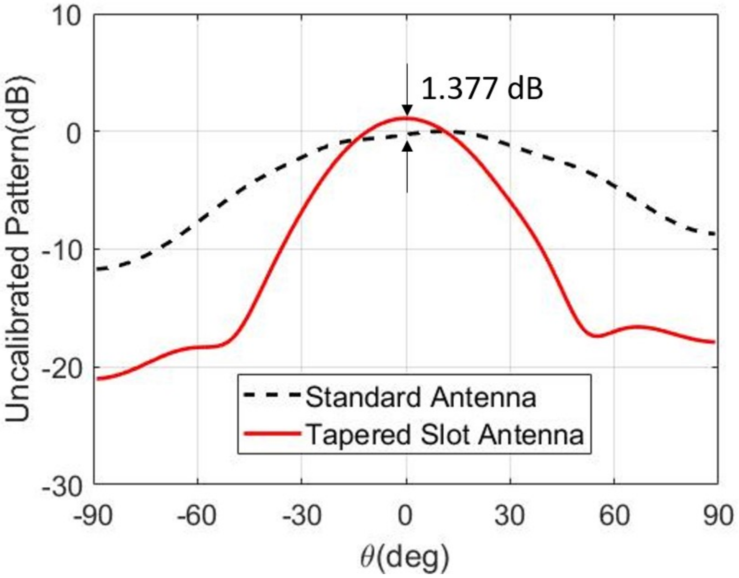

Figure 3.84: Uncalibrated radiation patterns of the tapered slot antenna and the standard gain antenna in the xz-plane.

3.5.4.2 Vertically Polarized Folded Monopole Antenna

The NF to FF method is also used to measure the gain and radiation pattern of a vertically polarized folded monopole antenna as shown in Figure 3.85. The antenna is fabricated on a multi-layer laminate with a total height of 1.12 mm. The fabricated antenna, together with the simulated and measured reflection coefficients, is shown in Figure 3.86. The slight frequency shift is due to fabrication errors.

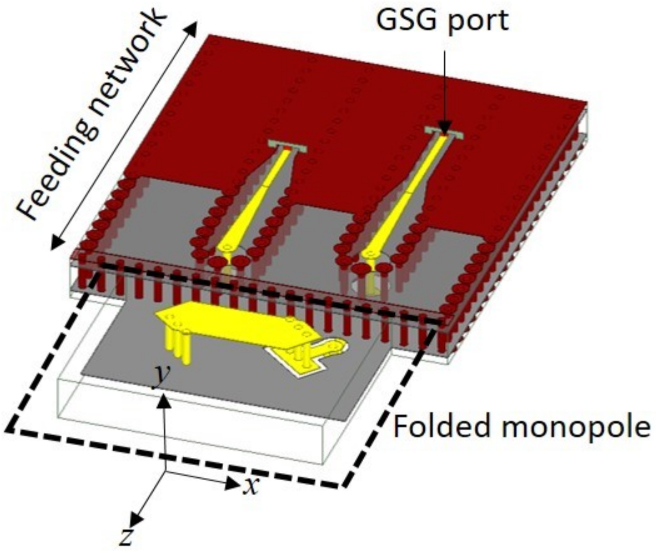

Figure 3.85: The geometry of the folded monopole antenna.

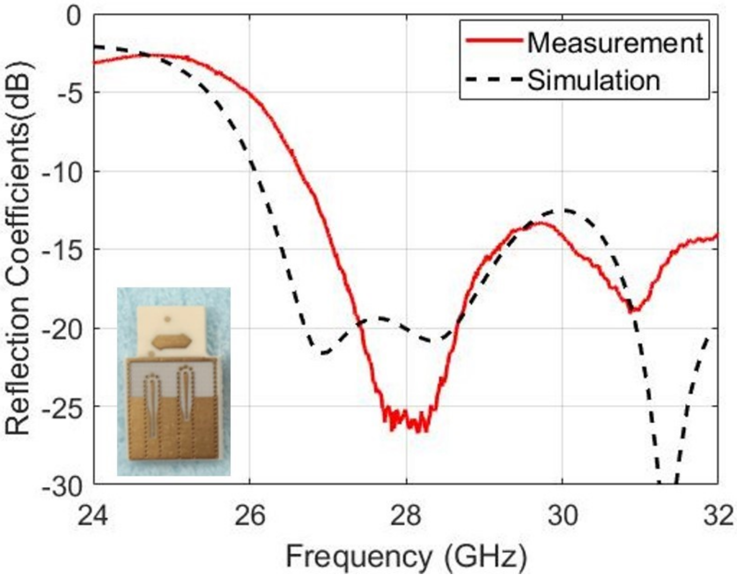

Figure 3.86: The fabricated folded monopole and its reflection coefficients.

Following the same procedure, the measured near-field distribution and normalized radiation patterns of the folded monopole antenna are presented in Figure 3.87 and 3.88, respectively. The measured radiation pattern in the xz-plane is in excellent agreement with the simulation. There are some discrepancies in the yz-plane due to the limited travel range of the scanner in the y-direction (maximum 20 mm travel distance). The uncalibrated radiation pattern of the folded monopole in the xz-plane is plotted in Figure 3.89. The value at $\theta = 0°$ for the folded monopole is 5.603 dB lower than that of the standard gain antenna, translating to an absolute gain of 1.52 dBi. For comparison, we also measure the gains of the tapered slot antenna and the folded monopole antenna using the image method. The results are summarized in Table 3.5 and compared with the simulated gains. Both methods provide excellent agreement for the estimation of the gain.

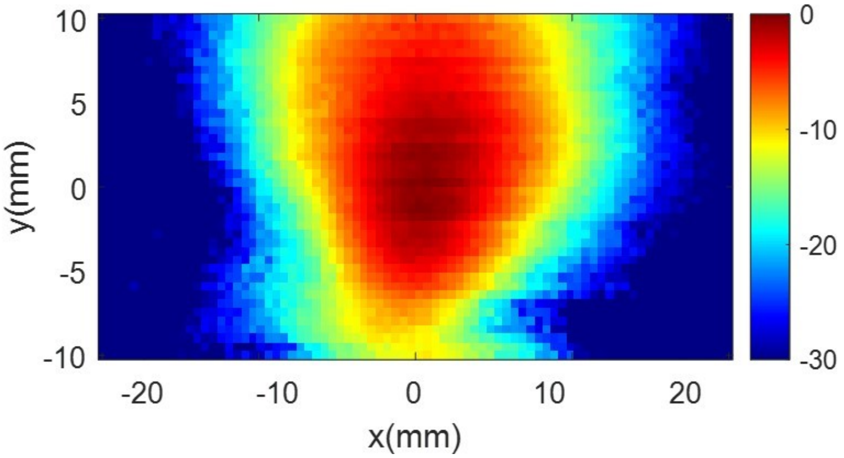

Figure 3.87: Measured near-field distribution of the folded monopole antenna. (Unit: dB)

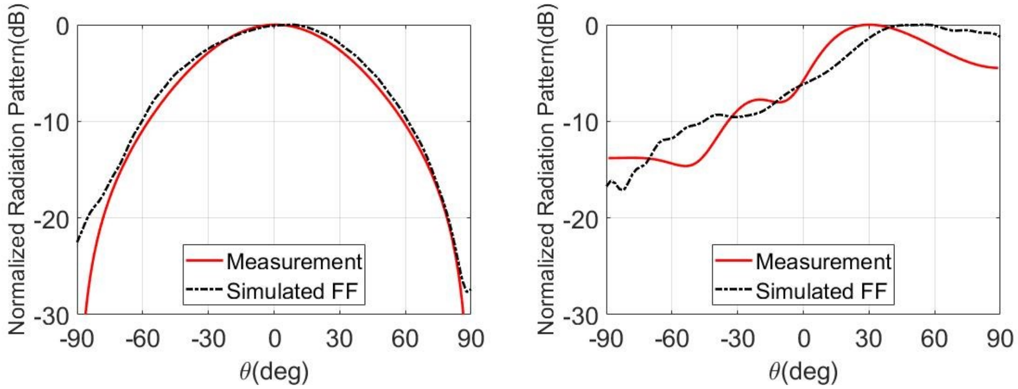

(a) (b)

Figure 3.88: Normalized radiation patterns of the folded monopole antenna in the (a) xz-plane and (b) yz-plane.

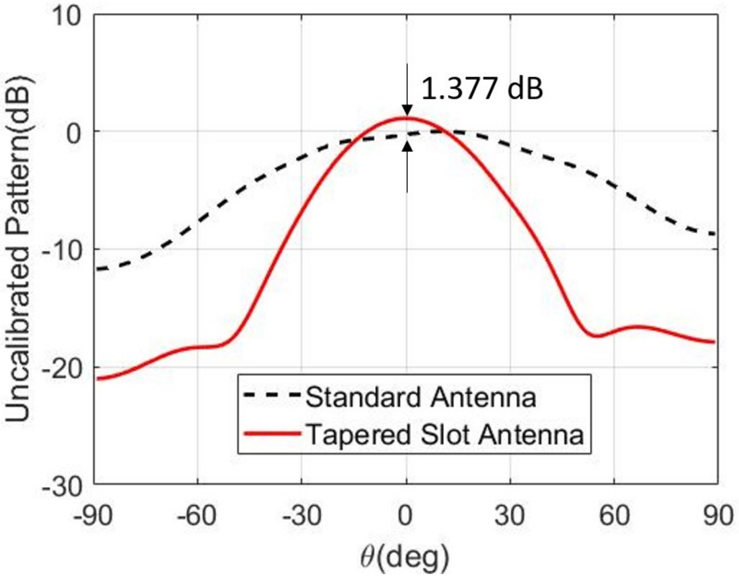

Figure 3.89: Uncalibrated radiation patterns of the folded monopole antenna and the standard gain antenna in the xz-plane.

	Simulation	Image Method	NF to FF Method
Tapered Slot Antenna	8.9 dBi	8.4 dBi	8.5 dBi
Folded Monopole	1.15 dBi	1.16 dBi	1.52 dBi

Table 3.5: Measured absolute gain of the tapered slot antenna and the folded monopole antenna at 28 GHz.

3.6 Conclusion

This chapter presents three mmWave antenna arrays for 5G applications. Design concepts, details and simulation results are provided for all three designs. A prototype based on the second design, i.e., a low-profile dual-band dual-polarized quasi-endfire phase array, was fabricated and tested. A major advantage of these antenna arrays is that they can be directly integrated with cellphone PCBs, offering low-cost solutions to mmWave 5G antennas for cellular devices. Useful measurement techniques for mmWave antenna characterization are also demonstrated in this chapter.

CHAPTER IV

Measurement of Electromagnetic Radiation from Bacterial Biofilms

4.1 Introduction

All biological organisms are complex systems comprised of a large number of interacting elements. They are constantly interchanging information with each other and with the external environment in order to respond/adapt to various conditions. Chemical signaling has been considered the dominant communication mechanism for biological organization and activities, where messages are carried by ligands transmitted by diffusion [43]. However, this type of signaling typically supports communication in the range of hundreds of nanometers, whereas biological systems interact and manifest a certain degree of order even on a macroscopic scale [44]. Since many biomacromolecules and their derivatives are electrically polarized, any oscillations of these structures can generate electromagnetic (EM) fields. The strong electrical polarity of biological objects suggests EM waves may play a role in intra- and inter-cell signaling. There have been extensive postulations of the existence, nature, and function of EM fields in biological systems. H. Fröhlich first proposed the idea that metabolic activities in biological systems may excite coherent electric vibrations, which enable long-range interactions and energy transfer within the system [45–47].

This theory built the foundation for later studies on EM activities in biological cells. The structure that generates EM waves in biological cells has not been identified yet, but it has been suggested that microtubules in eukaryotic cells are one of the possible sources [48–50]. Microtubules are lattices of oriented dipoles [48]. Theoretical analyses have indicated that the vibrations of microtubules and actin filaments can generate EM fields that mediate the energy transfer with their surroundings. These hypotheses are supported in part by a few experiments [51–53]. In [53], the resonance peaks of a single microtubule were identified in the frequency range of 10–30 MHz and 100–200 MHz. In [51], changes of electric field in the frequency range of 8–9 MHz were detected in the vicinity of the plasma membrane of yeast mitotic cells in the M phase of the cell cycle, which coincides with the period when the kinetochore microtubules in the mitotic spindle bind chromatids. In [52], it was suggested that possible EM activities in microtubules occured when a low-intensity electric field at 100–300 kHz was applied to mitotic cells. However, none of these experiments have directly detected EM radiation from cells. Other structures such as DNA or proteins are also found to be able to generate EM waves. In [54], it was shown that some bacterial DNA sequences can induce EM waves in the kHz range in high aqueous dilutions. In [55], delocalized modes in proteins were identified in the terahertz frequency domain. Nevertheless, these experiments are focused on molecular levels. It is unclear if these EM waves are purposeful signaling or just natural molecular vibrations.

A recent study has indicated that bacterial cells in biofilms may use EM signals to communicate [21]. Biofilms are one of the most ubiquitous forms of biological systems on earth, and are commonly associated with infectious diseases [13]. They are also responsible for contamination of medical devices and implants [16], deterioration of water quality [15], and microbial induced corrosion [16]. Further understanding of the communication mechanisms within biofilm communities is of great importance to effective biofilm control and management.

Biofilms are essentially aggregates of microorganisms in which cells are embedded in a self-produced matrix of extracellular polymeric substances (EPS) [121]. Within the EPS of specific types of biofilms (e.g., *Staphylococcus aureus*, and *Bacillus subtilis*), there are biological elements called amyloid fibrils, which are basically characterized as elastic helical fibers with permanent dipole charges at their ends [18–20]. The study reported in [21] postulates that these charged amyloid fibrils can act as mechanical antennas and may be responsible for purposeful signaling among cells in biofilms. A multi-physics model based on an electromagnetically coupled system of mechanical oscillators was developed to characterize the EM signals generated in *S. aureus* biofilms. The model predicts that possible EM radiation could occur within the kHz–GHz frequency range, depending on the mechanical properties of the cells and the amyloid fibrils. [56] compares EM signaling with quorum sensing. It was demonstrated that EM signaling can provide a substantially higher data rate over a much longer range while requiring far less energy than quorum sensing. Therefore, EM signaling may be the preferred method of communication used by cells in biofilms. However, there is no experimental evidence to support EM communications within biofilms so far.

This work is an experimental study designed to complement the theoretical study reported in [21]. We aim to explore the existence of the predicted EM signals in *S. aureus* biofilms. A wideband near-zone radiative system [122] that can operate from 1-50 GHz is first designed, implemented and characterized. It is shown that the system can detect the change in background emission with a signal level as low as -191 dBm/Hz. The system is used to search for the possible presence of radiation in the frequency spectrum from 1 to 50 GHz. After finding no indication of EM radiation above 20 GHz, we narrowed down the search to the frequency range 3-20 GHz. Notable EM radiation activity in the 3-4 GHz frequency band was observed multiple times on different biofilm samples. In the 3-4 GHz band, we conducted a 70-day longitudinal measurement on a group of 3 identical *S. aureus* biofilm samples using a spiral antenna system. The measurement was performed at a closer range with much finer spectral resolution. Over the course of the measurement, the radiation from all biofilm samples exhibited similar short- and long-term time cycles. The average power density generated by the biofilms was also calculated based on the measured power spectrum. The successful detection of such radiation verifies the theoretical model and represents substantial progress in understanding the mechanisms of EM signaling among cells in biofilms. However, in these measurements, the high sensitivity of the systems was achieved by using ultra low-noise high-gain amplifiers and by averaging a massive amount of data. Since the power radiated by biofilms is extremely weak, the maximum measured signal is only 0.3 dB above the noise. To remedy this issue, a regenerative RF sensing system was proposed. The operation of this system requires knowledge of the signal frequency. Based on the prior results, the system was designed to operate at 3.18 GHz. By utilizing the concept of regeneration, the system can substantially enhance the amplification of the target signal. In addition, the system has the capability of illuminating biofilm samples with external EM sources, which is especially useful for investigating the functionalities of EM signaling among cells. It was shown that the radiation from the illuminated biofilms is stronger than that from the unilluminated ones. These experiments validate the existence of EM radiation in bacterial biofilms. Furthermore, they prove such signaling is related to biological activities rather than thermal emission due to the movement of charges.

This is the first time that GHz EM radiation from bacterial biofilms has been observed and characterized. The successful detection of such radiation verifies the theoretical model and constitutes substantial progress in understanding the mechanisms of EM signaling among cells in biofilms. Correlation studies between EM radiation signals and cell gene expression and biofilm morphology are currently in progress, and will be reported in the future.

This chapter is organized as follows: In Section 4.1.1, the design details of the wideband near-zone radiative system are described. The sensitivity of the system is characterized. In Section 4.1.2, Section 4.1.3 and Section 4.1.4 a series experiments using the wideband near-zone radiative system, the spiral antenna system, and the regenerative RF sensing system are presented, respectively. Section 4.1.5 concludes the chapter.

4.1.1 Wideband Near-Zone Radiative System for Exploring the Existence of Electromagnetic Emission from Biological Cells

4.1.1.1 Issues with Existing Sensors for Detecting EM Radiation from Biological Cells

Prior to this work, no experiments had proved the existence EM signaling between biological cells in the GHz frequency range. The spectrum and the power level of such a signal, if it does exist, are still unknown. Based on the theoretical models developed in [21], the communication may occur somewhere between 1 and 50 GHz, depending on the physical parameters of the cells, and the power level is expected to be on the same order of magnitude as thermal noise. In order to explore the existence of radiation from biological samples, an ultra-wideband system with very high sensitivity is needed to perform the necessary measurements.

Radiative probes have several advantages over non-radiative capacitive probes (such as coaxial probes) which makes them more reliable for sensing the electromagnetic waves emanated by distributed sources. Non-radiative high-impedance probes capture the electromagnetic waves through their very near-field region, which is limited to the very small contact area around the tip of the probe [123]. In addition, the presence of the probe may significantly affect the environment and the field distribution of the sources producing the field. Another drawback of capacitive probes is their small collection area. Moreover, the probe should be in very close proximity of the source and is sensitive to positioning. Finally, on average, half of the power is missed due to polarization mismatch. Different radiative probes such as TEM cells have been proposed to measure radiation from electromagnetic sources or generate uniform electric fields over a wide bandwidth [124–130]. The first TEM cell was introduced by Crawford in 1974 [124]. Since then various shielded and unshielded TEM cells have been reported for different purposes including characterization of radiation from printed circuit boards [125], estimation of electromagnetic emission from electrically large equipment [126, 127], and pulse-exposure studies of biological specimens [128]. The bandwidth of a TEM cell is limited by the cutoff frequency of higher order modes. In [129], by suppressing higher order modes, a TEM cell design with 85% fractional bandwidth operating from 1 GHz to 2.5 GHz is reported. However, for certain applications where the spectrum of the emitted signal is not known, a system capable of detecting signals over a spectral range covering multiple octave bandwidth is required. Moreover, TEM cells only capture a single polarization which makes them deficient for detection of EM signals emanated by a collection of randomly oriented sources.

4.1.1.2 Wideband Radiative Signal Collector

To address these shortcomings, an EM-shielded and resonance-free structure is presented which allows for the capture of electromagnetic emission from a collection of distributed radiators confined in an area of $0.15\lambda_L \times 0.15\lambda_L$ placed inside the structure. This large sample size helps increase the Signal-to-Noise Ratio (SNR) of the received signal. The signal collector is designed to capture two orthogonal polarizations from 1 to 50 GHz.

The wideband dual-polarized signal collector is shown in Figure 4.1. It consists of a quadruple-ridged horn structure, which is backed by absorbers for EM shielding. The quadruple-ridged waveguide structure is chosen to increase the bandwidth towards lower frequencies by reducing the cutoff frequency of the dominant mode [131]. The absorber isolates the sample from possible external interference. Compared with a complete metal shield, terminating the aperture with absorbers does not disturb the input impedance and field distribution of the signal collector, and creates a resonance-free environment. The downside of using absorbers is that for isotropic distributed sources, half of the power is dissipated in the absorber. The structure is probed by two high frequency coaxial lines. The back of the feed section is terminated by an optimized ridged cavity with a linear tapered ridge profile for impedance matching as shown in Figure 4.2. The size and tapering of the ridges and the horn angle are optimized to achieve the maximum bandwidth possible, as well as the desired field distribution. A combination of linear and exponential function is used to improve the impedance match bandwidth [132]. With reference to Figure 4.1, the profile of the ridge curvature is given by:

$$y = (1-m)(a_i + (a_0 - a_i)\frac{z - L_i}{L}) + A(c_1 e^{R(z-L_i)} + c_2) \tag{4.1}$$

where

$$c_1 = \frac{a_0 - a_i}{e^{RL} - 1} \tag{4.2}$$

$$c_2 = \frac{a_i e^{LR} - a_0}{e^{RL} - 1} \tag{4.3}$$

and $m = 0.8, a_i = r/2, a_0 = H/2, L = l_{horn} - L_i$, and $R = 0.03$. A dielectric cone is inserted in the middle to slow down the phase front of the wave in the center of the structure so that a uniform phase distribution over a very wide bandwidth can be established at the base of the cone. The dielectric also assists with maintaining the field to be concentrated at the center all along the horn axis towards its opening where the sample is located. To correct for the phase difference between the waves traveling along the ridge and through the center of the horn, the dielectric constant of the cone can be approximately calculated from

$$\epsilon_r \approx (\frac{l_{ridge}}{l_{horn}})^2 \tag{4.4}$$

The optimized values of the parameters are listed in Table 4.1.

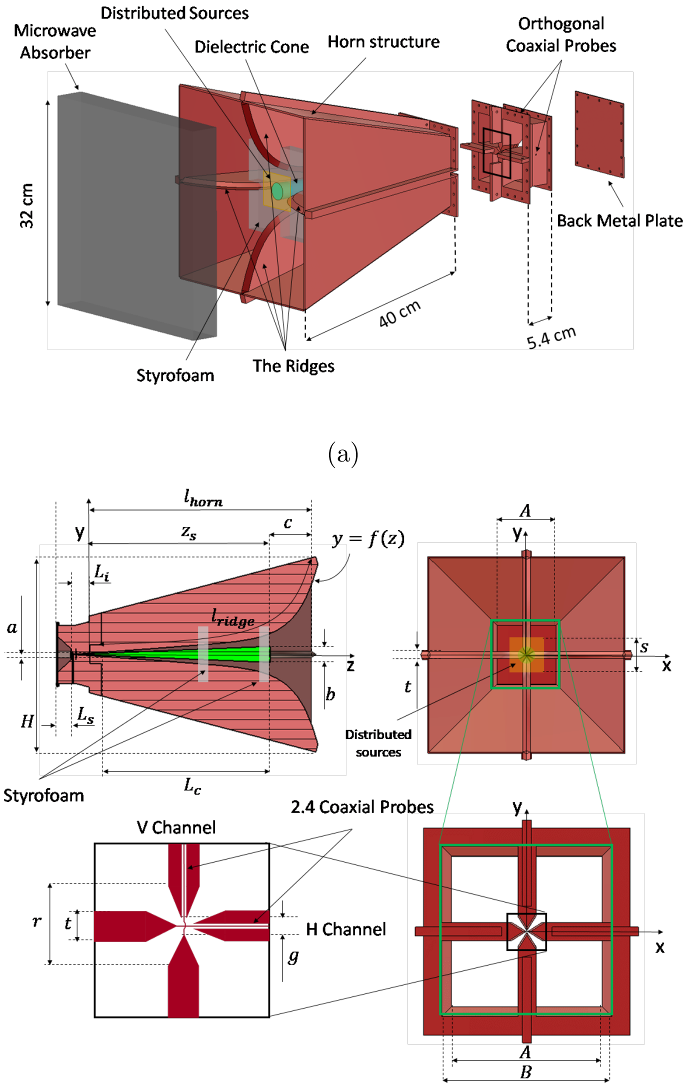

(a)

(b)

Figure 4.1: The wideband dual-polarized signal collector.

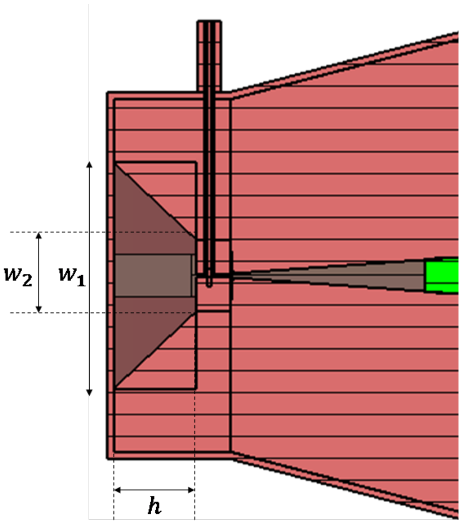

Figure 4.2: The quadruple-ridged cavity of the feed section.

Parameter	Value (mm)	Parameter	Value (mm)
h	320	g	1.1
l_{horn}	420	A	100
c	75	B	113
L_c	280	r	20
a	9.5	s	50
b	29	t	12
L_i	35	L_s	27
z_s	404	w_1	64
h	23.5	w_2	20
l_{ridge}	510		

Table 4.1: Optimized parameters of the signal collector

The horn structure consists of two parts. The top section (the aperture side) is fabricated by accurate CNC Aluminum machining and welding. The lower section (the feed side) is 3D printed out of AlSiMg. These sections are shown in Figure 4.3 (a) and (b) respectively. High frequency 2.4 mm coaxial connectors are used for probing the signal from the collector. To assemble the coaxial probes, two holes are created in the walls of the feed section which extend through the ridges as depicted in Figure 4.2. A brass bolt with an axial through-hole is used to connect the cable to the feed section. The coaxial cable is passed through the hole in the bolt and the outer conductor of the cable is soldered to the bolt. The bolt is then screwed to the waveguide body and the inner conductor of the cable is inserted into a blind hole on the ridge on the opposite side and is fixed in place using silver epoxy. The vertical and horizontal probes are spaced by 1.5 mm along the axis of the structure. The dielectric cone is fabricated from ECCOSTOCK®LoK material with $\epsilon_r = 1.7$ by CNC machining. Two Styrofoam holders are used to keep the dielectric cone in place. The biological sample is placed on the upper Styrofoam at the base of the cone. The fabricated parts and the assembled structure are shown in Figure 4.3.

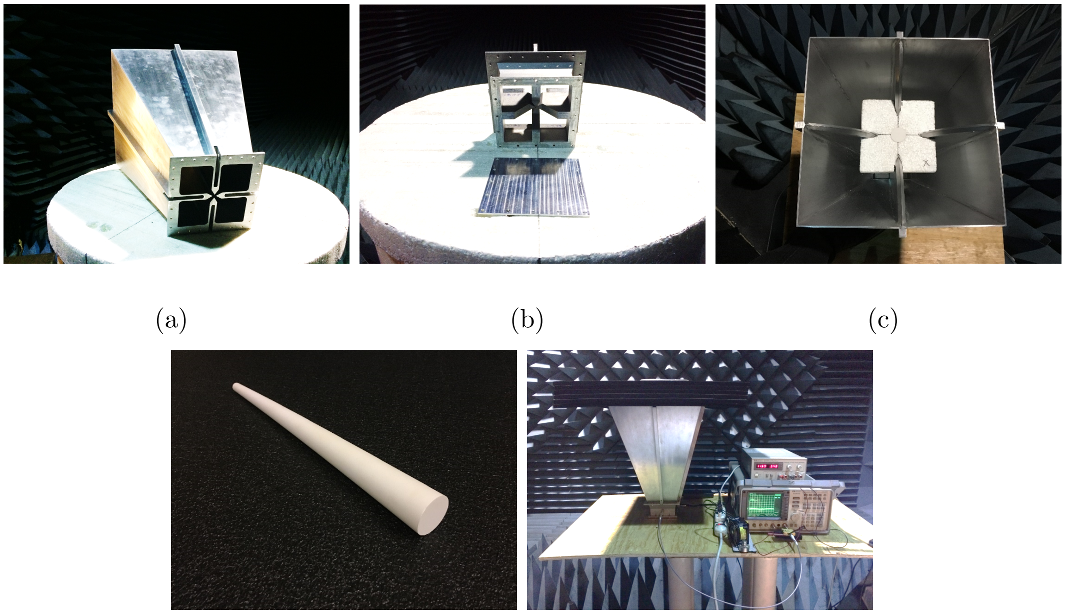

(a) (b) (c)

(d) (e)

Figure 4.3: The fabricated dual-polarized signal collector. (a) the horn structure, (b) the feed section, (c) the ridges inside the horn, (d) the dielectric cone, and (e) the assembled structure.

The simulated S-parameters with and without the dielectric cone are illustrated in Figure 4.4, along with the measurement results. The presence of the dielectric cone does not significantly affect the input impedance of the signal collector. The measured reflection coefficients are less than -6.5 dB over the entire band, which translates to more than 77.6% transmission of the energy from the sample to the system. The simulated field distribution at $z = z_s$ (the base of the dielectric cone) with and without the dielectric cone at different frequencies are presented in Figure 4.5 and Figure 4.6, respectively. Without the dielectric cone, the electric field diverges at the aperture, whereas with the dielectric cone, the electric field is collimated at the base of the cone, where the radiating sample sits, at all frequencies. Below 4 GHz, a spike in the electric field is observed in the E-plane around the tip of the ridge. The size of the focusing area varies from 5 cm × 5 cm at low frequencies to 2 cm × 2 cm at high frequencies. The measured field distribution at $z = z_s$ over an area of 8 cm × 8 cm using a NeoScan field measurement system [107] is plotted in Figure 4.7. The NeoScan probe is an electro-optic field probe with a crystal optic tip attached to an optical fiber. The probe tip is of dimensions 1 cm × 1 cm × 1 cm. The measurement is performed over an area of 80 cm × 80 cm in xy-plane with a resolution of 3 cm in both x and y directions. The measured field distribution validates the simulated ones. It should also be noted that the field concentration near the base of the cone is not very sensitive to the exact location. In fact, the electric fields remain concentrated within a few centimeters away from the base of the cone. This dual-polarized signal collector is used to build a radiometer system for the detection of electromagnetic signaling within biological systems.

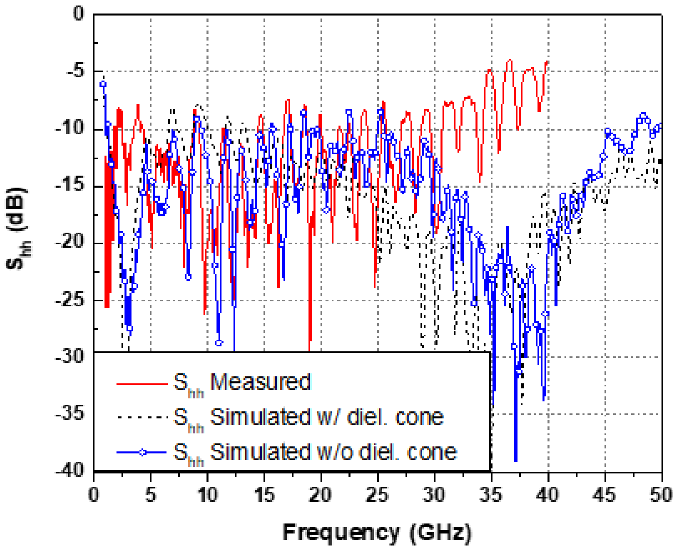

(a)

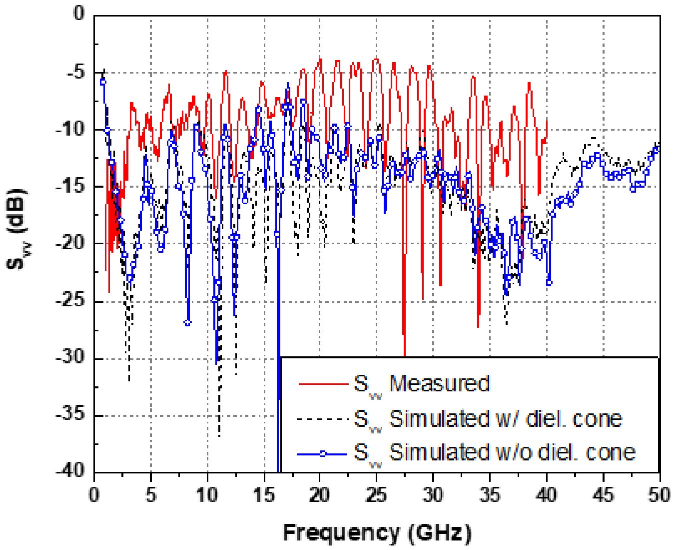

(b)

Figure 4.4: The simulated and measured S-parameters of (a) hh-polarization and (b) vv-polarization of the collector.

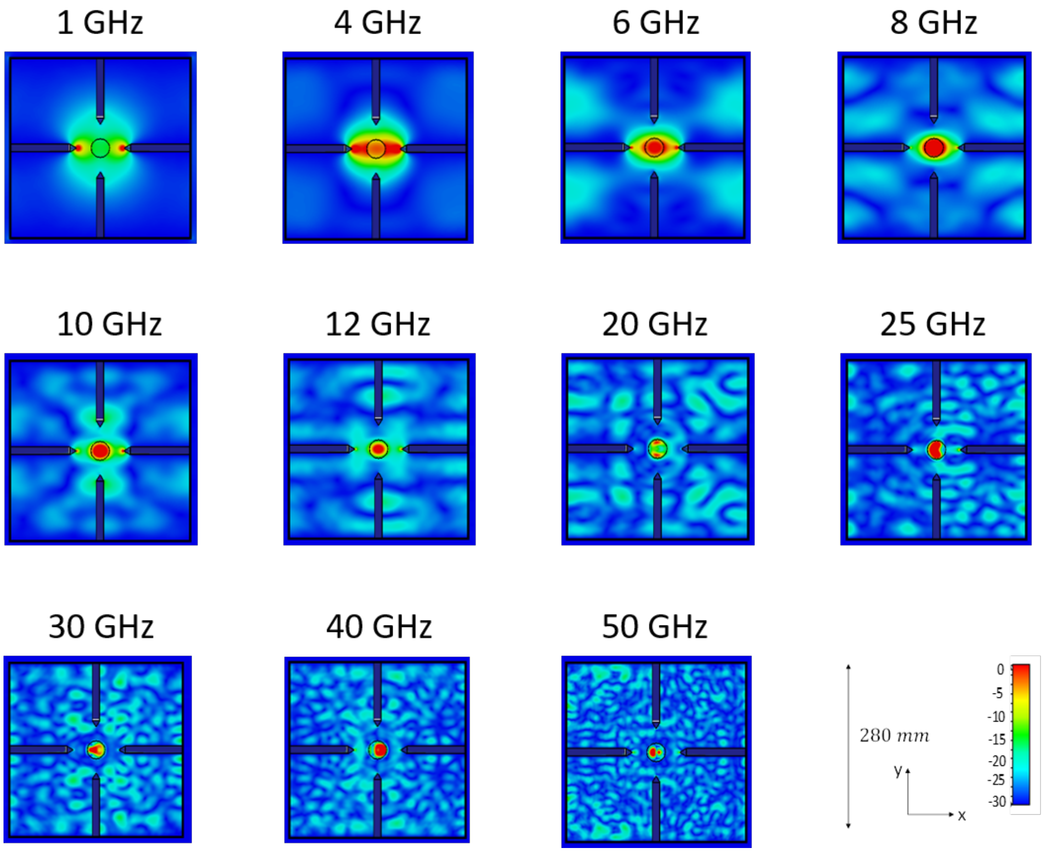

Figure 4.5: Simulated field distribution with the dielectric cone at $z = z_s$ (the base of the dielectric cone) when the x-oriented probe is excited.

4.1.1.3 Wideband Radiometer System

The receiver attached to the signal collector is similar to that of a very broadband Dicke radiometer whose setup is shown in Figure 4.8. The signal from each terminal of the collector is amplified by a broadband low-noise amplifier (RLNA00M50GA from RF-LAMBDA) and is recorded by a spectrum analyzer. Since the measurement can take up to several days, the gain of the amplifier may change over time. In order to eliminate the gain fluctuations of the amplifier, a SPDT switch (Mini-Circuits MSP2T-18XL+) is placed between the signal collector and the input of the amplifier. The other port of the switch is terminated with a 50 Ω matched load which serves as a constant (reference) noise source. The switch alternates between the signal collector and the matched load and the power measured from both cases are recorded. If the

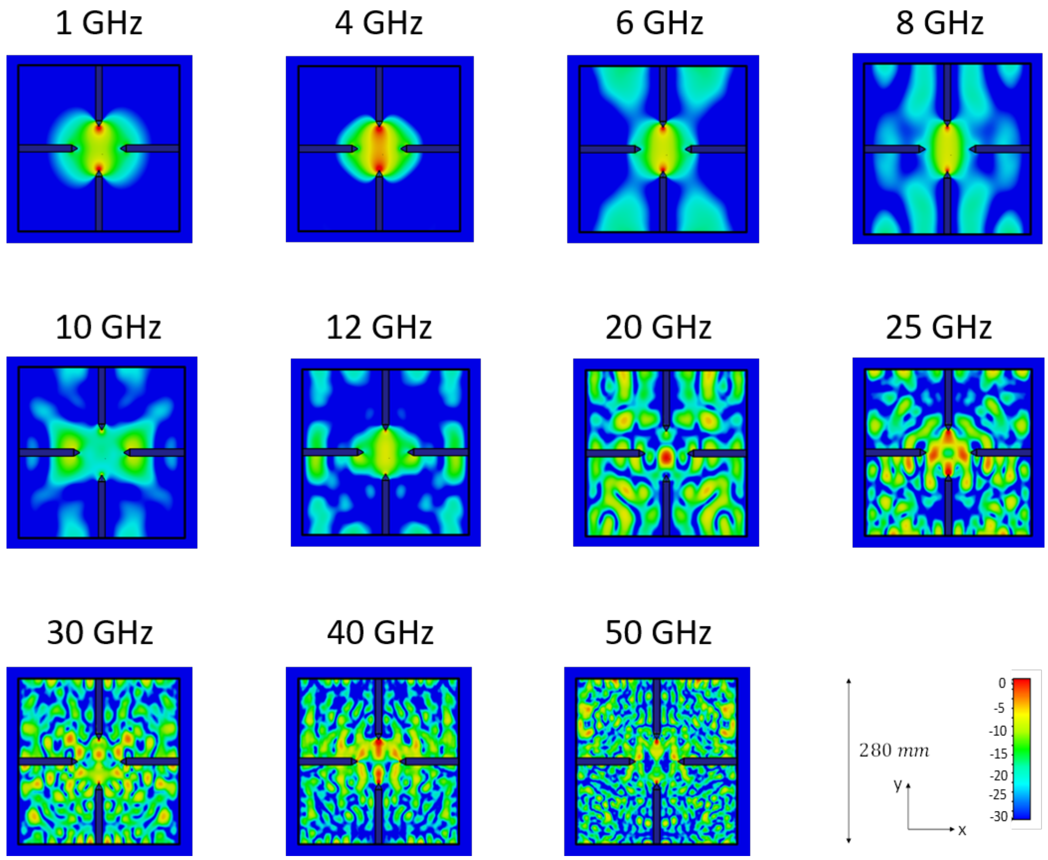

Figure 4.6: Simulated field distribution without the dielectric cone at $z = z_s$ (the base of the dielectric cone) when the x-oriented probe is excited.

sweep time of the spectrum analyzer is short enough (on the order of milliseconds), the gain of the amplifier is assumed constant during two consecutive sweeps. The gain variations of the amplifier can be eliminated by normalizing the power measured from the signal collector to that from the matched load.

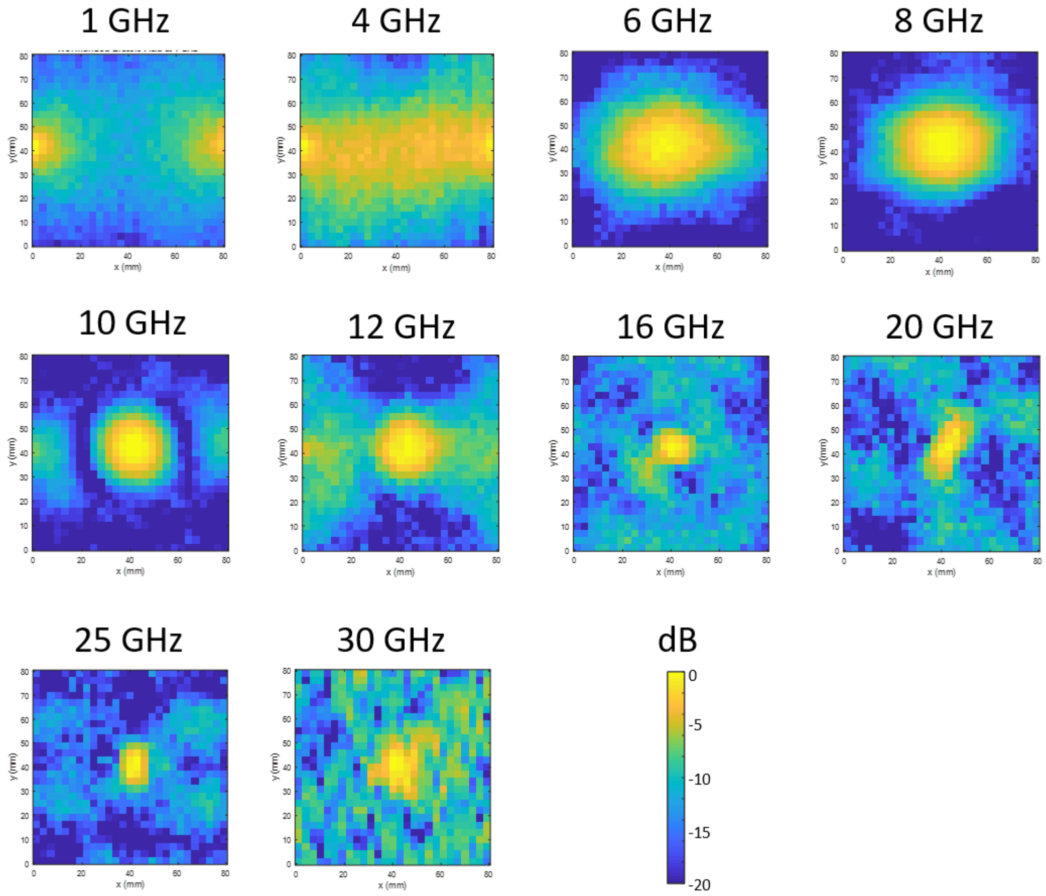

Figure 4.7: The normalized measured field distribution at $z = z_s$ (the base of the dielectric cone) using NeoScan measurement system.

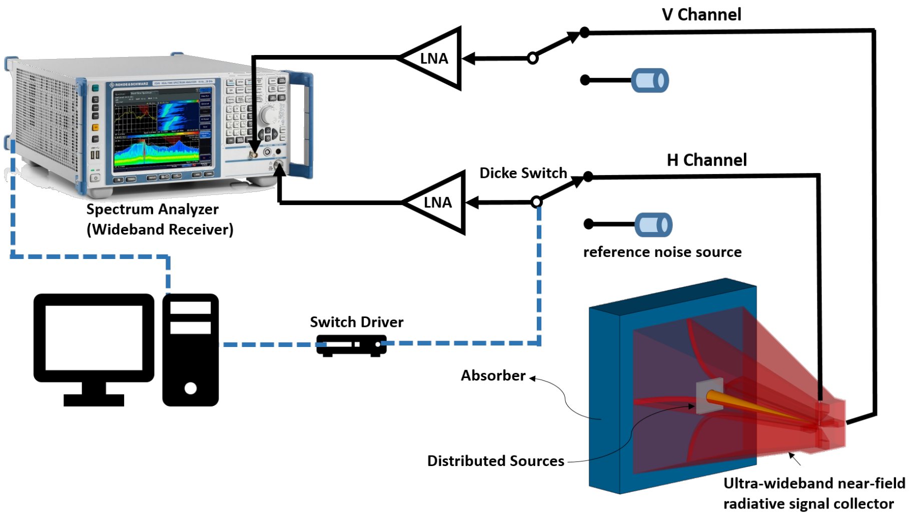

Figure 4.8: The wideband radiometer setup.

The total noise power delivered to the receiver is

$$P_{sys} = k(T_A + T_{rec})BG \tag{4.5}$$

where k is Boltzmann's constant, T_A is the equivalent noise temperature of the signal collector, T_{rec} is the noise temperature of the receiver alone (excluding the signal collector) referred to the input of the collector, B is the bandwidth and G is the total gain of the receiver. The noise temperature of the receiver is related to its noise factor by

$$T_{rec} = (F_{rec} - 1)T_0 \tag{4.6}$$

in which T_0 is the ambient temperature. The overall noise performance of the receiver is significantly affected by its first stage (i.e., the low noise amplifier (LNA) in our case). Figure 4.9 shows the noise figure of the system with one and two LNAs in each receiving path. With two amplifiers, the noise figure is only 2.5 dB at 10 GHz and remains below 7 dB from 1 to 40 GHz.

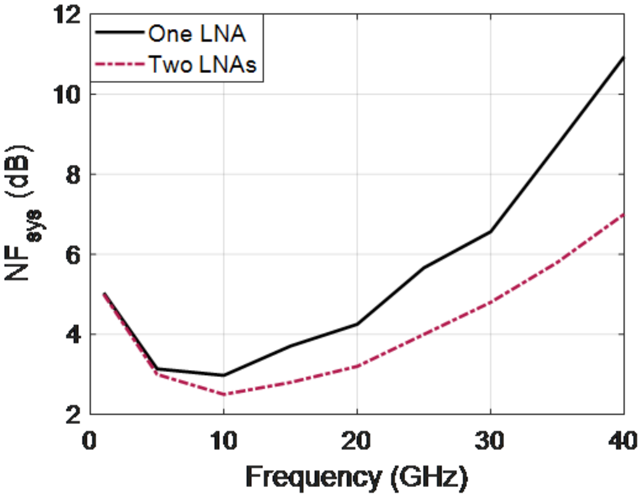

Figure 4.9: The measured noise figure of the system.

The measurement uncertainty (minimum detectable signal) of a superheterodyne receiver of bandwidth B and integration time constant τ is [133]

$$\Delta T = \frac{T_A + T_{rec}}{\sqrt{B\tau}} \tag{4.7}$$

In our case where a spectrum analyzer is used as the receiver, the bandwidth B is the resolution bandwidth (RBW), and the integration time is the reciprocal of the video bandwidth (VBW). Hence (4.7) can be rewritten as

$$\Delta T = \frac{T_A + T_{rec}}{\sqrt{\frac{\mathrm{RBW}}{\mathrm{VBW}}}} \tag{4.8}$$

For the system with RBW = 1 MHz and VBW = 300 Hz, the sensitivity is plotted in Figure 4.10. The minimum detectable signal using one and two LNAs are -180 dBm/Hz and -184 dBm/Hz at 40 GHz respectively, which correspond to the worst-case scenario. It should be noted that the system sensitivity can be improved by using amplifiers with lower noise figure and/or higher gain, reducing the video bandwidth, and/or increasing the resolution bandwidth. Furthermore, averaging N traces can reduce the uncertainty by a factor of $\sqrt{N}$.

The expression for the uncertainty ΔT given by (4.8) does not consider the gain variations of the amplifiers. As described previously, the absolute power measured from the signal collector will be normalized to a reference noise source. Since these two measurements are independent, the uncertainty of the normalized value can be approximated as [134]

$$\Delta R = \sqrt{\left(\frac{T_A + T_{rec}}{T_{ref} + T'_{rec}}\right)^2 \left[\left(\frac{\Delta T}{T_A + T_{rec}}\right)^2 + \left(\frac{\Delta T'}{T_{ref} + T'_{rec}}\right)^2\right]} \tag{4.9}$$

where T'_{rec} and $\delta T'$ are respectively the noise temperature of the receiver and the measurement uncertainty when the switch is connected to the matched load. If $T_A =$

$T_{ref} = T_0$ and $T_{rec} = T'_{rec}$, (4.9) can be simplified to

$$\Delta R = \sqrt{2}\frac{\Delta T}{F_{rec}T_0} = \sqrt{\frac{2\text{VBW}}{\text{RBW}}} \tag{4.10}$$

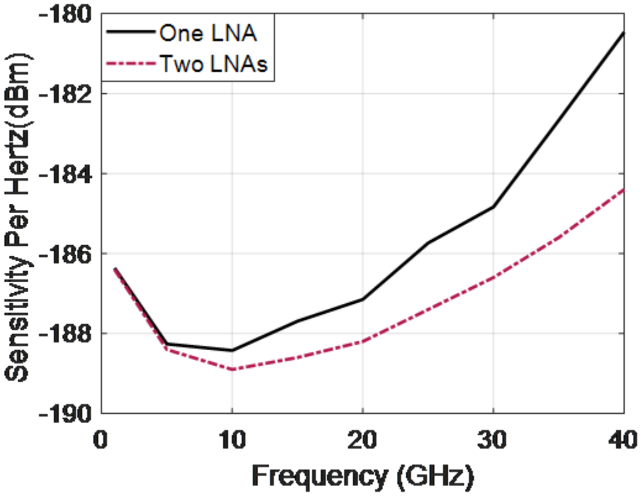

Figure 4.10: The sensitivity of the spectrum analyzer-based radiometer when the RBW is 1 MHz and the VBW is 300 Hz.

4.1.1.4 Measurement of Thermal Radiation from Water

To demonstrate the high sensitivity of the system, it is important to validate its performance using a known radiative source. Therefore, we measured thermal radiation from 30 milliliters of distilled water at multiple different temperatures, and then used it to estimate the sensitivity of our system. Figure 4.11 shows the measurement setup. The water is contained in the same petri dish (Fisherbrand,100mm×100mm, Sterile, Polystyrene) used for growing biological samples. Amplifiers with better noise figure (LNF-LNR6 1223Z 6-20 GHz from LOW NOISE FACTORY) were used in this measurement. The resolution bandwidth and video bandwidth of the spectrum analyzer are 2 MHz and 100 Hz, respectively. We first measured the water at room temperature ($22°C$) as the baseline and then gradually increased the temperature of the water until our system was able to distinguish its thermal radiation from the baseline. The minimum detectable power can be estimated from the temperature difference between the two water samples. The thermal emission measurement exactly mimics the biological sample measurement: the water sample at room temperature is equivalent to the background medium measurement and the increased radiation from the heated water can be considered as the additional emission from the biological samples. Therefore, the minimum detectable power in this setup is the minimum power that the biological samples should generate in order for our system to be able to detect it.

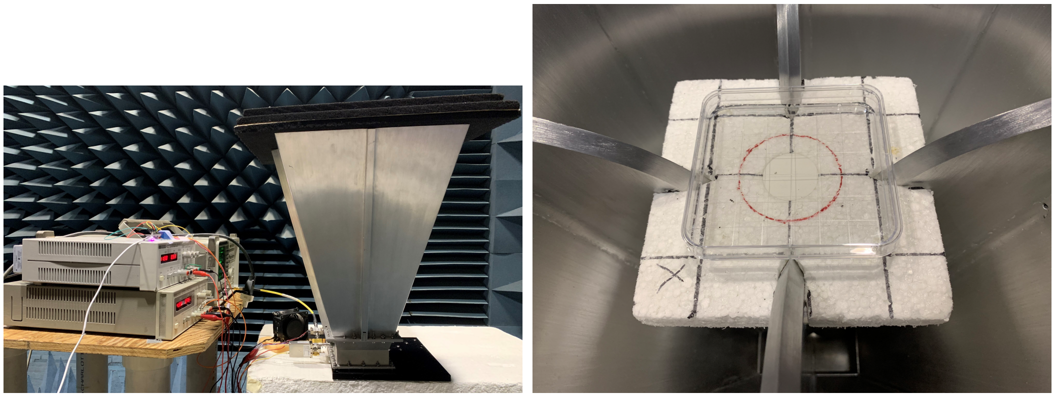

(a) (b)

Figure 4.11: (a) The measurement setup and (b) the water sample.

The brightness temperature of a infinite water layer T_{Bw} of thickness d above half space for p (hh or vv) polarization measured at normal incidence is [135]

$$T_{Bw} = \frac{1-r}{1-r^2e^{-2\kappa_a d}}(1-re^{-2\kappa_a d})T_w + (1-r)(T_w - T_0)e^{\kappa_a d} \qquad (4.11)$$

where T_0 is the ambient temperature, T_w is the physical temperature of the water, κ_a is the absorption coefficient of water, and r is the reflectivity at the boundary between the water and air at normal incidence and is given by

$$r = |\frac{\sqrt{\epsilon_w - 1}}{\epsilon_w + 1}|^2 \tag{4.12}$$

in which ϵ_w is the relative dielectric constant of water at temperature T_w.

The minimum detectable power per hertz for one polarization is approximately

$$P_{\min} = k(T^p_{Bw1} - T^p_{Bw0}) = k\Delta T^p_{Bw} \tag{4.13}$$

For a 3 mm water layer in the frequency range of 5-20 GHz, the minimum detectable physical temperature difference using hh polarization ΔT^h_{Bw} is $13°C$ above the baseline. The calculated minimum detectable power as a function of frequency is plotted in Figure 4.12. It is shown that the system can detect the change in background emission with a signal level as low as -191 dBm/Hz. The measurement is repeated 10 times and the results at 5, 10 and 15 GHz are shown in Figure 4.13. Our system can consistently distinguish the thermal radiation from these two water samples even from a single measurement. If averaging is performed among all the measurements, the sensitivity of the system can be further improved as explained in Section 4.1.1.3.

These results prove that the system is capable of detecting extremely weak electromagnetic radiation and is suitable for the intended applications such as examining the existence of electromagnetic emission from biological samples.

4.1.2 Measurement of EM Radiation from *Staphylococcus aureus* Biofilms Using the Wideband Near-Zone Radiative System

4.1.2.1 Sample Preparation

Methicillin-resistant *S. aureus* substrain USA300 was used in all experiments. A glycerol stock of the strain was maintained at −80°C and was plated on tryptic soy

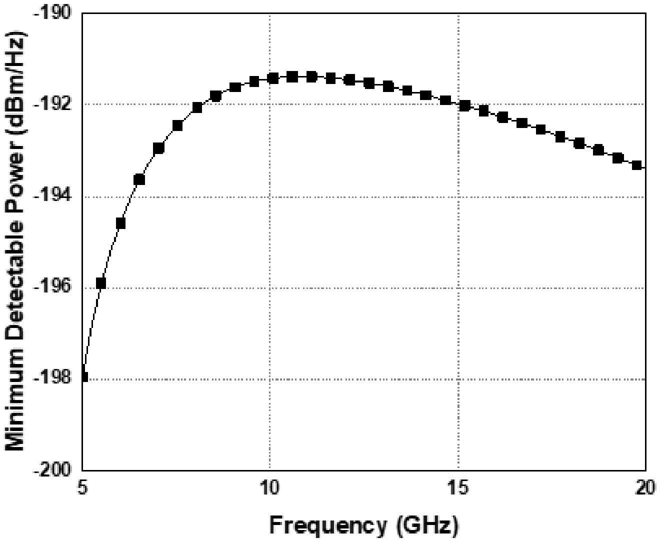

Figure 4.12: Calculated minimum detectable power as a function of frequency.

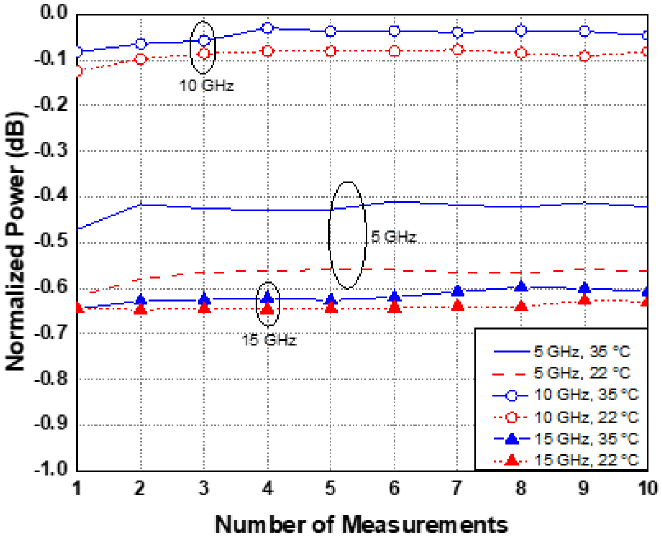

Figure 4.13: Measured normalized power of water samples at 5, 10 and 15 GHz.

agar. Single colony inoculates were grown overnight in peptone-NaCl-glucose media (PNG) under shaking conditions at 37°C. PNG is reported to induce formation of amyloid fibers [136]. Overnight cultures were then diluted 1:10 into fresh PNG and added to a 100 mm× 100 mm polystyrene square petri dish for a final volume of 20 ml and a final concentration of 2 × 105 CFU/ml. These samples were left to grow under static conditions at 37°C to facilitate biofilm formation. On the day of each measurement, the media were carefully removed and replaced with 10 ml fresh PNG media prior to beginning the measurement. Biofilms were maintained in this manner for the entire duration of the experiment. Figure 4.14 (a) and (b) show an 8-day-old and a 28-day-old sample, respectively. A set of three 10 ml fresh PNG media samples, without biofilms, are prepared in the same manner as a control group.

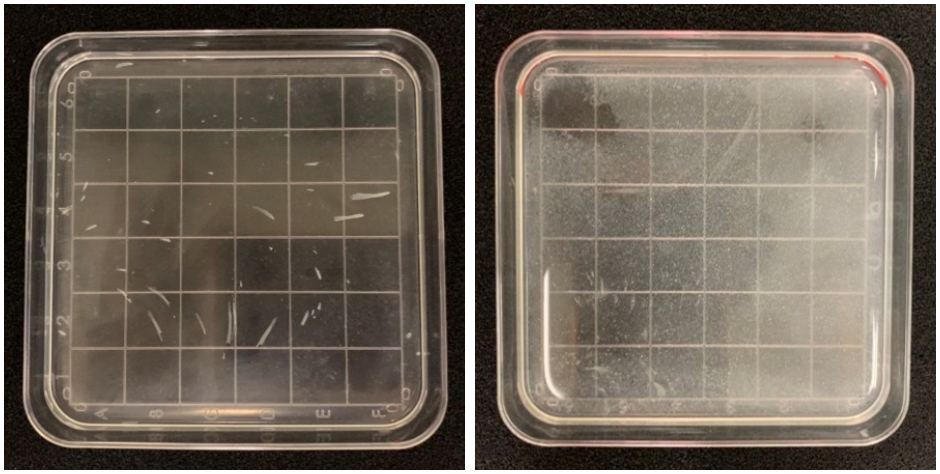

(a) (b)

Figure 4.14: (a) An 8-day-old sample and (b) a 28-day-old sample in a 100 mm × 100 mm polystyrene square petri dish.

4.1.2.2 Measurement Procedure, Data Acquisition and Analysis

The system is controlled by a computer through an automated data collection program. The measurement was first conducted from 1–50 GHz. Since there was no indication of any EM radiation above 20 GHz, we restricted our focus on the

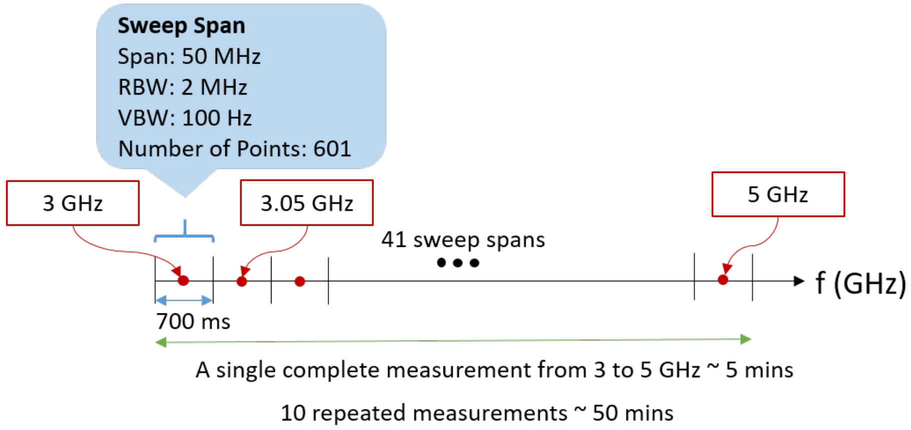

Figure 4.15: The data acquisition process for the 3–5 GHz frequency group. A single complete measurement from 3–5 GHz takes about 5 minutes. 10 repeated measurements take about 50 minutes.

lower portion of the GHz spectrum. To further improve the sensitivity of the system, we replaced the two broadband low-noise amplifiers with an ultra-low-noise amplifier (3-20 GHz) cascaded with a high-gain amplifier (0.8–21 GHz). For measurements from 3-20 GHz, the entire frequency span was partitioned into four frequency groups, specifically 3–5 GHz, 5–10 GHz, 10–15 GHz and 15–20 GHz, which were examined individually. Each frequency group is further divided into small "sweep spans". For each sweep span, the system takes a sweep and records the average value of 601 data points. If the measurements are repeated multiple times, the results are then averaged among all the measurements. Figure 4.15 illustrates the data acquisition process for the 3–5 GHz frequency group. The choices of the sweep span, resolution bandwidth, video bandwidth and the number of repeated measurements directly affect the measurement time and accuracy. We experimented with different settings and carefully evaluated the trade-off between the measurement time and accuracy. The final settings are listed in Table 4.2. For these settings, a single complete measurement from 3-5 GHz takes about 5 minutes. The measurement is repeated 10 times, for a total of 50 minutes. For the other three frequency groups, each takes 125 minutes to complete 10 repeated measurements.

span	50 MHz
Resolution Bandwidth (RBW)	2 MHz
Video Bandwidth (VBW)	100 Hz
Sweep Time	700 ms
Number of Repetitions	10

Table 4.2: Near-zone radiative system spectrum anlzyer settings.

The measurement is first performed on the biofilm samples, and then performed on the fresh PNG samples (control group). The power received from the biofilm sample is compared with that from the PNG sample by taking the ratio of the two measurements

$$R_{\text{sample}} = \frac{P_{\text{sample}}}{P_{\text{PNG}}} \tag{4.14}$$

A baseline is established by taking the ratio of two PNG measurements

$$R_{\text{baseline}} = \frac{P_{\text{PNG,2}}}{P_{\text{PNG,1}}} \tag{4.15}$$

The fluctuations between two PNG measurements (baseline) are less than ± 0.05 dB within the entire frequency range, indicating that any frequencies where $R_{\text{sample}} > 0.05$ dB are considered possible "communication bands". Figure 4.16 (a) and (b) show the results obtained from a 43-day-old sample and a 20-day-old biofilm sample, respectively, using the settings listed in Table 4.2. The power received from the biofilm sample is notably higher than that from the PNG sample in the 3–4 GHz frequency band, whereas no significant differences between the sample and the control are measured at other frequencies. It should be noted that the measurement was repeated 3-4 times every day from June 2019 to December 2019, and was performed on a large number of samples of different ages. Similar frequency responses were observed repeatedly.

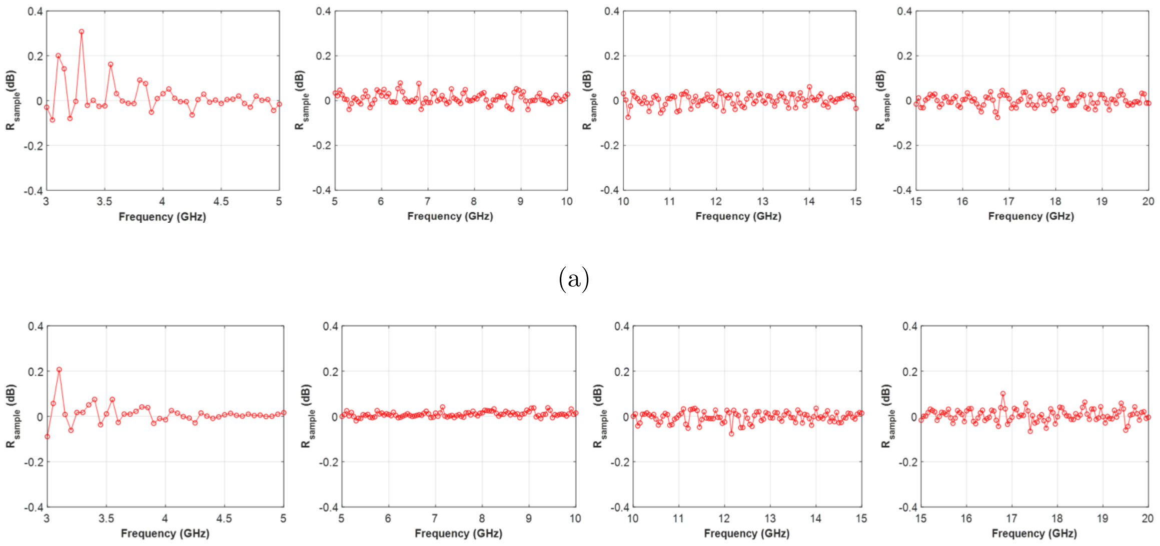

(a)

(b)

Figure 4.16: Measurement results from (a) a 43-day-old biofilm sample. Sample birth date: September 17th, 2019. Measurement date: October 30th, 2019, and from (b) a 20-day-old biofilm sample. Sample birth date: October 18th, 2019. Measurement date: November 7th, 2019.

4.1.2.3 ZnO-NPY Exposure Experiments on Biofilm Samples

The validity of a biological source of the radiation in the 3-4 GHz range was examined by exposing biofilms samples to ZnO nanopyramids (ZnO-NPY). ZnO nanopyramids with hexagonal base (ZnO-NPYs) are synthesized nanoparticles that have been characterized extensively [137–139]. It has been previously demonstrated that ZnO-NPYs have strong antibacterial effects on *S. aureus*. They disrupt cell membranes and metabolism without destroying the structure of the biofilms. For the ZnO-NPY exposure experiment, dry ZnO-NPY powder was measured and reconstituted into PNG media and sonicated for 5 minutes to ensure dispersion. Concentrations of ZnO-NPYs were made at 500 µg/ml to ensure lethality [138]. We first measured the biofilm sample following the procedure described in Section 4.1.2.2, then we added

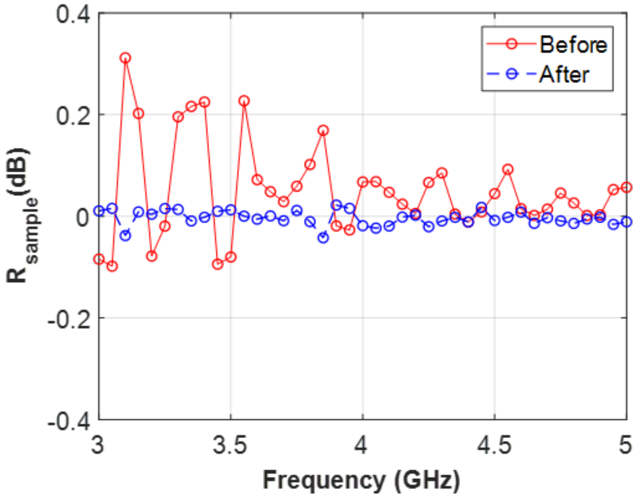

Figure 4.17: Frequency responses of a 30-day-old biofilm sample before and after the ZnO-NPY treatment. Sample birth date: November 12, 2019. Measurement date: December 4, 2019.

10 ml ZnO-NPY to both the biofilm sample and the PNG control sample, and took the measurement again. Figure 4.17 shows the frequency responses of a 30-day-old biofilm sample before and after the ZnO-NPY treatment. As observed previously, the biofilm sample exhibits strong radiation in the 3-4 GHz band in its natural state. After the ZnO-NPY treatment, the frequency response becomes relatively flat over the band of interest, indicating that the signal is indeed generated by the metabolic activities of the living constituent cells rather than by thermal emission of the biofilm material.

4.1.3 Monitoring Signal Timescales Using the Spiral Antenna System

The previous experiments prove the existence of EM radiation from living *S. aureus* biofilms. However, they do not provide further information about the biological functions of such a signal. Knowing the timescales of the signal can help relate EM radiation to key biological activities; hence, a rigorously controlled 70-day longitudinal experiment was conducted to monitor the signal intensity of 3 identical biofilm samples. Based on prior results, we now only focus on the 3–3.6 GHz frequency range.

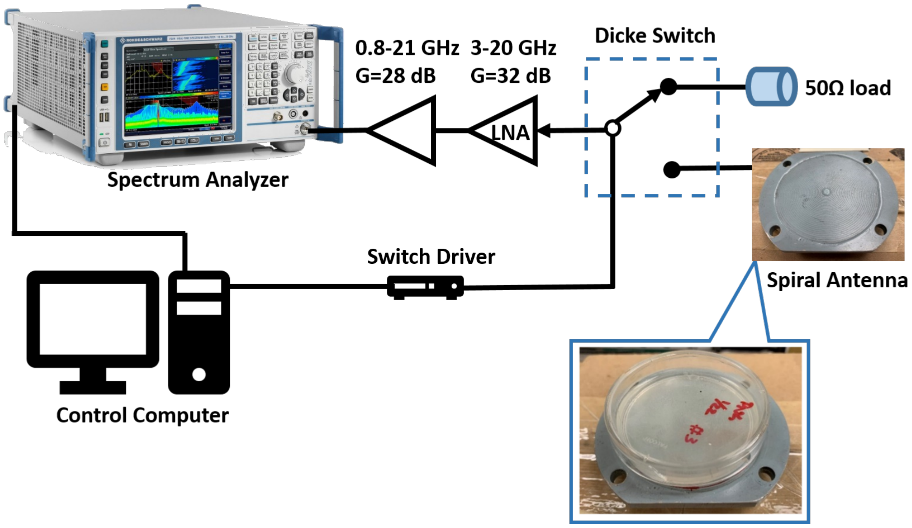

Figure 4.18: The spiral antenna system diagram with a close-up view of a biofilm sample on the spiral antenna.

A spiral antenna system operating from 2–8 GHz with a short far-field distance is chosen for this experiment. The new system is a slightly modified version of the wideband near-zone radiative system, in which the signal collector is replaced with a spiral antenna. Figure 4.18 shows the system diagram. The preparation of biofilm samples follows the same procedure described in Section 4.1.2.1. For the new system, the culture was diluted 1:10 into PNG and inoculated into a circular polystyrene petri dish with a diameter of 60 mm for a total final volume of 10 ml and a final concentration of 2×105 CFU/ml. The size of the petri dish is chosen such that the biofilms can cover the entire aperture of the spiral antenna. During the measurement, the petri dish is directly placed on top of the spiral antenna as shown in the close-up view in Figure 4.18.

Span	20 MHz
Resolution Bandwidth (RBW)	2 MHz
Video Bandwidth (VBW)	100 Hz
Sweep Time	500 ms
Number of Repetitions	10

Table 4.3: Spectrum analyzer settings for the spiral antenna system.

For data acquisition, a smaller span is chosen to achieve a shorter sweep time. The spectrum analyzer settings are listed in Table 4.3. The new system features less propagation path-loss and higher sensitivity. The fluctuations of the baseline are less than ±0.03 dB.

We grew 3 biofilm samples on July 13, 2020, and the measurements were conducted from July 15, 2020 (Day 2) through September 21, 2020 (Day 70). The measurements were started at the same time on each day to eliminate the possibility of signal fluctuation throughout the day. We aimed to take measurements on each sample every day (excluding weekends), however, due to the limited availability of the anechoic chamber, on some days, we could only measure one or two samples. Figures 4.19–4.23 show the frequency responses of the three samples over the course of the experiment. The red and black lines represent R_{sample} and R_{baseline} as given by (4.14) and (4.15), respectively. Photos of sample 3 on Day 7 (July 20^{th}) and Day 30 (August 12^{th}) are presented in Figure 4.24.

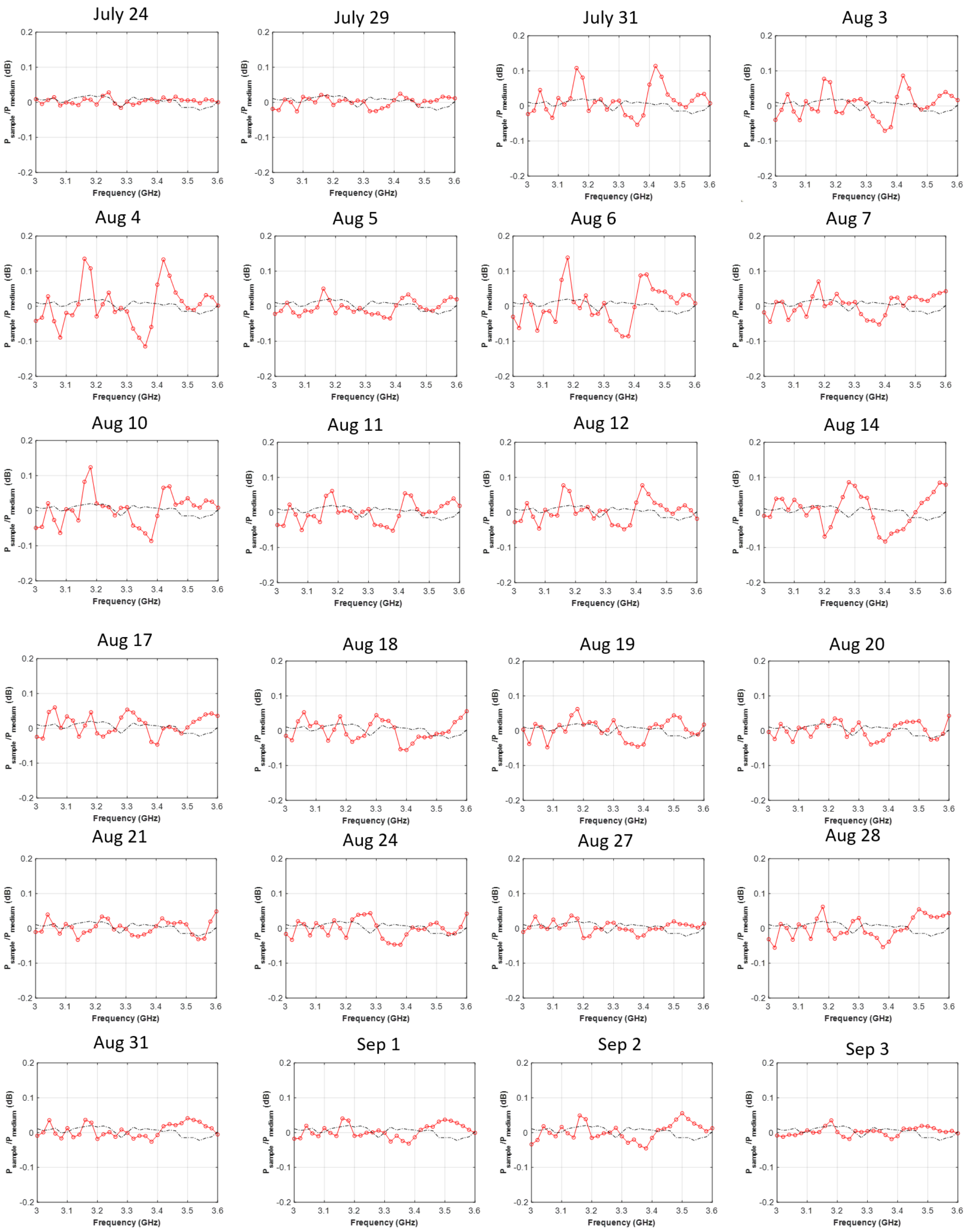
July 24
July 29
July 31
Aug 3
Aug 4
Aug 5
Aug 6
Aug 7
Aug 10
Aug 11
Aug 12
Aug 14
Aug 17
Aug 18
Aug 19
Aug 20
Aug 21
Aug 24
Aug 27
Aug 28
Aug 31
Sep 1
Sep 2
Sep 3

Figure 4.19: Frequency responses of Sample 1.

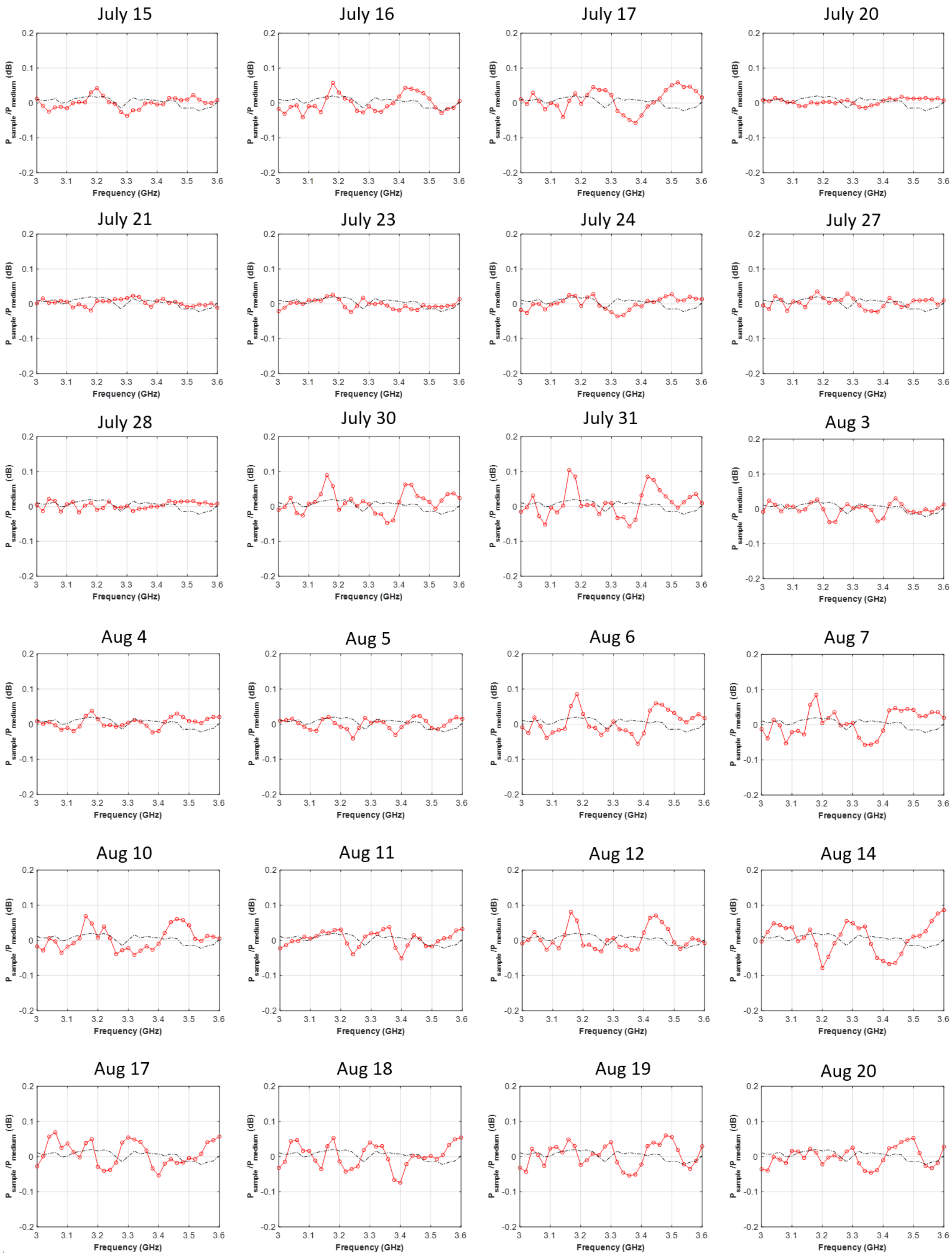

Figure 4.20: Frequency responses of Sample 2.

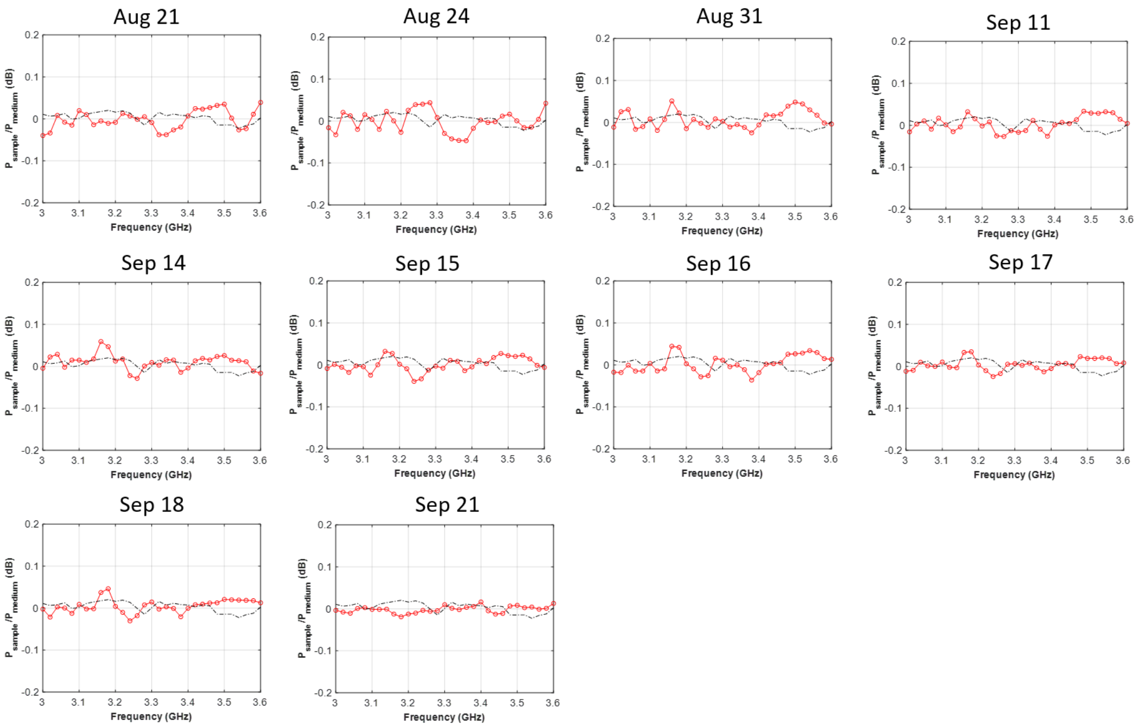

Figure 4.21: Frequency responses of Sample 2 (cont'd).

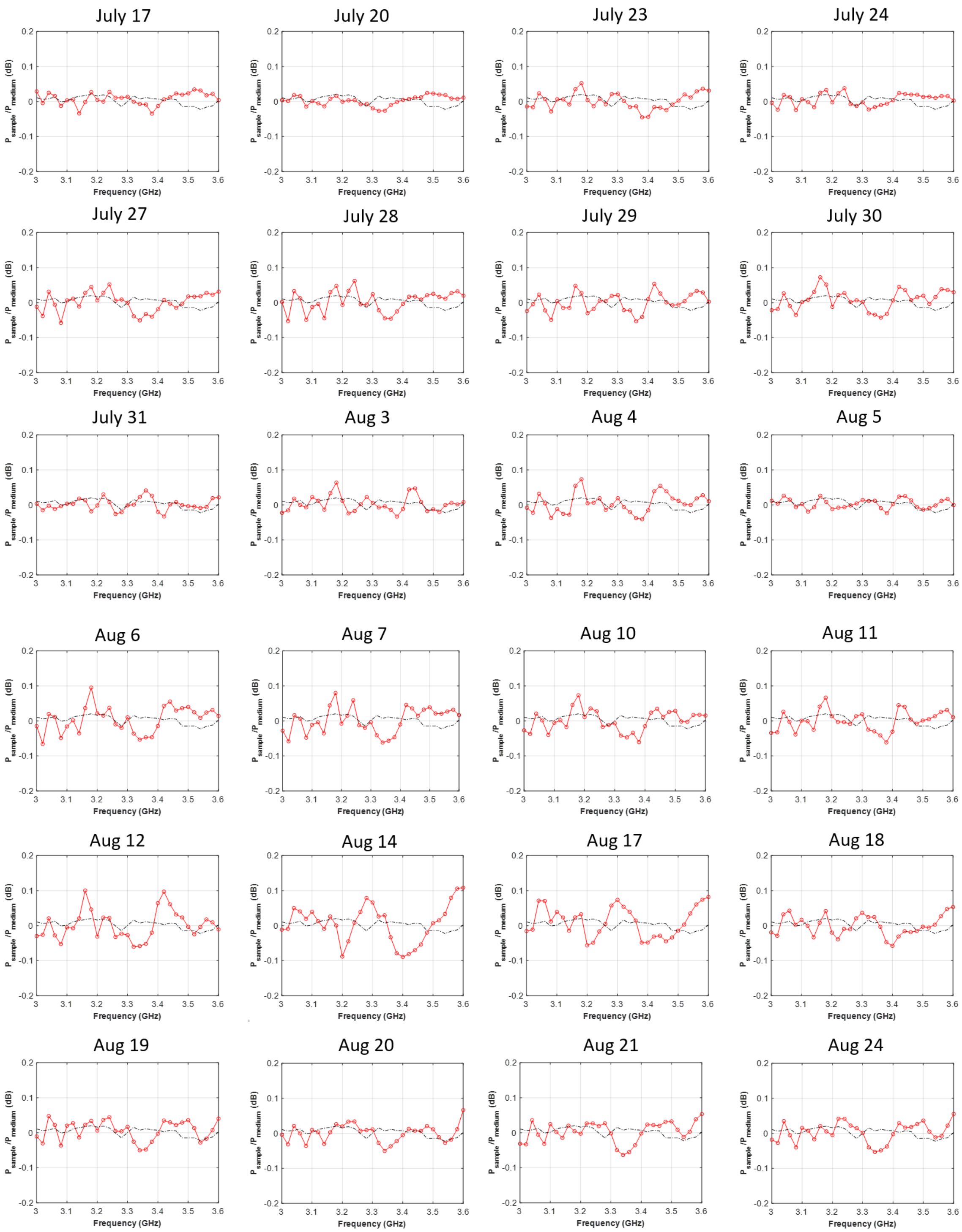

Figure 4.22: Frequency responses of Sample 3.

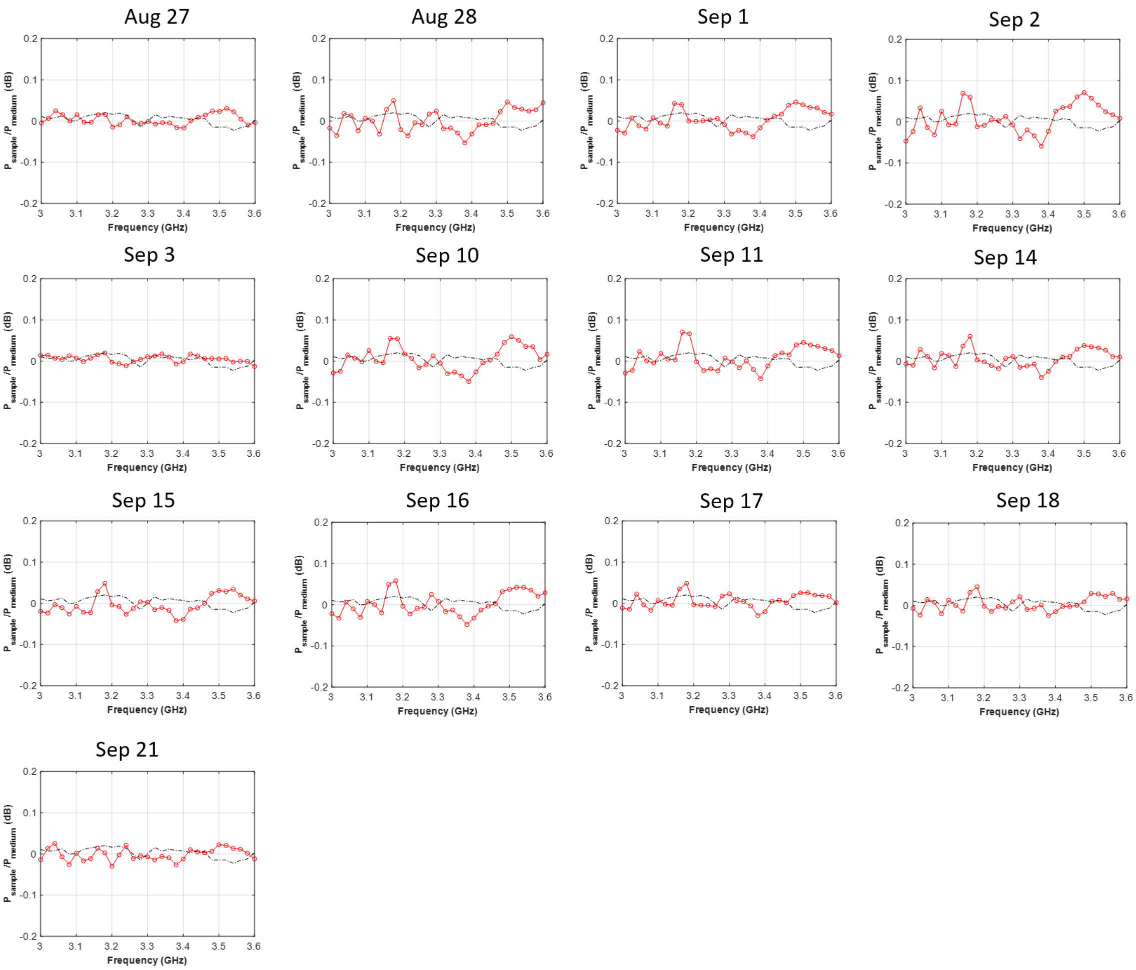

Figure 4.23: Frequency responses of Sample 3 (cont'd).

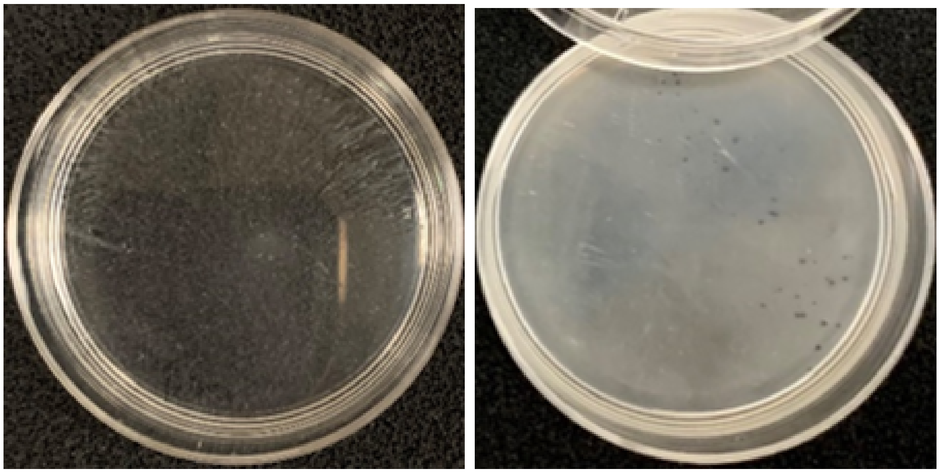

(a) (b)

Figure 4.24: Sample 3 on Day 7 (July 20^{th}) and Day 30 (August 12^{th}).

Two distinct communication bands are identified, which are the 3.15–3.2 GHz band and the 3.4–3.5 GHz band. The frequency responses of these biofilm samples are comparable to those observed using the wideband near-zone radiative system. The slight frequency shift could have resulted from the variations in the shape and size of the biofilm constituents. The smaller petri dish concentrates the inoculum over a smaller area, accelerating the initial biofilm forming process and may change the ultimate structure. Based on the multi-physics model [21], the frequency of the radiation directly depends on the dimensions of the cells and the amyloid fibrils. Moreover, since there is less total biomass in a small petri dish, the maximum amplitude of the signal is expected to be smaller than that measured from a large petri dish. Fig.4.25 (a) and (b) show the power spectrum of the biofilm sample and the PNG, in the 3.15–3.2 GHz band and the 3.4–3.5 GHz band, respectively. The results were obtained from the measurements conducted on August 12^{th}, when the strongest radiation was observed.

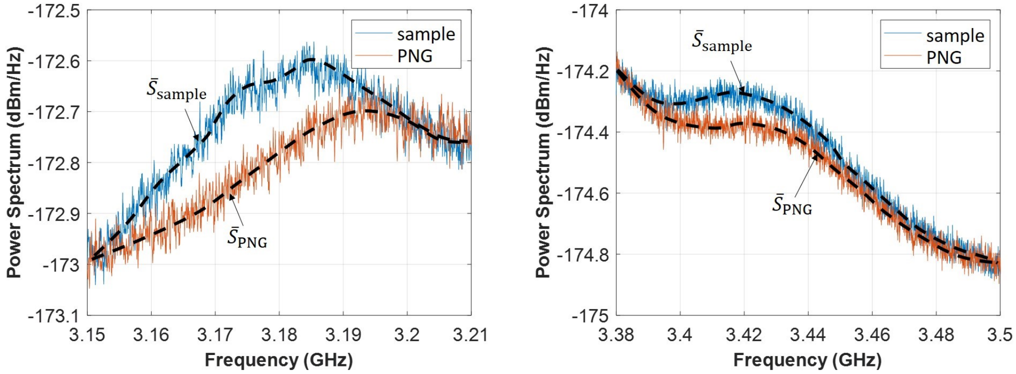

(a) (b)

Figure 4.25: Power spectrum of the biofilm sample and PNG in the (a) 3.15-3.2 GHz and (b) 3.4-3.5 GHz bands.

At first glance, the measured PSD of the biofilm sample is only about 0.2 dB above the measured PSD of the background noise. This difference may seem too small to claim signal detection. However, the following analysis clearly demonstrates that the 0.2 dB difference is actually a very large dynamic range and is strong evidence of the existence of EM radiation from biofilms.

First, it should be emphasized that Figure 4.25 is just a sample of many measurements that we have taken. Our detection criteria are based on the average (mean) values of the measured PSDs of the biofilm samples (S_{sample}) and background noise (S_{PNG}).

The PSD of the background noise S_{PNG} is a Gaussian process with a probability density function [133]

$$f(S_{\text{PNG}}) = \frac{1}{\Delta S\sqrt{2\pi}} e^{-\frac{1}{2}(\frac{S_{\text{PNG}} - \bar{S}_{\text{PNG}}}{\Delta S})} \tag{4.16}$$

where $\bar{S}_{\text{PNG}}$ is the average noise PSD and ΔS is the standard deviation (also known as measurement uncertainty). The measured PSD with 95% confidence is within

$$S_{\text{PNG}} = \bar{S}_{\text{PNG}} \pm 1.96\Delta S \tag{4.17}$$

The measurement accuracy is dictated by ΔS, which is related to the resolution bandwidth (RBW) and video bandwidth (VBW) of the spectrum analyzer, and the number of repeated measurements (N) used in estimating the average PSD [122]

$$\Delta S = \frac{\bar{S}_{\text{PNG}}}{\sqrt{N\frac{\text{RBW}}{\text{VBW}}}} \tag{4.18}$$

(4.18) indicates that we can reduce the uncertainty of the measurement by increasing the ratio between RBW and VBW, and by averaging over many repeated measurements. In our case, RBW = 2 MHz, VBW = 100 Hz and $N = 10$.

Referring to Figure 4.25 (a) as an example, for average background noise of $\bar{S}_{\text{PNG}} = -172.8$ dBm/Hz (5.2481×10^{-18} mW/Hz), the standard deviation of the measured noise PSD is

$$\Delta S = \frac{5.2481 \times 10^{-18}}{\sqrt{10 \times \frac{2\times10^{6}}{100}}} = 1.1735 \times 10^{-20}\text{mW/Hz} \tag{4.19}$$

The 95% confidence interval of the measured background noise is ($5.2481 \times 10^{-18} \pm 2.3001 \times 10^{-20}$) mW/Hz or ($-172.8 \pm 0.019$) dBm/Hz in logarithmic scale. The estimated mean value of the signal measured from the biofilm sample is -172.65 dBm/Hz (5.4325×10^{-18} mW/Hz); therefore, the average PSD generated by the biofilms is

$$S_{\text{bio}} = S_{\text{sample}} - S_{\text{PNG}} = 1.8443 \times 10^{-19}\text{mW/Hz} \tag{4.20}$$

This is 15.7 standard deviations away from the mean value of the noise. In signal detection, the probability of false detection for a given threshold T (i.e., when noise exceeds the threshold T) is given by [140]

$$P_r(S \geq) = \int_{T}^{\infty} f(S)dS = \frac{1}{2}[1 - \mathrm{erf}(\frac{T - \bar{S}}{\Delta S\sqrt{2}})] \tag{4.21}$$

in which $f(S)$ is the probability density function of the background noise given by (4.16) and $\mathrm{erf}(\cdot)$ is the error function. Table 4.4 lists the probability of false detection for different threshold values. Typically, the detection threshold is set to 2–3 standard deviations away from the mean value of the noise. For a signal that is more than 15 standard deviations away from the mean value of the background noise, the chance of it being noise is almost zero. Therefore, it is unquestionable that the measured signals are radiation generated by the biofilms.

n	1	2	3	15
P(false detection) %	15.8655	2.2750	0.1350	3.6710×10^{-49}

Table 4.4: Probability of false detection for different threshold values ($T = \bar{S} + n\Delta S$)

Based on the power spectrum, we can estimate the maximum total radiated power from the biofilms using

$$P = \int_{f_1}^{f_2} (S_{\mathrm{sample}-S_{\mathrm{PNG}}})df \tag{4.22}$$

where f_1 and f_2 are the lower and higher ends of the spectrum where the sample line is above the PNG line. The power density generated by the biofilms can be estimated from

$$P_v = \frac{P}{\pi r^2 t} \tag{4.23}$$

where $r = 30$ mm is the radius of the petri dish and t is the thickness of the biofilms. The thickness of the biofilms used in the experiments is in the range of $2 - 5$ μm. We use the average thickness $t = 3.5$ μm in the calculations. Table 4.5 summarizes the key parameters of the observed radiation.

	3.15-3.2 GHz band	3.4-3.5 GHz band
f_1	3.15	3.193
f_2	3.405	3.459
P	-112.5 dBm	-114.5 dBm
P_v	-122.5 dBm/mm^2	-124.5 dBm/mm^2

Table 4.5: Key parameters of the radiated signal.

The series of frequency responses shown in Figures 4.19–4.23 present the detailed frequency spectrum of the biofilm samples on each day. However, it is difficult to evaluate how the signal evolves over time based on the individual frequency responses. To quantitatively describe the radiation intensity in the entire frequency band and demonstrate the variation of the signal over time, a parameter Δ defined by

$$\Delta = \sum_{i=1}^{n} |R_{\text{sample}}(i)| - \sum_{i=1}^{n} |R_{\text{baseline}}(i)| \tag{4.24}$$

is introduced, where n is the number data points in the frequency response plot. Figure 4.26 shows Δ for each sample over the 70-day timescale. The radiation from Samples 2 and 3 exhibits similar long-term patterns: the radiation intensity increases gradually and reaches a maximum around day 32. After that, the radiation intensity gradually decreases. Sample 1 also exhibits significant radiation on day 32, but has two other radiation peaks on day 22 and day 24. In addition to the long-term pattern, several short-term fluctuations ranging from 1–5 days are also observed. The significance of these timeframes is still under investigation. One way to explain this behavior is by noting the presence of multiple harmonics with respect to the biofilm life cycles which depend on nutrients, temperature, strain, etc [141]. This phenomenon is quite similar to the dynamics of quorum sensing in biofilms [142–144].

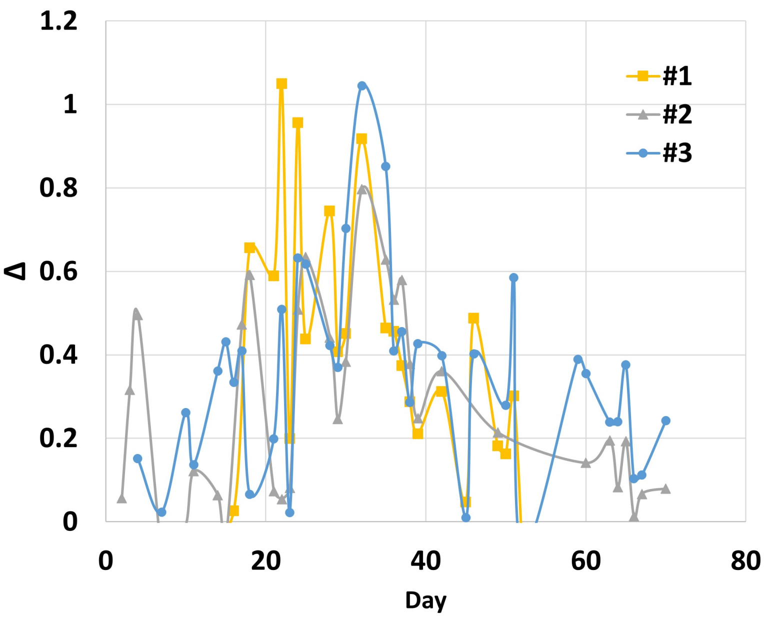

Figure 4.26: The radiation strength (Δ) of the four biofilm samples from Day 3 to Day 70.

ZnO-NPY exposure experiments are also performed using the spiral antenna system. Figure 4.27 shows the response of a 42-day-old sample.

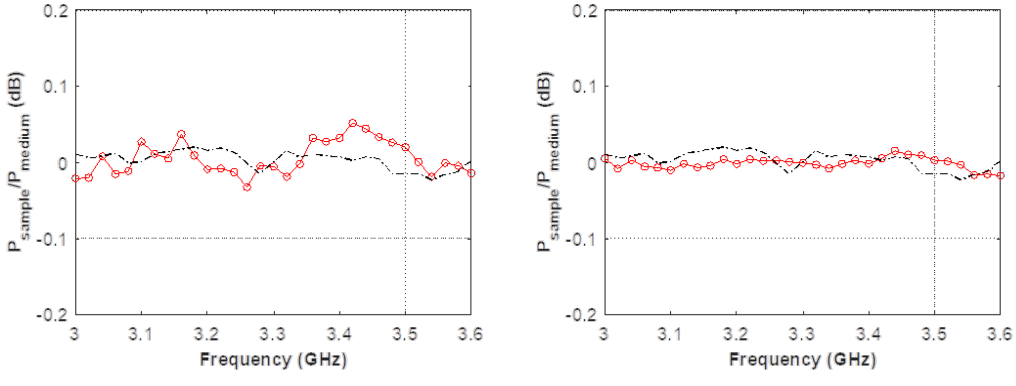

(a) (b)

Figure 4.27: Frequency response of a 42-day-old sample (a) before and (b) after the ZnO-NPY treatment. Sample birth date: January 22, 2020. Measurement date: March 5, 2020.

4.1.4 Observing Electromagnetic Activities in *S. aureus* Biofilms Using a Regenerative RF Sensing System

The previous measurements proved the existence of EM radiation from *S. aureus* biofilms. However, since the radiated power from biofilms is extremely weak, the maximum measured signal is only 0.3 dB above the noise.

In this section, a regenerative RF sensing system with enhanced amplification capability is designed and used to further examine EM radiation from *S. aureus* biofilms. The design concept and practical implementation are first introduced, and then, the measurements on biofilm samples are presented. In addition, an algorithm is developed to clearly demonstrate the change of the signal over time under different conditions.

4.1.4.1 Regenerative Sensing System Design Concept

Regeneration, also known as positive feedback, is a process in which the output of a system is applied back to its input so as to reinforce the response. This concept has been extensively studied and implemented in electronics for signal amplification. Before we proceed further, it should be noted that even though it originated from the same concept, our system is different from the super-regenerative circuits widely used in short-distance wireless communication receivers, which are based on repeated build-up and decay of self-oscillations in an oscillator [145–147]. Figure 4.28 shows a general positive feedback system. The output signal $V_o(f)$ is related to its input by

$$V_o(f) = \frac{G(f)}{1 - G(f)\beta(f)} V_i(f) \tag{4.25}$$

where $G(f)$ is the open loop gain and $G(f)/[1 - G(f)\beta(f)]$ is the total gain of the system with the feedback network $\beta(f)$. The condition for enhanced amplification using positive feedback at frequency f_0 is

$$|1 - G(f_0)\beta(f_0)| < 1 \tag{4.26}$$

which can be achieved by adjusting the amplitude and phase of the feedback network $\beta(f)$ at the desired frequency. Since the amplification decreases drastically as the frequency deviates from f_0, the frequency of the input signal must be known beforehand.

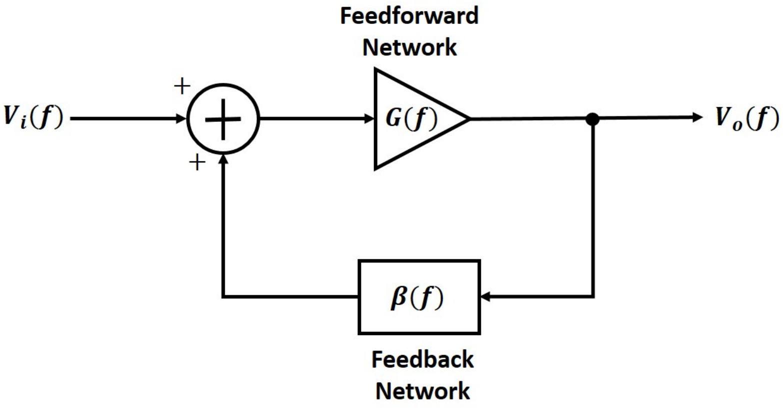

Figure 4.28: A general positive feedback system.

4.1.4.2 System Implementation

Based on the previous measurement results, the system is designed at 3.18 GHz. The block diagram of the proposed regenerative sensing system is illustrated in Figure 4.29. Two identical antennas are arranged facing each other and the *S. aureus* biofilm sample is placed in between. The radiation from the biofilms is received by Antenna 1 and is fed into a low-noise amplifier. The output of the amplifier is monitored and recorded by a spectrum analyzer through the first directional coupler. The signal travels along the entire loop and is fed back to the input by Antenna 2. The amplitude and phase of the feedback network is controlled by a tunable attenuator and a phase shifter, respectively. These two components collectively determine the total gain of the system, which is critical for a successful measurement. If the total gain is too low, the system is unable to detect the extremely weak signal; if the combination of the phase and amplitude is set too close to the oscillation conditions

$$\begin{aligned} &|G(f_0)\beta(f_0)| = 1 \\ &\angle G(f_0)\beta(f_0) = 2\pi n, n = 0, 1, ... \end{aligned} \tag{4.27}$$

the system becomes very sensitive to noise and can easily go into self-oscillation. The band-pass filter dictates the bandwidth of the system, and prevents out-of-band interference. A signal generator is attached to the loop through the second directional coupler. The signal generator serves two purposes: (a) during measurements, it injects a stable sinusoidal signal into the loop, which is used as a reference to calibrate the loop gain; and (b) in the illuminating experiment, it provides an external EM signal at the desired frequency to illuminate the bacterial biofilms. Figure 4.30 shows the fabricated system. The two antennas are held by a customized wooden frame. The biofilm sample is placed on a Styrofoam sample holder between the two antennas. The ultra-low-noise amplifier has a gain of 30 dB and a noise figure of 0.3 dB at 3 GHz. The two directional couplers are fixed on the roof of the wooden frame. A coupled-line bandpass filter with a center frequency of 3.18 GHz and 3-dB bandwidth of 180 MHz is placed at the input of Antenna 2.

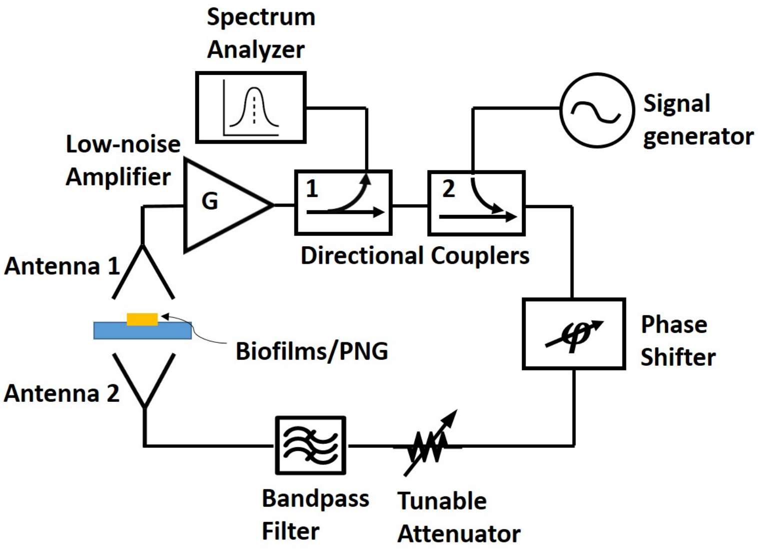

Figure 4.29: Block diagram of the proposed regenerative sensing system.

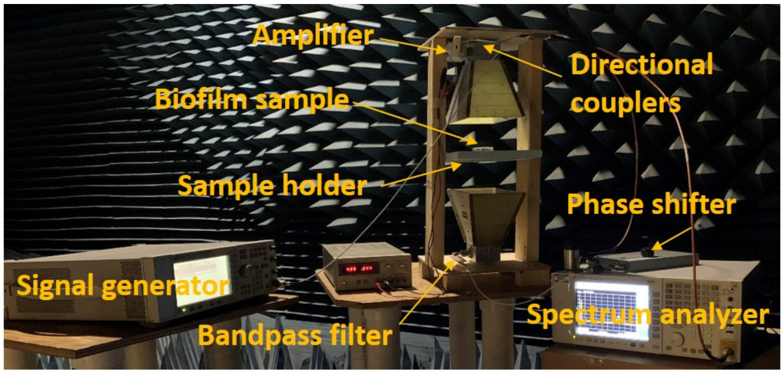

Figure 4.30: Measurement setup in the anechoic chamber.

4.1.4.3 Measurement Procedure

The measurements are conducted in the anechoic chamber at the University of Michigan to prevent any possible external interference. Biofilm samples are prepared in the same way as described in Section 4.1.2.1. 100 mm × 100 mm sqaure petri dishes are used to produce larger biomass. A set of fresh PNG samples without biofilms are prepared under the same condition as a control group.

The system is controlled by an automated data collection program. The measurement procedure is as follows:

1. Measure thermal radiation from PNG media. A PNG from the control group is randomly chosen and placed on the sample holder. The system continuously records the frequency response and collects a total of n_1 traces.
2. Replace the PNG media with a biofilm sample, and measure the radiation from the biofilm sample. The number of traces collected is n_2.
3. Illuminate the biofilm sample for a specified period of time.
4. Measure the radiation from the illuminated biofilm sample, and collect n_3 traces.
5. Repeat steps 3 and 4 as needed.

Step 1 is meant to establish a baseline for the measurements. It needs to be performed only once if multiple samples are measured in one sitting and all system parameters (i.e., the connection of the cables, values of the phase shifter and the attenuator, bias of the amplifiers, settings of the spectrum analyzer, etc) are kept unchanged. The observation period $T_{k=1,2,3}$ for each subject (PNG, unilluminated biofilm sample, and illuminated sample) is related to the number of traces $n_{k=1,2,3}$ by

$$T_k = (n_k - 1)\Delta t \tag{4.28}$$

where Δt is the time between two consecutive traces, which can be set independently through the program.

Figure 4.31 demonstrates a set of data obtained from a complete measurement, where a 27-day-old biofilm sample was examined. The biofilm sample was first measured in its natural state and then illuminated by a 3.18 GHz sinusoidal signal with an input power of -12 dBm for 20 minutes. In this measurement, we set $\Delta t = 1.3\ s$

and chose $n_1 = n_2 = n_3 = 1000$, each corresponding to an observation period of 22 minutes. Frequency responses of PNG media, and the biofilm sample before and after illumination are shown in Figure 4.31 (a)–(c), respectively. Each figure contains 1000 traces, represented by different colors. Each trace consists of 1001 data points. The red thick line represents the average power. As desired, the system exhibits the highest gain at 3.18 GHz. A reference signal at 2.9 GHz was provided by the signal source to monitor the status of the system. The reference signal is chosen such that it is far enough away from the band of interest so that it does not affect the system response. Notable differences at 3.18 GHz among the three cases were observed. The average amplitude of the PNG media, the biofilm sample before and after the illumination at 3.18 GHz are -70 dBm, -66 dBm and -62.5 dBm, respectively. The biofilm sample demonstrates higher radiated power than the PNG media before being exposed to the external EM signal. The radiation becomes even stronger after the illumination. It should be noted that similar responses were observed on a large number of biofilm samples of various ages.

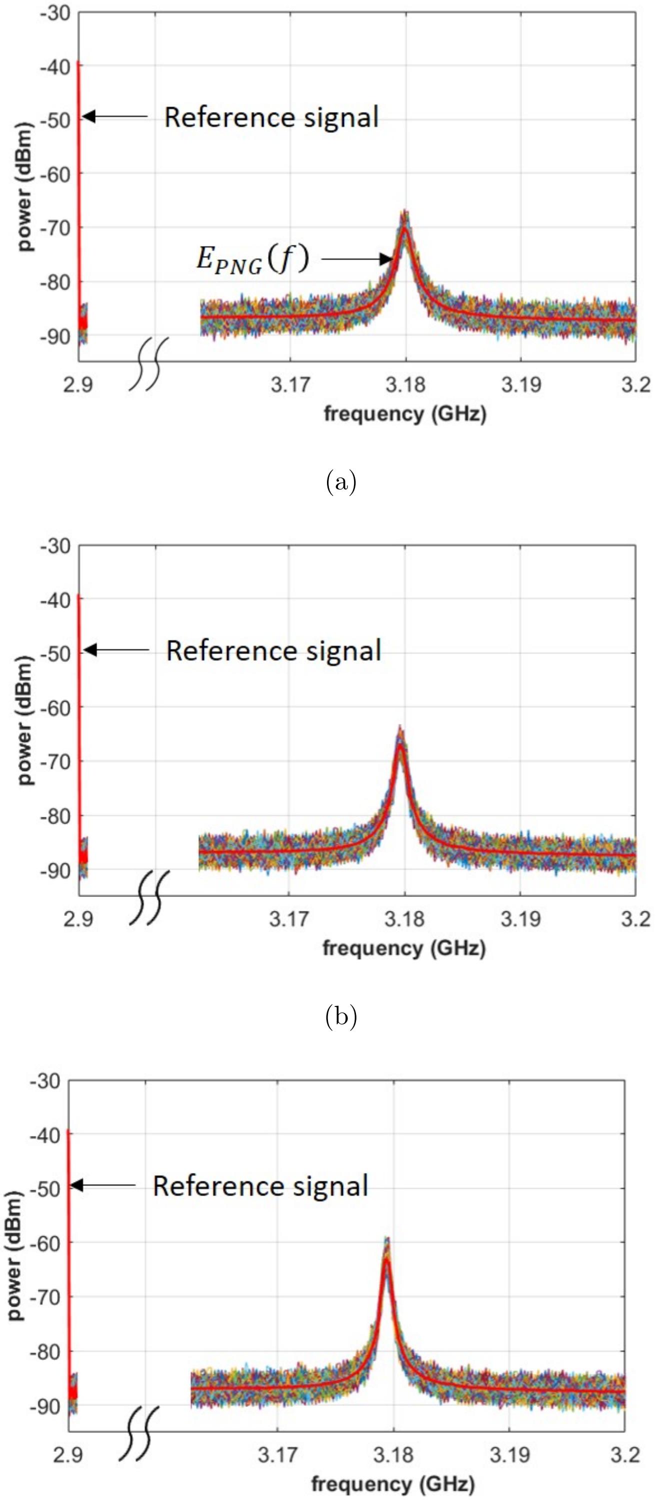

(a)

(b)

(c)

Figure 4.31: Frequency responses of (a) PNG media, and a 27-day-old biofilm sample (b) before and (c) after illumination.

4.1.4.4 Data Processing

The frequency responses shown in Figure 4.31 demonstrate that biofilms radiate EM waves and actively react to an external EM stimulus at 3.18 GHz. However, since all the traces overlap with each other, it is difficult to visualize the development of the signal throughout the entire experiment. To gain insight into the measurement, proper data processing is needed to extract useful information from the massive amount of data.

In this section, an algorithm is developed to process the measured data. The goal is to quantitatively describe the signal strength of each trace, and show the variation of the signal over time in a straightforward manner.

The average frequency response of a PNG based on n_1 traces is

$$\bar{P}_{\mathrm{PNG}}(f) = \frac{1}{n_1} \sum_{i=1}^{n_1} P_{\mathrm{PNG},i}(f) \tag{4.29}$$

where $P_{\mathrm{P}_{PNG,i}}(f)$ is the i_{th} trace obtained from step 1 as described in Section 4.1.4.3. $\bar{P}_{\mathrm{PNG}}(f)$ can be considered the baseline of the measurement or noise floor of the system. For PNG, the distance of each trace from the baseline is defined as

$$\Delta_{\mathrm{PNG},i}(f) = \Delta f \sum_{f=f_1}^{f_2} |P_{\mathrm{PNG},i}(f) - \bar{P}_{\mathrm{PNG}}(f)| \tag{4.30}$$

in which f_1 and f_2 are respectively the lower and upper bounds of the frequency band of interest, and Δf is the frequency sampling resolution. Similarly, for a biofilm sample, the distance of each trace from the baseline is

$$\Delta_{\mathrm{sample},i}(f) = \Delta f \sum_{f=f_1}^{f_2} |P_{\mathrm{PNG},i}(f) - \bar{P}_{\mathrm{PNG}}(f)|) \tag{4.31}$$

(4.30) and (4.31) remove the intrinsic loop response from the data, which helps us look directly at the net impact of the biofilms.

The average distance of PNG from the baseline based on n_1 traces is

$$\bar{\Delta}_{\text{PNG}} = \frac{1}{n_1} \sum_{i=1}^{n_1} \Delta_{\text{PNG},i} \tag{4.32}$$

It should be noted that since we use Manhattan distance [148] in (4.30) and (4.31), which is calculated as the sum of the absolute differences between the measured value and the baseline at each frequency, the final result obtained from (4.32) is always larger than 0.

Finally, the distance of each biofilm sample measurement $Delta_{\text{sample},i}$ is compared with the average distance of PNG Δ_{PNG} to yield the normalized distance

$$\Delta_{0,i}(\text{dB}) = \Delta_{\text{sample},i}(\text{dBm}) - \bar{\Delta}_{\text{PNG}}(\text{dBm}) \tag{4.33}$$

Here, Δ_0 is an indicator that quantitatively describes the deviation of the frequency response of a biofilm sample from PNG. Knowing the time slot between two consecutive traces Δt, we can plot Δ_0 as a function of time.

4.1.4.5 System Characterization and Experimental Results

A set of measurements were first conducted only on PNG media to characterize the system. In these measurements, the biofilm sample is replaced with a second PNG. The first PNG is used to establish the baseline and to compute $\bar{\Delta}_{\text{PNG}}$, while the second PNG is used to mimic the biofilm sample. The normalized distance obtained from PNG indicates the measurement uncertainty caused by temperature fluctuation, petri dish placement and other systematic errors. Figure 4.32 shows Δ_0 of a PNG as a function of time with $n_1 = n_2 = n_3 = 1000$, and $\Delta t = 1.3\ s$. The normalized distance is around 0.8 dB, which means that in biofilm measurements, only Δ_0 large than 0.8 dB will be considered meaningful. It should be pointed out that the establishment of the measurement uncertainty is based on a large number of replicated experiments and the results are reproducible. Another observation is that for PNG media, there is no difference between before and after illumination, which is expected.

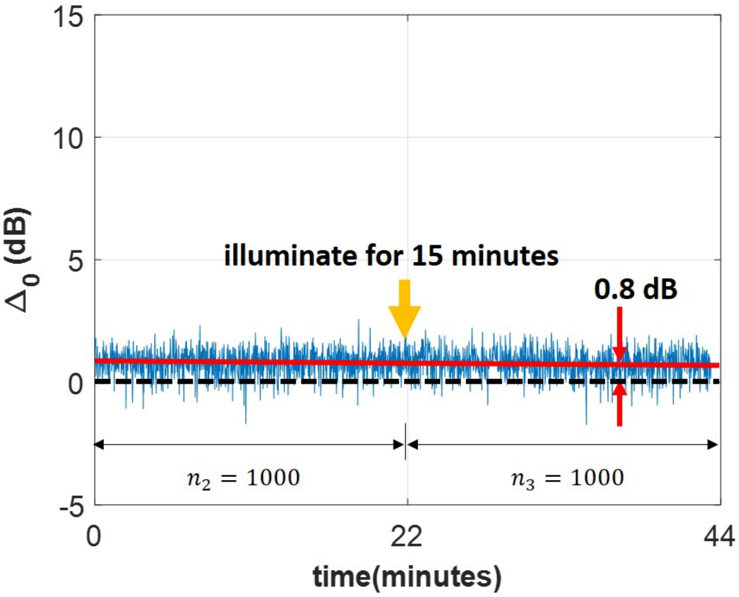

Figure 4.32: Characterization of measurement uncertainty.

Figure 4.33 plots Δ_0 of an 8-day-old biofilm sample before and after illumination. In this experiment, the sample is first measured in its natural state for about 22 minutes ($n_2 = 1000$), then illuminated by a 3.18 GHz sinusoidal signal with an input power of -12 dBm for 15 minutes. The sample is measured for another 22 minutes ($n_3 = 1000$) immediately after the illumination. For the biofilm sample, Δ_0 is much larger than 0.8 dB, suggesting the existence of biological EM radiation beyond the thermal emission from PNG media. More interestingly, the signal strength exhibits a significant increase after the illumination, and a slight decrease after reaching a peak value of 4.9 dB.

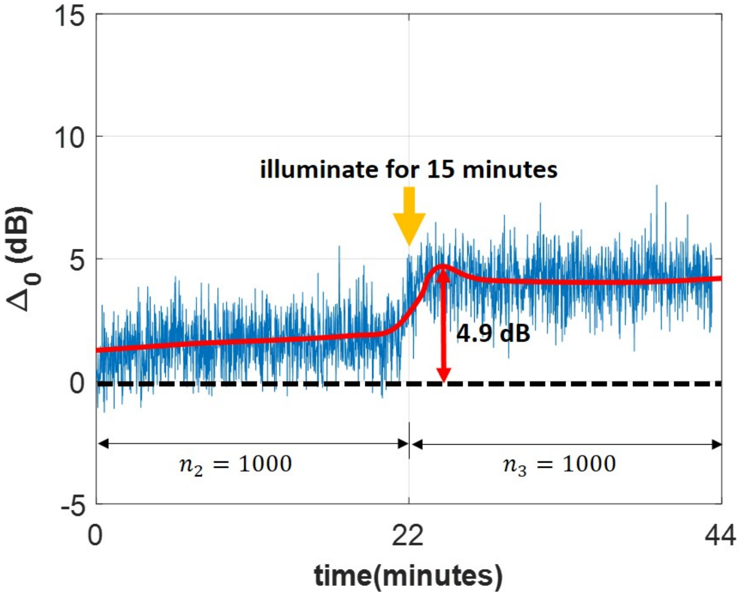

Figure 4.33: Δ_0 of a 8-day-old sample.

Figure 4.34 (a)-(c) show the results obtained from a 15-day-old sample, an 18-day-old sample and a 21-day-old biofilm sample, respectively. In these experiments, each sample is illuminated twice. The illumination time, the number of traces collected and the duration between two illuminating experiments for each case are indicated in the figures.

As clearly shown in the figures, Δ_0 is much larger than 0.8 dB for all three cases. The values of Δ_0 vary from sample to sample: the 18-day-old sample exhibits the strongest radiation with a maximum Δ_0 of 9 dB, whereas the 15-day-old and the 21-day-old have more mild responses with maximum Δ_0 of 4.5 dB and 5 dB, respectively. Similar to the 8-day-old sample, for all three samples, Δ_0 improves by about 2 dB after each illumination, and gradually decreases over time. However, we did not find any obvious dependence of the signal strength on the illumination time.

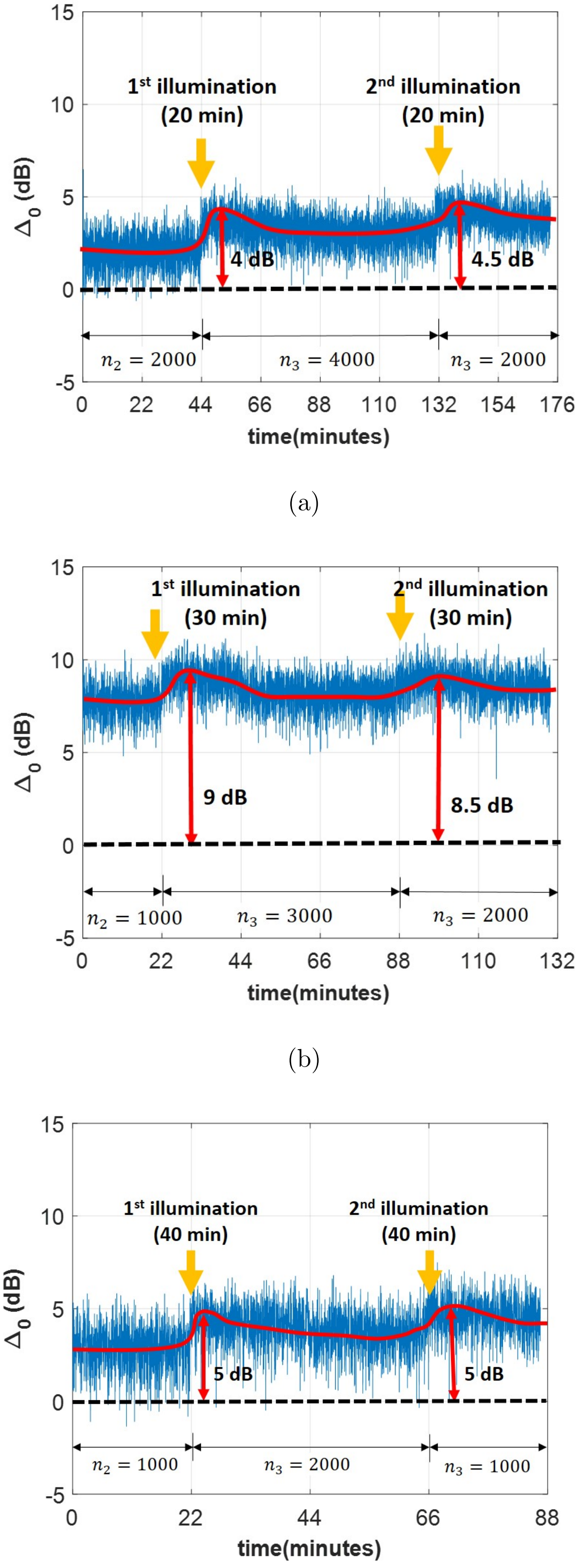

(a)

(b)

(c)

Figure 4.34: Δ_0 of (a) a 15-day-old, (b) an 18-day-old and (c) a 21-day-old samples.

As a complementary experiment, a similar system is built at 6.3 GHz, where no signal was observed using the wideband near-zone radiative system. Figure 4.35 shows Δ_0 of a 22-day-old biofilm sample over the course of 44 minutes. As expected, no significant difference is observed between the sample and the PNG. The response remains the same even after a 30-minute illumination.

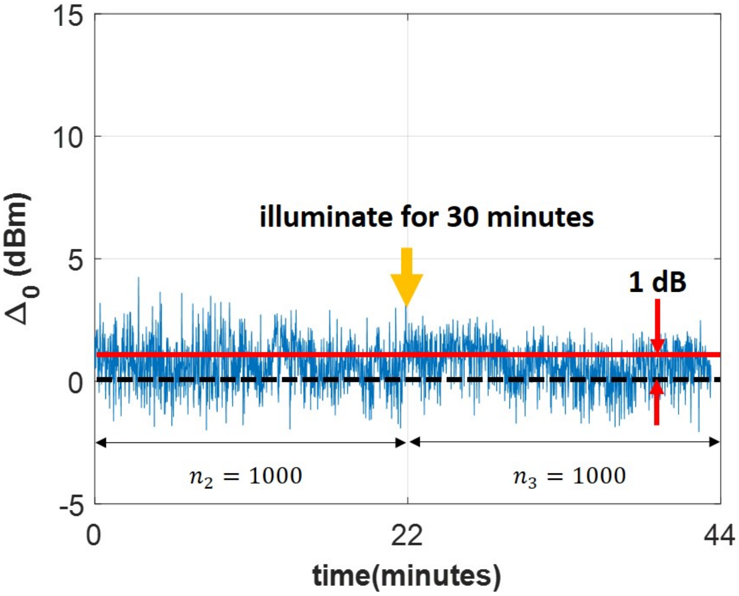

Figure 4.35: Δ_0 of a 22-day-old biofilm sample at 6.3 GHz. Sample birth date: December 17, 2021. Measurement date: January 8, 2021.

4.1.5 Conclusion

This work is the first successful attempt to measure EM radiation from *S. aureus* biofilms in the GHz frequency range. Three measurement systems - a wideband near-zone radiative system, a spiral antenna system, and a regenerative RF sensing system - are designed for this specific purpose. Two distinct radiating bands in the 3-4 GHz frequency range were identified. A long-term cycle of the radiated signal with short-term fluctuations is discovered in the course of a 70-day experiment. In addition, it is shown that bacterial cells can actively respond to external electromagnetic stimuli, indicating that the radiation is not simply thermal emission due to molecular vibration, but that it indeed plays a role in coordinating cells' activities. Last but not least, exposing biofilms with significant RF radiation to lethal doses of ZnO-NPYs, which inhibits metabolic activity, eliminates the biofilm RF emission.

CHAPTER V

Conclusion and Future Work

5.1 Research Summary and Contributions

This dissertation provides novel solutions to some emerging problems in modern applied electromagnetics as well as bioelectromagnetics. Major contributions of this dissertation include:

- A very low-profile composite monopole antenna for VHF applications. The proposed antenna is based on an extremely small monopole. By introducing 8 identical parasitic elements and utilizing the mutual coupling between them, we are able to improve the peak gain of the antenna by 10 dB.

- A method for measuring a monopole antenna with an electrically small ground plane. It is shown that using cascaded transformers at the antenna feed can effectively suppress the exterior currents on the feeding cable and thus significantly reduce the cable effects on antenna performance.

- Three compact mmWave antenna arrays for 5G mobile devices, which include (1) a 28 GHz differential dual-polarized array; (2) a low profile 28/39 GHz dual-band dual-polarized array; and (3) a very compact dual-polarized array supporting multiple 5G bands. The introduced antenna miniaturization and bandwidth enhancement techniques can be used to design other types of compact high-performance antennas for wireless communication systems.

- A near-field-based gain and pattern measurement technique for probe-fed mmWave antennas.
- The first successful detection of EM radiation from *S. aureus* biofilms. Three novel sensing systems, i.e., a very sensitive wideband near-zone radiative system, a spiral antenna system and a regenerative RF sensing system, were deployed for the measurement. Although these systems are specifically designed for detecting extremely small EM radiation from bacterial biofilms, they can be applied to many other applications as well.

5.2 Future Work

5.2.1 EM Radiation from Biofilms at Low Frequencies

We have made several attempts to measure EM radiation below 1 GHz. However, due to high noise levels at low frequencies, we were not able to observe notable radiation from biofilms.

The development of high sensitivity measurement systems in the kHz to MHz frequency range would be an interesting task. If successful, it will give us a more complete picture of EM signaling within biological cells.

5.2.2 Impact of ZnO-NPY on Biofilms

It is recommended further exploring other possible causes of the disappearance of the EM radiation after the ZnO-NPY treatment. For example, the ZnO-NPY nanoparticles may be attached to cells or amyloid fibrils, altering the physical dimensions of the ”mechanical antennas”, which in turn drives the radiation frequency out of the 3–5 frequency range.

5.2.3 Functionalities of EM Radiation in Cells

While the discovery of EM radiation within bacterial communities is a key requirement to demonstrate EM signaling among bacterial cells, it is only the first step toward demystifying how cells communicate. The next step is to understand the relationship between EM radiation and cells' biological activities. Further investigation on the significance of the time frames is also a promising and challenging task. It is recommended that future investigations be conducted jointly with biological researchers and develop a series experiments to identify the functionalities of EM radiation in bacterial biofilms. The insight may lead to major breakthroughs in biofilm control and disease treatment.

APPENDICES

APPENDIX A

Layout of the Dual-Band Dual-Polarized Antenna Array

The layout of the array element and the whole array are provided as follows.

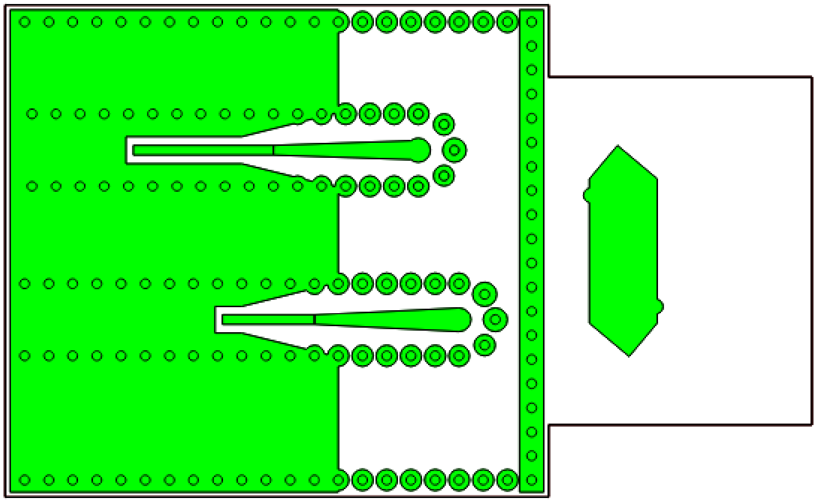

Figure A.1: Array element metal layer 1

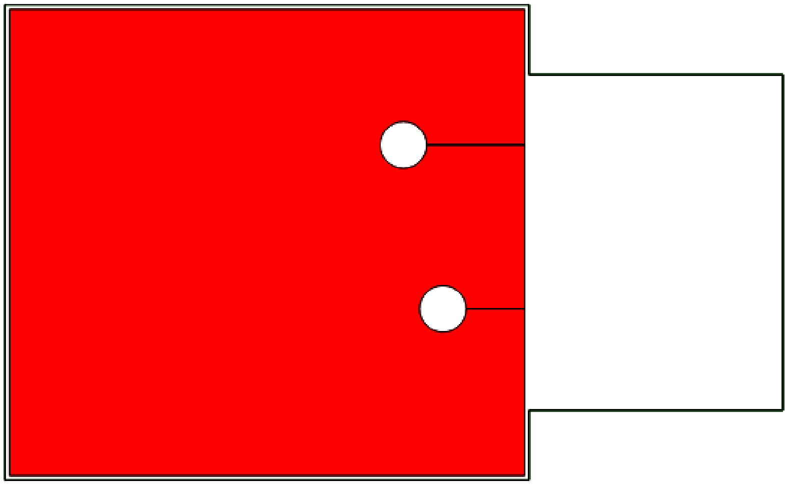

Figure A.2: Array element metal layer 2

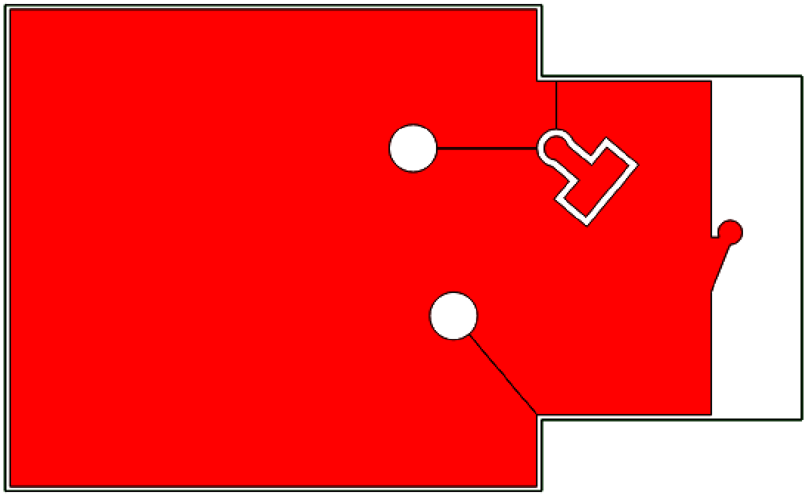

Figure A.3: Array element metal layer 3

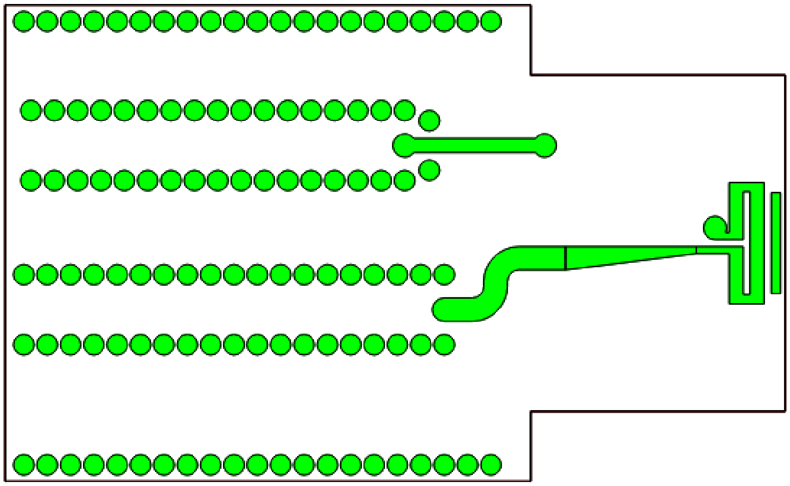

Figure A.4: Array element metal layer 4

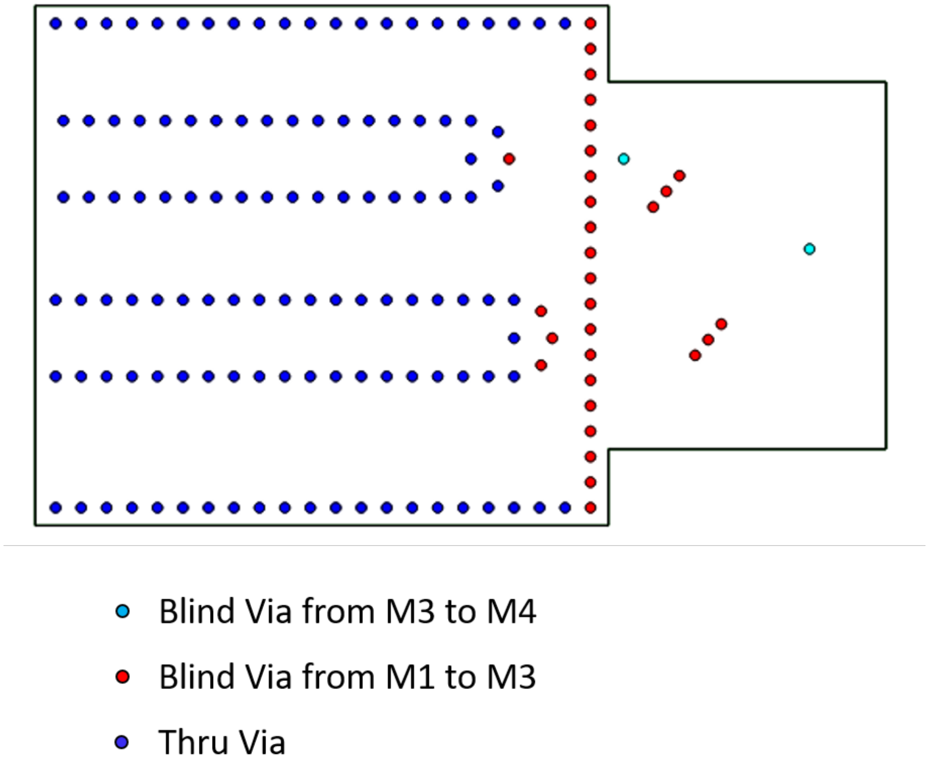

Figure A.5: Array element via configuration

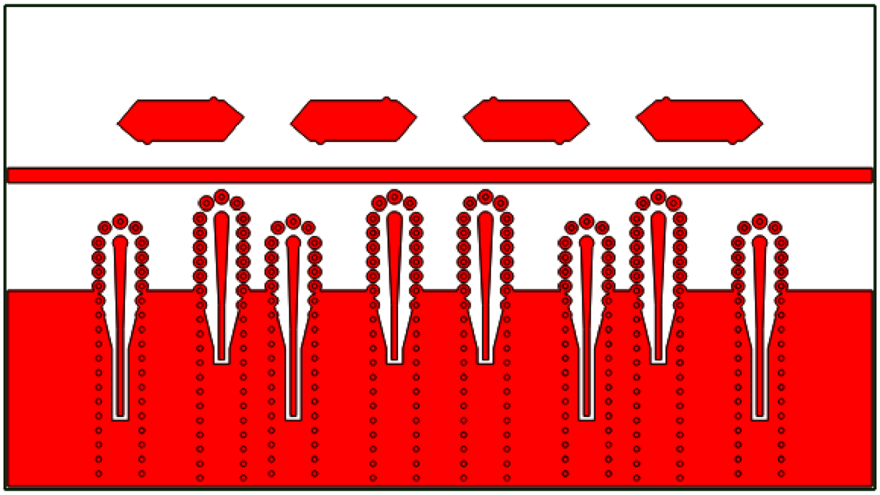

Figure A.6: Array metal layer 1

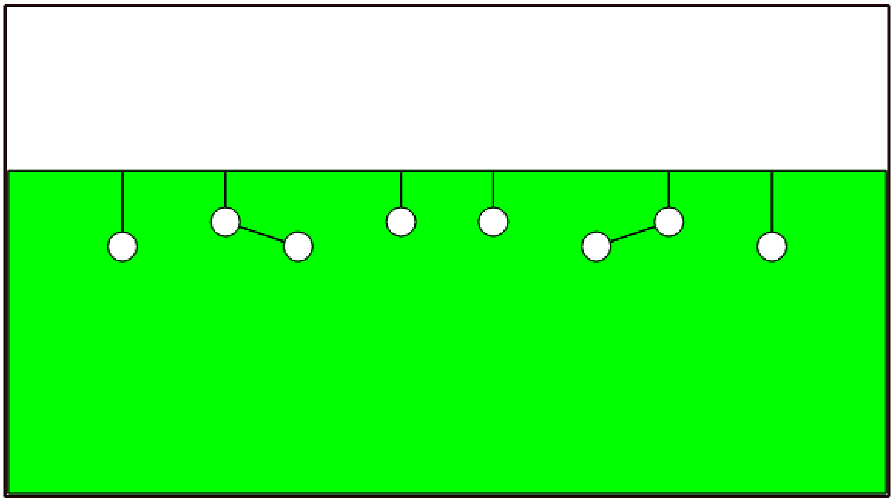

Figure A.7: Array metal layer 2

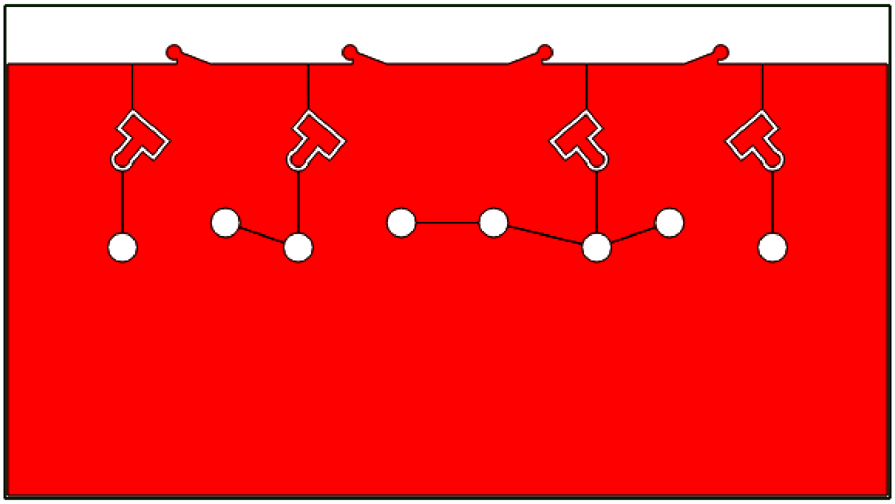

Figure A.8: Array metal layer 3

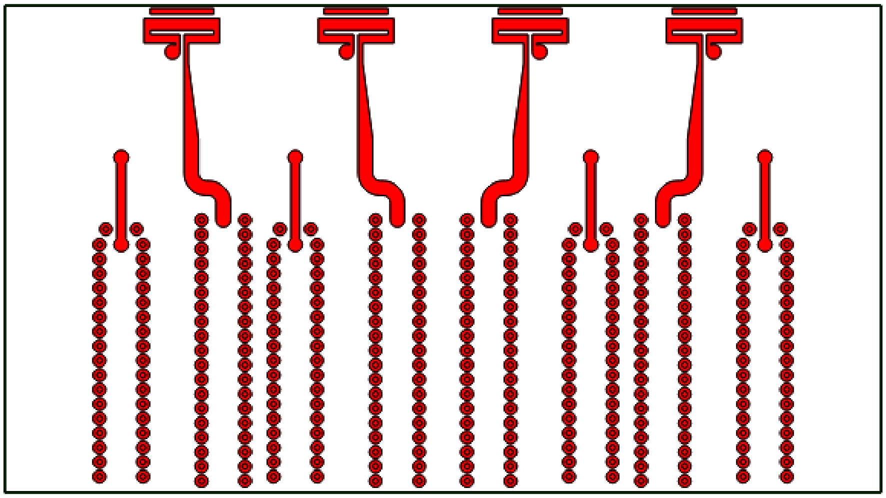

Figure A.9: Array metal layer 4

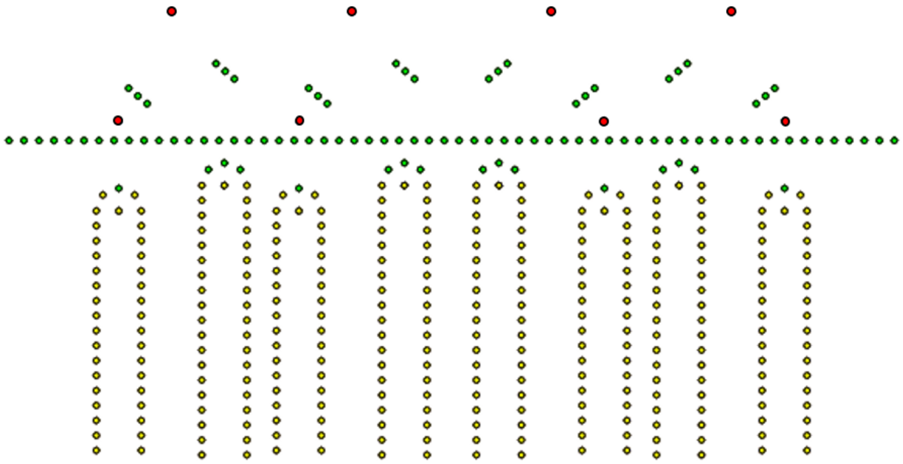

Figure A.10: Array via configuration

APPENDIX B

Measurement Setups for Low Frequencies

Despite our extensive efforts, we were not able to detect notable radiation from biofilms in the other two frequency groups due to high ambient noise. The pictures of the measurement setups used for measurements below 1 GHz are shown as follows.

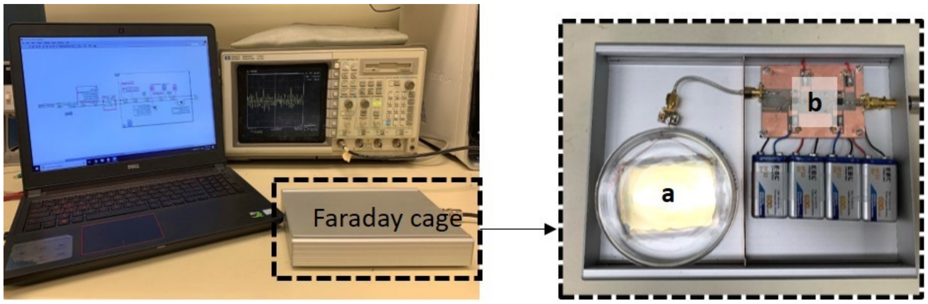

Figure B.1: Measurement setup for the low frequency range (below 1 MHz). (a) Interdigital capacitor sensor. (b) High-gain amplification circuit.

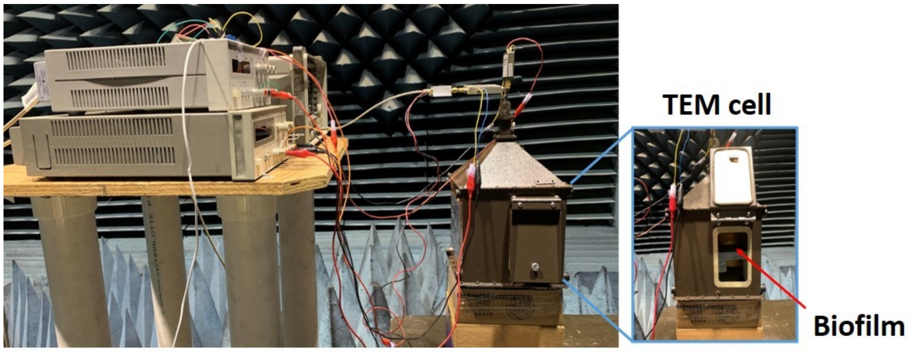

Figure B.2: Measurement setup for the MHz range.

BIBLIOGRAPHY

BIBLIOGRAPHY

[1] M. T. Bohr and I. A. Young, “CMOS scaling trends and beyond,” *IEEE Micro*, vol. 37, no. 6, pp. 20–29, 2017.

[2] W. Hong, “Solving the 5G mobile antenna puzzle: Assessing future directions for the 5G mobile antenna paradigm shift,” *IEEE Microwave Magazine*, vol. 18, no. 7, pp. 86–102, 2017.

[3] J. Oh, J. Choi, F. T. Dagefu, and K. Sarabandi, “Extremely small two-element monopole antenna for hf band applications,” *IEEE Transactions on Antennas and Propagation*, vol. 61, no. 6, pp. 2991–2999, 2013.

[4] W. Hong, K.-H. Baek, Y. Lee, Y. Kim, and S.-T. Ko, “Study and prototyping of practically large-scale mmwave antenna systems for 5G cellular devices,” *IEEE Communications Magazine*, vol. 52, no. 9, pp. 63–69, 2014.

[5] W. Hong, K.-H. Baek, and S. Ko, “Millimeter-wave 5G antennas for smartphones: Overview and experimental demonstration,” *IEEE Transactions on Antennas and Propagation*, vol. 65, no. 12, pp. 6250–6261, 2017.

[6] J. Wu and K. Sarabandi, “Compact omnidirectional circularly polarized antenna,” *IEEE Transactions on Antennas and Propagation*, vol. 65, no. 4, pp. 1550–1557, 2017.

[7] T. S. Rappaport, S. Sun, R. Mayzus, H. Zhao, Y. Azar, K. Wang, G. N. Wong, J. K. Schulz, M. Samimi, and F. Gutierrez, “Millimeter wave mobile communications for 5G cellular: It will work!” *IEEE Access*, vol. 1, pp. 335–349, 2013.

[8] W. Hong, K. Baek, and Y. Lee, “Quantitative analysis of the effects of polarization and pattern reconfiguration for mmwave 5G mobile antenna prototypes,” *2017 IEEE Radio and Wireless Symposium (RWS)*, pp. 68–71, 2017.

[9] S. Ranvier, M. Kyrö, C. Icheln, C. Luxey, R. Staraj, and P. Vainikainen, “Compact 3-d on-wafer radiation pattern measurement system for 60 ghz antennas,” *Microwave and Optical Technology Letters*, vol. 51, 02 2009.

[10] F. T. Dagefu, G. Verma, C. R. Rao, P. L. Yu, J. R. Fink, B. M. Sadler, and K. Sarabandi, "Short-range low-vhf channel characterization in cluttered environments," *IEEE Transactions on Antennas and Propagation*, vol. 63, no. 6, pp. 2719–2727, 2015.

[11] F. T. Dagefu, J. Choi, M. Sheikhsofla, B. M. Sadler, and K. Sarabandi, "Performance assessment of lower vhf band for short-range communication and geolocation applications," *Radio Science*, vol. 50, no. 5, pp. 443–452, 2015.

[12] D. Liao and K. Sarabandi, "Terminal-to-terminal hybrid full-wave simulation of low-profile, electrically-small, near-ground antennas," *IEEE Transactions on Antennas and Propagation*, vol. 56, no. 3, pp. 806–814, 2008.

[13] J. W. Costerton, K. Cheng, G. Geesey, T. I.Ladd, J. C. Nickel, M. Dasgupta, and T. J. Marrie, "Bacterial biofilms in nature and disease," *Annual review of microbiology*, vol. 41, pp. 435–464, 1987.

[14] A. Deva, W. Adams, Jr, and K. Vickery, "The role of bacterial biofilms in device-associated infection," *Plastic and reconstructive surgery*, vol. 132, no. 5, pp. 1319–1328, 2013.

[15] J. W. 1 and H.-C. Flemming, "Biofilms in drinking water and their role as reservoir for pathogens," *International journal of hygiene and environmental health*, vol. 214, no. 6, pp. 417–423, 2011.

[16] B. J. Little and J. S. Lee, "Microbiologically influenced corrosion: an update," *International Materials Reviews*, vol. 59, no. 7, pp. 384–393, 2014.

[17] H.-C. Flemming, J. Wingender, U. Szewzyk, P. Steinberg, S. A. Rice, and S. Kjelleberg, "Biofilms: an emergent form of bacterial life," *Nature Reviews Microbiology*, vol. 14, pp. 563–575, 2016.

[18] S. S. Rogers, J. P. Venema, P.and van der Ploeg, E. van der Linden, L. M. Sagis, and A. M. Donald, "Investigating the permanent electric dipole moment of beta-lactoglobulin fibrils, using transient electric birefringence," *Biopolymers*, vol. 82, no. 3, pp. 241–252, 2006.

[19] G. Yoon, J. Kwak, J. I. Kim, S. Na, and K. Eom, "Mechanical characterization of amyloid fibrils using coarse-grained normal mode analysis," *Advanced Functional Materials*, vol. 21, no. 18, pp. 3454–3463, 2011.

[20] N. Van Gerven, S. E. Van der Verren, D. M. Reiter, and H. Remaut, "The role of functional amyloids in bacterial virulence," *Journal of Molecular Biology*, vol. 430, no. 20, pp. 3657–3684, 2018, functional Amyloids in Health and Disease. [Online]. Available: https://www.sciencedirect.com/science/article/pii/S0022283618307605

[21] N. Barani and K. Sarabandi, "Theory of electromagnetic-based communication within bacterial communities," in *2019 IEEE International Symposium on Antennas and Propagation and USNC-URSI Radio Science Meeting*, 2019, pp. 1–2.

[22] J. McLean, H. Foltz, and G. Crook, "Broadband, robust, low profile monopole incorporating top loading, dielectric loading, and a distributed capacitive feed mechanism," in *IEEE Antennas and Propagation Society International Symposium. 1999 Digest. Held in conjunction with: USNC/URSI National Radio Science Meeting (Cat. No.99CH37010)*, vol. 3, 1999, pp. 1562–1565 vol.3.

[23] T. Noro and Y. Kazama, "Low profile and wide bandwidth characteristics of top loaded monopole antenna with shorting post," in *IEEE International Workshop on Antenna Technology Small Antennas and Novel Metamaterials, 2006.*, 2006, pp. 108–111.

[24] J. Oh and K. Sarabandi, "Low profile, miniaturized, inductively coupled capacitively loaded monopole antenna," *IEEE Transactions on Antennas and Propagation*, vol. 60, no. 3, pp. 1206–1213, 2012.

[25] W. Hong and K. Sarabandi, "Low-profile, multi-element, miniaturized monopole antenna," *IEEE Transactions on Antennas and Propagation*, vol. 57, no. 1, pp. 72–80, 2009.

[26] J. Choi, F. T. Dagefu, B. M. Sadler, and K. Sarabandi, "Electrically small folded dipole antenna for hf and low-vhf bands," *IEEE Antennas and Wireless Propagation Letters*, vol. 15, pp. 718–721, 2016.

[27] W. Roh, J.-Y. Seol, J. Park, B. Lee, J. Lee, Y. Kim, J. Cho, K. Cheun, and F. Aryanfar, "Millimeter-wave beamforming as an enabling technology for 5G cellular communications: theoretical feasibility and prototype results," *IEEE Communications Magazine*, vol. 52, no. 2, pp. 106–113, 2014.

[28] W. Hong, S.-T. Ko, Y. Lee, and K.-H. Baek, "Compact 28 ghz antenna array with full polarization flexibility under yaw, pitch, roll motions," in *2015 9th European Conference on Antennas and Propagation (EuCAP)*, 2015, pp. 1–3.

[29] W. El-Halwagy, R. Mirzavand, J. Melzer, M. Hossain, and P. Mousavi, "Investigation of wideband substrate-integrated vertically-polarized electric dipole antenna and arrays for mm-wave 5G mobile devices," *IEEE Access*, vol. 6, pp. 2145–2157, 2018.

[30] J. Park, D. Choi, and W. Hong, "37–39 ghz vertically-polarized end-fire 5G antenna array featuring electrically small profile," in *2018 IEEE International Symposium on Antennas and Propagation USNC/URSI National Radio Science Meeting*, 2018, pp. 637–638.

[31] R. N. Simons and R. Lee, "On-wafer characterization of millimeter-wave antennas for wireless applications," *IEEE Transactions on Microwave Theory and Techniques*, vol. 47, pp. 92–96, 1998.

[32] R. N. Simons, "Novel On-Wafer Radiation Pattern Measurement Technique for MEMS Actuator Based Reconfigurable Patch Antennas," NASA STI/Recon Technical Report N, p. 90931, Oct. 2002.

[33] N. Behdad, D. Shi, W. Hong, K. Sarabandi, and M. P. Flynn, "A 0.3mm¡sup¿2¡/sup¿ miniaturized x-band on-chip slot antenna in 0.13μm cmos," in *2007 IEEE Radio Frequency Integrated Circuits (RFIC) Symposium*, 2007, pp. 441–444.

[34] K. V. Caekenberghe, K. Brakora, W. Hong, K. Jumani, D. Liao, M. Rangwala, Y.-Z. Wee, X. Zhu, and K. Sarabandi, "A 2–40 ghz probe station based setup for on-wafer antenna measurements," *IEEE Transactions on Antennas and Propagation*, vol. 56, pp. 3241–3247, 2008.

[35] A. Shamim, L. Roy, N. Fong, and N. G. Tarr, "24 ghz on-chip antennas and balun on bulk si for air transmission," *IEEE Transactions on Antennas and Propagation*, vol. 56, no. 2, pp. 303–311, 2008.

[36] A. Jam and K. Sarabandi, "A submillimeter-wave near-field measurement setup for on-wafer pattern and gain characterization of antennas and arrays," *IEEE Transactions on Instrumentation and Measurement*, vol. 66, no. 4, pp. 802–811, 2017.

[37] K. Yang, G. David, J.-G. Yook, I. Papapolymerou, L. Katehi, and J. Whitaker, "Electrooptic mapping and finite-element modeling of the near-field pattern of a microstrip patch antenna," *IEEE Transactions on Microwave Theory and Techniques*, vol. 48, no. 2, pp. 288–294, 2000.

[38] K. Sabet, R. Darragh, A. Sabet, K. Sarabandi, and L. P. Katehi, "Using electro-optic field mapping for design of dual-band circularly polarized active phased arrays," in *2017 IEEE 18th Wireless and Microwave Technology Conference (WAMICON)*, 2017, pp. 1–5.

[39] K. Sabet, R. Darragh, A. Sabet, K. Sarabandi, K. Jamil, and S. Alhumaidi, "Characterization and diagnostics of active phased array modules using non-invasive electro-optic field probes with a cw laser source," in *2017 IEEE MTT-S International Microwave Symposium (IMS)*, 2017, pp. 1617–1619.

[40] K. Sarabandi, J. Choi, A. Sabet, and K. Sabet, "Pattern and gain characterization using nonintrusive very-near-field electro-optical measurements over arbitrary closed surfaces," *IEEE Transactions on Antennas and Propagation*, vol. 65, no. 2, pp. 489–497, 2017.

[41] G. Gaborit, P. Artillan, C. Bermond, G. Revillod, G. Chevrier-Gros, and L. Duvillaret, “20 ghz antenna radiation pattern obtained from near-field mapping with electrooptic probe on a single plane,” *IEEE Antennas and Wireless Propagation Letters*, vol. 19, no. 7, pp. 1177–1181, 2020.

[42] A. C. Newell, R. D. Ward, and E. McFarlane, “Gain and power parameter measurements using planar near-field techniques,” *IEEE Transactions on Antennas and Propagation*, vol. 36, pp. 792–803, 1988.

[43] C. Rye, W. Robert, V. Jurukovski, J. DeSaix, C. Jung, and Y. Avissar, *Biology.* OpenStax, 2016, ch. 247-264.

[44] B. Alberts, A. Johnson, D. Morgan, and M. Raff, *Molecular Biology of the Cell*, 6th ed. Garland Science, 2014.

[45] H. Fröhlich, *The Biological Effects of Microwaves and Related Questions.* Academic Press, 1980, vol. 53. [Online]. Available: https://www.sciencedirect.com/science/article/pii/S0065253908602590

[46] ——, *Coherent Excitation in Active Biological Systems.* Boston, MA: Springer US, 1986, pp. 241–261.

[47] ——, *Biological Coherence and response to external Stimuli.* Garland Science, 1988.

[48] J. Tuszyński, S. Hameroff, M. Satarić, B. Trpisová, and M. Nip, “Ferroelectric behavior in microtubule dipole lattices: Implications for information processing, signaling and assembly/disassembly,” *Journal of Theoretical Biology*, vol. 174, no. 4, pp. 371–380, 1995.

[49] J. Pokorný, F. Jelínek, V. Trkal, I. Lamprecht, and R. Hölzel, “Vibrations in microtubules,” *Journal of Biological Physics*, vol. 23, no. 3, pp. 171–179, 1997.

[50] M. Cifra, J. Pokorný, D. Havelka, and O. Kučera, “Electric field generated by axial longitudinal vibration modes of microtubule,” *Biosystems*, vol. 100, no. 2, pp. 122–131, 2010.

[51] J. Pokorný, J. Hašek, F. Jelínek, J. Šaroch, and B. Palán, “Electromagnetic activity of yeast cells in the m phase,” *Electro- and Magnetobiology*, vol. 20, no. 3, pp. 371–396, 2001.

[52] E. D. Kirson, Z. Gurvich, R. Schneiderman, E. Dekel, A. Itzhaki, Y. Wasserman, R. Schatzberger, and Y. Palti, “Disruption of cancer cell replication by alternating electric fields,” *Cancer research*, vol. 64, no. 9, pp. 3288–3295, 2004.

[53] S. Sahu, S. Ghosh, B. Ghosh, K. Aswani, K. Hirata, D. Fujita, and A. Bandyopadhyay, “Atomic water channel controlling remarkable properties of a single brain microtubule: Correlating single protein to its supramolecular assembly,” *Biosensors and Bioelectronics*, vol. 47, pp. 141–148, 2013. [Online]. Available: https://www.sciencedirect.com/science/article/pii/S0956566313001590

[54] L. Montagnier, J. Aïssa, S. Ferris, J.-L. Montagnier, and C. Lavallée, "Electromagnetic signals are produced by aqueous nanostructures derived from bacterial dna sequences," *Interdisciplinary sciences, computational life sciences*, vol. 1, pp. 81–90, 06 2009.

[55] D. A. Turton, H. M. Senn, T. Harwood, A. J. Lapthorn, E. M. Ellis, and K. Wynne, "Terahertz underdamped vibrational motion governs protein-ligand binding in solution," *Nature Communications*, vol. 1, 06 2014.

[56] N. Barani and K. Sarabandi, "Electromagnetic signaling and quorum sensing within biofilms: Which mechanism is the most probable means of communication?" in *IEEE Engineering in Medicine and Biology Society. Annual International Conference*, 2020, p. 2459–2462.

[57] L. Liu, S. Cheung, Y. Weng, and T. Yuk, *Cable Effects on Measuring Small Planar UWB Monopole Antennas.* []Online], 2012, https://www.intechopen.com/citation-pdf-url/39707. [Online]. Available: https://app.dimensions.ai/details/publication/pub.1047209798

[58] J. T. Bernhard, J. J. Adams, M. D. Anderson, and J. M. Martin, "Measuring electrically small antennas: Details and implications," in *2009 IEEE International Workshop on Antenna Technology*, 2009, pp. 1–4.

[59] G. R. Hoch, P. Nayeri, and A. Elsherbeni, "Bandwidth enhancement of dipole antennas using parasitic elements," in *2015 31st International Review of Progress in Applied Computational Electromagnetics (ACES)*, 2015, pp. 1–2.

[60] V. Iyer, S. Kulkarni, G. Zucchelli, and S. N. Makarov, "Increasing the impedance bandwidth of dipole and monopole antennas with parasitic elements," in *2016 10th European Conference on Antennas and Propagation (EuCAP)*, 2016, pp. 1–4.

[61] T. Au and K. Luk, "Effect of parasitic element on the characteristics of microstrip antenna," *IEEE Transactions on Antennas and Propagation*, vol. 39, no. 8, pp. 1247–1251, 1991.

[62] H. Wheeler, "Fundamental limitations of small antennas," *Proceedings of the IRE*, vol. 35, no. 12, pp. 1479–1484, 1947.

[63] J. Oh and K. Sarabandi, "A low-profile omnidirectional planar antenna with vertical polarization employing two in-phase elements," in *2011 XXXth URSI General Assembly and Scientific Symposium*, 2011, pp. 1–4.

[64] C. A. Balanis, *Antenna Theory: Analysis and Design*, 3rd ed. Wiley, 2012.

[65] Y.-J. Kim and M. Allen, "Surface micromachined solenoid inductors for high frequency applications," *IEEE Transactions on Components, Packaging, and Manufacturing Technology: Part C*, vol. 21, no. 1, pp. 26–33, 1998.

[66] C. R. Sullivan, W. Li, S. Prabhakaran, and S. Lu, "Design and fabrication of low-loss toroidal air-core inductors," in *2007 IEEE Power Electronics Specialists Conference*, 2007, pp. 1754–1759.

[67] S. Tang, S. Hui, and H. S.-H. Chung, "Coreless planar printed-circuit-board (pcb) transformers-a fundamental concept for signal and energy transfer," *IEEE Transactions on Power Electronics*, vol. 15, no. 5, pp. 931–941, 2000.

[68] S. Hui, S. Tang, and H. Chung, "Some electromagnetic aspects of coreless pcb transformers," in *30th Annual IEEE Power Electronics Specialists Conference. Record. (Cat. No.99CH36321)*, vol. 2, 1999, pp. 868–873 vol.2.

[69] S. Tang, S. Hui, and H.-H. Chung, "Characterization of coreless printed circuit board (pcb) transformers," *IEEE Transactions on Power Electronics*, vol. 15, no. 6, pp. 1275–1282, 2000.

[70] T. Co. Tem co. [Online]. Available: https://www.temcoindustrial.com

[71] Coil32. Coil32. [Online]. Available: http://coil32.net/theory/self-capacitance.html

[72] W. B. Kuhn and A. P. Boutz, "Measuring and reporting high quality factors of inductors using vector network analyzers," *IEEE Transactions on Microwave Theory and Techniques*, vol. 58, no. 4, pp. 1046–1055, 2010.

[73] Z. Pi and F. Khan, "An introduction to millimeter-wave mobile broadband systems," *IEEE Communications Magazine*, vol. 49, no. 6, pp. 101–107, 2011.

[74] T. S. Rappaport, S. Sun, R. Mayzus, H. Zhao, Y. Azar, K. Wang, G. N. Wong, J. K. Schulz, M. Samimi, and F. Gutierrez, "Millimeter wave mobile communications for 5G cellular: It will work!" *IEEE Access*, vol. 1, pp. 335–349, 2013.

[75] America's 5G future. [Online]. Available: https://www.fcc.gov/5G

[76] T. S. Rappaport, G. R. MacCartney, M. K. Samimi, and S. Sun, "Wideband millimeter-wave propagation measurements and channel models for future wireless communication system design," *IEEE Transactions on Communications*, vol. 63, no. 9, pp. 3029–3056, 2015.

[77] F. Wang and K. Sarabandi, "An enhanced millimeter-wave foliage propagation model," *IEEE Transactions on Antennas and Propagation*, vol. 53, no. 7, pp. 2138–2145, 2005.

[78] C.-H. Tseng, C.-J. Chen, and T.-H. Chu, "A low-cost 60-ghz switched-beam patch antenna array with butler matrix network," *IEEE Antennas and Wireless Propagation Letters*, vol. 7, pp. 432–435, 2008.

[79] F. Huang, W. Chen, and M. Rao, "Switched-beam antenna array based on butler matrix for 5G wireless communication," in *2016 IEEE International Workshop on Electromagnetics: Applications and Student Innovation Competition (iWEM)*, 2016, pp. 1–3.

[80] M. Ikram, M. S. Sharawi, K. Klionovski, and A. Shamim, "A switched-beam millimeter-wave array with mimo configuration for 5G applications," *Microwave and Optical Technology Letters*, vol. 60, no. 4, pp. 915–920, 2018.

[81] W. Hong, K.-H. Baek, Y. Lee, Y. Kim, and S.-T. Ko, "Study and prototyping of practically large-scale mmwave antenna systems for 5G cellular devices," *IEEE Communications Magazine*, vol. 52, no. 9, pp. 63–69, 2014.

[82] B. Sadhu, Y. Tousi, J. Hallin, S. Sahl, S. Reynolds, O. Renström, K. Sjögren, O. Haapalahti, N. Mazor, B. Bokinge, G. Weibull, H. Bengtsson, A. Carlinger, E. Westesson, J.-E. Thillberg, L. Rexberg, M. Yeck, X. Gu, D. Friedman, and A. Valdes-Garcia, "7.2 a 28ghz 32-element phased-array transceiver ic with concurrent dual polarized beams and 1.4 degree beam-steering resolution for 5G communication," in *2017 IEEE International Solid-State Circuits Conference (ISSCC)*, 2017, pp. 128–129.

[83] C. Deng, D. Liu, B. Yektakhah, and K. Sarabandi, "Series-fed beam-steerable millimeter-wave antenna design with wide spatial coverage for 5G mobile terminals," *IEEE Transactions on Antennas and Propagation*, vol. 68, no. 5, pp. 3366–3376, 2020.

[84] W. Hong, K. Baek, and Y. Lee, "Quantitative analysis of the effects of polarization and pattern reconfiguration for mmwave 5G mobile antenna prototypes," in *2017 IEEE Radio and Wireless Symposium (RWS)*, 2017, pp. 68–71.

[85] W. Hong, S.-T. Ko, Y. Lee, and K.-H. Baek, "Compact 28 ghz antenna array with full polarization flexibility under yaw, pitch, roll motions," in *2015 9th European Conference on Antennas and Propagation (EuCAP)*, 2015, pp. 1–3.

[86] N. Ojaroudiparchin, M. Shen, and G. F. Pedersen, "Design of vivaldi antenna array with end-fire beam steering function for 5G mobile terminals," in *2015 23rd Telecommunications Forum Telfor (TELFOR)*, 2015, pp. 587–590.

[87] M. Stanley, Y. Huang, T. Loh, Q. Xu, H. Wang, and H. Zhou, "A high gain steerable millimeter-wave antenna array for 5G smartphone applications," in *2017 11th European Conference on Antennas and Propagation (EUCAP)*, 2017, pp. 1311–1314.

[88] Z. Zhang, *Antenna design for mobile devices.* John Wiley & Sons, 2017.

[89] S. Lee, S. Kim, and J. Choi, "Dual-band dual-polarized proximity fed patch antenna for 28 ghz/39 ghz 5G millimeter-wave communications," in *2019 13th European Conference on Antennas and Propagation (EuCAP)*, 2019, pp. 1–5.

[90] B. Feng, X. He, J.-C. Cheng, and C.-Y.-D. Sim, "Dual-wideband dual-polarized metasurface antenna array for the 5G millimeter wave communications based on characteristic mode theory," *IEEE Access*, vol. 8, pp. 21 589–21 601, 2020.

[91] Y. He, M. Rao, Y. Liu, G. Jing, M. Xi, and L. Zhao, "28/39-ghz dual-band dual-polarized millimeter wave stacked patch antenna array for 5G applications," in *2020 International Workshop on Antenna Technology (iWAT)*, 2020, pp. 1–4.

[92] Z. Siddiqui, M. Sonkki, J. Chen, M. Berg, M. E. Leinonen, and A. Pärssinen, "Dual-band dual-polarized antenna for mm-wave 5G base station antenna array," in *2020 14th European Conference on Antennas and Propagation (EuCAP)*, 2020, pp. 1–4.

[93] W. Sun, Y. Li, L. Chang, H. Li, X. Qin, and H. Wang, "Dual-band dual-polarized microstrip antenna array using double-layer gridded patches for 5G millimeter-wave applications," *IEEE Transactions on Antennas and Propagation*, vol. 69, no. 10, pp. 6489–6499, 2021.

[94] J. Seo, I. Yoon, J. Jung, J. Ryoo, J. Park, W. Lee, D. Ko, and J. Oh, "Miniaturized dual-band broadside/endfire antenna-in-package for 5G smartphone," *IEEE Transactions on Antennas and Propagation*, vol. 69, no. 12, pp. 8100–8114, 2021.

[95] H.-N. Hu, F.-P. Lai, and Y.-S. Chen, "Dual-band dual-polarized scalable antenna subarray for compact millimeter-wave 5G base stations," *IEEE Access*, vol. 8, pp. 129 180–129 192, 2020.

[96] N. O. Parchin, M. Shen, and G. F. Pedersen, "End-fire phased array 5G antenna design using leaf-shaped bow-tie elements for 28/38 ghz mimo applications," in *2016 IEEE International Conference on Ubiquitous Wireless Broadband (ICUWB)*, 2016, pp. 1–4.

[97] R. Montoya Moreno, J. Ala-Laurinaho, A. Khripkov, J. Ilvonen, and V. Viikari, "Dual-polarized mm-wave endfire antenna for mobile devices," *IEEE Transactions on Antennas and Propagation*, vol. 68, no. 8, pp. 5924–5934, 2020.

[98] R. Lu, C. Yu, Y. Zhu, and W. Hong, "Compact millimeter-wave endfire dual-polarized antenna array for low-cost multibeam applications," *IEEE Antennas and Wireless Propagation Letters*, vol. 19, no. 12, pp. 2526–2530, 2020.

[99] N. O. Parchin, J. Zhang, R. A. Abd-Alhameed, G. F. Pedersen, and S. Zhang, "A planar dual-polarized phased array with broad bandwidth and quasi-endfire radiation for 5G mobile handsets," *IEEE Transactions on Antennas and Propagation*, vol. 69, no. 10, pp. 6410–6419, 2021.

[100] F. Xu and K. Wu, "Guided-wave and leakage characteristics of substrate integrated waveguide," *IEEE Transactions on Microwave Theory and Techniques*, vol. 53, no. 1, pp. 66–73, 2005.

[101] J. Thaysen, K. Jakobsen, and J. Appel-Hansen, “A wideband balun - how does it work?” *Applied Microwave & Wireless*, vol. 12, no. 10, pp. 40–50, Oct. 2000.

[102] W. Hong and K. Sarabandi, “Low profile miniaturized planar antenna with omnidirectional vertically polarized radiation,” *IEEE Transactions on Antennas and Propagation*, vol. 56, no. 6, pp. 1533–1540, 2008.

[103] W. Hong and K. Sarabandi, Kamal, “Low-profile, multi-element, miniaturized monopole antenna,” *IEEE Transactions on Antennas and Propagation*, vol. 57, no. 1, pp. 72–80, 2009.

[104] J. Oh and K. Sarabandi, “Low profile, miniaturized, inductively coupled capacitively loaded monopole antenna,” *IEEE Transactions on Antennas and Propagation*, vol. 60, no. 3, pp. 1206–1213, 2012.

[105] ——, “Low profile vertically polarized omnidirectional wideband antenna with capacitively coupled parasitic elements,” *IEEE Trans. Antennas Propag.*, vol. 62, no. 2, pp. 977–982, 2014.

[106] S. Ratnaker. (2021) Mobile phone size comparison – complete guide. [Online]. Available: https://inventionofmobilephones.com/mobile-phone-size-comparison-complete-guide/

[107] Neoscan. [Online]. Available: https://neoscan.com

[108] W. Stutzman L. and G. A. Thiele, *Antenna Theory and Design*, 3rd ed. John Wiley & Sons Inc, 2004.

[109] K. Zhao, S. Zhang, Z. Ho, O. Zander, T. Bolin, Z. Ying, and G. F. Pedersen, “Spherical coverage characterization of 5G millimeter wave user equipment with 3GPP specifications,” *IEEE Access*, vol. 7, pp. 4442–4452, 2019.

[110] H. Mosallaei and K. Sarabandi, “Antenna miniaturization and bandwidth enhancement using a reactive impedance substrate,” *IEEE Transactions on Antennas and Propagation*, vol. 52, no. 9, pp. 2403–2414, 2004.

[111] M. Rao and K. Sarabandi, “A dual-band dual-polarized 5G antenna for smartphones,” in *2020 IEEE International Symposium on Antennas and Propagation and North American Radio Science Meeting*, 2020, pp. 485–486.

[112] S. Silver, *microwave antenna theory and design.* New York: McGraw-Hill, 1949.

[113] P. Coquet, K. Mahdjoubi, and C. Terret, “Automatic antenna gain measurement at high frequencies,” *Electronics Letters*, vol. 28, no. 14, p. 1339, Jul. 1992.

[114] G. Felic, “Antenna gain measurements in the v-band: A single-antenna method,” in *2009 Electromagnetic Compatibility Symposium Adelaide*, 2009, pp. 98–101.

[115] J. Zheng, J. Ala-Laurinaho, and A. V. Räisänen, "On the one-antenna gain measurement method in probe station environment at mm-wave frequencies," *IEEE Transactions on Instrumentation and Measurement*, vol. 68, pp. 4510–4517, 2019.

[116] S. Beer and T. Zwick, "Probe based radiation pattern measurements for highly integrated millimeter-wave antennas," in *Proceedings of the Fourth European Conference on Antennas and Propagation*, 2010, pp. 1–5.

[117] J. Ala-Laurinaho, J. Zheng, and A. Raisanen, "One-antenna gain measurement in a probe station," in *2018 IEEE Conference on Antenna Measurements & Applications (CAMA)*, 09 2018, pp. 1–4.

[118] H. Kim and C. Jung, "Ultra-wideband endfire directional tapered slot antenna using cpw to wide-slot transition," *Electronics Letters*, vol. 46, pp. 1183–1185(2), August 2010.

[119] J. Oh and K. Sarabandi, "Low profile vertically polarized omnidirectional wideband antenna with capacitively coupled parasitic elements," *IEEE Transactions on Antennas and Propagation*, vol. 62, no. 2, pp. 977–982, 2014.

[120] R. E. Collin, *Antennas and Radiowave Propagation.* New York: McGraw-Hill, 1985.

[121] Y. Wu, J. Liang, K. Rensing, and M. Chou, T. M.and Libera, "Extracellular matrix reorganization during cryo preparation for scanning electron microscope imaging of staphylococcus aureus biofilms," *Microscopy and microanalysis*, vol. 20, no. 5, pp. 1348–1355, 2014.

[122] S. M. Amjadi, M. Rao, and K. Sarabandi, "Wideband near-zone radiative system for exploring the existence of electromagnetic emission from biological samples," *IEEE Transactions on Instrumentation and Measurement*, vol. 69, no. 10, pp. 8344–8351, 2020.

[123] V. Ranieri, A. Deutsch, G. Kopcsay, and G. Arjavalingam, "A novel 24-ghz bandwidth coaxial probe," *IEEE Transactions on Instrumentation and Measurement*, vol. 39, no. 3, pp. 504–507, 1990.

[124] M. L. Crawford, "Generation of standard em fields using tem transmission cells," *IEEE Transactions on Electromagnetic Compatibility*, vol. EMC-16, no. 4, pp. 189–195, 1974.

[125] D. Pouhe, "Rf radiation properties of printed-circuits boards in a gtem cell," *IEEE Transactions on Electromagnetic Compatibility*, vol. 48, no. 3, pp. 468–475, 2006.

[126] S. Deng, T. H. Hubing, and D. G. Beetner, "Using tem cell measurements to estimate the maximum radiation from pcbs with cables due to magnetic field

coupling," *IEEE Transactions on Electromagnetic Compatibility*, vol. 50, no. 2, pp. 419–423, 2008.

[127] T.-H. Loh and M. J. Alexander, "A method to minimize emission measurement uncertainty of electrically large euts in gtem cells and fars above 1 ghz," *IEEE Transactions on Electromagnetic Compatibility*, vol. 48, no. 4, pp. 634–640, 2006.

[128] Z. Ji, C. Hagness, H. Booske, S. Mathur, and M. Meltz, "Fdtd analysis of a gigahertz tem cell for ultra-wideband pulse exposure studies of biological specimens," *IEEE Transactions on Biomedical Engineering*, vol. 53, no. 5, pp. 780–789, 2006.

[129] P. Alotto, D. Desideri, F. Freschi, A. Maschio, and M. Repetto, "Dual-peec modeling of a two-port tem cell for vhf applications," *IEEE Transactions on Magnetics*, vol. 47, no. 5, pp. 1486–1489, 2011.

[130] S. Deng, D. Pommerenke, T. Hubing, and D. Shin, "An experimental investigation of higher order mode suppression in tem cells," *IEEE Transactions on Electromagnetic Compatibility*, vol. 50, no. 2, pp. 416–419, 2008.

[131] W. Sun and C. Balanis, "Analysis and design of quadruple-ridged waveguides," *IEEE Transactions on Microwave Theory and Techniques*, vol. 42, no. 12, pp. 2201–2207, 1994.

[132] J. L. Kerr, "Short axial length broad-band horns." *IEEE Transactions on Antennas and Propagation*, vol. 21, pp. 710–714, Jan. 1973.

[133] F. Ulaby, D. Long, W. Blackwell, C. Elachi, A. Fung, C. Ruf, K. Sarabandi, J. Zyl, and H. Zebker, *Microwave Radar and Radiometric Remote Sensing.* University of Michigan Press, 01 2014.

[134] [Online]. Approximations for mean and variance of a ratio. [Online]. Available: https://www.stat.cmu.edu/ hseltman/files/ratio.pdf

[135] L. Tsang, J. A. Kong, and K. Ding, *Scattering and Emission by Layered Media.* nthoseth: John Wiley & Sons, Ltd, 2000, pp. 199–229.

[136] K. Schwartz, A. K. Syed, R. E. Stephenson, A. H. Rickard, and B. R. Boles, "Functional amyloids composed of phenol soluble modulins stabilize staphylococcus aureus biofilms," *PLOS Pathogens*, vol. 8, no. 6, pp. 1–11, 06 2012.

[137] M. Yang, K. Sun, and N. A. Kotov, "Formation and assembly-disassembly processes of zno hexagonal pyramids driven by dipolar and excluded volume interactions," *Journal of the American Chemical Society*, vol. 132, no. 6, pp. 1860–1872, 2010.

[138] M. McGuffie, J. Hong, J. H. Bahng, E. Glynos, P. F. Green, N. A. Kotov, J. G. Younger, and J. S. VanEpps, "Zinc oxide nanoparticle suspensions and layer-by-layer coatings inhibit staphylococcal growth," *Nanomedicine : nanotechnology, biology, and medicine*, vol. 12, no. 1, pp. 33–42, 2016.

[139] U. Kadiyala, E. S. Turali-Emre, J. H. Bahng, N. A. Kotov, and J. S. VanEpps, "Unexpected insights into antibacterial activity of zinc oxide nanoparticles against methicillin resistant staphylococcus aureus (mrsa)," *Nanoscale*, vol. 10, no. 10, p. 4927–4939, 2018.

[140] R. McDonough and A. Whalen, *Detection of signals in noise*. Academic Press, 1995.

[141] S. Periasamy, H.-S. Joo, A. C. Duong, T.-H. L. Bach, V. Y. Tan, S. S. Chatterjee, G. Y. C. Cheung, and M. Otto, "How staphylococcus aureus biofilms develop their characteristic structure," *Proceedings of the National Academy of Sciences*, vol. 109, no. 4, pp. 1281–1286, 2012. [Online]. Available: https://www.pnas.org/content/109/4/1281

[142] J. Pérez-Velézquez, M. Gölgeli, and R. García-Contreras, "Mathematical modelling of bacterial quorum sensing: A review." *Bulletin of Mathematical Biology*, vol. 78, p. 1585–1639, 2016.

[143] M. Marenda, M. Zanardo, A. Trovato, F. Seno, and A. Squartini, "Modeling quorum sensing trade-offs between bacterial cell density and system extension from open boundaries," *Scientific Reports*, vol. 6, no. 39142, 2016.

[144] J. M. Yarwood, D. J. Bartels, E. M. Volper, and E. P. Greenberg, "Quorum sensing in staphylococcus aureus biofilms," *Journal of bacteriology*, vol. 186, no. 6, 2004.

[145] E. Armstrong, "Some recent developments of regenerative circuits," *Proceedings of the Institute of Radio Engineers*, vol. 10, no. 4, pp. 244–260, 1922.

[146] A. Vouilloz, M. Declercq, and C. Dehollain, "A low-power cmos super-regenerative receiver at 1 ghz," *IEEE Journal of Solid-State Circuits*, vol. 36, no. 3, pp. 440–451, 2001.

[147] J. L. Bohorquez, A. P. Chandrakasan, and J. L. Dawson, "Frequency-domain analysis of super-regenerative amplifiers," *IEEE Transactions on Microwave Theory and Techniques*, vol. 57, no. 12, pp. 2882–2894, 2009.

[148] P. Sharma. 4 types of distance metrics in machine learning," 2020. [Online]. Available: https://www.analyticsvidhya.com/blog/2020/02/4-types-of-distance-metrics-in-machine-learning/